



HAL
open science

Optimization of a high temperature solar receiver by polydispersion of particles

Freddy Ordóñez Malla Ordóñez Malla

► **To cite this version:**

Freddy Ordóñez Malla Ordóñez Malla. Optimization of a high temperature solar receiver by polydispersion of particles. Chemical and Process Engineering. Université Paris-Est, 2014. English. NNT : 2014PEST1072 . tel-01127486

HAL Id: tel-01127486

<https://theses.hal.science/tel-01127486>

Submitted on 7 Mar 2015

HAL is a multi-disciplinary open access archive for the deposit and dissemination of scientific research documents, whether they are published or not. The documents may come from teaching and research institutions in France or abroad, or from public or private research centers.

L'archive ouverte pluridisciplinaire **HAL**, est destinée au dépôt et à la diffusion de documents scientifiques de niveau recherche, publiés ou non, émanant des établissements d'enseignement et de recherche français ou étrangers, des laboratoires publics ou privés.



Thèse présentée pour obtenir le grade de
Docteur de l'Université Paris-Est

Spécialité : Génie des Procédés

par

Freddy Ordóñez Malla

Ecole Doctorale : SCIENCES, INGÉNIERIE ET ENVIRONNEMENT

*Optimisation d'un récepteur solaire haute
température à polydispersion de particules*

Thèse soutenue le 10 octobre 2014 devant le jury composé de :

Françoise BATAILLE	Professeur, Université de Perpignan	<i>Co-directrice de thèse</i>
Jean-Jacques BEZIAN	Ingénieur de recherche, Ecole des Mines d'Albi	<i>Rapporteur</i>
Pascal BOULET	Professeur, Université de Lorraine	<i>Rapporteur</i>
Cyril CALIOT	Chargé de recherche CNRS, Lab. PROMES	<i>Co-encadrant de thèse</i>
Gilles FLAMANT	Directeur de recherche CNRS, Lab. PROMES	<i>Examineur</i>
Guy LAURIAT	Professeur, Université Paris-Est	<i>Directeur de thèse</i>

Résumé

Les centrales solaires à concentration sont des technologies prometteuses pour la production d'énergie d'origine renouvelable. Celles mettant en œuvre des cycles thermodynamiques à hautes températures, tels que les cycles combinés, permettent d'augmenter l'efficacité de la conversion solaire. Ces cycles nécessitent le développement de nouveaux récepteurs à haute température ($T > 1100K$), tels que les récepteurs solaires à particules (SPRs). Ce travail porte sur l'optimisation numérique des principaux paramètres pilotant l'efficacité de ce type de récepteurs, l'enjeu principal étant de minimiser les pertes par rayonnement thermique.

Dans un premier temps, un modèle simplifié des transferts radiatifs dans un SPR a été développé. Le modèle considère un milieu particulaire soumis à un flux solaire concentré et collimaté. Le milieu émet, absorbe et diffuse le rayonnement de manière anisotrope. L'équation de transfert radiatif est résolue par une méthode à deux-flux (géométrie $1D$) avec l'approximation delta-Eddington, permettant une obtention rapide des résultats. Cette méthode a été choisie pour son adéquation aux cas d'émission et de diffusion anisotropes. L'hypothèse de diffusion indépendante est utilisée afin de déterminer les propriétés optiques du milieu. La théorie de Lorenz-Mie a été utilisée pour calculer les efficacités optiques des particules. Ce modèle est mis en œuvre avec un algorithme d'optimisation par essais particuliers, dans le but de déterminer la taille des particules, leur fraction volumique, et leur indice de réfraction optimums.

Dans un deuxième temps, six matériaux réels sont sélectionnés afin de tenter de retrouver le résultat optimum obtenu précédemment avec un matériel idéal. Ces matériaux (HfB_2 , ZrB_2 , HfC , ZrC , W et SiC) sont pertinents du fait de leur comportement sélectif ou de leur absorptivité élevée. Afin de déterminer leurs indices de réfraction, la relation de dispersion de Kramers-Kronig a été utilisée à partir de données de réflectance issues de la littérature. Trois configurations de récepteurs ont été étudiées : a) un milieu homogène comprenant un seul type de particules, b) un milieu inhomogène comprenant deux matériaux différents, c) un milieu homogène comprenant des particules enrobées. D'après les résultats de ces configurations, les particules de W enrobées de SiC permettent d'atteindre des performances proches du cas idéal optimisé.

Enfin, un modèle numérique de transfert thermique par convection et rayonnement a été développé, pour étudier l'influence de l'écoulement sur les pertes radiatives du récepteur. Il est basé sur une géométrie simple constituée d'un écoulement d'un

mélange de gaz et de particules circulant entre deux plaques planes, l'une étant une fenêtre par laquelle pénètre perpendiculairement le flux solaire. Le modèle radiatif développé précédemment permet de calculer la divergence du flux radiatif, tandis que l'équation de l'énergie est résolue en régime turbulent en utilisant des modèles d'écoulement et de diffusivité thermique turbulente simplifiés. Ainsi, les conditions de l'écoulement et des propriétés radiatives qui minimisent les pertes du récepteur sont déterminées.

De futurs travaux pourront être élargis à de nouveaux matériaux candidats pour les récepteurs solaires à particules. Leur indice de réfraction pourra être mesuré et comparé aux valeurs théoriques obtenues par les codes développés dans le cadre de ce travail.

Mots clés : Récepteur solaire à particules à haute température, optimisation, modélisation, méthode à deux-flux.

Abstract

Solar Particle Receivers (SPRs) are promising candidates to work at high temperatures ($T > 1100\text{ K}$) in Central Solar Power (CSP) plants. They will permit the use of high efficient thermodynamic cycles, such as a combined cycle (Brayton cycle + Rankine cycle). Nevertheless, the optimal conditions that reduce the receiver losses (and consequently maximize the receiver efficiency) still remain to be studied. In this work, the principal parameters that drive the receiver efficiency are numerically optimized.

For this end, a simplified radiative model is developed, which allows one to run the high number of simulations needed in such optimization. This model consists in a $1D$ slab of particulate media submitted to a collimated and concentrated solar flux. The medium emits, absorbs and anisotropically scatters energy. A two-stream method with a delta-Eddington approximation is implemented to fast solve the radiative transfer equation. Among the several two-stream approximations, the one proposed by Joseph *et al.* (1976) is chosen due to its good treatment of the anisotropic scattering. The volume optical properties are computed under the independent scattering hypothesis and the single-particle optical properties with the Lorenz-Mie theory. Such a model is used with a Particle Swarm Optimization algorithm to find the optimal particle size, volume fraction and complex refractive index to be used in the receiver.

Once the ideal optimal conditions for a SPR are found, the replication of these results is attempted by using real materials. Six materials (HfB_2 , ZrB_2 , HfC , ZrC , W and SiC) are chosen because of their spectral selective behavior or their high absorptivity. At this stage, an important difficulty is the lack of information about the refractive indexes of materials. Therefore, the Kramers-Kronig dispersion relations are utilized to find the refractive indexes from reflectance data. Then, three SPR configurations are considered: (a) a homogeneous medium with only one kind of particles, (b) a medium with a mixture of two materials and, (c) a homogeneous medium with coated particles. The three configuration results are compared with those obtained using particles made of an ideal material. A remarkable result is obtained when W -particles coated with SiC are used. This configuration decreases the radiative losses approaching to the ideal minimal.

Finally, the influence of the fluid flow on the radiative losses is studied through the implementation of a convection-radiation heat transfer model. A simple geometry is adopted for a gas-particles mixture flow between two parallel plates, where one of them is a window. The concentrated solar radiation then affects perpendicularly the fluid flow. The energy equation is solved using a low-Mach approximation and the divergence

of the radiative flux with the radiative model developed before. A parametric study is conducted to investigate the influence of the optical properties on the radiative losses.

In the future, more materials remain to be investigated to be used in solar particle receivers. To this end, the refractive indexes of a number of materials should be measured. The developed codes will be useful for this investigation.

Key words

High temperature solar particle receiver, optimization, modeling, two-stream method.

Per a l'Irene
Gràcies per compartir aquest moment amb mi

Acknowledgments

This work is the result of the contributions of many people, which in several ways, have helped me to achieve such results.

I would like to express my gratitude to all the staff (researchers, technicians, students, kitchen staff, cleaning staff, etc.) of PROMES and MSME Laboratories. Without their great help, their advice, their good willingness and all our scientific (and most of the times not at all scientific) discussions, this work would have not reached the end.

And thanks to the people that believed in me and gave me their support. To my family and to my friends, because they are my example and my inspiration.

Table of contents

Résumé	iii
Abstract	v
Nomenclature	xv
Introduction	1
References	5
1 Literature review	7
1.1 Solar particle receivers	7
1.1.1 SPRs using small entrained particles	7
1.1.2 SPRs using large free-falling particles	11
1.1.3 SPRs using fluidized beds of particles	12
References	14
2 Physical radiative model	17
2.1 Introduction	17
2.2 Model description	18
2.3 The Radiative Transfer Equation (RTE)	19
2.3.1 The plane parallel problem	20
2.3.2 The two-stream method	21
2.3.3 The multiple-layer two-stream solution	25
2.3.4 Radiative boundary conditions	26
2.4 Volume radiative properties of a cloud of particles	26
2.4.1 Mono-dispersion of particles	27
2.4.2 Poly-dispersion of particles	27
2.5 Radiative properties of a spherical single-particle	29
2.5.1 The Mie coefficients, cross sections and efficiencies	30
2.5.2 The asymmetry factor and the phase function	31
2.6 The monochromatic algorithm	33
2.6.1 Validation of the subroutines	33
2.7 Conclusions	38
References	39

3	The accuracy of the two-stream method to model a solar particle receiver	41
3.1	Introduction	41
3.2	Treatment of the errors	43
3.3	The Henyey-Greenstein and the Lorenz-Mie phase functions	44
3.4	General accuracy of the two-stream method	46
3.4.1	Cold media with an incident flux	47
3.4.2	Emissive media without incident flux	48
3.5	The two-stream method for computing the optimized radiative losses	50
3.5.1	Radiative losses using the Monte Carlo method and the Henyey-Greenstein phase function	50
3.5.2	Radiative losses using the Monte Carlo method and the Lorenz-Mie phase function	51
3.6	Conclusion	53
	References	54
4	Optimization of the optical particle properties for a high temperature solar particle receiver	57
4.1	Introduction	57
4.2	The Particle Swarm Optimization algorithm	58
4.3	The mono-dispersion as a representation of the poly-dispersion of particles	59
4.4	Parametric study of a cold SPR.	60
4.4.1	Radiative transport properties of a single particle	61
4.4.2	Radiative transport properties of a homogeneous slab of particles dispersion	61
4.5	The optimal radiative properties for a SPR	63
4.5.1	Particle receiver conditions	63
4.5.2	The ideal material to use in a particle receiver	64
4.5.3	Influence of the volume fraction	67
4.5.4	Influence of the particle radius	68
4.6	Two layer simulations	69
4.7	Conclusion	72
	References	73
5	Improvement of radiative performances using coated particles and mixtures in a high temperature solar particle receiver	75
5.1	Introduction	75
5.2	Solar particle receiver conditions	76
5.3	Materials optical properties	77
5.3.1	The reflectivity and the phase-shift Kramers-Kronig dispersion relations	78
5.3.2	The refractive index of the materials	79
5.4	Improvements of the radiative performances in a SPR	80
5.4.1	The optimized ideal material	81
5.4.2	Homogeneous layer with a single-material	82

5.4.3	Homogeneous layer composed of mixtures of <i>SiC</i> with another material	84
5.4.4	Homogeneous layer with coated particles	84
5.5	Conclusions	86
	References	88
6	Numerical study of the radiative and convective heat transfer coupling in a high temperature SPR	91
6.1	Introduction	91
6.2	Model description	92
6.3	Model development	93
6.3.1	General formulation of the energy equation	93
6.3.2	Convection heat transfer in a parallel plate channel	95
6.3.3	Approximate turbulent modeling	97
6.3.4	Thermal boundary conditions	97
6.3.5	Enthalpy flux balance	98
6.3.6	Velocity profiles	99
6.3.7	Variable density flow consideration	102
6.3.8	Radiative heat dissipation	103
6.4	Numerical solution	104
6.4.1	Turbulent flow between two parallel plates with an uniform heat generation rate	105
6.4.2	Effects of temperature dependent thermo-physical properties	110
6.4.3	Absorbing, scattering and emitting slug flow between two parallel plates	115
6.5	Radiative and convective heat transfer coupling	117
6.6	Parametric study of a SPR with a radiative and convective coupling model	122
6.6.1	Influence of the back wall reflectivity and the volume fraction	123
6.6.2	Influence of the particles material	126
6.7	Conclusions	128
	References	130
7	General conclusions	133
A	The two-stream method approximation	137
A.1	The γ -terms in the Meador and Weaver two-stream approximation	137
A.2	The multi-layer, two-stream solution using a tridiagonal matrix	140
A.3	The radiative losses for the cold solar particle receiver	144
B	The Monte Carlo method	147
B.1	The Monte Carlo method for the radiative transfer in a participating media	147
C	The Kramers-Kronig dispersion relations	153
C.1	Comparison using the Lorentzian function	153
C.2	Comparison using the <i>SiC</i> refractive index	154

Table of contents

D Numerical method for solving the energy equation and validation tests.	157
D.1 Control volume method discretization	157
D.2 Code validations	161
List of tables	176
List of figures	182

Nomenclature

Latin letters

a, b	gamma distribution parameters
a_f	fluid thermal diffusivity [m^2/s]
a_n, b_n	Mie coefficients
A	power-law velocity profile constant
c_s	sound speed [m/s]
c_1, c_2	local and global acceleration in the PSO algorithm
C	concentration of solar energy
C_m	meshing constant coefficient
C_p	constant pressure heat thermal capacity [$J/(kgK)$]
C_v	constant volume heat thermal capacity [$J/(kgK)$]
$C_{p,r}$	reference heat thermal capacity (evaluated at T_r) [$J/(kgK)$]
C_{abs}	absorption cross-section [m^2]
C_{ext}	extinction cross-section [m^2]
C_{sca}	scattering cross-section [m^2]
D	depth receiver [m]
D_h	hydraulic diameter [m]
Ec	Eckert number
f_v	volume fraction
G	source function in the radiative transfer equation [$W/m^2 sr \mu m$]
G^\pm	forward and backward source function [$W/m^2 \mu m$]
g	asymmetry factor
\tilde{g}	single-particle asymmetry factor
\bar{h}_e	external convection heat transfer coefficient [$W/m^2 K$]
\bar{h}_i	interior convection heat transfer coefficient [$W/m^2 K$]
I	specific intensity [$W/m^2 sr \mu m$]
I_b	blackbody emission intensity [$W/m^2 sr \mu m$]
I_c	collimated intensity [$W/m^2 sr \mu m$]
I_d	diffuse intensity [$W/m^2 sr \mu m$]
I_0	initial intensity in the Monte Carlo method [$W/m^2 sr \mu m$]
k	imaginary part of refractive index
k_f	fluid thermal conductivity [$W/(mK)$]
K	von Karman constant
l_m^+	dimensionless mixing length
L	length receiver [m]
\mathcal{L}	reference length [m]

m	complex refractive index
\dot{m}	mass flow rate [kg/s]
Ma	Mach number
N	number of the events in the Monte Carlo method
$N(r)$	number density distribution in a particle polydispersion
Nr	radiation-conduction parameter
Nu	Nusselt number
N_0	total number of particles per unit volume in a particle polydispersion
n	real part of refractive index
n_x	discretization in the x -direction
n_y	discretization in the y - direction
n_μ	angle discretization in the χ_0 computations
p	scattering phase function
p_{HG}	Henyey-Greenstein phase function
\tilde{p}	single-particle scattering phase function
p_k^i, p_k^g	best i -position and best global swarm position at the pseudo-time step k in the PSO algorithm
P	thermodynamic pressure [Pa]
Pe	Peclet number
Pr	Prandtl number
Pr_t	turbulent Prandtl number
q_0	incident solar flux [W/m^2]
q^\pm	forward and backward radiative heat fluxes [W/m^2]
q_r	radiative flux in the energy equation [W/m^2]
q_w	wall boundary flux [W/m^2]
Q_{abs}	single-particle absorption efficiency
Q_{ext}	single-particle extinction efficiency
Q_{sca}	single-particle scattering efficiency
\dot{Q}'''	energy source term [W/m^3]
Q_{ext}/r	average extinction efficiency to particle radius ratio
r	particle radius [μm]
r_{mp}	most probable radius [m]
r_{mp}/r_{32}	width parameter
\tilde{r}_R	complex reflectivity amplitude
r_R	real part of the reflectivity amplitude
r_1, r_2	uniform random numbers for the PSO algorithm
r_{32}	32 moment radius [m]
R	reflectance
Re	Reynolds number
RL	radiative losses [kW/m^2]
R_{cond}	conduction resistance [m^2K/W]
$R_{thermal}$	thermal resistance [m^2K/W]
R_1	random number in the Monte Carlo method
\bar{R}	particular constant of the air [$J/(kgK)$]
s	optical path length
S	source function

S_R	sampling result in the Monte Carlo method
S_1, S_2	complex amplitude functions
T	temperature into the receiver [K]
T_{amb}	external ambient temperature [K]
T_{in}	inlet temperature [K]
T_m	mixing-cup temperature [K]
T_r	reference temperature [K]
T_w	wall temperature [K]
u	x -component of the fluid velocity [m/s]
u_f	friction velocity
u_m	mean velocity [m/s]
u_{max}	maximum velocity [m/s]
u_r	x -component reference fluid velocity [m/s]
u^+	dimensionless velocity
\bar{U}	overall heat transfer coefficient [W/(m ² K)]
v	y -component of the fluid velocity [m/s]
v_k^i	velocity for the particle i at the pseudo-time step k in the PSO algorithm
\vec{V}	velocity vector [m/s]
w	inertia weight in PSO algorithm
W	weight of the energy packet in the Monte Carlo method
x	parameter size
y_k^i	position for the particle i at the pseudo-time step k in the PSO algorithm
y^+	dimensionless depth

Greek letters

α_1, α_2	α -terms in the two-stream method
α_w	wall absorptivity
β	volume extinction coefficient [m ⁻¹]
β_f	fluid thermal coefficient [K ⁻¹]
ε	slab emissivity
ε_w	wall emissivity
ϵ_H	thermal eddy diffusivity [m ² /s]
ϵ_m	momentum eddy diffusivity [m ² /s]
ϵ^+	dimensionless eddy diffusivity [m ² /s]
γ	heat capacity ratio
γ_{PSO}	velocity factor in the PSO algorithm
γ_L	band-width at half height in the Lorentzian function
$\gamma_1, \gamma_2, \gamma_3, \gamma_4$	γ -terms in the two-stream solution
η	receiver efficiency
θ	dimensionless temperature
θ_R	imaginary part of the reflectivity amplitude
κ	volume absorption coefficient [m ⁻¹]
λ	wavelength [μ m]

μ	cosine of the polar angle $\mu = \cos\theta$
μ_f	fluid dynamic viscosity [$Pa \cdot s$]
μ_r	reference dynamic viscosity (evaluated at T_r) [$Pa \cdot s$]
μ_0	cosine direction of the collimated incident flux
ν	ν -term in the two-stream approximation
ν_f	fluid kinematic viscosity [m^2/s]
Φ	viscous dissipation function [s^{-2}]
ρ_f	fluid density [kg/m^3]
ρ_r	reference fluid density (evaluated at T_r) [kg/m^3]
ρ_w	wall reflectivity
σ	volume scattering coefficient [m^{-1}]
σ_{MC}	statistical variance
σ_{SB}	Stefan Boltzmann constant [$W/(m^2K^4)$]
τ	optical depth
τ_c	cumulative optical depth
χ_0	χ_0 -term for the modified Eddington approximation
Ω	solid angle [sr]
ω	wave frequency [s^{-1}]
ω_0	scattering albedo
$\tilde{\omega}_0$	single-particle scattering albedo
ω_t	transport albedo

Acronyms

CFD	Computational Fluid Dynamics
CSP	Concentrated Solar Power
DOM	Discrete Ordinates Method
HG	Henyey-Greenstein phase function
KK	Kramers-Kronig dispersion relations
MCM	Monte Carlo Method
PSO	Particle Swarm Optimization algorithm
RTE	Radiative Transfer Equation
SPR	Solar Particle Receiver
UHTC	Ultra-High Temperature Ceramic

Introduction

The world primary energy demand is continuously increasing (i.e. from near 6 Gt to 12 Gt of oil equivalent per year from 1970 to 2009), being the fossil fuels the principal product consumed (in 2009, the 27.2%, 32.9% and 20.9% of world energy demand correspond to the coal, oil and gas respectively) [7]. As the consequence, environmental (energy production by burning hydrocarbons is responsible of about 65% of global anthropogenic greenhouse-gas emissions [6]) and geopolitical conflicts (the pressure in fossil fuels supplier regions increases [1], led conflicts to control the production areas [8]) are involved. Reductions in the typical energy consumption patterns and the use of the renewable energy sources claim to be implemented. Concentrated Solar Power (CSP) plants with optical concentration technologies are important candidates for becoming a major renewable energy resource in the medium-term [2]. It is nevertheless necessary to rise up their overall efficiencies to become competitive with fossil fuel power plants. As an example, an annual efficiency of 20% is expected for a CSP plant face to an annual efficiency that surpasses the 50% for a gas combined cycle [9].

One relevant solution to increase the STPP efficiency is working with a combined cycle. The most general solar combined cycle uses a gas turbine (Brayton cycle) followed by a steam turbine (Rankine cycle) (see figure 1). In this case the energy source is a concentrated solar flux. The solar radiation is concentrated by a field of mirrors (heliostats) and pointed to a receiver located at the top of a tower. The receiver absorbs the concentrated solar radiation and transfer the heat to the working fluid (normally a gas). The heated gas then may be used directly in the Brayton cycle and after in the recuperation exchanger for the Rankine cycle.

The receiver is a key component in a CSP plant, because it drives the working temperature of the thermodynamic cycle and consequently its global efficiency. In actual CSP plants, surface receivers are the most useful, due to its ease of implementation. However, limitations in the working temperature are imposed in this kind of receiver to maintain moderate radiative losses and to preserve the thermo-mechanical properties of the material. Volumetric receivers with gas as heat transfer fluid (normally air) present great advantages in comparison to surface receivers, such as the ability to work at high temperatures. It is because the solar radiation is not absorbed on an outer surface but in the depth (inside the volume) of the structure [9], reducing the energy losses by emission. In Fig. 1.2 the schematic comparison between a surface receiver and a volumetric receiver is shown.

Nowadays, two main concepts of volumetric receivers are investigated. First, porous receivers that use highly porous structures made of metals, ceramic or other adequate material for the concentrated solar radiation absorption. The heat transfer fluid is forced to flow through the porous structure, and is heated by convection [2]. Secondly,

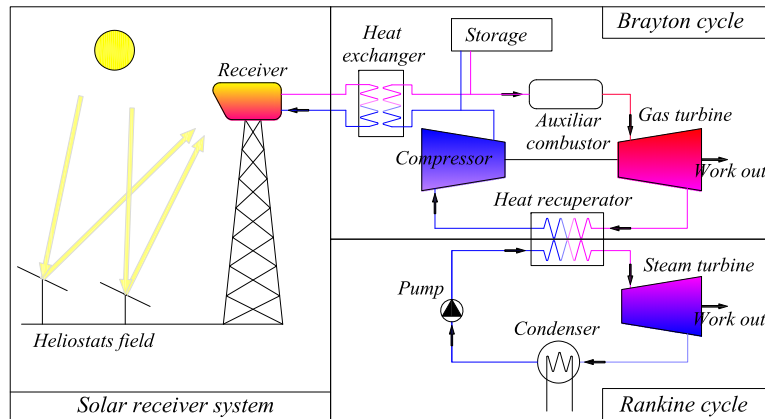


Figure 1: Schematic of a Concentrated Solar Power plant using a combined cycle

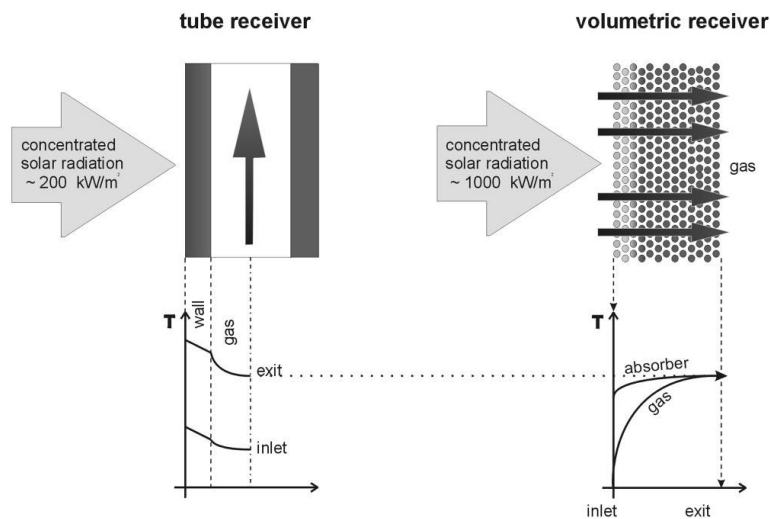


Figure 2: Schematic representation of absorption and heat transfer of a surface and a volumetric receiver (Fig. taken from [9])

particle receivers that use sub-micron [5], micron [4] or millimetric particles [3] to absorb the incident solar radiation. The particles are embedded in the heat transfer fluid, which is heated by the particles by convection and conduction.

The optimal conditions that maximize the efficiency of a high temperature SPR are still insufficiently studied. A theoretical approach is required to define the influence of particle optical properties and the best configuration possible to reach a maximal efficiency. The effect of the temperature distribution within a particle layer and the presence of different particles were not previously studied.

Objectives

The principal objective in this work is the optimization of the radiative behavior of a high temperature solar particle receiver. Various secondary objectives become detached of it. They are the following:

- Development and validation of a model of a high temperature SPR. Such model needs to be less expensive in computational time in order to be used in a optimization algorithm.
- Investigation of the optimal idealized material properties (refractive index) and conditions (particle radii, particle number, particle distribution) to be used in a high temperature SPR.
- Approximation to the ideal behavior through the use of real materials.
- Study of the influence of the fluid flow in the SPR on the radiative behavior of an optimized SPR.

Methodology

To achieve the objectives proposed above the following methodology is planned:

- In Chapter 1, a literature review about solar particle receivers starts this work. Special attention is done to the materials and conditions used in the different investigations. The adopted classification includes SPRs with small entrained particles, with large free-falling particles and fluidized beds.
- The high temperature SPR is modeled as a $1D$ slab of particles dispersion submitted to a collimated and concentrated incident solar flux. In order to reduce the computational time needed to solve the radiative transfer equation (RTE) a two-stream method is used. This model is solved for a single wavelength to take into account the spectral variation of the refractive index and the incident flux. Also, an imposed temperature is considered. Such model is presented in Chapter 2.
- The main simplification in the proposed model is the use of the two-stream method. Several authors investigated the accuracy of that method, but for other purposes. A lack of information about the accuracy of this method for SPR modeling remains. In Chapter 3 an investigation about the accuracy of the two-stream method used in the SPR modeling is carried on. The influence of the use of the Henyey-Greenstein phase function approximation instead of the Mie phase function is also studied.
- Once the model is validated, an optimization of the refractive index, particle radius and volume fraction is conducted. The use of a mono-dispersion instead a poly-dispersion is analyzed. The optimization uses a particle swarm optimization algorithm (PSO), which is an heuristic optimization algorithm. Heuristic

optimization methods are recommendable for problems with large number of variables. An ideal material that minimizes the radiative losses is provided. This investigation is done in Chapter 4.

- Next, in Chapter 5, several materials are studied as candidates to approach to the ideal optimal behavior. *SiC*, *W* and a number of ultra high temperature ceramics are considered. The improvements found when mixtures or coated particles are reported.
- Finally, the influence of the fluid flow on the radiative behavior of the optimized SPR is studied. The energy equation is coupled with the radiative model for the optimal conditions. This study is presented in Chapter 6.

References

- [1] K. Aleklett and C. Campbell. The peak and decline of world oil and gas production. *Minerals and Energy - Raw Materials Report*, 18:5–20, 2003.
- [2] A. Ávila-Marín. Volumetric receivers in solar thermal power plants with central receiver system technology: a review. *Solar Energy*, 85:891–910, 2011.
- [3] G. Baud. *Conception de récepteurs solaires à lit fluidisé sous flux radiatif concentré*. PhD thesis, Institut National Polytechnique de Toulouse, 2011.
- [4] B. Gobereit, L. Amsbeck, R. Buck, R. Pitz-Paal, and H. Muller-Steinhagen. Assessment of a falling solid particle receiver with numerical simulation. In *SolarPaces: Concentrating Solar Power and Chemical Energy Systems, Marrakech-Morocco*, September 2012.
- [5] A. Hunt and F. Miller. Small particle heat exchanger receivers for solar thermal power. In *SolarPaces: Concentrating Solar Power and Chemical Energy Systems, Perpignan-France*, September 2010.
- [6] IEA. *CO₂ emissions from fuel combustion highlights*. Technical report, International Energy Agency, 2011.
- [7] IEA. *World energy outlook*. Technical report, International Energy Agency, 2011.
- [8] M. Klare. *Blood and oil*. Henry Holt and Company, LLC, 2006.
- [9] M Romero, R Buck, and J Pacheco. An update on solar central receiver systems, projects and technologies. *Journal of Solar Energy Engineering*, 124:98–108, 2002.

Chapter 1

Literature review

Abstract

A bibliographic study about solar particle receivers is conducted. It is carried on the published literature and on the patented devices, and includes solar particle reactors. The classification allows for SPRs using entrained small particles, SPRs using free-falling large particles and fluidized beds. The principal examples found in the literature are revisited.

1.1 Solar particle receivers

The use of particles in a solar receiver was proposed for the first time by Hunt [16] and Abdelrahman [1], independently. In particle receivers the concentrated solar radiation is absorbed by particles, which are embedded in the fluid gas, increasing their temperature. The absorbed heat is then transferred to the gas by convection and conduction. High temperatures are expected in this kind of receivers. Currently they are being studied, both to drive a gas turbine for electricity, and to carry out suitable chemical reactions. In this section a review of advances in particles volumetric receivers is presented in accordance with the size of particles used in the receiver.

1.1.1 SPRs using small entrained particles

Several researches have been devoted to study the use of small entrained particles in solar receivers. A great advantage claimed is the near selective behavior at high temperatures given by small particles. A first approach for the optical behavior of small particles was given by Abdelrahman *et al.* [1]. They studied the dependence between the absorptance of small particles as a function of their radii and their imaginary part of the refractive index. A particle radius of $r = 0.5 \mu m$ and an imaginary refractive index of $k = 0.6$ which corresponds approximately to those of graphite were recommended. Independently, Hunt [16] proposed submicron particles of graphite and vitreous carbon as the best absorber in a particle receiver. Iron and silicon are also suggested as alternative materials. A receiver efficiency above 95% and high achievable temperature

1.1. Solar particle receivers

(2375 K) were estimated. In Fig. 1.1 are presented two devices proposed following its work. In Fig. 1.1a the system for radiant energy transform [17], while in Fig. 1.1b its solar receiver [18] are shown.

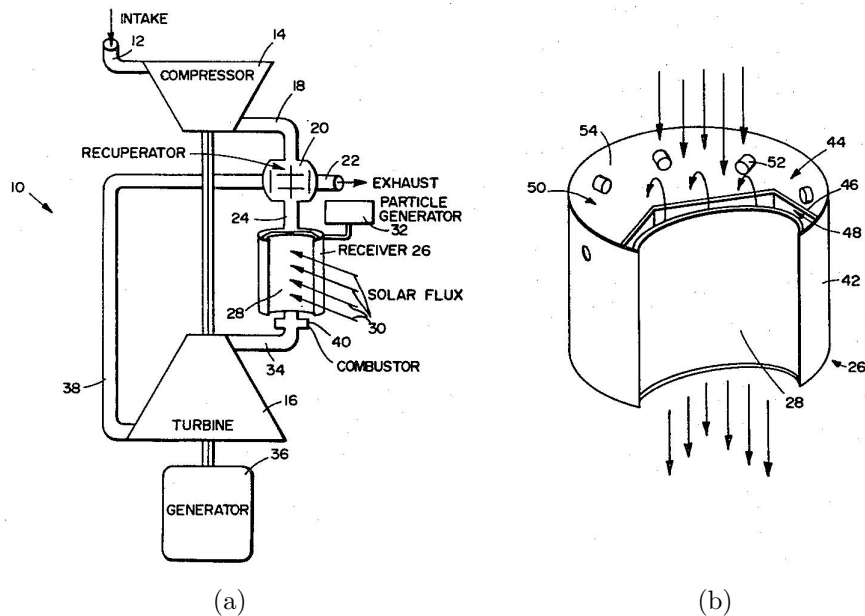


Figure 1.1: Devices proposed by Hunt [17, 18] (a) Schematic view of the system which includes a radiation receiver (b) Schematic view of the embodiment of the radiation receiver

Continuing with these investigations, a design and construction of a Small Particle Heat Exchanger Receiver (SPHER) of 30 kW was carried out. A new design for the receiver was proposed [19]. Experimental output temperatures of 1023 K were reported [20]. More recently, Miller and coworkers developed a coupled fluid flow and radiation model [6] and a Monte Carlo radiation model [35] in a cylindrical small particle solar receiver, which represents the SPHER receiver. Their theoretical results show that for an imposed output temperature of 1400 K, receiver efficiencies greater than 90% may be achieved for a carbon particles dispersion with $0.2 \mu\text{m}$ of radius and 0.3 g/m^3 . In Fig. 1.2 the schematic of the SPHER receiver is shown.

Kribus *et al.* proposed other kind of particle solar receiver [29] adapted to work with a multicomponent fluid mixture, comprising a suspension of particles made of an absorbent material. The authors claimed the capacity of the receiver to work at high pressures in the range of 1 to 100 atm. In Fig. 1.3 an axial cross-sectional view of that receiver is shown.

In the same way, Bertocchi *et al.* [3] reported a non-isothermal high temperature solar particle receiver. This receiver was conceived for applications using a process gas at temperatures of 1500–2000 K. It may be used to produce electricity (as in a Brayton cycle for example) or for chemical reactions (fuel generation via chemical reactions). An experimental prototype of 10 kW was tested. Sub-micron carbon particles with diameters smaller than 600 nm were used. The receiver was conceived to work under atmospheric pressure but closed with a window to maintain a controlled atmosphere.

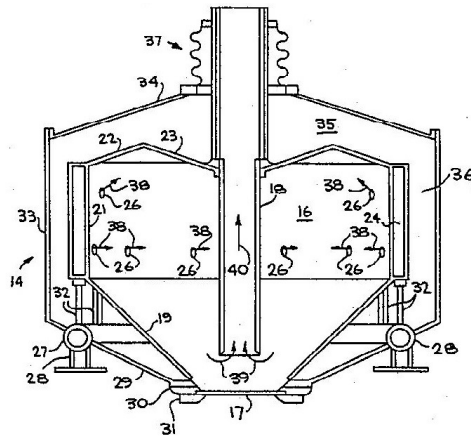


Figure 1.2: Schematic of a Small Particle Heat Exchanger Receiver (SPHER) by Hunt [19]

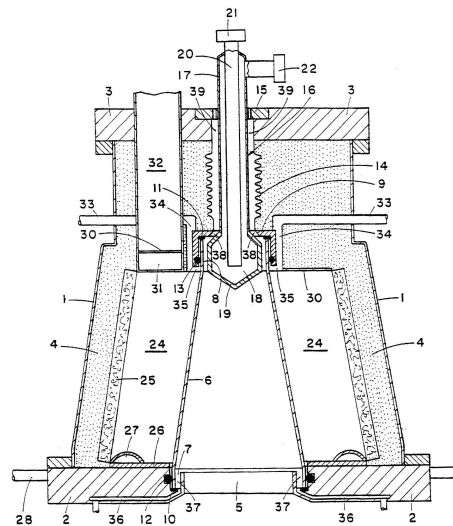


Figure 1.3: Axial cross-sectional view of a central solar receiver proposed by Kribus *et al.* [29]

Temperatures above 2100 K were reported when the working gas was nitrogen, and of 2000 K or 1900 K with air or CO_2 , respectively. An efficiency that exceeds 80% was estimated. Klein et al [25] developed a refined model for that receiver. Their results suggest that carbon particles with effective radius smaller than 100 nm do not absorb enough energy. They recommended a particle radius between 100 and 1000 nm as the best size for carbon particles. Additionally, a tornado flow configuration is proposed as an effective method to protect the window in a solar reactor [27]. In Fig. 1.4 the receiver model is shown [21]. The great advantage of such receiver is its capacity to work with particles with different sizes, materials or concentrations.

Otherwise, particle receivers are also investigated as solar particle reactors. Some designs and some prototypes for different chemical reactions are presented in the literature. Steinfeld and al. [38] presented a 3 kW conical cyclone gas-particle separator to investigate the thermal decomposition of calcium carbonate at 1300 K . An efficiency of

1.1. Solar particle receivers

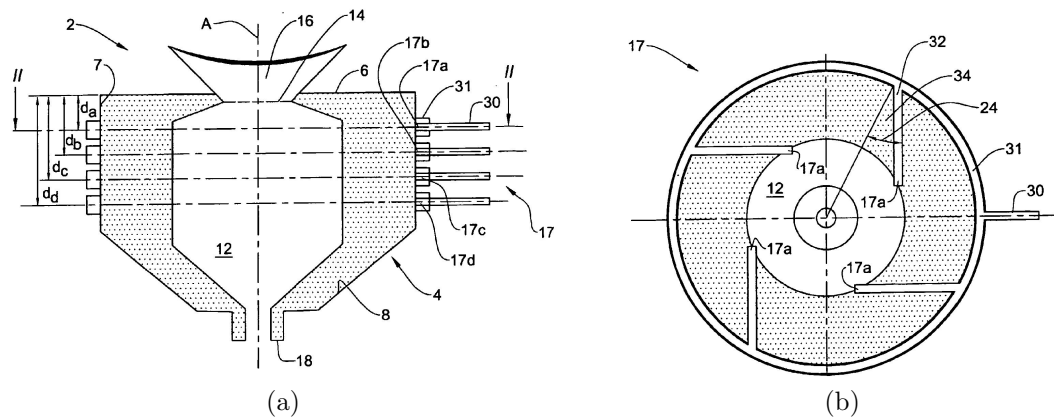


Figure 1.4: Solar particle receiver by Karni and Bertocchi [21] (a) Schematic illustration of a solar energy receiver (b) Cross-section in the solar energy receiver

43% and a high degree of calcination were reported. Also, Haueter *et al.* [12] proposed a 10kW windowed rotating cavity-receiver for conducting the thermal dissociation of ZnO into Zn and O_2 at above 2000 K . Fig. 1.5 shows the schematic of this solar particle reactor.

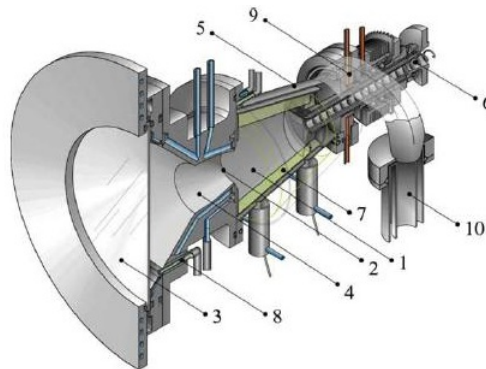


Figure 1.5: Cross-sectional view of a solar particle "rotating-cavity" receiver by Haueter et al [13]

Hirsch and Steinfeld [14] proposed a 5 kW "vortex-flow" solar reactor to produce hydrogen by thermal decomposition of natural gas at 1600 K . For such reactor, a detailed model [30] was proposed. Maximum chemical conversion of CH_4 to H_2 and C of 67% at 1600 K and 1 bar was reported [41, 14, 42, 30]. Ozalp and JayaKrishna [33] investigated the effect of carving in this reactor with a Computational Fluid Dynamics (CFD) analysis. Fig. 1.6 shows the reactor design with and without carving [33]. The results show that carving has a significant influence on the flow behavior, however, it has very little effect on the outlet temperature.

However the great advantages in terms of selectivity given by small particles, they also may conduct to some inconvenients. Small particles tend to agglomerate because the larger surface forces [16] that push to use complicated and non friendly environmental methods to produce in situ the carbon particles, as the pyrolysis of hydrocarbons [24].

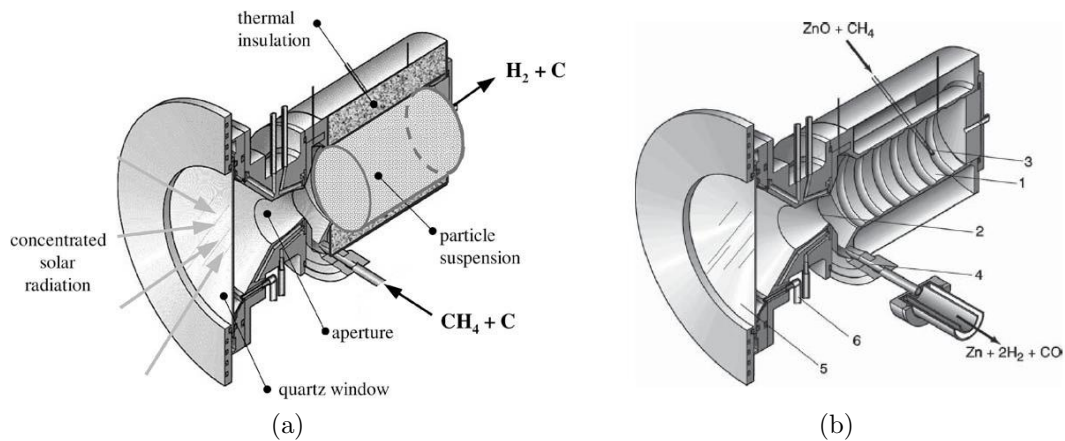


Figure 1.6: Cross-sectional view of vortex solar reactor [33] (a) Without helical carving (b) With helical carving

1.1.2 SPRs using large free-falling particles

An other kind of particle receiver investigated is the free-falling particle receiver. Large size refractory particles ($r \sim 0.5 \text{ mm}$) are falling down freely inside a solar receiver to form a curtain that directly absorbs the concentrated solar radiation. A great advantage mentioned by the authors is that the particles themselves may be used as the storage medium. Such receiver was conceived for the solar-driven water-splitting thermo-chemical process to produce hydrogen [39]. Martin and Vitko [31] gave a first approach to this kind of receiver. Next, Falcone *et al.* [8] proposed a design of a particle falling down receiver having a 100 MW thermal power. A simplified model and some possibilities of materials were presented. A more complete feasibility study was presented by Hruby [15]. Special attention was taken to the receiver design and to the particle material selection [37]. A two-dimensional model was presented and validated with experiments [7]. Performances of 60% were estimated using alumina based commercial particles of $650 \mu\text{m}$. More recently, a detailed three dimensional CFD model was used to analyze the increase in the performance of this receiver when no bottom opening exists [5]. The influence of the wind in the free-falling receiver was extensively studied using modeling or experimental set-up [23, 22]. The effect of the use of an aerowindow as protection [40] was also investigated. An on-sun testing of a prototype of 2 MW thermal power and its optical characterization were conducted by Siegel and Kolb [36]. Receiver efficiencies near to 60% and temperature increments from 600 to 900°C were reported. In Fig. 1.7 the free-falling particle receiver and the suction recirculation device are shown.

A modification of the original design, called face-down solid particle receiver, was modeled to increase the receiver efficiency [34, 11]. Receiver efficiencies that exceed 92% are reported for a receiver of 350 MW thermal power, when the particles increase their temperature from 300 to 800°C . Fig. 1.8 shows the receiver and a segment of it.

1.1. Solar particle receivers

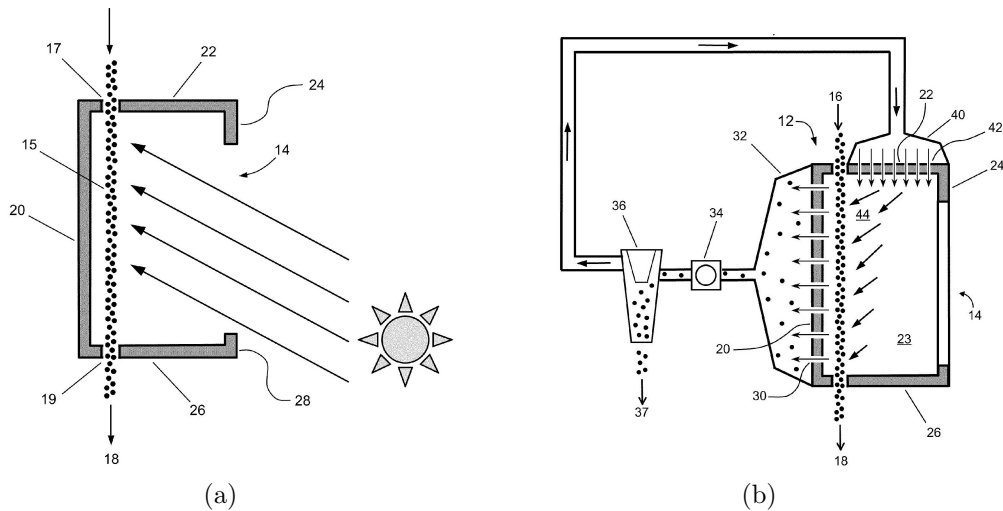


Figure 1.7: Free-falling particles receiver by Kolb [28] (a) Solar particle receiver (b) Suction-recirculation device for stabilizing particle flows within a SPR

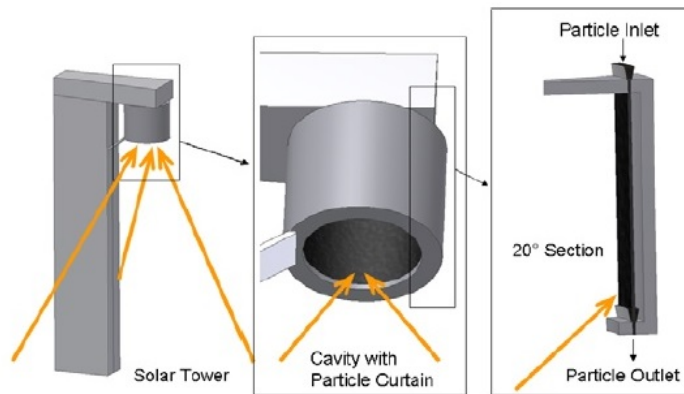


Figure 1.8: Face-down free-falling down solid particle receive. A below view in the left side and a segment of cavity in the right side [11]

1.1.3 SPRs using fluidized beds of particles

The concept of fluidized beds has also been investigated to be used as solar receiver. Flamant and Olalde [10] began with a comparison between packed and fluidized beds to use as high temperature receivers. Maximal efficiencies of 40 and 24% were achieved for fluidized beds using SiC and ZrO_2 in the range of 700 – 900 K and 800 – 1000 K respectively. The authors concluded that fluidized beds work better than packed beds as solar receivers. Koenigsdorff and Kienzle [26] reviewed the early researches about solar receiver fluidized beds. In Fig. 1.9 schematics of those investigations are shown.

Later, Flamant *et al.* [9] presented a theoretical and experimental investigation of a 50kW solar fluidized bed receiver prototype. A predicted efficiency of 73% and an experimental efficiency of 65% for the receiver, working at 905°C, were reported. The use of two-slab of different materials was also investigated [32]. Experimental results for two packed beds receivers using glass-beads and silica honeycomb for the first slab and SiC particles for the second slab were reported. Receiver efficiency of 78% for

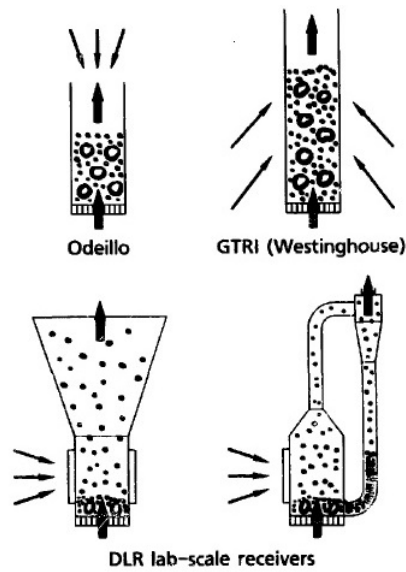


Figure 1.9: Schematics of early researches on direct-absorption fluidized bed receivers [26]

gas outlet temperature of 800°C were obtained for the honeycomb/*SiC* receiver. More recently, a design of a change section fluidized bed was presented [4]. Radiative losses of about 35% at 1000 K were reported. The mathematical 1D model of radiative transfer based on Monte Carlo method was developed [2]. Fig. 1.10 shows the schematic of the section-change fluidized bed solar receiver proposed.

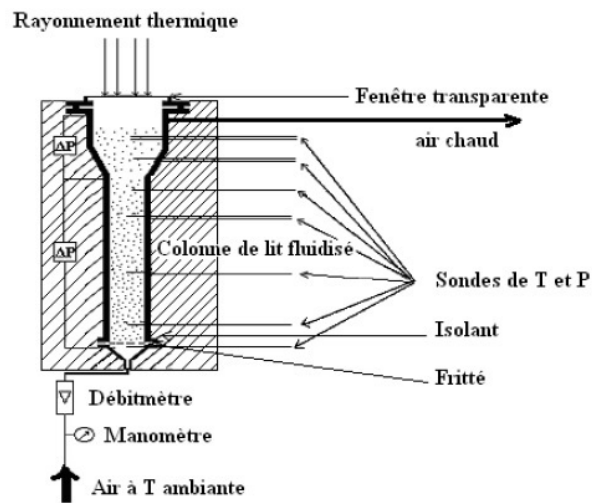


Figure 1.10: Schematic of a section-change fluidized bed receiver by Bounaceur [4]

References

- [1] M. Abdelrahman, P. Fumeaux, and P. Suter. Study of solid-gas suspensions used for direct absorption of concentrated solar radiation. *Solar Energy*, 22:45–48, 1979.
- [2] G. Baud. *Conception de récepteurs solaires à lit fluidisé sous flux radiatif concentré*. PhD thesis, Institut National Polytechnique de Toulouse, 2011.
- [3] R. Bertocchi, J. Karni, and A. Kribus. Experimental evaluation of a non-isothermal high temperature solar particle receiver. *Energy*, 29:687–700, 2004.
- [4] A. Bounaceur. *Interaction lit fluidisé de particules solides-rayonnement solaire concentré pour la mise au point d'un procédé de chauffage de gaz à plus de 1000 K*. PhD thesis, Ecole Nationale Supérieure des Mines de Paris, 2008.
- [5] H. Chen, Y. Chen, H Hsieh, and N. Siegel. Computational fluid dynamics modeling of gas-particle flow within a solid-particle solar receiver. *Journal of Solar Energy Engineering*, 129:160–171, 2007.
- [6] A. Crocker and F. Miller. Fluid flow and radiation modeling of a cylindrical small particle solar receiver. In *SolarPaces: Concentrating Solar Power and Chemical Energy Systems, Granada - Spain*, September 2011.
- [7] G. Evans, W. Houf, R. Greif, and C. Crowe. Gas-particle flow within a high temperature solar cavity receiver including radiation heat transfer. *Transactions of the ASME*, 109:134–142, 1987.
- [8] P.K. Falcone, J.E. Noring, and J.M. Hruby. Assessment of a solid particle receiver for a high temperature solar central receiver system. Technical report, Sandia National Laboratories, 1985.
- [9] G. Flamant, D. Gauthier, C. Boudhari, and Y. Flitris. A 50 kW fluidized bed high temperature solar receiver: heat transfer analysis. *Journal of Solar Energy Engineering*, 110:313–320, 1988.
- [10] G. Flamant and G. Olalde. High temperature solar gas heating comparison between packed and fluidized bed receivers - I. *Solar Energy*, 31:463–471, 1983.
- [11] B. Gobereit, L. Amsbeck, R. Buck, R. Pitz-Paal, and H. Muller-Steinhagen. Assessment of a falling solid particle receiver with numerical simulation. In *SolarPaces: Concentrating Solar Power and Chemical Energy Systems, Marrakech-Morocco*, September 2012.
- [12] P. Haueter, S. Moeller, R. Palumbo, and A. Steinfeld. The production of zinc by thermal dissociation of zinc oxide - solar chemical reactor design. *Solar Energy*, 67:1–3, 1999.
- [13] P. Haueter, S. Moeller, Palumbo R, and A. Steinfeld. Furnace for thermal and thermochemical treatment of raw materials, comprises rotary chamber surrounded by casing with window passing heating radiation. Patent N° 692927A5, 2002.

- [14] D. Hirsch and A. Steinfeld. Solar hydrogen production by thermal decomposition of natural gas using a vortex-flow reactor. *International Journal of Hydrogen Energy*, 29:47–55, 2004.
- [15] J.M. Hruby. A technical feasibility study of a solid particle solar central receiver for high temperature applications. Technical report, Sandia National Laboratories, 1986.
- [16] A. Hunt. Small particle heat exchanger. Technical report, Lawrence Berkeley Laboratory, 1978.
- [17] A. Hunt. Radiant energy collection and conversion apparatus and method. Patent N^o 4313304, 1982.
- [18] A. Hunt. Radiation receiver. Patent N^o 4403601, 1983.
- [19] A. Hunt, L. Hansen, and D. Evans. Solar heat receiver. Patent N^o 4499893, 1985.
- [20] A. Hunt and F. Miller. Small particle heat exchanger receivers for solar thermal power. In *SolarPaces: Concentrating Solar Power and Chemical Energy Systems, Perpignan-France*, September 2010.
- [21] J. Karni and R. Bertocchi. Solar receiver with a plurality of working fluid inlets. Patent N^o 0210876A1, 2005.
- [22] K. Kim, S. Moujaes, and G. Kolb. Experimental and simulation study on wind affecting particle flow in a solar receiver. *Solar Energy*, 84:263–270, 2010.
- [23] K. Kim, N. Siegel, G. Kolb, V. Rangaswamy, and S. Moujaes. A study of solid particle flow characterization in solar particle receiver. *Solar Energy*, 83:1784–1793, 2009.
- [24] K. Kitzmiller and F. Miller. Thermodynamic cycles for small particle heat exchange receiver used in concentrating solar power plants. In *ASME 4th Conference on Energy Sustainability, Vol 2*, 2010.
- [25] H. Klein, J. Karni, R. Ben-Zvi, and R. Bertocchi. Heat transfer in a directly solar receiver/reactor for solid-gas reactions. *Solar Energy*, 81:1227–1239, 2007.
- [26] R. Koenigsdorff and P. Kienzle. Results of and prospects for research on direct-absorption fluidized bed solar receivers. *Solar Energy Materials*, 24:279–283, 1991.
- [27] A. Kogan and M. Kogan. The tornado flow configuration - an effective method for screening of a solar reactor window. *Journal of Solar Energy Engineering*, 124:206–214, 2002.
- [28] G. Kolb. Suction-recirculation device for stabilizing particle flows within a solar powered solid particle receiver. Patent N^o 8109265B1, 2012.
- [29] A. Kribus, P. Doron, and J. Karni. Central solar receiver with a multi component working medium. Patent N^o 5947114, 1999.

References

- [30] G. Maag, W. Lipinski, and A. Steinfeld. Particle gas reacting flow under concentrated solar irradiation. *International Journal of Heat and Mass Transfer*, 52:4997–5004, 2009.
- [31] J. Martin and J. Vitko. ASCUAS: a solar central receiver utilizing a solid thermal carrier. Technical report, Sandia National Laboratories, 1982.
- [32] T. Menigault, G. Flamant, and B. Rivoire. Advanced high-temperature two-slab selective volumetric receiver. *Solar Energy Materials*, 24:192–203, 1991.
- [33] N. Ozalp and D. JayaKrishna. CFD analysis on the influence of helical carving in a vortex flow reactor. *International Journal of Hydrogen Energy*, 35:6248–6260, 2010.
- [34] M. Roger, L. Amsbeck, B. Gobereit, and R. Buck. Face-down solid particle receiver using recirculation. In *SolarPaces: Concentrating Solar Power and Chemical Energy Systems, Perpignan-France*, September 2010.
- [35] S. Ruther and F. Miller. Monte Carlo radiation simulation of a cylindrical small particle solar receiver. In *SolarPaces: Concentrating Solar Power and Chemical Energy Systems, Perpignan-France*, September 2010.
- [36] N. Siegel and G. Kolb. Design and on-sun testing of a solid particle receiver prototype. In *Energy Sustainability, Jacksonville-Florida-USA*, August 2008.
- [37] K.A. Stahl, J.W. Griffin, B.S. Matson, and R.B. Pettit. Optical characterization of solid particle solar central receiver materials. Technical report, Sandia National Laboratories, 1986.
- [38] A. Steinfeld, A. Imhof, and D. Mischler. Experimentally investigation of an atmospheric-open cyclone solar reactor for solid-gas thermochemical reactions. *Journal of Solar Energy Engineering*, 114:171–174, 1992.
- [39] T. Tan and Y. Chen. Review of study on solid particle solar receivers. *Renewable and Sustainable Energy Reviews*, 14:265–276, 2010.
- [40] T. Tan, Y. Chen, Z. Chen, N. Siegel, and G. Kolb. Wind effect on the performance of solid particle solar receivers with and without the protection of an aerowindow. *Solar Energy*, 83:1815–1827, 2009.
- [41] D. Trommer, D. Hirsch, and A. Steinfeld. Kinetic investigation of the thermal decomposition of CH_4 by direct irradiation of a vortex-flow laden with carbon particles. *International Journal of Hydrogen Energy*, 29:627–633, 2004.
- [42] A. Z'Graggen and A. Steinfeld. Heat and mass transfer analysis of a suspension of reacting particles subjected to concentrated solar radiation - application to the steam-gasification of carbonaceous materials. *International Journal of Heat and Mass Transfer*, 52:385–395, 2009.

Chapter 2

Physical radiative model

Abstract

A radiative model for a high temperature solar particle receiver is presented in this chapter. Due to the computational time constraints, a simplified model is developed. The SPR is considered as a $1D$ slab filled with a particle dispersion and submitted to an incident radiative flux. The RTE is solved with a two-stream method. Two approximations based on the Eddington-delta function are employed (proposed by Meador and Weaver and by Joseph *et al.*). These approximations are taken into account because their ability to treat highly anisotropy scattering. The scattering is considered independent and the single-particle radiative properties are computed with the Lorenz-Mie theory (spherical particles). The monochromatic algorithm is presented and the numerical code is validated through the comparison with analytical, numerical and published references. Good agreement is found in these comparisons.

2.1 Introduction

In order to optimize the radiative performances of a SPR, a computationally fast and accurate model is required owing to the large number of simulations involved. The transport of radiative energy in a particulate media is the basis in this study. The main equation that represents such transport is the Radiative Transfer Equation (RTE). Explicit analytical solutions are available only for a few number of highly simplified situations. Therefore, approximate solution methods are used for more involved scenarios [15]. Concerning the SPR-modeling, mainly two methods are used: the discrete ordinates method (for example [6, 8, 4]) and the Monte Carlo method (for example [16, 12, 13]). Both methods have the advantage of their high accuracy in the modeling of the radiation transfer into a semitransparent media, even if the involved geometry is complicated. However, an important drawback in their use is the high computational effort requirement [17]. In this work, the two-stream method is used to compute the radiative heat transfer into the receiver. The main advantage of this method lies in the short computational time involved to solve the RTE. Several authors reported a high accuracy for such a method [11, 19, 5]. Nevertheless, a more specific validation of the two-stream method used in the modeling of a SPR is done in Chapter 3.

2.2. Model description

The proposed model is based on what follows :

- One dimensional geometry
- Temperature imposed as the two extreme boundaries of the expected temperature profile inside of a SPR: constant or linear temperature profiles
- Highly anisotropic scattering
- Spectral dependency of the optical properties of the materials

The programming of the model was based on subroutines written in the FORTRAN language. In section 2.2 a complete description of the model is done. In sections 2.3 to 2.5 the physical and mathematical basis are presented. The monochromatic algorithm is described in section 2.6. Finally, concluding remarks are presented in section 2.7.

2.2 Model description

The SPR is viewed as a non-homogeneous slab of particles dispersion submitted to a collimated concentrated solar heat flux. To decrease as much as possible the computational time and because the influence of lateral walls decreases in a particle receiver for high optical thickness, the geometry is simplified to $1D$, such as in some solar particle reactors [13]. A slab thickness of $D = 1\text{ m}$ is chosen, but the optical thickness is varied through changes in the volume fraction of particles. A non-homogeneous temperature profile is assumed within the SPR and, the gas-particle flow is assumed to occur in a perpendicular direction to the solar flux. The spectrum analyzed is between $0.3 - 12.4\ \mu\text{m}$. The incoming or outgoing energy out of this range are neglected in the calculations. The spectrum is discretized in small spectral bands ($\Delta\lambda = 0.02$ when $0.3 \leq \lambda < 4\ \mu\text{m}$ and $\Delta\lambda = 0.1$ when $4 \leq \lambda < 12.4\ \mu\text{m}$) and a pseudo-monochromatic RTE is solved in each band using a two-stream method. Two approximations are used in the two-stream method: the first suggested by Meador and Weaver (hybrid modified Eddington-delta function approximation [14]) and the second by Joseph *et al.* (delta-Eddington modified approximation [10]). The band discretization in the solar range is much finer than outside due to the high energy and high variability of the solar spectrum (each cell contains an average of 0.5% of the incoming energy). Out of this range, the discretization is coarser. The single-particle optical properties (asymmetry factor \tilde{g} , the extinction and scattering Mie efficiencies Q_{ext} and Q_{sca}) are modeled using the Lorenz-Mie theory which involves the particle radius (r), the wavelength (λ) and the spectral refractive index $m_\lambda = n_\lambda + i k_\lambda$. The Meador and Weaver approximation uses a χ_0 -term to modify the usual Eddington approximation. This term makes use of the complete phase function, which in this work is approximated by the Henyey-Greenstein phase function. The volumetric optical properties (the extinction (β) and the scattering (σ) coefficients and the χ_0 -term) are then computed as a sum of the properties of each particle (independent scattering hypothesis, since the volume fraction is bounded to $f_v < 0.0006$). The non-homogeneity of the slab is accounted for by dividing it into layers with uniform optical properties (see Fig. 2.1). In the present work, up to 500 layers are used to perform the total heat flux calculations.

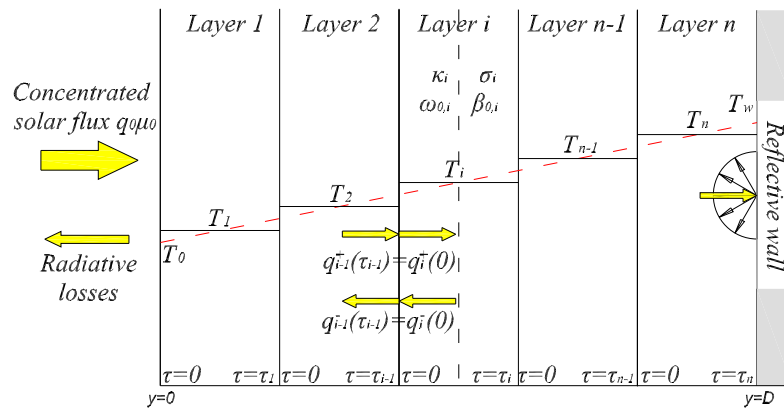


Figure 2.1: Schematic for the model formulation of a 1D solar particle receiver

2.3 The Radiative Transfer Equation (RTE)

The radiative transfer theory is used here to formulate the radiative heat transfer into a particulate media. The basic differential equation in this theory is known as the radiative transfer equation (RTE). The transported quantity in the radiative transfer of energy inside a participating medium is the specific intensity $I(r, \hat{s})$. It is defined as the radiative energy transferred per unit time, solid angle, spectral variable and area normal to the direction of rays, and it is measured in $Wm^{-2}\mu m^{-1}sr^{-1}$ (if the wavelength expressed in μm is chosen as the spectral quantity). r denotes the position and \hat{s} the direction of incident rays. Then, the RTE represents the variation of the specific intensity, when it travels through a differential space ds in the main path direction of rays. This equation takes into account the attenuation of intensity by absorption and scattering and the augmentation of intensity in the \hat{s} -direction by emission (assumed isotropic and governed by the Planck law for a medium in local thermodynamic equilibrium) and by the scattering of the radiation incoming from directions others than \hat{s} . Fig. 2.2 shows schematically these phenomena.

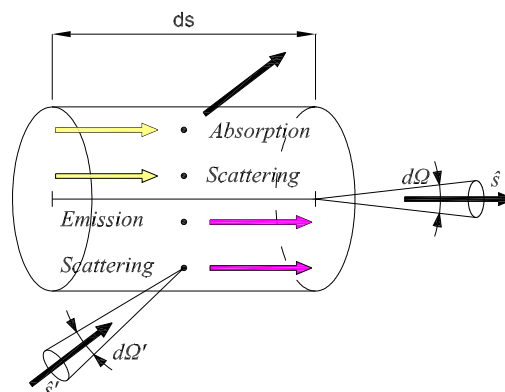


Figure 2.2: Absorption, scattering and emission by a differential volume of a participating medium

If the medium is considered as homogeneous, stationary, at local thermodynamic

2.3. The Radiative Transfer Equation (RTE)

equilibrium and if the Kirchoff law is assumed valid (i.e., the absorption and emission coefficients are equal), the monochromatic RTE may be written as

$$\frac{dI_\lambda(r, \hat{s})}{ds} = \kappa I_{b,\lambda}(r, \hat{s}) - \kappa I_\lambda(r, \hat{s}) - \sigma I_\lambda(r, \hat{s}) + \frac{\sigma + \kappa}{4\pi} \int_{4\pi} I_\lambda(r, \hat{s}') p_\lambda(\hat{s}', \hat{s}) d\Omega' \quad (2.1)$$

where κ is the volume absorption coefficient (m^{-1}), σ is the volume scattering coefficient (m^{-1}), Ω is the solid angle and $p_\lambda(\hat{s}', \hat{s})$ is the scattering phase function, which describes the probability that a ray coming from the direction \hat{s}' scatters into the direction \hat{s} [15]. In Eq. 2.1 the first term in the right hand side represents the gain of intensity due to the emission by temperature, the second term represents the loss of intensity by absorption, the third term the loss of intensity by scattering and the last term represents the gain of intensity by scattering from other directions [17]. The subscript b indicates blackbody and the superscript ' a direction different from the main path direction (see Fig. 2.2).

The volume extinction coefficient (β), the optical depth (τ) and the scattering albedo are defined as

$$\beta = \kappa + \sigma \quad (2.2)$$

$$\tau = \int_0^s (\kappa + \sigma) ds \quad (2.3)$$

$$\omega_0 = \frac{\sigma}{\kappa + \sigma} \quad (2.4)$$

Note that the subscript λ has been omitted in the writing of the various medium optical properties (i.e. κ , σ , β , ω_0 and τ). Inserting the above quantities (2.2, 2.3 and 2.4) into Eq. 2.1, the RTE can be expressed in terms of the optical depth and the scattering albedo

$$\frac{dI_\lambda(\tau, \hat{s})}{d\tau} = \hat{s} \cdot \nabla I_\lambda(\tau, \hat{s}) = -I_\lambda(\tau, \hat{s}) + (1 - \omega_0) I_{b,\lambda}(\tau, \hat{s}) + \frac{1}{4\pi} \int_{4\pi} I_\lambda(\tau, \hat{s}') p_\lambda(\hat{s}', \hat{s}) d\Omega' \quad (2.5)$$

The intensity of radiation emitted by a blackbody $I_{b,\lambda}$ is given by the Planck law

$$I_{b,\lambda}(T) = \frac{C_1}{\lambda^5 [e^{\frac{C_2}{\lambda T}} - 1]} \quad (2.6)$$

where $C_1 = 1.1910 \text{ W}\mu\text{m}^4/\text{m}^2$ and $C_2 = 14387.8 \mu\text{mK}$ are the first and second Planck constants, respectively.

2.3.1 The plane parallel problem

The wave propagation through a medium bounded by two parallel planes is a well-known problem [3, 9]. It may represent with a fairly good agreement the behavior of a solar particle receiver as it was shown by Maag *et al.* [13]. Moreover, such a model has the advantage of low computational time requirements. In what follows, the general RTE is formulated as a 1D slab of particulate medium, submitted to a concentrated and collimated solar flux, as in Fig. 2.1.

To solve the RTE (Eq. 2.5), it is convenient to split the spectral specific intensity $I_\lambda(r, \hat{s})$ into two components: the diffuse intensity $I_{d,\lambda}$ and the collimated intensity $I_{c,\lambda}$.

$$I_\lambda(r, \hat{s}) = I_{d,\lambda}(r, \hat{s}) + I_{c,\lambda}(r, \hat{s}) \quad (2.7)$$

The collimated intensity is the reduction of the collimated flux $q_{0,\lambda}$ in the main path direction ($\mu_0 = \cos(\theta_0)$, where θ_0 is the angle between the direction normal to the slab and the incoming radiation). Using Eq. 2.7 on Eq. 2.5, and integrating with respect to the azimuthal angle over the 2π domain, the RTE is split in two terms. The collimated intensity then is written as

$$I_{c,\lambda}(\tau, \mu) = q_{0,\lambda} \exp\left(-\frac{\tau}{\mu_0}\right) \delta(\mu - \mu_0) \quad (2.8)$$

where $\delta(\mu - \mu_0) = 1$ if $\mu = \mu_0$, and 0 otherwise, and Eq. 2.8 may be solved analytically. For the diffuse intensity, the RTE may be written as [3, 15]

$$\mu \frac{dI_{d,\lambda}(\tau, \mu)}{d\tau} = -I_{d,\lambda}(\tau, \mu) + \frac{1}{2} \int_{-1}^{+1} p_\lambda(\mu, \mu') I_{d,\lambda}(\tau, \mu') d\mu' + G_\lambda(\tau, \mu) \quad (2.9)$$

where $G_\lambda(\tau, \mu)$ is a source function, $\mu = \cos(\theta)$ with θ measured positive in the forward direction and μ_0 is the forward direction that corresponds to the direction of the collimated flux $q_{0,\lambda}$. The source function reads

$$G_\lambda(\tau, \mu) = \frac{1}{2} p_\lambda(\mu, \mu_0) q_{0,\lambda} \exp\left(-\frac{\tau}{\mu_0}\right) + (1 - \omega_0) I_{b,\lambda}(\tau, \hat{s}) \quad (2.10)$$

Even though several techniques exist for solving Eq. 2.9 (as described in standard Radiative Heat Transfer handbooks), the two-stream method will be used considering the number of spectral bandwidths used.

2.3.2 The two-stream method

The two-stream method refers to an approximate scheme to solve the RTE in which only a forward flux and a backward flux are considered. Hence, various and sometimes radically different approximations exist. The appropriate approximation should be chosen according to the main characteristics of the problem. In the SPR case, a high absorptance is desirable in the visible region while a low emittance must be obtained in the near infrared region. Moreover, in the visible region, the light scattering is highly anisotropic due to the large size of particles ($r > \lambda$). In consequence, an approximation that treats well the anisotropy of the scattering as well as the thermal emission is needed. The approximations suggested by Meador and Weaver [14] and by Joseph *et al.* [10] seem to satisfy these conditions.

The two-stream method implies the separation of the radiative diffuse flux in two parts: the forward flux (q_λ^+), that travels in the main path direction ($0 < \mu < 1$) and the backward flux (q_λ^-), that travels in the opposite of main path direction ($-1 < \mu < 0$). A schematic of the forward and backward fluxes is shown in Fig. 2.3. These fluxes are defined as

$$q_\lambda^+(\tau) = \int_0^1 I_{d,\lambda}(\tau, \mu) \mu d\mu \quad (\mu \geq 0) \quad \text{and} \quad q_\lambda^-(\tau) = \int_{-1}^0 I_{d,\lambda}(\tau, \mu) \mu d\mu \quad (\mu \leq 0) \quad (2.11)$$

2.3. The Radiative Transfer Equation (RTE)

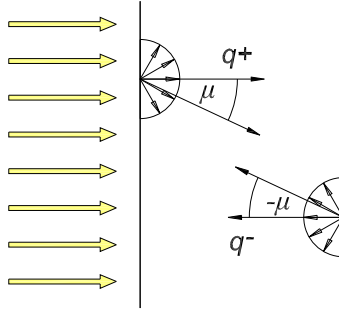


Figure 2.3: Forward and backward fluxes for a plane parallel problem in a two-stream method

or more compactly as

$$q_{\lambda}^{\pm}(\tau) = \pm \int_0^1 I_{d,\lambda}(\tau, \pm\mu) \mu d\mu \quad \mu \geq 0 \quad (2.12)$$

By introducing Eq. 2.9 into Eq. 2.12, the two main equations of the two-stream method read

$$\frac{dq_{\lambda}^+}{d\tau} = - \int_0^1 I_{d,\lambda}(\tau, \mu) d\mu + \frac{1}{2} \int_0^1 \int_{-1}^{+1} p_{\lambda}(\mu, \mu') I_{d,\lambda}(\tau, \mu') d\mu' d\mu + G_{\lambda}^+(\tau, \mu) \quad (2.13)$$

$$\frac{dq_{\lambda}^-}{d\tau} = \int_0^1 I_{d,\lambda}(\tau, -\mu) d\mu - \frac{1}{2} \int_0^1 \int_{-1}^{+1} p_{\lambda}(-\mu, \mu') I_{d,\lambda}(\tau, \mu') d\mu' d\mu - G_{\lambda}^-(\tau, \mu) \quad (2.14)$$

where the source functions are

$$G_{\lambda}^+(\tau, \mu) = \frac{1}{2} \int_0^1 p_{\lambda}(-\mu, \mu_0) q_{0,\lambda} \exp\left(-\frac{\tau}{\mu_0}\right) + 2\pi(1 - \omega_0) I_{b,\lambda}(T) \quad (2.15)$$

$$G_{\lambda}^-(\tau, \mu) = \frac{1}{2} \int_0^1 p_{\lambda}(\mu, \mu_0) q_{0,\lambda} \exp\left(-\frac{\tau}{\mu_0}\right) + 2\pi(1 - \omega_0) I_{b,\lambda}(T) \quad (2.16)$$

Meador and Weaver [14] proposed a generalization of the two-stream methods which allows a simplification of the Eqs. 2.13 to 2.16 to expressions that involve new terms (the γ -terms)

$$\frac{dq_{\lambda}^+}{d\tau} = \gamma_1 q_{\lambda}^+ - \gamma_2 q_{\lambda}^- + q_{0,\lambda} \omega_0 \gamma_3 \exp\left(-\frac{\tau}{\mu_0}\right) + 2\pi(1 - \omega_0) I_{b,\lambda}(T) \quad (2.17)$$

$$\frac{dq_{\lambda}^-}{d\tau} = \gamma_2 q_{\lambda}^+ - \gamma_1 q_{\lambda}^- - q_{0,\lambda} \omega_0 \gamma_4 \exp\left(-\frac{\tau}{\mu_0}\right) + 2\pi(1 - \omega_0) I_{b,\lambda}(T) \quad (2.18)$$

In the Meador and Weaver paper, the positive axis direction is inverted in regard to the positive depth of the atmosphere. This strange geometrical configuration is usual in atmospheric sciences, where the positive axis direction starts at the ground and the atmosphere depth starts at the top of the atmosphere. For that reason, the third

terms on the right hand side in Eqs. 2.17 and 2.18 differ from these given by Meador and Weaver [14]. The solution for the radiative forward and backward fluxes may be obtained by solving Eqs. 2.17 and 2.18.

$$q_{\lambda}^{+}(\tau) = \gamma_2 K_{1,\lambda} \exp(\nu\tau) + \gamma_2 K_{2,\lambda} \exp(-\nu\tau) + G_{\lambda}^{+}(\tau) \quad (2.19)$$

$$q_{\lambda}^{-}(\tau) = (\gamma_1 - \nu) K_{1,\lambda} \exp(\nu\tau) + (\gamma_1 + \nu) K_{2,\lambda} \exp(-\nu\tau) + G_{\lambda}^{-}(\tau) \quad (2.20)$$

with

$$G_{\lambda}^{+}(\tau) = \frac{q_{0,\lambda}\omega_0\mu_0}{1 - \nu^2\mu_0^2} [\alpha_2\mu_0 - \gamma_3] \exp\left(-\frac{\tau}{\mu_0}\right) + 2\pi \frac{1 - \omega_0}{\gamma_1 - \gamma_2} I_{b,\lambda}(T) \quad (2.21)$$

$$G_{\lambda}^{-}(\tau) = \frac{q_{0,\lambda}\omega_0\mu_0}{1 - \nu^2\mu_0^2} [\alpha_1\mu_0 + \gamma_4] \exp\left(-\frac{\tau}{\mu_0}\right) + 2\pi \frac{1 - \omega_0}{\gamma_1 - \gamma_2} I_{b,\lambda}(T) \quad (2.22)$$

The $K_{1,\lambda}$ and $K_{2,\lambda}$ constants depend on the boundary conditions. The α and ν terms are defined as

$$\alpha_1 = \gamma_1\gamma_4 + \gamma_2\gamma_3 \quad ; \quad \alpha_2 = \gamma_1\gamma_3 + \gamma_2\gamma_4 \quad ; \quad \nu = (\gamma_1^2 - \gamma_2^2)^{1/2} \quad (2.23)$$

Remember that the radiative constants (g , ω_0 and τ) and all variables that are function of the above quantities are dependent on the wavelength (subscript λ omitted). To find the γ -terms, an appropriate approximation of the diffuse intensity, that define each model, need to be introduced. This approximation is used to evaluate the integrals in Eqs. 2.13 and 2.14. The γ -terms are found by direct comparison with Eqs 2.17 and 2.18. This procedure is the same utilized by Meador and Weaver [14].

The Meador and Weaver approximation

On the one hand, the Eddington solution (which is used in the actual approximation and in the Joseph *et al.* approximation) starts with the assumption that the intensity and the phase function may be approximated as the two first terms ($N = 1$) of Legendre polynomials.

$$I_{d,\lambda}(\tau, \mu) = \sum_{l=0}^{N=1} I_l(\tau) P_l(\mu) = I_0(\tau) + \mu I_1(\tau) \quad (2.24)$$

Eq. 2.24 applied in Eq. 2.12 gives as result the expression of the diffuse intensity for the Eddington solution.

$$I_{d,\lambda}(\tau, \pm\mu) = \frac{1}{2} [(2 \pm 3\mu)q^{+}(\tau) + (2 \mp 3\mu)q^{-}(\tau)] \quad \mu \geq 0 \quad (2.25)$$

On the other hand, the delta-function method approximates the intensity as a delta function. This approximation is useful when the particles scatters very asymmetrically into the μ_0 direction.

$$I_{d,\lambda}(\tau, \pm\mu) = \frac{1}{\mu_0} I_{d,\lambda}(\tau) \delta(\mu - \mu_0) \quad \mu \geq 0 \quad (2.26)$$

Meador and Weaver introduced a new hybrid modified Eddington-delta function method that gives good performances when the scattering is highly anisotropic [14].

2.3. The Radiative Transfer Equation (RTE)

The method uses an approximation of intensity $I_{d,\lambda}(\tau, \mu)$ that yields the Eddington approximation when the asymmetry factor is $g = 0$ and the delta-function method when $g = \pm 1$. The delta-function is accurate in the extreme case of highly anisotropic phase function, while the Eddington method is more accurate for isotropic phase functions. With a linear combination of Eqs. 2.25 and 2.26 the following expression is used in this approximation.

$$I_{d,\lambda}(\tau, \pm\mu) = \frac{1}{1 - g^2(1 - \mu_0)} \left\{ (1 - g^2) \left[\left(1 \pm \frac{3\mu}{2}\right) q_{\lambda}^+ + \left(1 \mp \frac{3\mu}{2}\right) q_{\lambda}^- \right] + g^2 \delta(\mu - \mu_0) q_{\lambda}^{\pm} \right\} \quad (2.27)$$

The average cosine of the scattering angle g is an indicator of the preferential scattering direction by the particles. The modification to the standard Eddington method is made through the definition of the χ_0 term:

$$\chi_0 = \frac{1}{2\omega_0} \int_0^1 p_{\lambda}(\mu_0, -\mu') d\mu' = 1 - \frac{1}{2\omega_0} \int_0^1 p_{\lambda}(\mu_0, \mu') d\mu' \quad (2.28)$$

By introducing Eq. 2.27 into Eqs. 2.13 and 2.14 and by comparing the results with Eqs. 2.17 and 2.18, the γ -terms may be derived. The details of the procedure are presented in Appendix A.1.

$$\gamma_1 = -\frac{7 - 3g^2 - \omega_0(4 + 3g) + \omega_0 g^2(4\chi_0 + 3g)}{4[1 - g^2(1 - \mu_0)]} \quad (2.29)$$

$$\gamma_2 = \frac{1 - g^2 - \omega_0(4 - 3g) - \omega_0 g^2(4\chi_0 + 3g - 4)}{4[1 - g^2(1 - \mu_0)]} \quad (2.30)$$

$$\gamma_3 = 1 - \chi_0 \quad ; \quad \gamma_4 = \chi_0 \quad (2.31)$$

The Joseph *et al.* approximation

Joseph *et al.* developed a delta-Eddington approximation by combining a Dirac delta function and a the Eddington approximation. They starts with the assumption of a phase function as

$$p(\mu, \mu') = 2g^2 \delta(\mu - \mu') + (1 - g^2) \left(1 + \frac{3g\mu\mu'}{1 + g} \right) \quad (2.32)$$

This approximate phase function have the same asymmetry factor and second moment of the Henyey-Greenstein phase function expressed in terms of Legendre polynomials. In practice, the Joseph *et al.* approximation is solved in the same way as the Eddington method. It is due to the main equations of these methods are similar when the g , ω_0 and τ parameters are transformed as [10]

$$g' = \frac{g}{1 + g} \quad (2.33)$$

$$\omega'_0 = \frac{(1 - g^2)\omega_0}{1 - \omega_0 g^2} \quad (2.34)$$

$$\tau' = (1 - \omega_0 g^2) \tau \quad (2.35)$$

In consequence, the approximation of intensity $I_{d,\lambda}(\tau, \mu)$ is that for the Eddington approximation (see Eq. 2.25). Implementing the same procedure as in the last section, the γ -terms are found as follows

$$\gamma_1 = -\frac{1}{4} [7 - \omega'_0(4 + 3g')] \quad (2.36)$$

$$\gamma_2 = \frac{1}{4} [1 - \omega'_0(4 - 3g')] \quad (2.37)$$

$$\gamma_3 = 1 - \gamma_4 \quad ; \quad \gamma_4 = \frac{1}{4} (2 - 3g'\mu_0) \quad (2.38)$$

2.3.3 The multiple-layer two-stream solution

The two-stream method is a very rapid approximation to solve the RTE. The principal advantage of such a method is that it may be solved analytically. However, it is constrained to an homogeneous medium. In order to model the radiative heating rates in a medium with different temperatures or compositions along of the geometry, a multi-layer schema must be implemented. The methodology developed by Toon *et al.* [19] for a non-homogeneous atmosphere with a two-stream method then is used. It is based on a tridiagonal matrix solution for a multiple-layered, inhomogeneous slab of particles dispersion. Details of the tridiagonal matrix solution are presented in Appendix A.2. Equations 2.19 and 2.20 applied to a multiple-layer problem can be expressed for layer i as

$$q_{i,\lambda}^+(\tau) = \gamma_{2,i} K_{1,i,\lambda} \exp(\nu_i \tau) + \gamma_{2,i} K_{2,i,\lambda} \exp(-\nu_i \tau) + G_{i,\lambda}^+(\tau) \quad (2.39)$$

$$q_{i,\lambda}^-(\tau) = (\gamma_{1,i} - \nu_i) K_{1,i,\lambda} \exp(\nu_i \tau) + (\gamma_{1,i} + \nu_i) K_{2,i,\lambda} \exp(-\nu_i \tau) + G_{i,\lambda}^-(\tau) \quad (2.40)$$

where $0 \leq \tau \leq \tau_i$ is the optical depth beginning at the end of layer $i - 1$ (see Fig. 2.1). For multiple layers, τ_c is the cumulative optical depth of the $i - 1$ first layers defined as [19]

$$\tau_c = \sum_{j=1}^{i-1} \tau_j = \sum_{j=1}^{i-1} \beta_j (z_j - z_{j-1}) \quad (2.41)$$

The wavelength dependence has been ignored in the writing of the optical depths and β_i denotes the monochromatic extinction coefficient of the homogeneous layer i . The G -terms are shown to have the following forms

$$G_{i,\lambda}^+(\tau) = \frac{q_{0,\lambda} \omega_{0,i} \mu_0}{1 - \nu_i^2 \mu_0^2} [\alpha_{2,i} \mu_0 - \gamma_{3,i}] \exp\left(-\frac{\tau_c + \tau}{\mu_0}\right) + 2\pi \left[\frac{1 - \omega_{0,i}}{\gamma_{1,i} - \gamma_{2,i}} \right] I_{b,i,\lambda}(T_i) \quad (2.42)$$

$$G_{i,\lambda}^-(\tau) = \frac{q_{0,\lambda} \omega_{0,i} \mu_0}{1 - \nu_i^2 \mu_0^2} [\alpha_{1,i} \mu_0 + \gamma_{4,i}] \exp\left(-\frac{\tau_c + \tau}{\mu_0}\right) + 2\pi \left[\frac{1 - \omega_{0,i}}{\gamma_{1,i} - \gamma_{2,i}} \right] I_{b,i,\lambda}(T_i) \quad (2.43)$$

2.4. Volume radiative properties of a cloud of particles

2.3.4 Radiative boundary conditions

For a slab consisting of n layers, the following boundary conditions are introduced:

- Forward radiative heat flux at the inlet ($y = 0$) and backward radiative flux at the diffuse receiver wall ($y = D$) assumed diffuse with a reflectivity $\rho_{w,\lambda}$

$$q_{1,\lambda}^+(0) = 0 \quad (2.44)$$

$$q_{n,\lambda}^-(\tau_n) = \rho_{w,\lambda} \left[q_{n,\lambda}^+(\tau_n) + q_{0,\lambda} \mu_0 \exp \left(- \frac{\tau_c + \tau_n}{\mu_0} \right) \right] + (1 - \rho_{w,\lambda}) \pi I_{b,\lambda}(T_w) \quad (2.45)$$

where T_w is the temperature of the receiver wall.

- Radiative heat flux continuity at a layer interface, both in backward and forward directions

$$q_{i,\lambda}^+(\tau_i) = q_{i+1,\lambda}^+(0) \quad (2.46)$$

$$q_{i,\lambda}^-(\tau_i) = q_{i+1,\lambda}^-(0) \quad (2.47)$$

The forward, backward and total heat fluxes are

$$q_i^\pm(\tau) = \int_0^\infty q_{i,\lambda}^\pm(\tau) d\lambda \quad (2.48)$$

$$q_i(\tau) = \int_0^\infty [q_{i,\lambda}^+(\tau) - q_{i,\lambda}^-(\tau)] d\lambda \quad (2.49)$$

A subroutine called TSLAYER has been written following the two-stream procedure exposed above, which is able to solve a multiple-layer configuration. The integration of the Eq. 2.48 is made numerically with a trapezoidal integration method.

2.4 Volume radiative properties of a cloud of particles

The extinction of the incident radiation into a particulate media depends on the composition, shape and number of particles. The scattering may be considered as independent if the density number of particles is low enough in order that the scattering of a particle is not affected by the secondary fields of the neighboring particles. Tien and Drolen [18] summarized the limits for the scattering independent assumption and related it with the volume fraction of particles (f_v) (see Fig. 2.4). The volume fraction is defined as the volume occupied by the particles in the total volume. Note that for volume fraction values smaller than $f_v = 0.006$, the scattering may be considered as independent, without regarding the particle size. Consequently the scattering is treated as independent in all the simulations due to the low amount of particles needed in a SPR. Because to this reason, the spectral radiative volume properties of the medium are the sum of the radiative properties of all single particle [15].

The simplest consideration for a dispersion of particles is to suppose that all particles have the same size. However, more accurate analysis can consider different particle sizes. The investigations and comparisons of both situations will be carried on in the next sections.

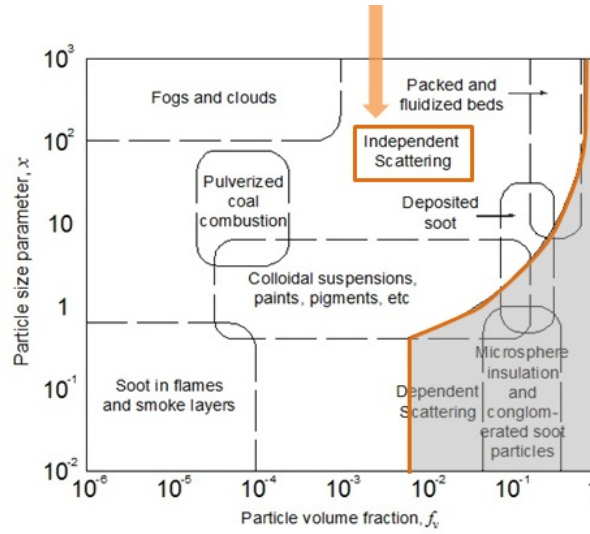


Figure 2.4: Scattering regime map for independent and dependent scattering [18]

2.4.1 Mono-dispersion of particles

The simple model considers dispersion by equal size particles, which is called a mono-dispersion (mono disperse media). For such a particle dispersion, the volume radiative properties may be written as

$$\beta = N_0 \pi r^2 Q_{ext} = \frac{f_v}{4/3\pi r^3} \pi r^2 Q_{ext} = 0.75 \frac{f_v}{r} Q_{ext} \quad (2.50)$$

$$\sigma = N_0 \pi r^2 Q_{sca} = \frac{f_v}{4/3\pi r^3} \pi r^2 Q_{sca} = 0.75 \frac{f_v}{r} Q_{sca} \quad (2.51)$$

where N_0 is the number of particles involved in the dispersion process, r is the particle radius and Q_{ext} and Q_{sca} are the Mie efficiencies. The volume scattering phase function (p), and consequently the volume asymmetry factor (g), are coincident with those for a single-particle (represented by a tilde).

$$p(\mu, \mu') = \tilde{p}(\mu, \mu') \quad \text{and} \quad g = \tilde{g} \quad (2.52)$$

Due to the simplicity of the treatment of this kind of dispersion, the programming has been included in the TSLAYER subroutine.

2.4.2 Poly-dispersion of particles

A more relevant analysis needs to take into account different sizes of particles. For a particle poly-dispersion consisting in particles having the same composition, the volume radiative properties are the summation over particle size only. For a size distribution represented as a continuous function $N(r)$ (number density distribution), they can be represented as follows

$$\beta = \int_0^\infty \pi r^2 Q_{ext}(r) N(r) dr \quad (2.53)$$

2.4. Volume radiative properties of a cloud of particles

$$\sigma = \int_0^{\infty} \pi r^2 Q_{sca}(r) N(r) dr \quad (2.54)$$

$N(r)dr$ is the number of particles per unit volume with radius between r and $r + dr$ [2]. The total number of particles per unit volume and the particles volume fraction are then

$$N_0 = \int_0^{\infty} N(r) dr \quad (2.55)$$

$$f_v = \frac{4}{3} \pi \int_0^{\infty} r^3 N(r) dr \quad (2.56)$$

A very usual distribution used for poly-dispersions is the gamma-distribution function [2]. It assumes a monomodal distribution described by only two parameters (a and b). It is defined as

$$N(r) = \frac{N_0 b^{a+1}}{\Gamma(a+1)} r^a \exp(-br) \quad (2.57)$$

It is useful to express the total number of particles and the number density distribution in terms of the volume fraction as

$$N_0 = \frac{3b^3 \Gamma(a+1)}{4\pi \Gamma(a+4)} f_v \quad (2.58)$$

$$N(r) = \frac{3b^{a+4}}{4\pi \Gamma(a+4)} f_v r^a \exp(-br) \quad (2.59)$$

By introducing Eq. 2.59 in Eqs. 2.53 and 2.54, the volume extinction and scattering properties of the particles cloud are found as

$$\beta = \frac{3 \Gamma(a+1)}{4 \Gamma(a+4)} b^3 \int_0^{\infty} Q_{ext}(r) r^{a+2} \exp(-br) dr \quad (2.60)$$

$$\sigma = \frac{3 \Gamma(a+1)}{4 \Gamma(a+4)} b^3 \int_0^{\infty} Q_{sca}(r) r^{a+2} \exp(-br) dr \quad (2.61)$$

It is usual to represent the gamma distribution in terms of the most probable radius (r_{mp}) and the width parameter (r_{mp}/r_{32}). The most probable radius is the radius where $dN/dr = 0$, as well as the width parameter is the r_{mp} and r_{32} ratio, where the Sauter's mean radius (r_{32}) is defined as [2]

$$r_{32} = \frac{\int_0^{\infty} r^3 N(r) dr}{\int_0^{\infty} r^2 N(r) dr} \quad (2.62)$$

For instance, Fig. 2.5 illustrates the influence of r_{mp} and r_{mp}/r_{32} in the gamma-distribution function for $a = 2$, $b = 1.7594$ and $N_0 = 10^{10}/m^3$

Equation 2.57 helps to find the most probable radius and the Sauter's mean radius as

$$r_{32} = \frac{3+a}{b} \quad (2.63)$$

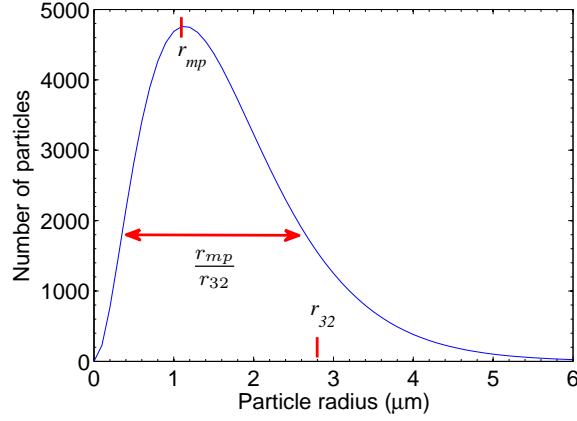


Figure 2.5: Gamma size distribution function. In this example, $a=2$, $b=1.7594$, $N_0 = 10^{10}/m^3$, $r_{mp} = 1.14$, $r_{32} = 2.84$ and $r_{mp}/r_{32} = 0.4$

$$r_{mp} = \frac{a}{b} \quad (2.64)$$

Finally, the phase function and the asymmetry factor for a poly-disperse cloud of particles using a gamma-distribution function are found as

$$p(\mu, \mu') = \frac{1}{\sigma} \frac{3 \Gamma(a+1)}{4 \Gamma(a+4)} b^3 \int_0^\infty \tilde{p}(\mu, \mu') Q_{ext}(r) r^{a+2} \exp(-br) dr \quad (2.65)$$

$$g = \frac{1}{\sigma} \frac{3 \Gamma(a+1)}{4 \Gamma(a+4)} b^3 \int_0^\infty \tilde{g}(r) Q_{sca}(r) r^{a+2} \exp(-br) dr \quad (2.66)$$

The VPPOLY subroutine has been written to compute the volume properties of a cloud of poly-dispersion of particles using a gamma-distribution function.

2.5 Radiative properties of a spherical single-particle

In this work the shape of particles is considered spherical. This simplification is largely used because the averaged behavior of millions of irregular shapes tends to smooth the irregularities [15]. It allows the use of the Lorenz-Mie theory to determine the radiative properties of a single particle. Such a theory describes the exact solution of Maxwell's equations for the scattering of the electromagnetic radiation by a single sphere. It was developed independently by Ludvig Lorenz (1890s) and Gustav Mie (1908) and it works for all sphere sizes. In spite of that, it is generally used when the size of the particle have the same order of magnitude as the involved wavelength, where other simpler models may be used (i.e. geometrical optics, Rayleigh, etc.). Because of the applicability of this theory or another depends on the wavelength, the parameter size, which is dimensionless number, is defined. It is defined as the ratio of the particle perimeter to the wavelength $x = 2\pi r/\lambda$. Therefore the criterion to use the Lorenz-Mie theory is outside of this region: Rayleigh solution if $x < 1$ and geometric optics if $x \gg 1$ as well as $kx \gg 1$, where k is the complex part of the refractive index [1].

2.5. Radiative properties of a spherical single-particle

The radiative intensity of an electromagnetic wave interacting with a spherical particle may be changed by absorption (if the energy changes its typology, for example to thermal energy) or by scattering (if the wave changes its direction). Scattering is due to three different phenomena: diffraction, reflection and refraction (see Fig. 2.6). Under the Lorenz-Mie theory frame, the single-particle radiative properties (scattering efficiency Q_{sca} , extinction efficiency Q_{ext} and single-particle asymmetry factor \tilde{g}) are dependent only on the parameter size x and on the complex refractive index $m = n + ik$ [15].

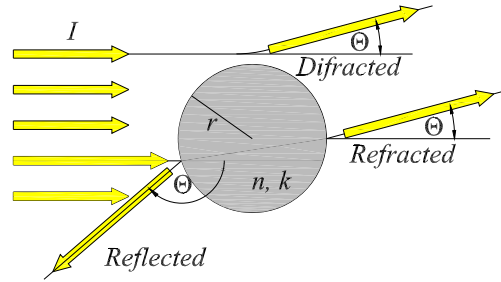


Figure 2.6: Geometrical optics representation of radiation scattering phenomena by a single spherical particle

2.5.1 The Mie coefficients, cross sections and efficiencies

In the Lorenz-Mie theory, the key parameters are the Mie coefficients a_n and b_n , which compute the amplitudes of the scattered field. These coefficients are complex functions of x and mx and can be calculated as

$$a_n = \frac{\psi'_n(mx)\psi_n(x) - m\psi_n(mx)\psi'_n(x)}{\psi'_n(mx)\xi_n(x) - m\psi_n(mx)\xi'_n(x)} \quad (2.67)$$

$$b_n = \frac{m\psi'_n(mx)\psi_n(x) - \psi_n(mx)\psi'_n(x)}{m\psi'_n(mx)\xi_n(x) - \psi_n(mx)\xi'_n(x)} \quad (2.68)$$

where the functions ψ_n and ξ_n are the Riccati-Bessel functions. The large inconvenient with the use of these functions is that they diverge at high values of kx . This effect is specially strong for metals (high values of k) and for high size particles (high values of x). To avoid divergence problems the logarithmic derivative D_n of ψ_n has been proposed [1].

$$D_n(x) = \frac{\psi'_n(x)}{\psi_n(x)} \quad (2.69)$$

and Eqs. 2.67 and 2.68 become

$$a_n = \frac{[D_n(mx)/m + n/x]\psi_n(x) - \psi_{n-1}(x)}{[D_n(mx)/m + n/x]\xi_n(x) - \xi_{n-1}(x)} \quad (2.70)$$

$$b_n = \frac{[mD_n(mx) + n/x]\psi_n(x) - \psi_{n-1}(x)}{[mD_n(mx) + n/x]\xi_n(x) - \xi_{n-1}(x)} \quad (2.71)$$

When a single particle is illuminated by a plane wave, the extinction cross section C_{ext} specifies the amount of light for unit of incident irradiance absorbed or scattered in a given direction. This quantity is sized in units of area measurements. Similar concepts are stipulated for the scattering cross section C_{sca} and the absorption cross section C_{abs} . The extinction cross section may be represented as an imaginary area, different from the geometric area, which absorbs and scatters an amount of energy of incident irradiance due to the presence of the particle. In geometrical terms, it is possible to say that the particle "casts a shadow" of an area C_{ext} . This "shadow" can be considerably greater -or smaller- than the particle geometric shadow (see fig. 2.7) [15].

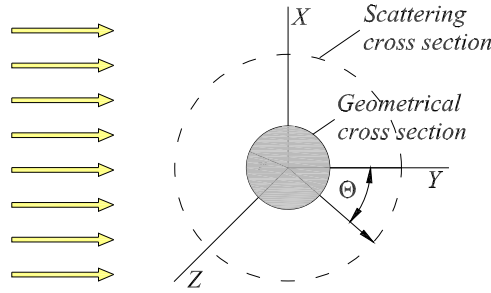


Figure 2.7: Schematic of the scattering cross section by a single particle

The efficiency factors are dimensionless cross sections. These factors are the result of dividing the different cross sections by the geometrical cross section. They may be calculated from the Mie coefficients a_n and b_n with the help of expansion series of the scattered field.

$$Q_{ext} = \frac{C_{ext}}{\pi r^2} = \frac{2}{x^2} \sum_{n=1}^{\infty} (2n+1) \text{Re}(a_n + b_n) \quad (2.72)$$

$$Q_{sca} = \frac{C_{sca}}{\pi r^2} = \frac{2}{x^2} \sum_{n=1}^{\infty} (2n+1) (|a_n|^2 + |b_n|^2) \quad (2.73)$$

$$Q_{abs} = Q_{ext} - Q_{sca} \quad (2.74)$$

2.5.2 The asymmetry factor and the phase function

The magnitude and the direction of the scattered energy at all points of the space may be known through the knowledge of the Poynting vector. The Poynting vector is defined as the vectorial product of the electric field E and the magnetic field H ($S = E \times H$). For a sphere, it is related with the two complex amplitude functions $S_1(\theta)$ and $S_2(\theta)$, where the amplitude functions may be determined as

$$S_1(\cos\theta) = \sum_{n=1}^{\infty} \frac{2n+1}{n(n+1)} (a_n \tau_n + b_n \pi_n) \quad (2.75)$$

$$S_2(\cos\theta) = \sum_{n=1}^{\infty} \frac{2n+1}{n(n+1)} (a_n \tau_n - b_n \pi_n) \quad (2.76)$$

2.5. Radiative properties of a spherical single-particle

The functions π_n and τ_n describe the angular scattering patterns of the spherical harmonics used to describe S_1 and S_2 . These functions follow the recurrence relationships

$$\pi_n = \frac{2n-1}{n-1}\pi_{n-1}\cos\theta - \frac{n}{n-1}\pi_{n-2} \quad (2.77)$$

$$\tau_n = n\pi_n\cos\theta - (n+1)\pi_{n-1} \quad (2.78)$$

starting with

$$\pi_0 = 0 ; \pi_1 = 1 ; \pi_2 = 3\cos\theta \quad (2.79)$$

$$\tau_0 = 0 ; \tau_1 = \cos\theta ; \tau_2 = 3\cos(2\theta) \quad (2.80)$$

The single-particle scattering phase function may be then solved as

$$\tilde{p}(\theta) = 2 \frac{|S_1|^2 + |S_2|^2}{x^2 Q_{sca}} \quad (2.81)$$

It is usually normalized to one. However, in this work the normalization to the single-particle scattering albedo $\tilde{\omega}_0$ is used to follow the procedure suggested by Meador and Weaver [14, 9].

$$\frac{1}{2} \int_{-1}^1 \tilde{p}(\mu, \mu') d\mu = \tilde{\omega}_0 \quad (2.82)$$

To compute the exact Mie phase function a large number of the discretized angles must be applied. To reduce the time needed to calculate the phase function the approximate Henyey-Greenstein phase function [7] is adopted. This approximate phase function showed good agreement with complete Mie scattering calculations when used in some RTE solutions methods [17]. In the section 3.2 the pertinence of its use in the present model will be analyzed. It is defined as

$$p_{HG}(\theta) = \frac{1-g^2}{(1+g^2-2g\cos\theta)^{3/2}} \quad (2.83)$$

For simpler analysis, the directional scattering behavior may be described by the single-particle asymmetry factor \tilde{g} . It is the average cosine of the scattering angle and is defined as

$$\tilde{g} = \overline{\cos\theta} = \frac{1}{2\tilde{\omega}_0} \int_{-1}^1 \tilde{p}(\mu, \mu') \mu d\mu \quad (2.84)$$

The asymmetry factor vanishes if the scattering is isotropic, it is positive with the maximum value $\tilde{g} = 1$ when the radiation is scattered in the forward direction and it is negative with the minimum value $\tilde{g} = -1$ when the radiation is scattered in the backward direction. For spherical particles, the asymmetry factor is quickly obtained from the integration of amplitude functions.

$$\tilde{g} = \frac{4}{x^2 Q_{sca}} \left[\sum_{n=1}^{\infty} \frac{n(n+2)}{n+1} \text{Re}(a_n a_{n+1}^* + b_n b_{n+1}^*) + \sum_{n=1}^{\infty} \frac{2n+1}{n(n+1)} \text{Re}(a_n b_n^*) \right] \quad (2.85)$$

Note that Eq. 2.85 permits to compute the asymmetry factor quickly without to solve all the phase function. In contrast, to compute the phase function the μ -domain

should be discretized in small angles, that may entrain high computational costs.

The single particle radiative properties are computed with the BHMIE subroutine (written by Bohren and Huffman [1] and converted to F90 by M. Walters [20]). This subroutine has been largely used with high confidence in the results.

2.6 The monochromatic algorithm

The complete algorithm to compute the radiative losses in a high temperature SPR, makes use of the different subroutines mentioned above.

- The single-particle optical properties are calculated with the BHMIE subroutine.
- If the Meador and Weaver approximation is used, the χ_0 -term uses a Henyey-Greenstein phase function (PFHG subroutine) computed from the single-particle asymmetry factor and the single-particle scattering albedo.
- The VPPOLY subroutine computes the volume radiative properties when a poly-dispersion distribution is used.
- The TSLAYER subroutine includes the computation of the mono-dispersion volume coefficients and the computation of the forward and backward radiative fluxes.

The non-homogeneity of the layer (linear temperature profile and two-layer media filled with different properties particles) is considered in the TSLAYER subroutine. All the subroutines are compared with reference results, in order to guarantee the confidence on them. This algorithm is then used to compute the total radiative losses by integration along to the working spectrum (0.2 to 12.4 μm). In Fig. 2.8 the flowchart of the algorithm is presented.

2.6.1 Validation of the subroutines

Each of the subroutines used in the model formulation needs to be checked to ensure the best confidence in the overall simulation results. In this section, the results obtained with the developed model are compared with results reported in the literature or with analytical and numerical methods. The normalized radiative losses (RL) are used to do this comparison. Good agreements with the references are reported.

$$RL = \frac{q^-(0)}{q_0\mu_0} \quad (2.86)$$

A. The two-stream radiative subroutine

The TSLAYER subroutine permits to compute the radiative heat fluxes in media with nonuniform temperatures and with nonuniform compositions, where no analytical solution exists. Moreover, the fact that this subroutine uses a tridiagonal matrix solution,

2.6. The monochromatic algorithm

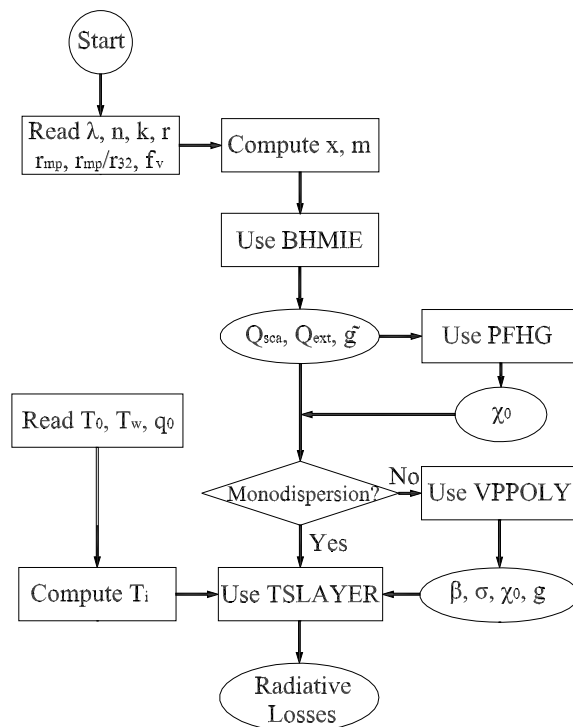


Figure 2.8: Flowchart of the algorithm used to compute the monochromatic radiative losses

reduces considerably the computational time needed. It is a great advantage in regard other existing numerical solutions (for example the `bvp4c` solver by MATLAB), that are very expensive in computation time. The validation of the TSLAYER subroutine is conducted in multiple stages. Four different cases are considered, as shown in Table 2.1. An analytic solution is taken as the reference only for the first case. For all cases the `bvp4c` solver available in MATLAB is used. The `bvp4c` solver computes solutions of boundary problems governed by ordinary differential equations, as those corresponding to the two-stream method (Eqs. 2.17 and 2.18). Note that the purpose in this section is not to investigate the accuracy of the solution (as in Chapter 3), but the confidence using the subroutines. In all comparisons a collimated incident flux and a purely reflective back wall ($\rho_w = 1$) are used.

Case 1: Anisotropic and cold media

The most simplified case for the present model is a slab of particles dispersion that scatter anisotropically and does not emit energy. That case may be solved analytically. The conditions used are: a parameter size $x = 10$, two optical depths, $\tau_n = 1$ and $\tau_n = 10$, and two refractive indexes, $m = 2 - 0.001i$ and $m = 2 - 1i$, that represent either a slight or a strong absorbing medium. The comparison is shown in Table 2.2.

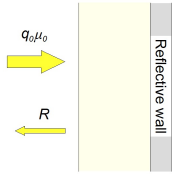
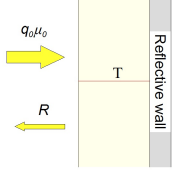
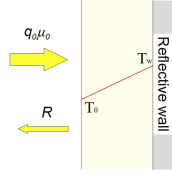
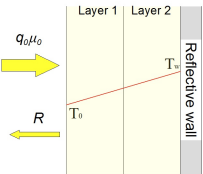
Case 1		Anisotropic and cold media, collimated incident flux and reflective wall at the back	Analytic solution bvp4c (matlab)
Case 2		Anisotropic and emitting media, constant temperature profile, collimated incident flux and reflective wall at the back	bvp4c (matlab)
Case 3		Anisotropic and emitting media, linear temperature profile, collimated incident flux and reflective wall at the back	bvp4c (matlab)
Case 4		Anisotropic and emitting two-layers media, linear temperature profile, collimated incident flux and reflective wall at the back	bvp4c (matlab)

Table 2.1: Validation cases for the TSLAYER subroutine. In column 2 a schematic of each case, in column 3 a brief explanation and in column 4 the methods taken as reference.

		$\tau_n = 1$	$\tau_n = 10$
$\mathbf{m} = 2 - 0.001i$	Analytic solution	0.9278	0.5589
	bvp4c (MATLAB)	0.9278	0.5589
	TSLAYER	0.9277	0.5585
$\mathbf{m} = 2 - 1i$	Analytic solution	0.3589	0.0315
	bvp4c (MATLAB)	0.3589	0.0315
	TSLAYER	0.3589	0.0316

Table 2.2: Comparison of the radiative losses for an anisotropic and cold slab of particles dispersion ($x = 10$, $q_{0,\lambda} = 200 \text{ kW}/\text{m}^2 \mu\text{m}$)

Case 2: Anisotropic and emitting media with constant temperature profile

Two anisotropic and emitting media with constant temperature profile are compared in Table 2.3. The conditions used are: a parameter size $x = 10$, two optical depths, $\tau_n = 1$ and $\tau_n = 10$, and two refractive indexes, $m = 2 - 0.001i$ and $m = 2 - 1i$, that represent a slight and a strong absorbing media as in case 1. A constant temperature

2.6. The monochromatic algorithm

profile, $T = 1000K$, and an incident monochromatic flux, $q_{0,\lambda} = 200 \text{ kW}/m^2\mu m$, are used. These values may be taken as representatives of a high temperature SPR, even if the incident flux is the lower as possible in order to highlight the emission effect.

		$\tau_n = 1$	$\tau_n = 10$
$\mathbf{m = 2 - 0.001i}$	bvp4c (MATLAB)	0.9282	0.5607
	TSLAYER	0.9280	0.5602
$\mathbf{m = 2 - 1i}$	bvp4c (MATLAB)	0.3624	0.0365
	TSLAYER	0.3623	0.0365

Table 2.3: Comparison of the radiative losses for an anisotropic and emitting slab of particles dispersion ($x = 10$, $T = 1000K$, $q_{0,\lambda} = 200 \text{ kW}/m^2\mu m$)

Case 3: Anisotropic and emitting media with a linear temperature profile

Two anisotropic and emitting media with linear temperature profile are compared in Table 2.4. As in Table 2.3, the conditions used are: a parameter size $x = 10$, two optical depths, $\tau_n = 1$ and $\tau_n = 10$, and two refractive indexes, $m = 2 - 0.001i$ and $m = 2 - 1i$. That represents a slight or a strong absorbing media as in case 1. The linear temperature profile begins at $T_0 = 800K$ and ends at $T_w = 1600K$ at the reflective wall. The incident flux is $q_{0,\lambda} = 200 \text{ kW}/m^2\mu m$.

		$\tau_n = 1$	$\tau_n = 10$
$\mathbf{m = 2 - 0.001i}$	bvp4c (MATLAB)	0.9410	0.6130
	TSLAYER	0.9409	0.6126
$\mathbf{m = 2 - 1i}$	bvp4c (MATLAB)	0.4908	0.0462
	TSLAYER	0.4908	0.0462

Table 2.4: Comparison of the radiative losses for an anisotropic and emitting slab of particles dispersion. A linear temperature profile starting at $T_0 = 800K$ and ending at $T_w = 1600K$ is used ($x = 10$, $q_{0,\lambda} = 200 \text{ kW}/m^2\mu m$)

Case 4: Anisotropic and emitting two-layers media with a linear temperature profile

Finally, a similar problem to the one to be optimized is considered in this subsection. To this end, the hemispherical fluxes (q^+ and q^-) inside of a two-layers media are computed. A total optical depth $\tau_n = 1$ is imposed. Each layer is about the half of the total optical depth and it is composed by different particles. Slight absorbing particles are in the first layer while strong absorbing particles are in the second layer. The size parameter is maintained at $x = 10$ in both layers. The linear temperature profile starts at $T_0 = 800K$ and ends at $T_w = 1600K$. The incident monochromatic flux is still $q_{0,\lambda} = 200 \text{ kW}/m^2\mu m$. These simulation conditions are shown in Table 2.5

Figure 2.9 presents the comparison between the forward and backward fluxes computed with the bvp4c solver and those obtained with the TSLAYER subroutine. Note that the fluxes represented in this figure are the diffuse fluxes. It explains the different value for q^+ and q^- at $\tau = 1$ ($\rho = 1$), where the reflected collimated flux augments the

layer 1	layer 2
$0 < \tau < 0.5$	$0.5 < \tau < 1$
$m = 2 + 0.001i$	$m = 2 + 1i$
$x = 10$	$x = 10$

Table 2.5: Optical particle properties used in the comparison of an anisotropic and emitting two-layer medium

q^- value. The results show a good agreement of the TSLAYER subroutine with the references, giving high confidence on its use. In Chapter 3, this subroutine is investigated with respect to its accuracy.

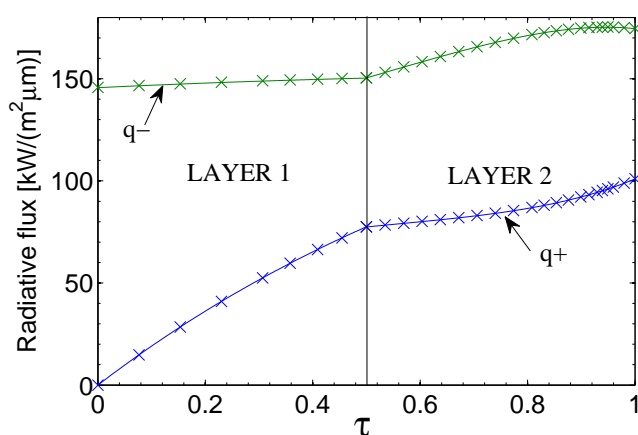


Figure 2.9: Hemispherical fluxes (q^+ and q^-) into an anisotropic and emitting two-layer media. The continuous lines are computed with the TSLAYER subroutine and the crosses with the bvp4c solver ($x = 10$ in both layers, the linear temperature profile starts at $T_0 = 800K$ and ends at $T_w = 1600K$ and $q_{0,\lambda} = 200 kW/m^2 \mu m$)

B. The volume radiative properties subroutine

As mentioned before, the treatment of particle mono-dispersion is simpler and no complicated evaluations are needed. For the particle mono-dispersion, the volume radiative coefficients are calculated with a basic formulation (Eqs. 2.50 and 2.51). The other optical properties have the same values as for a single-particle ($g = \tilde{g}$ and $p = \tilde{p}$, Eq. 2.52). Then, the model for a mono-dispersion is included in the TSLAYER subroutine. In contrast, the treatment of the particles poly-dispersion is quite different. A distribution function (in terms of the particle radii) needs to be used and appropriately discretized (Eqs. 2.60 and 2.61). The VPPOLY subroutine is in charge to model a poly-dispersion of particles using a gamma distribution function. The confidence of such subroutine is then studied. To this purpose, the results for two particle poly-dispersions reported in Modest ([15], pp. 397, Table 12.1) are considered as references. These dispersions use a gamma distribution of particles with $a = 2$, $b = 1.7594$ and $N_0 = 10^{10} m^{-3}$. The wavelength is $\lambda = 3.1416 \mu m$ and the complex refractive index

2.7. Conclusions

are $m = 2 - i$ for the first case and $m = 2$ for the second case. Table 2.6 shows that the comparisons allow a high confidence in the VPPOLY subroutine.

	Modest	VPPOLY	Modest	VPPOLY
	$m = 2 - i$		$m = 2$	
Absorption coefficient κ [m^{-1}]	0.1524	0.1524	0	0
Scattering coefficient σ [m^{-1}]	0.1674	0.1674	0.3363	0.3291
Extinction coefficient β [m^{-1}]	0.3198	0.3198	0.3363	0.3291

Table 2.6: Volume radiative coefficients computed with the VPPOLY subroutine and taken from Modest [15]. The particles gamma distribution parameters are $a = 2$, $b = 1.7594$ and $N_0 = 10^{10} m^{-3}$ and the wavelength is $\lambda = 3.1416 \mu m$

2.7 Conclusions

A radiative model for a high temperature SPR is suggested in this chapter. The receiver is modeled as $1D$, multiple layered slab, filled either with a particle mono-dispersion or with a particle poly-dispersion. The radiative properties of the single particle are computed with the Lorenz-Mie theory and the Henyey-Greenstein phase function. The RTE is solved with a two-stream method, using two different approximations for the diffuse intensity. These approximations seem to be appropriate to model highly anisotropic scattering, as in a high temperature SPR. A number of subroutines are coded in the FORTRAN language, and the algorithm used for the model is presented. The confidence in the different subroutines is studied through comparisons with analytical and numerical results and with results found in the literature: high confidence is found for the subroutines analyzed. The accuracy of the models will be analyzed in the next chapter

References

- [1] C. Bohren and D. Huffman. *Absorption and Scattering of Light by Small Particles*. John Wiley, 1983.
- [2] M. Quinn Brewster. *Thermal Radiative Transfer & Properties*. John Wiley & Sons, 1992.
- [3] S. Chandrasekhar. *Radiative Transfer*. Dover Publication, 1960.
- [4] H. Chen, Y. Chen, H Hsieh, and N. Siegel. Computational fluid dynamics modeling of gas-particle flow within a solid-particle solar receiver. *Journal of Solar Energy Engineering*, 129:160–171, 2007.
- [5] Q. Fu, K.N. Liou, M.C. Cribb, T.P. Charlock, and A. Grossman. Multiple scattering parameterization in thermal infrared radiative transfer. *Journal of the Atmospheric Sciences*, 54:2799–2812, 1997.
- [6] B. Gobereit, L. Amsbeck, R. Buck, R. Pitz-Paal, and H. Muller-Steinhagen. Assessment of a falling solid particle receiver with numerical simulation. In *SolarPaces: Concentrating Solar Power and Chemical Energy Systems, Marrakech-Morocco*, September 2012.
- [7] L.G. Henyey and J.L. Greenstein. Diffuse radiation in the galaxy. *Astrophysical Journal*, 93:70–83, 1941.
- [8] C. Ho, S. Khalsa, and N. Siegel. Modeling on-sun tests of a prototype solid particle receiver for concentrating solar power processes and storage. In *ASME 2009 3rd International Conference on Energy Sustainability collocated with the Heat Transfer and the InterPACK09 Conferences*, 2009.
- [9] A. Ishimaru. *Wave Propagation and Scattering in Random Media*. IEEE Press, New York, 1997.
- [10] J.H. Joseph, W.J. Wiscombe, and J.A. Weinman. The delta-Eddington approximation for radiative flux transfer. *Journal of the Atmospheric Sciences*, 33:2452–2459, 1976.
- [11] M.D. King and Harshvardhan. Comparative accuracy of selected multiple scattering approximations. *Journal of the Atmospheric Sciences*, 43:784–801, 1985.
- [12] H. Klein, J. Karni, R. Ben-Zvi, and R. Bertocchi. Heat transfer in a directly solar receiver/reactor for solid-gas reactions. *Solar Energy*, 81:1227–1239, 2007.
- [13] G. Maag, W. Lipinski, and A. Steinfeld. Particle gas reacting flow under concentrated solar irradiation. *International Journal of Heat and Mass Transfer*, 52:4997–5004, 2009.
- [14] W. Meador and W. Weaver. Two-stream approximation to radiative transfer in planetary atmospheres: An unified description of existing methods and new improvement. *Journal of the Atmospheric Sciences*, 37:630–643, 1979.

References

- [15] M. Modest. *Radiative Heat Transfer*. Academic Press, second edition, 2003.
- [16] S. Ruther and F. Miller. Monte Carlo radiation simulation of a cylindrical small particle solar receiver. In *SolarPaces: Concentrating Solar Power and Chemical Energy Systems, Perpignan-France*, September 2010.
- [17] R. Siegel and J. Howell. *Thermal Radiation Heat Transfer*. Taylor & Francis, 1992.
- [18] C.L. Tien and B.L. Drolen. Thermal radiation in particulate media with dependent and independent scattering. *Annual Review of Numerical Fluid Mechanics and Heat Transfer*, 1:1–32, 1987.
- [19] O. B. Toon, C.P. McKay, and T.P. Ackerman. Rapid calculation of radiative heating rates and photodissociation rates in inhomogeneous multiple scattering atmospheres. *Journal of Geophysical Research*, 94:16287–16301, 1989.
- [20] M. Walters. <http://rime.aos.wisc.edu/mw/models/src/bhmie.f90>, 2002.

Chapter 3

The accuracy of the two-stream method to model a solar particle receiver

Abstract

The accuracy of the two-stream method to model a high temperature SPR is investigated in this chapter. Between the several approximations existing for the two-stream method, the hybrid modified Eddington-delta function (here called Meador and Weaver) and the delta-Eddington (here called Joseph *et al.*) are used. These approximations are chosen because their capacity to treat absorbing and highly anisotropic scattering media. Since both approximations use intrinsically the Henyey-Greenstein phase function approximation, its uses instead of the Lorenz-Mie phase function is studied. Results show that the Henyey-Greenstein phase function underestimates the radiative losses for large optical thicknesses as in a SPR (optically thick medium in some wavelength intervals). Absolute errors of about 4.5% are reported under those conditions. Concerning to the two-stream method, the Meador and Weaver and the Joseph *et al.* approximations seems to have similar accuracies in the spectral solar region ($0.3 < \lambda < 1.4$) and in the IR region ($\lambda > 2.5$). In contrast, the Joseph *et al.* approximation seems to be more accurate in the spectral region between $1.4 < \lambda < 2.5$. Absolute errors less than 2% are reported when both two-stream approximations are compared with the Monte Carlo method using the Lorenz-Mie phase function, for the optimal conditions in a SPR. In this study, a serious drawback found about the Meador and Weaver approximation is the non-physical solutions for the emission computed when the scattering is highly anisotropic: normalized emissivities of $\varepsilon = 2$ may be found when the asymmetry factor is $g = 1$.

3.1 Introduction

The two-stream method may be a powerful tool to compute the heat radiative transfer inside a $1D$ high temperature SPR. A great advantage in the use of this method is the non-expensive computational time associated. It permits its use in processes where the radiative transfer equation (RTE) should be solved a large number of times, e.g.

3.1. Introduction

in an optimization process. Traditionally, the two-stream method has been developed for atmospheric sciences, for example for General Circulation Models [7, 18]. Other applications include the modeling of composite materials [17] and the analysis of packed beds [19]. The two-stream method refers to an approximate scheme for solving the RTE in which only one forward and one backward fluxes are concerned. Hence, various and sometimes radically different approximations exist. The appropriate approximation should be chosen according to the characteristics of the problem. This method was proposed at the first time for the scattering stellar atmospheres [15] (Schwarschild, Milne and Eddington) assuming the scattering of the specific intensity isotropic. Later on, a number of authors refined the method with different approximations, either for isotropic [2, 10, 22] or for anisotropic scattering [3, 9].

Because its extended use in atmospheric sciences, several authors have explored its accuracy. The accuracy for a cold, absorbing and scattering media has been deeply treated. Meador and Weaver [13] compared the accuracy of seven different approximations proposed by various authors and by themselves (Eddington, modified Eddington, quadrature, modified quadrature, hemispheric constant, delta function and hybrid modified Eddington delta function) for a plane-parallel atmosphere submitted to an incident collimated radiation. The study was conducted for an asymmetry factor $g = 0.75$ with a Henyey-Greenstein phase function for four optical thicknesses ($\tau = 0.25$, $\tau = 1$, $\tau = 4$ and $\tau = 16$) and for two single scattering albedos ($\omega_0 = 1$ and $\omega_0 = 0.8$). Results showed that for a normal incidence of radiation, the hybrid modified Eddington-delta function (in what follows called Meador and Weaver approximation) have the best accuracy, with errors lesser than 10%. In all cases, the accuracy decreases when the optical thickness increases and when the medium become absorptive. Truelove [21] showed that the inclusion of a delta-Eddington approximation, suggested by Joseph *et al.* [9] (in what follows called Joseph *et al.* approximation), turns the original Eddington approximation (isotropic scattering) into a method satisfactory accurate for media with high anisotropic scattering. The ranges of investigation for the optical thickness τ_0 was $[0.1 - 100]$ and was $[0.1 \mu m - 100 \mu m]$ for the particle radius. A single scattering albedo $\omega_0 = 1$ (conservative medium) and the phase function computed from Lorenz-Mie theory for spherical particles with a refractive index $n = 1.21$ were used. King and Harshvardhan [11] investigated the accuracy of eight different approximations (asymptotic theory, Eddington, delta-Eddington, Coakley-Chýlek I, Coakley-Chýlek II, hybrid modified Eddington delta function, practical improved flux method and delta-discrete ordinates) for an anisotropic scattering medium ($g = 0.843$) that represents a typical fair weather cumulus cloud. The phase function was computed with the Lorenz-Mie theory. A range of investigation for the optical thickness between $0.1 - 100$ was used for four single scattering albedos ($\omega_0 = 0.8$, $\omega_0 = 0.9$, $\omega_0 = 0.99$ and $\omega_0 = 1$). Results showed that the Joseph *et al.* and the Meador and Weaver were the best approximations for the cases proposed with errors lesser than 15%. The Joseph *et al.* approximation was more accurate for conservative media ($\omega_0 = 1$), but its accuracy decreased for absorbing media ($\omega_0 = 0.8$), while the Meador and Weaver approximation was less accurate for conservative media, but its accuracy is increased when the media become absorbing.

The accuracy of the method was also investigated for atmospheres with thermal emission like in a SPR. Toon *et al.* [20] explored its use in atmospheres with anisotropic

multiple scattering with the presence of thermal emission. Some approximations of the two-stream method were used (delta-hemispherical mean, delta-Eddington and the source function using a delta-hemispherical mean of two-stream scattering intensity) to find fluxes in the infrared spectrum for three cases chosen to represent highly forward scattering, highly absorbing and isothermal water clouds ($\omega_0 = 0.9881$, $g = 0.8010$; $\omega_0 = 0.5245$, $g = 0.9311$ and $\omega_0 = 0.3637$, $g = 0.8487$) for small and large optical depths ($0 \leq \tau \leq 100$). They showed that the accuracy is usually better than 10%, but it may increase in cases when the solar zenith angle is large or when the quantity computed is small. Later, Fu *et al.* [5] investigated the absorption approximation and the modified hemispheric mean two-stream to be used in atmospheres that emit and anisotropically scatter energy. The optical thicknesses was varied in the range of $0.1 \leq \tau \leq 50$ for four combinations of single scattering albedo ω_0 and asymmetry factor g ($\omega_0 = 0.3637$, $g = 0.8487$; $\omega_0 = 0.4982$, $g = 0.9467$; $\omega_0 = 0.7105$, $g = 0.9044$ and $\omega_0 = 0.7771$, $g = 0.7720$). Results showed that the modified hemispheric mean two-stream was the best method, having an accuracy better than 6% in all cases studied, except for very small optical depths.

No closed conclusion is possible to draw from the above discussion about the accuracy of this method when applied to the modeling of a SPR. Moreover, it must be take into account that the conditions inside a SPR change when the wavelength change (isotropy of the scattering, thermal emission, etc.). In this section, the accuracies of two approximations (Meador and Weaver approximation [13] and Joseph *et al.* approximation [9]) are explored. These approximations seem appropriate because their capacity to treat high anisotropy of scattering as well as emission. This investigation is conducted through the comparison with the Monte Carlo method, a purely numerical method which may lead to highly accurate solutions of the RTE provided the number of photon bundles is very high ([4]). The use of the Henyey-Greenstein phase function approximation in the two-stream method is also studied.

3.2 Treatment of the errors

The general objective of the optimization of a high temperature SPR is to find the optimal conditions which permit the receiver to absorb the maximum of incident solar radiation and to minimize the losses due to reflection and emission. In consequence, the radiative losses ($q^-(0)$) computed with such optimal conditions should approach to zero. In order to compare the accuracy of the two-stream method, radiative losses at different conditions will be compared. The use of the relative error (that is the comparison of the approximated results in regard to reference values) may lead to some misleading, owing to the small values calculated. For example, the monochromatic incident solar radiation is around $882 \text{ kW}/(\text{m}^2 \cdot \mu\text{m})$ for $\lambda = 0.5 \mu\text{m}$. Most of the incident energy is absorbed and only 1.4% (reference) of the energy is reflected, which means about $12.4 \text{ kW}/(\text{m}^2 \cdot \mu\text{m})$. For that case, the two-stream method computes $23.8 \text{ kW}/(\text{m}^2 \cdot \mu\text{m})$, that means 2.7% of the incident energy. The absolute error involved is then 1.3%. For the purposes of the optimization, the two-stream method is accurate enough, due to the small difference between computations ($11 \text{ kW}/(\text{m}^2 \cdot \mu\text{m})$ over $882 \text{ kW}/(\text{m}^2 \cdot \mu\text{m})$). However, the relative error between both computations is close to 100%. For that

3.3. The Henyey-Greenstein and the Lorenz-Mie phase functions

reason, the absolute error will be used in what follows.

3.3 The Henyey-Greenstein and the Lorenz-Mie phase functions

The Mie-phase function permits to exactly compute the angular behavior of the energy scattered by a spherical particle. However, the strong oscillations associated with such a phase function may enormously complicate the computations for a given wavelength. For that reason, it is sometimes desirable to approximate the phase function by simpler expressions having a regular behavior [14]. For dielectric materials and for large particle sizes, as those used in high temperatures SPRs, the scattering of energy have usually strong forward-direction peaks. An approximation that has been largely used with good results for this kind of scattering behavior is the Henyey-Greenstein phase function approximation. To illustrate this statement, a comparison between the Lorenz-Mie and the Henyey-Greenstein phase functions is shown in Fig. 3.1. It is made at a wavelength $\lambda = 0.5 \mu m$ for small and large parameter sizes. The refractive index is $m = 2.58 + i0.107$, which corresponds to the *SiC* at this wavelength. Obviously, the scattering behavior changes at each parameter size and therefore at each wavelength or particle radius.

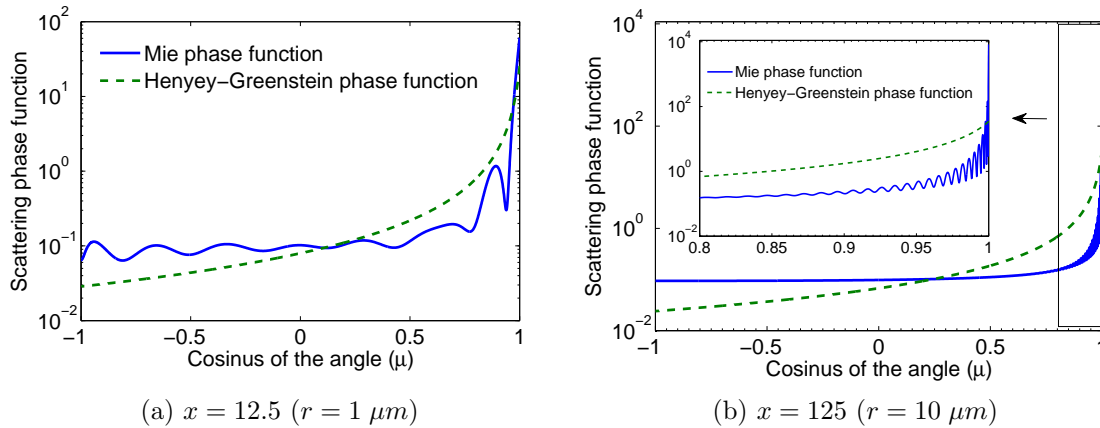


Figure 3.1: Lorenz-Mie and Henyey-Greenstein phase functions for a particle with two different parameter sizes ($\lambda = 0.5 \mu m$ and $m = 2.58 + i0.107$, which correspond to the *SiC* at this wavelength)

In most of the two-stream methods, a complete information about the scattering phase function is not needed. It is because the anisotropy of the scattering is treated through the use of the asymmetry factor, which can be computed directly from the Lorenz-Mie coefficients (Eq. 2.82). That is the case of the Joseph *et al.* approximation, in which only the g -value is needed. However, in its development the phase function is approximated by the HG phase function. Moreover, to increase the accuracy of the method, Meador and Weaver proposed the modification of the γ_3 and γ_4 terms (Eqs. 2.28 and 2.35) through the inclusion of the χ_0 -term. The χ_0 -term is obtained from the integration of the phase function (Eq. 2.25). The analysis that follows, then, concerns to the two-stream methods that use in any way the Henyey-Greenstein phase function

approximation, (both methods in this work). A difficulty in the numerical integration of the Lorenz-Mie phase function lies in its high sensitivity to the angular discretization: that implies high computational efforts. It is specially true for large particles. The Henyey-Greenstein phase function approximation permits to avoid this inconvenience, owing to the lower angular discretizations needed. In Fig. 3.2 the asymmetry factor computed from the Lorenz-Mie formulation and from the integration of the Lorenz-Mie phase function are compared. The computations are made for a particle with a refractive index of $m = 0.28 + 0.107i$, which corresponds to the *SiC* at $\lambda = 0.5 \mu m$. The parameter size is varied from 0.1 to 1000, and two angular discretizations ($n_\mu = 10000$ and $n_\mu = 100000$) are used.

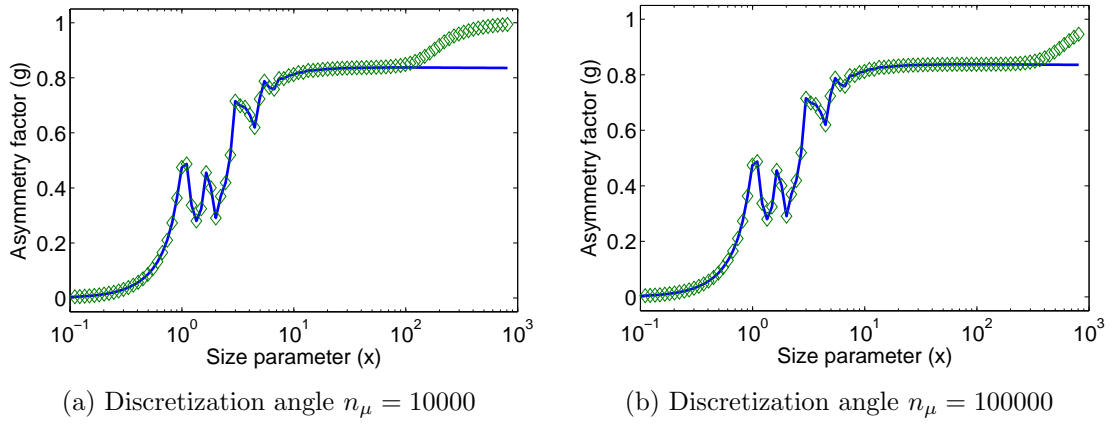


Figure 3.2: Asymmetry factor for a spherical particle computed from the Lorenz-Mie formulation (continuous line) and from the integration of the phase function (diamonds) ($m = 2.58 + 0.107i$ and $\lambda = 0.5 \mu m$)

For small parameter sizes ($x < 1$) the scattering is nearly isotropic ($g \sim 0$) and the phase function does not present high oscillations. In consequence, low angular discretizations are needed to reach the true asymmetry factor through the integration of the Lorenz-Mie phase function. In contrast, for large parameter sizes ($x > 1$), the scattering becomes highly anisotropic in the forward direction ($g \rightarrow 1$), and the angular discretization need to become higher. Note that for parameter sizes between $x = 1$ and $x = 10$ the asymmetry factor oscillates as a consequence of the strong oscillation behavior of the phase function in this region. To study the error associated to the use of the HG phase function in the χ_0 -term computation, the radiative losses of a cold media filled with particles having a refractive index $m = 2.58 + 0.107i$ at a wavelength $\lambda = 0.5 \mu m$ (*SiC*) is considered. The χ_0 -terms computed by using both Lorenz-Mie and Henyey Greenstein phase functions for two parameter sizes are given in Table 3.1.

The χ_0 -terms computed with the HG phase function are much lower than those computed with the Lorenz-Mie phase function. Nevertheless, such large discrepancies between the χ_0 -values has not a large impact on the radiative losses, as it is highlighted in Fig. 3.3.

For the two parameter sizes, the use of the HG phase function overestimates the losses at thin media, while underestimates the losses at thick media. For optically thin media ($\tau \sim 1$), the maximum error found for $\tau < 3$ is about 13% (absolute error based

3.4. General accuracy of the two-stream method

	Lorenz-Mie	Henyeey-Greenstein
$x = 12.5$	7.72×10^{-2}	4.43×10^{-2}
$x = 125$	7.78×10^{-2}	3.96×10^{-2}

Table 3.1: χ_0 -term computed for two parameter sizes with the Lorenz-Mie and the Henyeey-Greenstein phase functions ($m = 2.58 + 0.107i$ and $\lambda = 0.5 \mu m$)

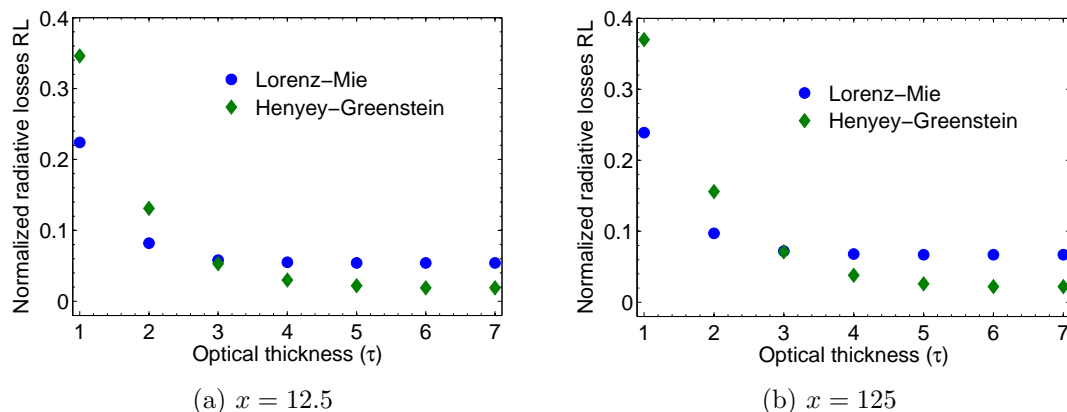


Figure 3.3: Comparison of the radiative losses when using the Lorenz-Mie and the Henyeey-Greenstein phase functions in a cold SPR model solved with a two-stream method ($m = 2.58 + 0.107i$ and $\lambda = 0.5 \mu m$)

on the incident flux). In contrast, for optically thick media ($\tau > 5$), the errors found are between 3.5 – 4.5%. Because the radiative losses of an optimized SPR should be minimized, Figure 3.3 shows that the optical thickness of an optimized SPR must be large enough. Consequently, the error associated to the use of the Henyeey-Greenstein phase function is around 4%, which may be assumed acceptable.

3.4 General accuracy of the two-stream method

The accuracy of the two-stream method using both the Meador and Weaver [13] and the Joseph *et al.*[9] approximations is investigated. The Monte Carlo method is used as the reference to compare the radiative losses (Eq. 2.83) in the SPR model [4]. This method is highly accurate when sufficiently numbers of packets of energy (bundles) are used in the simulations. However, the computational time needed may become large [14, 16]. Many authors have studied this method for radiative heat transfer[6, 8], such as for the modeling of the radiative heat transfer in participating media subjected to a collimated beam [1, 12]. For the present comparisons, at least 10^6 bundles are used for ensuring the accuracy of the reference data. A more extended explanation of this method may be found in annexe B.

Two situations are considered in this study: the first is for a cold media with an incident flux, the second is for an emissive media without incident flux. The asymmetry factor taken into consideration is from isotropic to highly anisotropic in the forward

direction ($0 \leq g \leq 1$). Therefore, the scattering albedo must overlap materials with several degrees of scattering ($0 \leq \omega_0 \leq 1$), and the optical thickness must vary from $\tau_0 \approx 1$ to $\tau_0 \approx 7$.

3.4.1 Cold media with an incident flux

The first case investigated is a cold media with an incident flux. It may be representative of the behavior of a SPR at low wavelengths ($\lambda < 1.5$). In this spectral region, the emission due to the temperature inside the SPR may be assumed negligible in regard to the phenomena of light absorption and scattering. Moreover, the most important fraction of incident solar radiation is present in this region. In Fig. 3.4, comparisons for such media are presented. Simulations are conducted for four asymmetry factors ($g = 0.1, g = 0.5, g = 0.75$ and $g = 0.99$) and for four scattering albedo ($\omega_0 = 0.25, \omega_0 = 0.5, \omega_0 = 0.75$ and $\omega_0 = 0.9$). Results for $\omega_0 = 0.5$ are not presented in Fig. 3.4 to improve readability by avoiding overlaps of the curves.

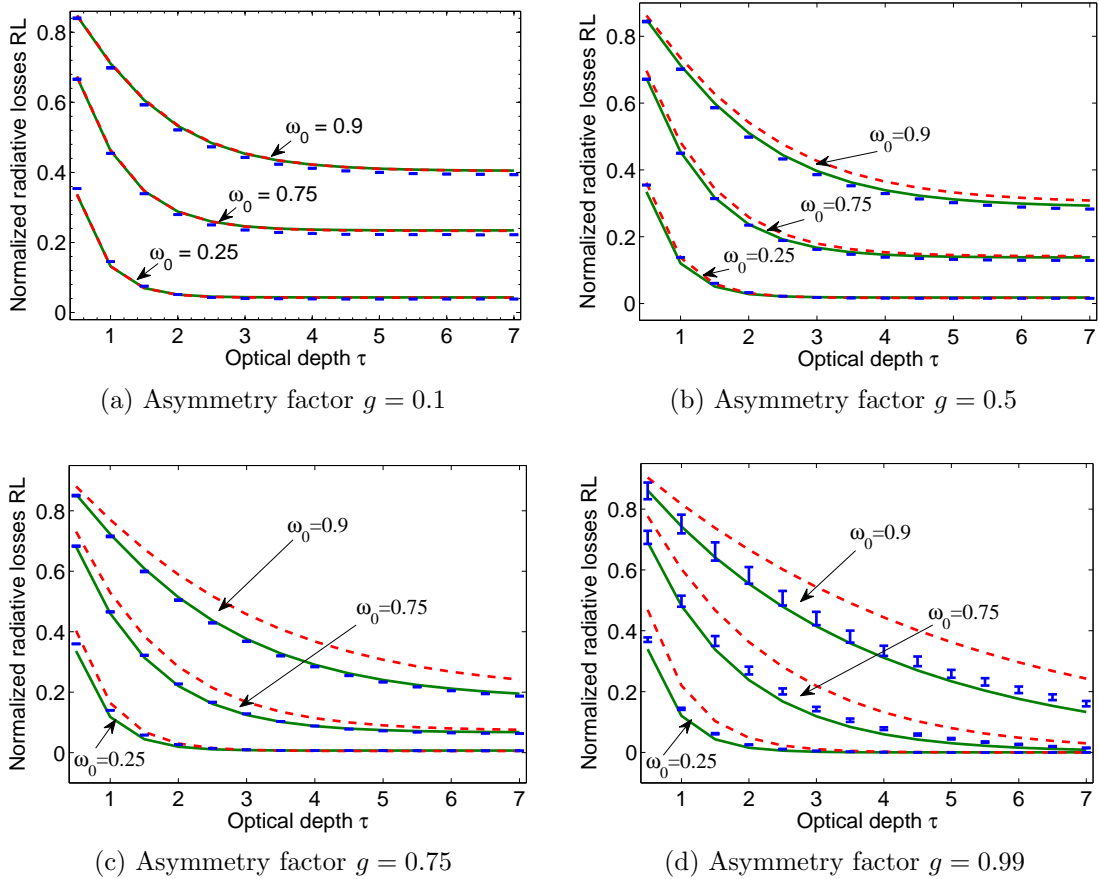


Figure 3.4: Radiative losses for a SPR computed with a Monte Carlo (errorbars) and two two-stream (solid lines for the Joseph *et al.* and dashed lines for the Meador and Weaver approximations) methods. The SPR is assumed cold, submitted to a concentrated and collimated solar flux and with a reflective wall at the back ($\rho_w = 1$).

Both approximations are highly accurate when the scattering is isotropic ($g \rightarrow 0$),

3.4. General accuracy of the two-stream method

independently of the absorption degree of the particles (see Fig. 3.4a). The fact that both approximations become like the Eddington approximation explains the high accuracy achieved. For example, the highest accuracy is found when the absorption is higher ($\omega_0 = 0.25$) and the scattering is near isotropic ($g = 0.1$). Absolute errors lower than 0.5% are found, which in practice are not noticeable. Otherwise, when the anisotropy increases, the accuracy decreases (see Figs. 3.4b, 3.4c and 3.4d). Nevertheless, note that for all cases the error is lower when the absorption is higher ($\omega_0 = 0.25$), being around of 10% for thin thicknesses and 0.5% for thick thicknesses. In such case the Meador and Weaver approximation is slightly more accurate than the Joseph *et al.* approximation. In contrast, when the media is low absorptive ($\omega_0 = 0.9$), the error becomes higher. It becomes around 10% for the Meador and Weaver approximation and 3% for the Joseph *et al.* approximation.

In summary, the Joseph *et al.* approximation is generally more accurate than the Meador and Weaver approximation at high anisotropies. However, the accuracy of the Joseph *et al.* approximation decreases when the absorption increases while the Meador and Weaver approximation seems slightly more accurate for high absorption rates. It suggests that both approximations are useful for simulating a **cold** SPR, provided the SPR is optically thick and mainly absorptive.

3.4.2 Emissive media without incident flux

The case of an emissive media without incident flux may represent the behavior of the SPR at high wavelengths. The solar incident flux becomes lower and may be negligible in regards to the importance of the particles emission owing their high temperature. Toon *et al.* [20] noted that some two-stream approximations may give non exact results in the extreme case of a purely absorbing medium that only emits energy. In consequence, the capability of both approximations to model such media is analyzed. The two-stream equations (see Eqs. 2.19 to 2.22) are solved analytically making the incident flux to a zero value ($q_0 = 0$). The analysis is conducted for an optically thick media ($\tau \rightarrow \infty$). For these conditions, the source functions terms (G^\pm) are reduced to terms containing the emission term only. The slab emissivity is defined as the backward flux at the front of the slab compared with the blackbody flux emitted at the same temperature. The wall reflectivity is kept at the value $\rho_w = 1$.

$$\varepsilon = \frac{q^-(0)}{\pi I_b} \quad (3.1)$$

where I_b is the intensity of radiation from a blackbody, given by the Planck's law (Eq. 2.6). Under these conditions, the slab emissivity for any two-stream method becomes

$$\varepsilon = \frac{2(1 - \omega_0)(\gamma_1 - \gamma_2 + \nu)}{\gamma_2(\gamma_1 - \gamma_2)} \quad (3.2)$$

For a purely absorbing medium ($\omega_0 = 0$) the emissivity of the slab should become 1. Applying this constraint, the γ -terms and the emissivity for the two approximations used are shown in Table 3.2.

For the Joseph *et al.* approximation, emissivities higher than 1 are computed independently of the asymmetry factor. Even though this inconvenient, it may becomes

	γ_1	γ_2	ε
Joseph et al approximation	$-\frac{7}{4}$	$\frac{1}{4}$	1.07
Meador and Weaver approximation	$-\frac{7-3g^2}{4}$	$\frac{1-g^2}{4}$	$\frac{8(2-g^2-\nu)}{(1-g^2)(2-g^2)}$

Table 3.2: γ -terms and slab emissivity for a purely absorptive ($\omega_0 = 0$) and optically thick ($\tau \rightarrow \infty$) media without incident flux. The comparison is done for the two-tream approximations studied

irrelevant when real materials have emissivity lower than 1 ($\omega_0 > 0$). On the other hand, the slab emissivity is dependent on the asymmetry factor for the Meador and Weaver approximation. For isotropic scattering ($g \sim 0$), the approximation becomes as the Eddington approximation and consequently the emissivity becomes $\varepsilon \sim 1.07$. On the other hand, for anisotropic scattering ($g \rightarrow 1$) the emissivity increases its value until non-physical values close to 2. To illustrate this fact, in Fig. 3.5 the slab emissivity for two asymmetry factors and for two scattering albedo is compared for both approximations.

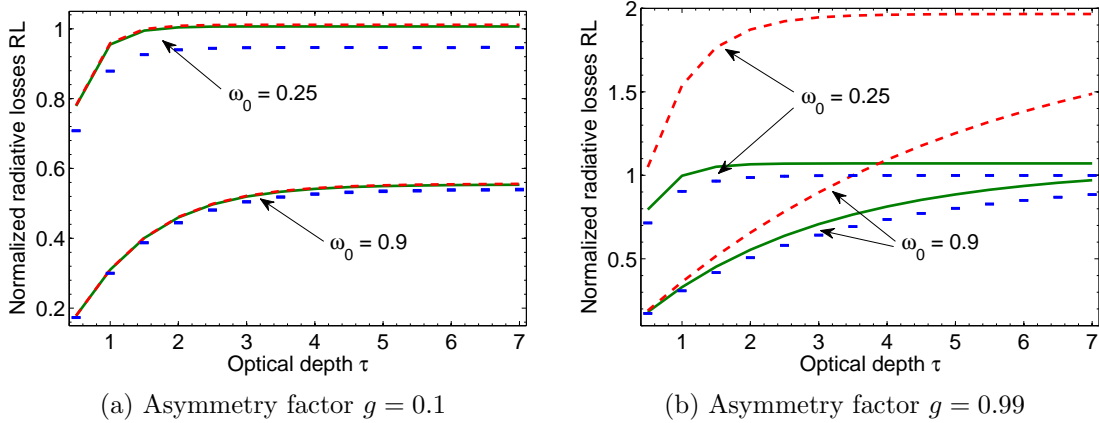


Figure 3.5: Radiative losses for a SPR computed with a Monte Carlo (bars) and a two-stream (solid lines for the Joseph *et al.* and dashed lines for the Meador and Weaver approximations) methods. The SPR is assumed only emissive without incident flux ($\rho_w = 1$)

If the media is isotropically diffusive ($g = 0.1$) and highly scattering ($\omega_0 = 0.9$), both approximations are in good agreement and, in comparison with the Monte-Carlo results (assumed exact), the errors are less than 2%. For such media the accuracy decreases when the albedo decreases, having errors up to 6%. Because the ideal media in a SPR at high wavelengths should be weakly emissive and with isotropically scattering, both approximations are accurate enough for such a modeling. Nevertheless, when the scattering become anisotropic, the accuracy fails for the Meador and Weaver approximation, achieving errors of around 100% (see Fig. 3.5b). This serious drawback is specially important for media with high absorptivity. In consequence, the Meador

3.5. The two-stream method for computing the optimized radiative losses

and Weaver approximation is not recommendable for modeling the emission when the media is highly anisotropic. For the Joseph *et al.* approximation, the discrepancies with the Monte-Carlo are small whatever the degree of anisotropy (i.e. $0.1 \leq g \leq 1$), the albedo-value and the optical thickness within the range $1 \leq \tau_0 \leq 7$).

3.5 The two-stream method for computing the optimized radiative losses

A solar particle receiver should be able to absorb the maximum of energy in the solar wavelength region, and at the same time to reduce its emission at higher wavelengths. A material with such characteristics should have, *a priori*, a high anisotropic behavior in the first region and an almost isotropic behavior in the second one. From the analysis given in section 3.4, the best two-stream approximation among the both analyzed depends on the anisotropy of the scattering.

Results of the optimization that will be discussed in Chapter 4 are used to compare the behavior of both approximations in a specific way. The radiative losses computed with a Monte Carlo method are used as reference [4]. The Monte Carlo simulations are conducted with at least 10^6 bundles of ray achieving high confidence interval (statistical error lower than 0.1 %). In the following subsections, the radiative losses computed with the two-stream method using the Meador and Weaver and the Joseph *et al* approximations is compared, first with the radiative losses using the Monte Carlo method and the Henyey Greenstein phase function and, next using the Monte Carlo method and the Lorenz-Mie phase function. The first comparison allows on to analyze the accuracy of the two-stream method without regard to the phase function, and the second one permits to analyze the accuracy of the complete model.

3.5.1 Radiative losses using the Monte Carlo method and the Henyey-Greenstein phase function

The accuracy of the two-stream method, excluding the error linked to the approximation of the phase function, is investigated in a representative SPR case. For that, the two-stream method is compared with the Monte Carlo method using the Henyey-Greenstein phase function approximation. The refractive index, particle size and volume fraction used are the optimal found for an ideal material that minimizes the radiative losses in a SPR (as given in Table 4.6 and in Fig. 4.2b). A constant temperature profile ($T = 1100 K$) and a concentration of the solar energy of $C = 600$ are considered. In Fig. 3.6 this comparison is shown.

The comparison shows that at short wavelengths ($0.3 < \lambda < 1.4 \mu m$), the Meador and Weaver approximation is slightly more accurate. In this wavelength interval, the material is highly absorptive ($\omega_0 \sim 0.5$) and the scattering is highly anisotropic ($g \sim 1$). High accuracy is found for this approximation even if the quantities to be computed are very small in comparison with the very high incident flux. The maximum error found is less than 0.5% at wavelength $\lambda = 1.3 \mu m$. Otherwise, the Joseph *et al.* approximation overestimate the losses, achieving errors up to 1.5%. In contrast, for the wavelength region between $1.4 < \lambda < 2.5 \mu m$ the Joseph *et al.* approximation

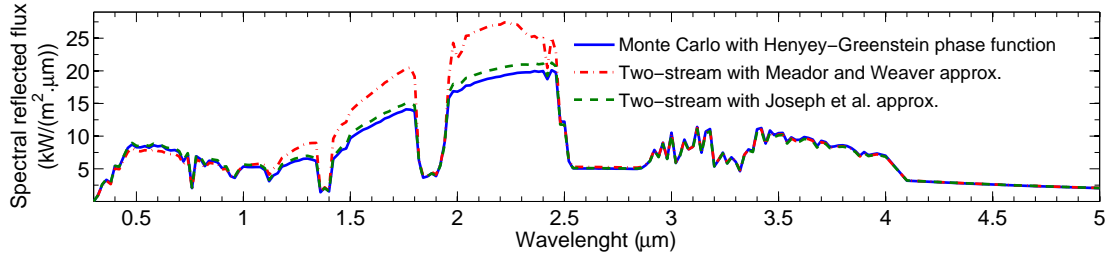


Figure 3.6: Radiative losses computed with the two-stream method and a reference Monte Carlo method [4]. The MC method uses the Henyey-Greenstein phase function approximation. The refractive index, particle size and volume fraction used are the optimal found for a constant temperature profile ($T = 1100 K$) and a solar radiation concentration $C = 600$

is the most accurate approximation. The absorption and the scattering behavior of the slab particles changes in this region, becoming more reflective and less anisotropic. Medium values of the asymmetry factor are still found in this region, that explain the overestimation of the emission by the Meador and Weaver approximation. The maximum error given by the Joseph *et al.* approximation in this region is around 0.5%. For the Meador and Weaver approximation, the maximum error reaches 1.4%. For wavelengths higher than $2.5 \mu m$, both approximations are highly accurate, with errors less than 0.2%.

3.5.2 Radiative losses using the Monte Carlo method and the Lorenz-Mie phase function

The complete accuracy of the model is investigated in this section. To this end, the radiative losses computed with the Monte Carlo method using the Lorenz-Mie phase function are compared with those obtained with the two-stream method. As in the last comparison, the refractive index, particle size and volume fraction are the optimal ones for an ideal material. The temperature is constant at $T = 1100 K$ and the concentration of the solar energy is $C = 600$. Fig. 3.7 shows this comparison.

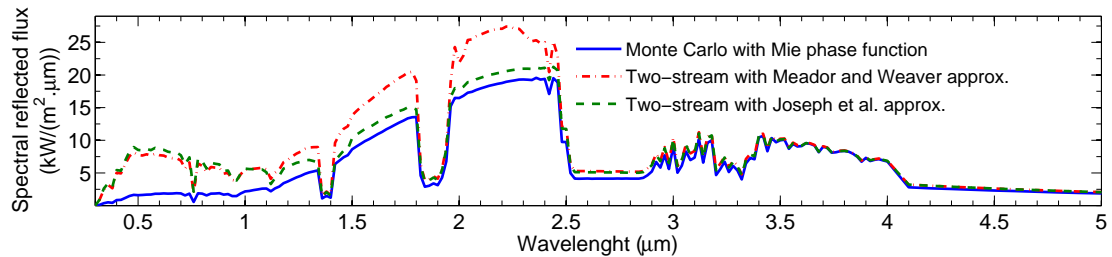


Figure 3.7: Radiative losses computed with the two-stream method and a reference Monte Carlo method [4]. The MC method uses the Lorenz-Mie phase function. The refractive index, particle size and volume fraction used are the optimal found for a constant temperature profile ($T = 1100 K$) and a solar radiation concentration $C = 600$

Results show that the use of the Lorenz-Mie phase function instead of the Henyey-

3.5. The two-stream method for computing the optimized radiative losses

Greenstein approximation produces noticeable differences in the spectral solar region ($0.3 < \lambda < 1.4 \mu m$). It is because of the high absorptance and the high anisotropy of the scattering in this region. Both two-stream approximations overestimate the radiative losses, being the Meador and Weaver approximation slightly more accurate. Errors up to 1% for the Meador and Weaver approximation, and up to 2.7% for the Joseph *et al.* approximation are found in this region. In the wavelength region between $1.4 < \lambda < 2.5 \mu m$ the relative error decreases, and become similar than those obtained using the Henyey-Greenstein phase function. The maximal errors are 0.6% for the Joseph *et al.* approximation and 1.5% for the Meador and Weaver approximation. For wavelengths higher than $2.5 \mu m$, the accuracy of both approximations becomes higher.

The comparisons of the radiative losses computed using the two-stream method demonstrate small differences with the reference data. The maximal spectral errors found and the normalized radiative losses computed with the Monte Carlo and the two-stream methods are reported in Table 3.3.

	Max. spectral error	Norm. radiative losses
MC method with MIE phase function	--	5.67%
MC method with HG phase function	1.2%	6.76%
TS method with M&W approximation	1.5%	7.71%
TS method with J&al. approximation	2.7%	7.64%

Table 3.3: Comparison of the maximal spectral error and the integrated normalized radiative losses for a high temperature SPR using the optimized ideal material. MC means Monte Carlo method, TS means two-stream method, HG means Henyey-Greenstein phase function, M&W means Meador and Weaver approximation and J&al. means Joseph *et al.* approximation

The maximal spectral errors are found in the $0.3 < \lambda < 1.4 \mu m$ region for all comparisons, except in the case of the Meador and Weaver approximation for which it is found in the $1.4 < \lambda < 2.5 \mu m$ region. In the $0.3 < \lambda < 1.4 \mu m$ region, the use of the Henyey-Greenstein phase function is the main cause of errors, independently of the approximation used for the two-stream method. It is due to the highly anisotropy of the scattering and to the high absorptance of the material. The two-stream method with the Meador and Weaver approximation is more accurate than that with the Joseph *et al.* approximation. In contrast, in the $1.4 < \lambda < 2.5 \mu m$ region where the anisotropy of the scattering is lower, the error due to the use of the Henyey-Greenstein phase function is lesser. The two-stream method with the Joseph *et al.* approximation is the more accurate in this region, owing to the bad capacity to treat the emission by the Meador and Weaver approximation. In this region the errors become lower. Finally, for wavelengths $\lambda > 2.5 \mu m$, where the scattering become nearly isotropic, both two-stream approximations become very accurate.

Regarding the integrated normalized radiative losses (third column in Table 3.3), both two-stream approximations compute values close to the reference ($\sim 5.7\%$ for the Monte Carlo using the Lorenz-Mie phase function): $\sim 7.6\%$ for both two-stream approximations. These results mean that the use of any of the two-stream approximations leads to similar results, with enough accuracy. For the analysis that follows in the next chapters the Joseph *et al.* approximation is utilized owing to its slightly

better accuracy.

3.6 Conclusion

The accuracy of the models used to compute the radiative losses in the high temperature SPR model, presented in the Chapter 2, is studied. The two-stream method based either on the Meador and Weaver formulation (hybrid modified Eddington-delta function) or on the Joseph *et al.* formulation (delta-Eddington) are compared to a Monte Carlo method, considered as the reference. The influence on the accuracy of the two-stream method by the use of the Henyey-Greenstein phase function is also investigated. The absolute error is the quantity retained for comparisons. Results show that the use of the Henyey-Greenstein phase function may produce high inaccuracies when the scattering is highly anisotropic. Concerning to the two-stream methods, the Meador and Weaver approximation works better for high absorptive and high anisotropic scattering media. Such conditions are typical of the $0.3 < \lambda < 1.4 \mu m$ spectral region, where the incident solar radiation is important. In contrast, the Meador and Weaver approximation has a serious drawback in the computation of the radiative emission. This approximation produces non-physical emissivities (up to 2) for high anisotropic scattering. However, due to the near-isotropic behavior of the scattering at high wavelength values, this problem may be not noticeable in the optimization process. The Joseph *et al.* approximation works better in spectral regions where the emission and the anisotropy of the scattering are important, as the $1.4 < \lambda < 2.5 \mu m$ region. Finally, for nearly isotropic scattering and emission, both approximations are found to be accurate enough. These conditions are found in the $\lambda > 2.5 \mu m$ region.

References

- [1] S. Avriplier, E. Tinet, and E. Delettre. Monte Carlo simulation of collimated beam transmission through turbid media. *Journal of Physics*, 51(22):2521–2542, 1990.
- [2] S. Chandrasekhar. *Radiative Transfer*. Dover Publication, 1960.
- [3] J. Coakley and P. Chýlek. The two-stream approximation in radiative transfer: Including the angle of the incident radiation. *Journal of the Atmospheric Sciences*, 32:409–418, 1975.
- [4] J. Delatorre, G. Baud, J.J. Beziau, S. Blanco, C. Caliot, J.F. Cornet, C. Coustet, J. Dauchet, M. El Hafi, V. Eymet, R. Fournier, J. Gautrais, O. Gourmel, D. Joseph, N. Meilhac, A. Pajot, M. Paulin, P.Perez, B. Piaud, M. Roger, J. Rolland, F. Veynandt, and S. Weitz. Monte Carlo advances and concentrated solar applications. *Solar Energy*, 103:653–681, 2013.
- [5] Q. Fu, K.N. Liou, M.C. Cribb, T.P. Charlock, and A. Grossman. Multiple scattering parameterization in thermal infrared radiative transfer. *Journal of the Atmospheric Sciences*, 54:2799–2812, 1997.
- [6] J.R. Howell. The Monte Carlo method in radiative heat transfer. *Journal of Heat Transfer*, 120:547–560, 1998.
- [7] R.G. Isaacs, W.C. Wang, R.D. Worsham, and S. Goldenberg. Multiple scattering treatment for use in the LOWTRAN and FASCODE models. Technical report, Atmospheric and Environmental Research, Inc. (AER), 1986.
- [8] H. Iwabuchi. Efficient Monte Carlo method for radiative transfer modeling. *Journal of the Atmospheric Sciences*, 63:2324–2339, 2006.
- [9] J.H. Joseph, W.J. Wiscombe, and J.A. Weinman. The delta-Eddington approximation for radiative flux transfer. *Journal of the Atmospheric Sciences*, 33:2452–2459, 1976.
- [10] Y. Kawata and W. Irvine. The Eddington approximation for planetary atmospheres. *The Astrophysical Journal*, 160:787–790, 1970.
- [11] M.D. King and Harshvardhan. Comparative accuracy of selected multiple scattering approximations. *Journal of the Atmospheric Sciences*, 43:784–801, 1985.
- [12] X. Lu and P. Hsu. Reverse Monte Carlo method for transient radiative transfer in participating media. In *ASME International Mechanical Engineering Congress*, 2003.
- [13] W. Meador and W. Weaver. Two-stream approximation to radiative transfer in planetary atmospheres: An unified description of existing methods and new improvement. *Journal of the Atmospheric Sciences*, 37:630–643, 1979.
- [14] M. Modest. *Radiative Heat Transfer*. Academic Press, second edition, 2003.

- [15] A. Schuster. Radiation through a foggy atmosphere. *The Astrophysical Journal*, 21:1–22, 1995.
- [16] R. Siegel and J. Howell. *Thermal Radiation Heat Transfer*. Taylor & Francis, 1992.
- [17] C. M. Spuckler and R. Siegel. Two-flux and diffusion methods for radiative transfer in composite layers. *Heat Transfer with Combined Modes*, 299:41–49, 1994.
- [18] P.W. Stackhouse and G.L. Stephens. A theoretical and observational comparison of cirrus cloud radiative properties. Technical report, Department of Atmospheric Science, Colorado State University, 1989.
- [19] C.L. Tien and B.L. Drolen. Thermal radiation in particulate media with dependent and independent scattering. *Annual Review of Numerical Fluid Mechanics and Heat Transfer*, 1:1–32, 1987.
- [20] O. B. Toon, C.P. McKay, and T.P. Ackerman. Rapid calculation of radiative heating rates and photodissociation rates in inhomogeneous multiple scattering atmospheres. *Journal of Geophysical Research*, 94:16287–16301, 1989.
- [21] J.S. Truelove. The two-flux model for radiative transfer with strongly anisotropic scattering. *International Journal of Heat and Mass Transfer*, 27:464–466, 1984.
- [22] W. Unno and E. Spiegel. The Eddington approximation in the radiative heat equation. *Publications of the Astronomical Society of Japan*, 18:85–95, 1966.

Chapter 4

Optimization of the optical particle properties for a high temperature solar particle receiver

Abstract

The SPR model presented in Chapter 2 is implemented to optimize the optical properties of particles to be used in the SPR. First, the mono-dispersion is compared with the poly-dispersion using a gamma function distribution. No noticeable influence is found by employing the concept of equivalent particle radius. Second, a parametric study with the aim at determining the influences of the refractive index, particle radius and volume fraction on the radiative losses is conducted. Regions of n and k that minimize the radiative losses are suggested. Finally, a non-homogeneous slab of particle dispersion composed of two-layers at high temperature, submitted to a concentrated and collimated solar radiation flux with a reflective receiver back wall is considered as a model of a solar particle receiver.

A Particle Swarm Optimization (PSO) algorithm is used to optimize the particle radius ($0.1 \mu m \leq r \leq 100 \mu m$), the volume fraction ($1 \times 10^{-7} \leq f_v \leq 1 \times 10^{-4}$) and the refractive index ($2.0 \leq n \leq 4.5$ and $0.0001 \leq k \leq 25$) of an ideal (theoretical) material intended for solar particle receivers. Single- and two-layer receivers with known temperature profiles are optimized to maximize the receiver efficiencies. Spectral selective behavior of the optimized refractive index, influence of particle radii and volume fractions are discussed. The ideal optical properties found for the particles give the maximum efficiency reachable by the receivers considered and show that an optimized single-layer receiver will perform as well as a two-layer receiver.

4.1 Introduction

Several materials (refractive index) with different geometrical properties (particle radius and volume fraction) have been proposed to be used in high temperature SPRs.

4.2. The Particle Swarm Optimization algorithm

As underlined in Chapter 1, small and large particles were proposed. For instance, a number of investigations were conducted for small particles. High absorptive materials as graphite, vitreous carbon and carbon [6, 1] were adopted, achieving high theoretical efficiencies (for example around 90% for an output temperature of 1400 K [2]) and, also high experimental efficiencies (around 80% with temperatures above 2100 K [1]). In the same way, large particles were also studied. Some advantages as low agglomeration tendency and feasibility of using the particles as storage media are claimed [9]. Alumina based commercial particles were used in some different designs of SPRs [4, 5]. The authors suggest that high efficiencies are reachable using large particles. As example, theoretical receiver efficiencies exceeding 92% were estimated for a 350 MWth receiver working from 600 K to 1100 K [5]. To increase the efficiency in the actual SPRs, additional investigations on the optimal radiative properties (refractive index) as well as the best receiver composition (particle size and volume fraction) should be conducted. The effect of the temperature distribution within a particle layer and the influence of the use of different particles were not studied previously. In this chapter, an optimization of the equivalent radius, volume fraction and refractive index of particles is presented. This study aims to highlight the influence of these parameters on the efficiency of such a SPR. The influence of the mass loading (single or two layers) and the temperature profiles (constant or linear) are also studied.

4.2 The Particle Swarm Optimization algorithm

Amongst the multiple possibilities of solving an optimization problem, the evolutionary algorithms became recently very popular. It is because of their good confidence and the low computational efforts required. In general, they are less time consumers than exact algorithms. It makes to evolutionary algorithms a good alternative when the search space is large [10]. The particle swarm optimization (PSO) algorithm is an heuristic process capable of solving complex problems of search. The PSO exploits simple analogies of social interaction, rather than purely individual cognitive abilities. Some advantages of the PSO algorithm are the ease of code parallelization and its simplicity in formulation and computer implementation [13]. Note that in this subsection the word “particle” describes a vector of parameters to be optimized, with respect to the original terminology [10].

The PSO is applied to a swarm of particles and conducts search in space in the following manner. For the particle i , the next position y_{k+1} is updated as

$$y_{k+1}^i = y_k^i + v_{k+1}^i \quad (4.1)$$

with the velocity v^i calculated by

$$v_{k+1}^i = wv_k^i + c_1r_1(p_k^i - y_k^i) + c_2r_2(p_k^g - y_k^i) \quad (4.2)$$

subscript k indicates a pseudo-time increment, p_k^i represents the best position of particle i at time k , p_k^g represents the global swarm best position at time k , r_1 and r_2 represent uniform random numbers between 0 and 1, c_1 (local acceleration) is the individual cognitive factor and c_2 (global acceleration) is the social cognitive factor. The position,

velocity and acceleration factors are dimensionless quantities. The inertia weight (w) introduces a preference for the particle to continue its motion in the same direction as the one at the previous iteration. It was introduced for a better control of exploration and exploitation [3]. Additionally, a limitation of velocity has been specified. This rule prevents large step sizes that may destabilize the algorithm. The maximum velocity is calculated as a specified fraction of the distance between the bounds of the search domain.

$$v^{max} = \gamma_{PSO}(y_{UB} - y_{LB}) \quad (4.3)$$

where v^{max} is the maximum velocity that a particle may achieve, γ_{PSO} is the velocity factor and y_{UB} and y_{LB} are the positions of the upper and lower limits. All these factors represent the stiffness of the springs pulling a particle and changing them makes the PSO more or less efficient [10].

Despite the good performance of the PSO algorithm, its principal drawback is the factor problem dependency. Schutte and Groenwold [13] evaluated some variants of the PSO algorithm and attempted to propose optimal factor values applied for an extended Dixon-Szegö bound constrained test. Following their suggestions, the factors used in this work are shown in Table 4.1.

Number of particles (i)	25
Local acceleration (c_1)	2.6
Global acceleration (c_2)	1.5
Inertia weight (w)	0.5
Velocity factor (γ_{PSO})	0.5

Table 4.1: Constraint factors used in the PSO algorithm

In the present chapter, the PSO algorithm is used to find the optimal radiative properties adapted to a high temperature SPR. First, an investigation of the correspondence for using a poly-dispersion and a mono-dispersion with an equivalent radius is conducted. Next, the receiver model and the PSO algorithm are used to find the optimal radius, volume fraction and complex refractive index of an ideal material that minimizes the radiative losses.

4.3 The mono-dispersion as a representation of the poly-dispersion of particles

The time needed to calculate the volume radiative properties by using a model of particles poly-dispersion may increase considerably in comparison with a mono-dispersion model. To compute numerically Eqs. 2.57, 2.58, 2.62 and 2.63 large numbers of discretizations of the particle radius are required. Many authors suggested that the use of an equivalent particle radius may avoid this difficulty [8]. The impact on the optimal radiative losses (RL), when adopting an equivalent radius instead a more realistic poly-dispersion model in the optimization process, is investigated here. To this end, two cold $1D$ receivers are optimized at a specific wavelength ($\lambda = 0.5\mu m$, close to the maximum solar emission). The first receiver is filled with a particle mono-dispersion,

4.4. Parametric study of a cold SPR.

whereas the second one is filled with a particle poly-dispersion using a gamma distribution function. The parameters used in the PSO algorithm are those given in Table 4.1. The research range for the optimization is shown in Table 4.2.

	min. value	max. value
n	1.5	4
k	1×10^{-4}	5
r and r_{mp}	1	100
r_{mp}/r_{32}	0.4	0.9
f_v	1×10^{-6}	$f_v \rightarrow \tau_0 = 8$

Table 4.2: Parameter ranges used for the cold particle receiver optimization. The particle radius and most probable radius are in μm

Because the emission is not considered, the optimization algorithm of the cold receiver will always give the maximum volume fraction as a result. In fact, there is a threshold value for the volume fraction after which the radiative losses do not change anymore. For that reason, the maximum value for the optical thickness is set to $\tau_{0,max} = 8$. The results obtained for both simulations are shown in Table 4.3.

	Mono-dispersion	Poly-dispersion
RL	2.7×10^{-3}	2.8×10^{-3}
n	1.5	1.5
k	4.3×10^{-2}	4.4×10^{-3}
r	4.6	–
r_{mp}	–	4.5
r_{mp}/r_{32}	–	0.9
f_v	2.3×10^{-5}	2.5×10^{-5}

Table 4.3: Optimized radiative losses for a cold SPR using a mono-dispersion and a poly-dispersion of particles ($\lambda = 0.5 \mu m$)

Results show that similar radiative losses may be obtained using a mono-dispersion (second column) or a poly-dispersion (third column). In both cases the optical properties of the material are the same, provided that similar complex refractive index (n and k) are found. Analogous conclusions are obtained for the particle volume fractions. This volume fraction value corresponds to the maximum optical thickness imposed ($\tau_{0,max} = 8$). Finally, the results demonstrate that the optimum r_{mp}/r_{32} ratio for a particle poly-dispersion approaches the one of a mono-dispersion ($r \sim r_{mp}$ and $r_{mp}/r_{32} \rightarrow 1$). It emphasizes the weak influence of the introduction of the concept of equivalent particle radius on the radiative loss computations. This observation will be used later on to save computational time by avoiding the discretization of the radii of a particle poly-dispersion.

4.4 Parametric study of a cold SPR.

Before the application of the PSO algorithm to the optimization problem, a parametric study is conducted to investigate the influence of the main parameters (n , k , r , f_v)

on the radiative losses of a SPR. The parametric study is applied to a single particle and to a slab of a particle mono-dispersion, both in cold conditions at a specific wavelength. The radiative response, computed by a Mie code, is analyzed when varying the refractive index and the volumetric fraction for three different size parameters ($x = 6$, $x = 63$, $x = 190$). These parameters correspond, approximately, to the following radius of particles ($r = 0.5\mu m$, $r = 5\mu m$, $r = 15\mu m$) at the representative solar wavelength of $\lambda = 0.5\mu m$. The n and k constant values are the ones corresponding to carbon at the studied wavelength ($m = 2.27496 + 0.87417i$), and the f_v constant value is chosen as representative of the ranges to be analyzed ($f_v = 5 \times 10^{-6}$).

4.4.1 Radiative transport properties of a single particle

To obtain an indicator of the amount of the energy absorbed and scattered and beside its directionality, the transport albedo is defined as

$$\omega_t = \frac{Q_{sca}(1 - g)}{(1 - g)Q_{sca} + Q_{abs}} \quad (4.4)$$

This ratio indicates the directional dependency of scattering through the asymmetry factor. Small transport albedo values imply that incident wave energy is either absorbed or scattered in the forward direction. These values are reachable when the asymmetry factor tends to one (scattering in forward direction), while the scattering albedo tends to zero (absorption efficiency much larger than scattering efficiency). In fact, the transport albedo is smaller when the separation between ω_0 and g is large. The behavior of the transport albedo for a single particle is studied when the real or the imaginary parts of the refractive index varies. The results of this parametric study are shown in Fig. 4.1.

For a fixed imaginary part of the refractive index, the transport albedo becomes smaller when the real part of refractive index (n) tends toward one (Fig. 4.1a). A minimum value of ω_t that depends on the n -value exists close to one. For this n -value, the particle scatters radiation in the forward direction ($g \rightarrow 1$). However, no solid material exists with n -values close to one. Therefore, the lowest n -value is limited to 1.5 in this study. Figure 4.1b shows that a k region that minimizes the transport albedo exists. This region is wider for large particles than for small particles. It suggests that large particles offer better possibilities for finding materials that perform small transport albedo. In contrast, for the same conditions small particles absorb energy better than large particles (see Figs. 4.1c and 4.1d). The reason is that small particles ($r \sim \lambda$) may achieve Mie efficiencies greater than one as can be seen in Figs. 4.1c and 4.1d for $x = 6$.

4.4.2 Radiative transport properties of a homogeneous slab of particles dispersion

The normalized radiative losses (RL in %) are used to compare the radiative behavior of a homogeneous slab of particle mono-dispersion. They are computed by varying the real part and the imaginary part of the refractive index and the volume fraction, for three size parameters. Figure 4.2 shows the results obtained.

4.4. Parametric study of a cold SPR.

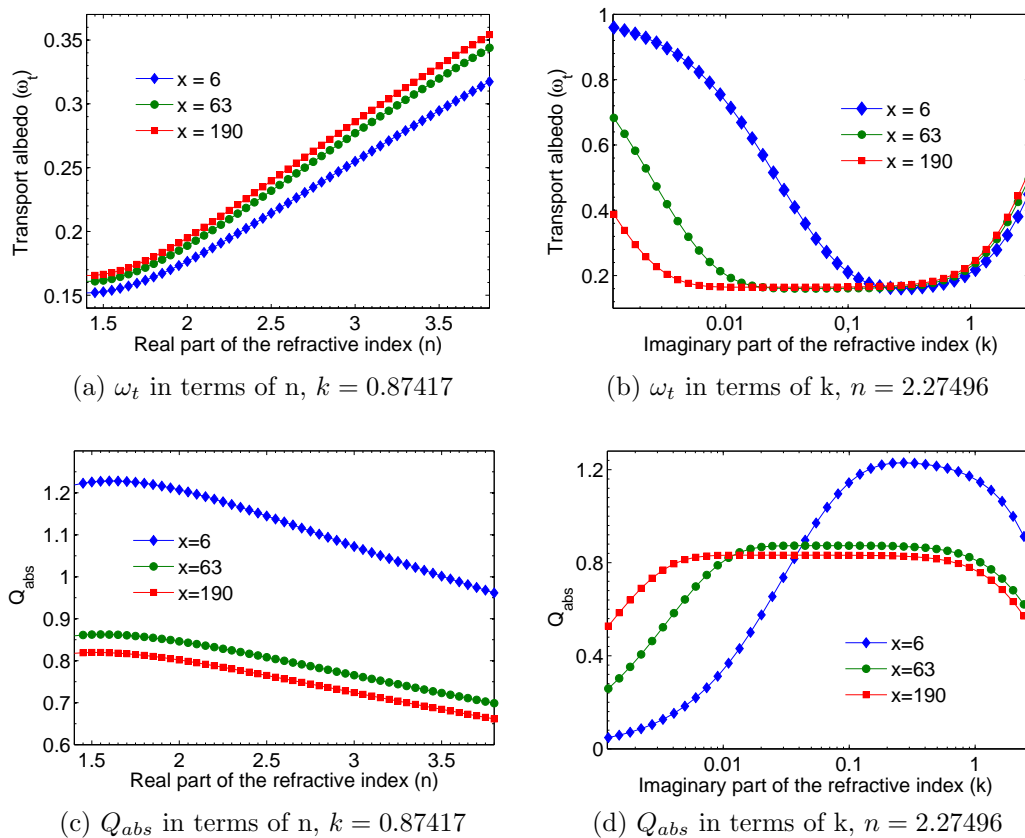


Figure 4.1: Transport albedo (ω_t) and absorption efficiency (Q_{abs}) variation vs the refractive index for a single spherical particle

Multiple scattering tends to flatten the radiative losses curve as a function of the n -variation (see Fig. 4.2a). That results suggests the possibility of using particles with n -values different from the optimum value while the increase in the radiative losses are rather small. Figure 4.2b shows that a slab of particles dispersion has a radiative behavior similar to that of a single particle (see Fig. 4.1b), when the imaginary part of refractive index varies. No noticeable effects exist due to multiple scattering in comparison with the single scattering. Large particles offer a larger range of k -values that permits to minimize the radiative losses. Note that, for the above calculations, the volume fraction is kept constant without regard to the particle size. It implies smaller number of particles in the case of large particle radius, leading to higher slab radiative losses. Figure 4.2c shows that higher values of volumetric fraction are required to reach the same radiative losses when the size particle is large (higher volume of particles). In addition, for each particle radius, there is an asymptotic value of the reflectance as f_v increases. The minimum possible reflectance augments slightly with the particle radius.

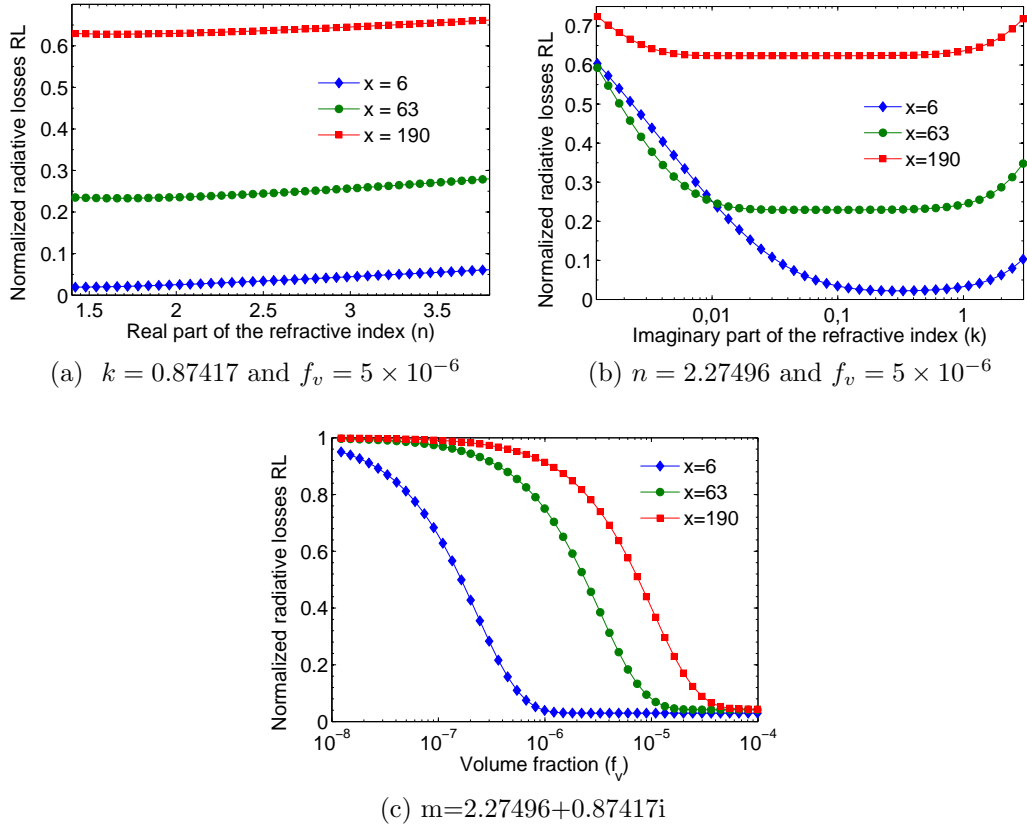


Figure 4.2: Normalized radiative losses by varying (a) the real part of the refractive index, (b) the imaginary part of the refractive index, and (c) the volume fraction

4.5 The optimal radiative properties for a SPR

4.5.1 Particle receiver conditions

The radiative losses (measured in $kW/(m^2 \cdot \mu m)$ or in kW/m^2) are used as the function to be minimized with the PSO algorithm. Note that the radiative losses take into account only the losses due to the reflection of the incident solar flux and the emission flux by the receiver, while do not consider other losses, as environmental losses (wind, etc.), conduction or convection by the walls, etc. In a volumetric receiver the expected temperature profile monotonically grows from a low temperature to a high temperature [11]. In this work, two extreme cases for the temperature profile are assumed: a linear and a constant temperature profile. For the constant profile a temperature $T = 1100 K$ is used, which is the operating temperature for a central solar power plant using a Brayton cycle [11]. For the linear profile, a temperature difference $\Delta T = 400 K$ starting at $700 K$ is used. Schematics of these temperature profiles are shown in Fig. 4.1. The incident collimated and concentrated solar flux is taken as $q_0 = 600 kW/m^2$. This solar flux and the receiver temperature are in accord with these given to reach the maximum theoretical efficiency in an ideal solar cavity-receiver [14]. Finally, the wall reflectivity is taken as $\rho = 0.8$ as a real reflective material. It permits to highlight the radiative behavior of the particle slab, reducing the emission contribution of the wall.

4.5. The optimal radiative properties for a SPR

The conditions used to conduct the optimization of the receiver are reported in Table 4.4.

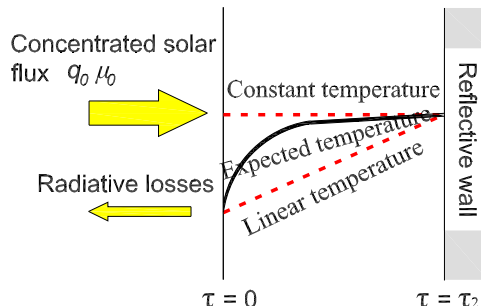


Figure 4.3: Schematic of the temperature profile in a volumetric receiver. The dashed lines represent the limiting temperature profiles and the solid line represents the expected temperature profile

Constant temperature profile	1100 K
Linear temperature profile	from 700 K to 1100 K
Collimated solar radiation	$q_0 \mu_0 = 600 \text{ kW/m}^2$
Wall reflectivity	$\rho_w = 0.8$

Table 4.4: Conditions used for the particle receiver optimization

The search range for the particle radius includes small and large radii and the volume fraction is compatible with the validity of the independent scattering assumption [15]. For the refractive index, the representative ranges are those corresponding to dielectric and metals. The wavelength region investigated is from $0.3 \mu\text{m}$ to $12.4 \mu\text{m}$. Table 4.5 shows the parameter ranges considered in the optimization procedure.

	min. value	max. value
Particle radius (μm)	0.1	100
Volume fraction	1×10^{-7}	6×10^{-4}
Real part of refractive index	2.0	4.5
Imaginary part of refractive index	1×10^{-4}	25.0

Table 4.5: Parameter ranges used in the particle receiver optimization

4.5.2 The ideal material to use in a particle receiver

The optimum particle radii and volume fractions, having an optimum spectral refractive index given in Figs. 4.4 and 4.5, for constant and linear temperature profiles are reported in Table 4.6. These results show that the particle size that minimizes the receiver losses is close to $r = 1 \mu\text{m}$ for the two temperature profiles. Particles with micron sizes ($r \sim 1 \mu\text{m}$) increase the absorption efficiency. This results support previous suggestions concerning the best size of particle [7, 8]. However, if particles with this

size are present in a gas-solid flow, they will collide and will form large aggregates with diameter greater than $1 \mu m$ [6]. Concerning the optimized volume fraction, a value minimizing the receiver losses exists when a constant temperature profile is assumed. In contrast, when a linear temperature profile is used, there are no minimum losses and the volume fraction tends to its highest permitted value. Considering that the radiative losses reach an asymptotic value when increasing the volume fraction (see Fig. 4.6), the $f_v = 7.5 \times 10^{-6}$ value is imposed for the layer with the linear temperature profile.

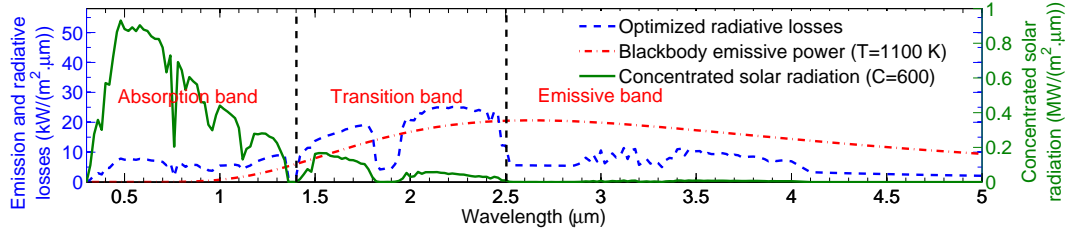
	Constant temperature	Linear temperature
Particle radius	$1.0 \mu m$	$1.3 \mu m$
Volume fraction	4.0×10^{-6}	7.5×10^{-6}
Mean optical thickness	7	10
Radiative losses (kW/m^2)	45.8	16
Normalized radiative losses (%)	7.6	2.7

Table 4.6: Optimized parameters for a single-layer SPR with two different temperature profiles

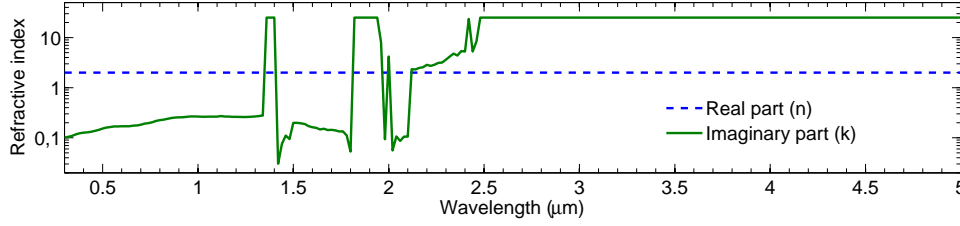
Figures 4.4a and 4.5a present the spectral concentrated solar radiation, the black-body emissive power for the two limit temperatures and the optimized receiver losses. Figures 4.4b and 4.5b present the optimized refractive index and Figures 4.4c and 4.5c show the scattering albedo and the asymmetry factor (see equations 2.4 and 2.82) computed from the optimized refractive index for a constant and a linear temperature profile, respectively. These figures are plotted for wavelengths up to $\lambda = 5 \mu m$, because the curves tendencies are the same for $\lambda \geq 5 \mu m$. To analyze the results, three spectral bands are considered (see Figs. 4.4a and 4.5a). First, the absorption band where the emission is negligible while the absorption is the most important phenomenon. Second, the transition band where the emission and the absorption have a similar importance. Third, the emissive band, where the contribution of concentrated solar radiation is almost negligible and major radiative losses are due to the particle emission. The limits of these bands depend on the temperature in the receiver. High temperatures at the receiver inlet lead a transition band located closer to the visible region. Under the conditions studied in this work, the transition bands are located in the range $[1.35 - 2.5 \mu m]$ for the constant temperature profile, and in the range $[2.4 - 4.0 \mu m]$ for the linear temperature profile. The absence of incident solar radiation in the regions close to $\lambda = 1.4 \mu m$, $\lambda = 1.9 \mu m$, and $\lambda = 2.8 \mu m$, due to the atmospheric absorption by CO_2 and H_2O molecules, originates the discontinuities in the k -curve. In these solar spectral bands, the material tends to be highly reflective.

At all wavelengths, the n -values that minimize the radiative losses are the minimal possible (i.e. $n = 2.0$), except in the transition band where the n -values are highly noised and oscillate (results not shown) between the minimum and the maximum possible values ($n = 2.0$ and $n = 4.5$). Specifically in the zones where the solar spectrum curve intersects the emissive power curve. It is due to the overestimation of the losses by the two-stream method in this region, that added to the use of an actual solar spectrum, lead to noisy n -results. This noise is not presented here, where the n -values are constrained to $n = 2.0$ because these oscillations have a marginal effect on the global radiative losses (about 0.07%).

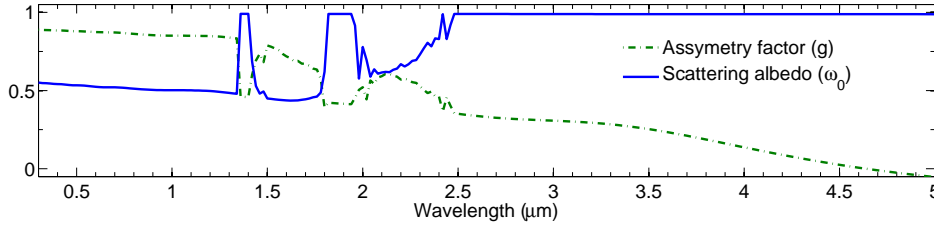
4.5. The optimal radiative properties for a SPR



(a) Concentrated solar radiation, optimized radiative losses and emissive power



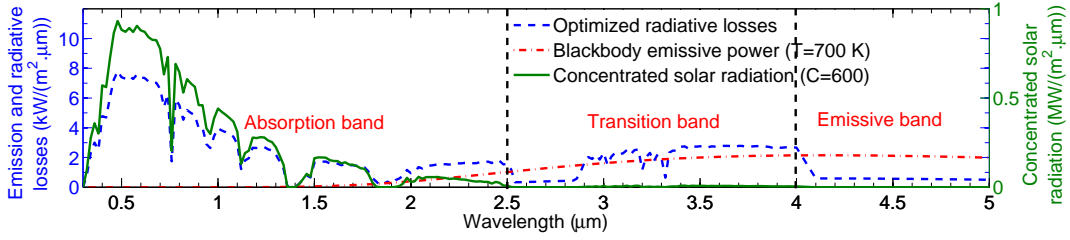
(b) Optimized real and imaginary parts of the refractive index



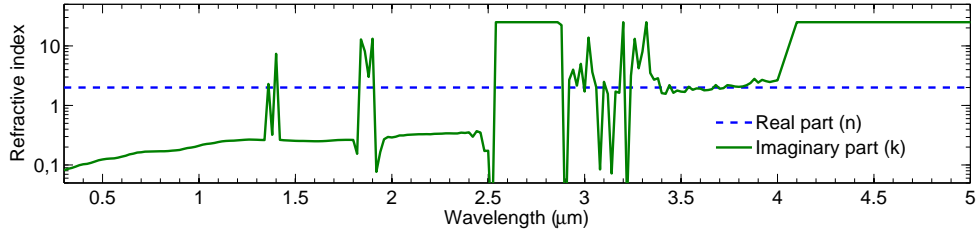
(c) Asymmetry factor and scattering albedo

Figure 4.4: Concentrated solar radiation, emissive power, receiver losses, refractive index, asymmetry factor and scattering albedo for an optimized SPR with a constant temperature profile ($T = 1100 K$)

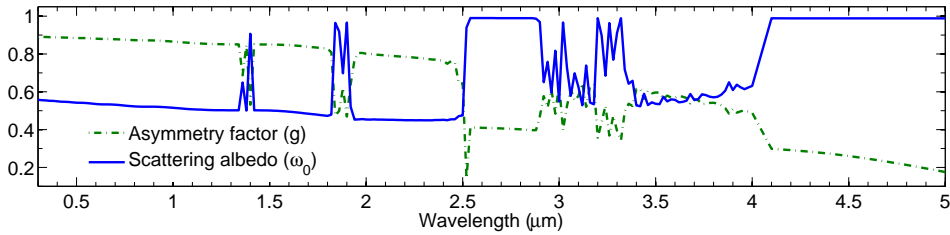
Differently, the imaginary part of the refractive index linearly rises up, within the absorption spectral band, from 0.1 to 0.3 (Figs. 4.4b and 4.5b) for both temperature profiles. These k -values render the medium highly absorbing with scattering albedo values close to 0.5 (Figs. 4.4c and 4.5c), which in addition to the low constant n -values ($n = 2$) yield a small slab reflectivity. The scattering becomes thus highly anisotropic in the forward direction ($g \sim 1$), increasing the probability for a scattered photon to be absorbed by another particle inside the slab. In the transition band, the k -values rise from 0.3 to 25 (Figs. 4.4b and 4.5c), changing the spectral radiative behavior from absorbent to reflective. The scattering albedo increases from 0.5 to 1 and the particle layer becomes a purely, isotropically, scattering medium since the asymmetry factor decreases from 0.9 to 0 (Figs. 4.4c and 4.5c). Finally, the high k -values in the emission band (Figs. 4.4b and 4.5b), yield the slab highly reflective, hence lowly emissive with near isotropic scattering ($\omega_0 \sim 1$ and $g \sim 0$, Figs. 4.4c and 4.5c). Another theoretical solution to obtain a non-emitting media is to lower the k -values to $k = 0$. It implies a transparent material in this region that does not emit at all. Crystals are representative solid materials with $k = 0$, while metals achieve high k -values. Besides, the k -values for ceramic materials tend to be greater than 0.1 for large wavelengths ($\lambda > 4 \mu m$). The



(a) Concentrated solar radiation, optimized radiative losses and emissive power



(b) Optimized real and imaginary parts of the refractive index



(c) Asymmetry factor and scattering albedo

Figure 4.5: Concentrated solar radiation, emissive power, receiver losses, refractive index, asymmetry factor and scattering albedo for an optimized SPR with a linear temperature profile (700 – 1100 K)

choice of working with a highly reflective material is made to include ceramic materials and metals, which have been reported as candidates in high temperature SPRs.

Nowadays, no real material has been reported with a refractive index close to the optimal one reported here. In the spectrum of interest, ceramic materials, such as silicon carbide or alumina-based materials, have high capacity of absorption in the absorption and the transition band (n is close to 2 and k is close to 0.01). However their emission in the emission band is very high (k maintains its value close to 1). On the other hand, metals like tungsten, weakly absorb in the absorption and transition bands (n is close to 2 and k is higher than 1). But usually, they have high reflectivity in the emission band, that reduces the radiative losses in this band (k takes very high values). In the next chapter several existing materials will be considered to use in a high temperature SPR.

4.5.3 Influence of the volume fraction

Small amount of particles into a SPR implies low absorption of the incident solar flux. However, big amount may increase the losses by emission due to the high number of

4.5. The optimal radiative properties for a SPR

particles. To study the influence of the number of particles into the SPR, a parametric study of the radiative losses when varying the volume fraction is conducted. It is shown in Fig. 4.6 for the two temperature profiles. The particle radii and the refractive index are the optimal ones reported in Table 4.6 and Figs. 4.4b and 4.5b.

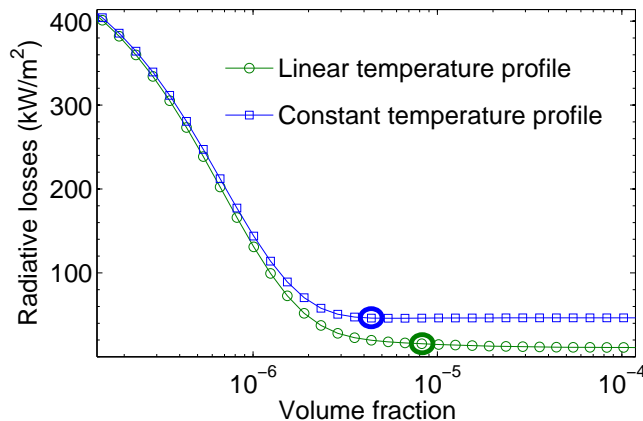


Figure 4.6: Radiative losses vs. volume fraction for an optimized SPR with constant and linear temperature profiles. The circle on the curves denotes the threshold value

Results show that at small volume fractions the reflected solar flux is higher, owing to the high reflectivity of the back wall, as well as the emission by the particles is lower. Otherwise, at high volume fractions the reflected solar flux stabilizes at a constant value corresponding mainly to the reflection by the particles and the particles emission reaches a constant value given by a threshold value of concentration. Therefore, the total radiative losses may reach a minimum which depends on the balance between their three components: the solar flux reflection, the particles emission and the wall emission. Because the emission strongly depends on the temperature close to the receiver opening, the receiver losses are lower at all volume fractions, when a linear profile is assumed. The optical thicknesses corresponding to the calculated threshold values are given in Table 4.6.

4.5.4 Influence of the particle radius

A small particle radius in the range of $1 \mu m \leq r \leq 1.3 \mu m$ is the best one to minimize the radiative losses from the receiver considered here. Small particles have indeed an appropriate spectral selectivity because they mainly absorb the short wavelengths and reduce the scattering behavior [12, 8]. However, small particles tend to agglomerate due to the large surface forces [6]. To avoid agglomeration, it is desirable to use particles of radius between $r = 10 \mu m$ and $r = 100 \mu m$ or larger. Figure 4.5 shows the radiative losses found for four particle radii versus their corresponding volume fraction that minimize the radiative losses. The optimized refractive index reported in Fig. 4.4b for a constant temperature profile is used.

For very small particles ($r \leq 0.1 \mu m$) there exist a cut-off wavelength for the spectral absorption efficiency located in the ultra-violet region. It leads to low efficiency of particles for light absorption in the visible spectrum. Consequently, for a given mate-

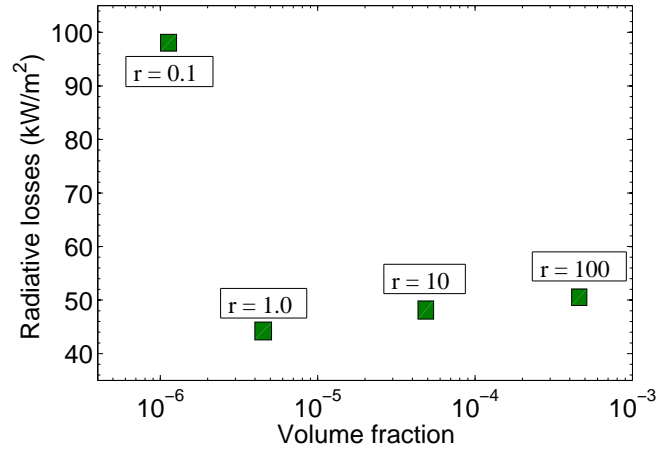


Figure 4.7: Optimized radiative losses for different particle radius (r in μm). The volume fraction for each particle radius corresponds to the threshold value and the temperature profiles is constant ($T = 1100 \text{ K}$)

rial (refractive index imposed), there exists a small radius that minimizes the radiative losses. Large particles with smooth surface roughness do not present a selective absorption property due to their size. However, for a material with a selective behavior due to its optical properties, it is possible to predict similar receiver radiative losses provided that the volume fraction is appropriate. As can be seen in Fig. 4.7, an increase in one order of magnitude in size of large particles ($r \geq 10 \mu\text{m}$), produces the same increase in the magnitude of the optimum volume fraction.

4.6 Two layer simulations

To investigate if some advantage exists using different mass loading of ideal particles, a particle receiver composed of two layers is studied in this section. The two layers have the same thicknesses (i.e. 0.5 m , meaning that the second layer temperature starts at 900 K for linear profile), but their optical thicknesses are optimized according to the volume fraction. The optimization is conducted for both constant and linear temperature profiles (see Fig. 4.3). Concerning the isothermal particle receiver, the results (not presented here) show that the optimized parameters are equal in both layers with values equal to those obtained with the single layer optimization (Table 4.6 and Fig. 4.4b). Indeed, there is no benefit to use particles with different optical properties in each layer because the receiver temperature is uniform. On the other hand, the optimized parameters found (results not presented here) for the two-layer receiver with a linear temperature profile lead to a receiver having a first, optically thick layer ($\tau_1 \approx 300$) with optical properties identical to the one for a single-layer receiver (Table 4.6 and Fig. 4.5b). The optical thickness of this first layer is so large that the second layer has no influence. This optimization results are similar to a spectrally selective and optically thick single-layer slab.

To study in detail the results in the optimization, two cases are considered (see Table 4.7). The particle radius and the optical depth are imposed and the refractive

4.6. Two layer simulations

index are optimized using the PSO algorithm. The first case corresponds to r -values obtained by the single layer optimization with a linear temperature profile and the corresponding f_v -value. In the second case, a larger particle radius is chosen for the first layer and the volume fraction is computed to maintain its optical thickness at 5. For both cases, the volume fractions used correspond to a cumulative optical thickness $\tau_c = 10$. Those chosen values are considered as being the most realistic for a SPR. The first case allows one to study the effect of the two layers compared with the single layer results, and the second case is chosen to investigate the effect of larger particle radii in the first layer. A linear temperature profile is adopted in both cases.

	Layer 1		Layer 2	
	Particle radius	Volume fraction	Particle radius	Volume fraction
Case 1	1.3 μm	7.5×10^{-6}	1.3 μm	7.5×10^{-6}
Case 2	100 μm	6×10^{-4}	1.3 μm	7.5×10^{-6}

Table 4.7: Representative cases considered for the study of a SPR composed by two layers. A linear temperature profile (700 – 1100 K) is assumed

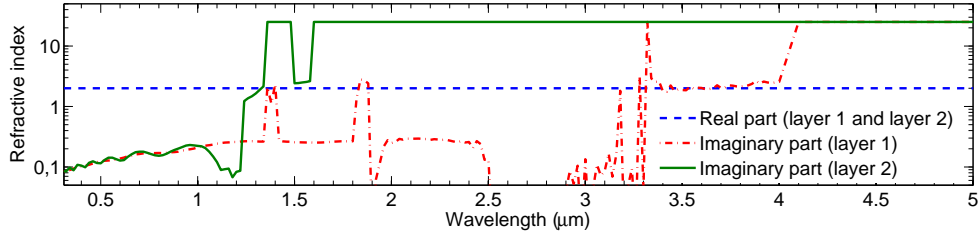
The simulations results for both cases are exposed in Table 4.8 and in Figs. 4.8 and 4.9.

	Case 1	Case 2
Optical thickness	10.0	10.0
Radiative losses (kW/m^2)	15.6	20.4
Normalized radiative losses (%)	2.6	3.4

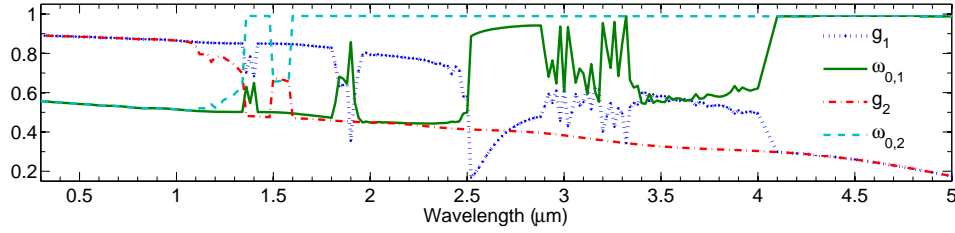
Table 4.8: Optical thickness, radiative losses and receiver efficiency for the two cases reported in Table 4.7

For the case 1, Figure 4.8 presents the optimized refractive index, the asymmetry factor and the scattering albedo for both layers. The k -values in layer 1 (Fig. 4.8a) are similar to those found for a receiver composed of only one homogeneous layer. The absorption, emission and scattering behaviors of layer 1 for the optimized k -values were explained in section 4.5.2. In layer 1, the solar incoming flux is almost entirely absorbed. Layer 2 absorbs and scatters similarly as layer 1 up to the cut-off wavelength $\lambda = 1.6 \mu m$. Beyond $1.6 \mu m$, this layer becomes highly reflective (high k -values lead to high scattering albedo and low asymmetry factor) in order to avoid emission by high temperature particles. This optimization procedure leads to define two layers: the first one at low temperature, which is highly absorbent while the second layer at high temperature is highly reflective.

Figure 4.9 presents the optimized refractive index, the asymmetry factor and the scattering albedo for the case 2 reported in Table 4.7. Layer 1 absorbs less than in case 1 because the particles are much larger, and the scattering is mainly in the forward direction in the absorption band (up to $2.5 \mu m$, see Fig. 4.9b). Beyond $2.5 \mu m$, the radiative properties of the particles have the same behavior as in case 1: the particles become highly reflective. Concerning the second layer of case 2, it has the same behavior as in case 1, with only a slight shift of the cut-off wavelength toward $1.8 \mu m$. This optimization for case 2 that includes large particles in the first layer leads

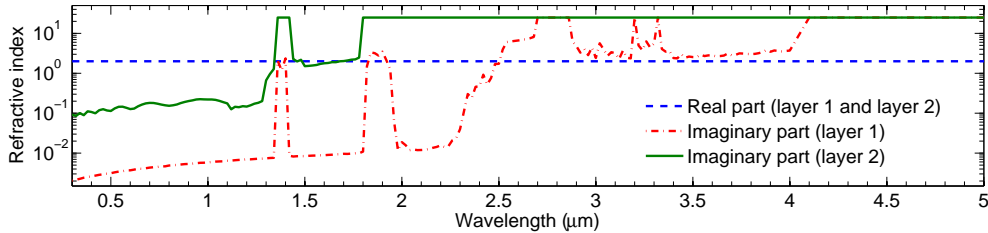


(a) Refractive index for the case 1

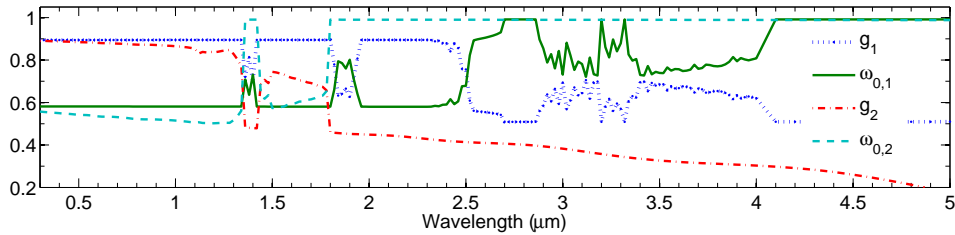


(b) Asymmetry factor and scattering albedo for each layer for the case 1

Figure 4.8: Optimized refractive index, asymmetry factor and scattering albedo for a SPR composed by two layers following the conditions of case 1: $r_1 = 1.3 \mu\text{m}$, $f_{v,1} = 7.5 \times 10^{-6}$, $r_2 = 1.3 \mu\text{m}$ and $f_{v,2} = 7.5 \times 10^{-6}$ and linear temperature profile (700 – 1100 K)



(a) Refractive index for the case 2



(b) Asymmetry factor and scattering albedo for each layer for the case 2

Figure 4.9: Optimized refractive index, asymmetry factor and scattering albedo for a SPR composed by two layers following the conditions of case 2: $r_1 = 100 \mu\text{m}$, $f_{v,1} = 6 \times 10^{-4}$, $r_2 = 1.3 \mu\text{m}$ and $f_{v,2} = 7.5 \times 10^{-6}$ and linear temperature profile (700–1100 K)

to similar arrangements of the optical properties in both layers when compared to case 1, resulting in an absorbing first layer at low temperature and a reflective second layer at high temperature. However, the cut-off wavelength for the second layer of case 2 is

4.7. Conclusion

slightly shifted (from $1.6 \mu m$ in case 1 to $1.8 \mu m$ in case 2) because the large particles of layer 1 do not absorb optimally so layer 2 should absorb more. This shift implies larger emission losses while the absorption of solar radiation is increased. The efficiencies for both cases are given in Table 4.8. The efficiency of the receiver for case 2 is slightly lower because of the particle size.

4.7 Conclusion

The optimization of the radiative properties of a SPR working at high temperature has been conducted in order to minimize its radiative losses. First, a mono-dispersion is compared with a poly-dispersion. No noticeable influence is found by using an equivalent particle radius model instead of a dispersion function model. Second, a parametric study is conducted to study the influence of the main optical parameters (refractive index, particle size and volume fraction) on the SPR radiative losses. Regions of n and k that minimize the radiative losses are suggested. Finally, an one-layer model subjected to a concentrated, collimated solar flux and a two-layer model are investigated. The two-stream method is employed for solving the monochromatic radiative transfer equation in 251 spectral bands between $0.3 - 12.4 \mu m$ for a homogeneous slab, partially filled with spherical particles, which scatter radiation anisotropically. Two temperature profiles (constant temperature and linear temperature) inside the receiver are considered as the limiting temperature profiles in a volumetric receiver. For the constant temperature profile ($T = 1100K$), as well as for the linear temperature profile (T varies from $700K$ to $1100K$), the solar radiation is normalized to $q_0 = 600kW/m^2$. A Particle-Swarm-Optimization algorithm is used to optimize the particle radius, the volume fraction and the refractive index (real and imaginary parts) with the objective to minimize the radiative losses from the SPR.

The results of the optimization of a SPR considered as a single, isothermal layer show that a particle radius $r = 1 \mu m$ and a volume fraction $f_v = 4 \times 10^{-6}$ with optimized optical properties allow a minimal radiative losses to be reached. The optimized real part of the refractive index is $n = 2$ while the imaginary part k is found to be spectrally dependent. For a wall reflectivity $\rho = 0.8$ over the full wavelength range (gray and diffuse surface), a minimal radiative losses of 7.6% and 6.7% are predicted for particle receivers with a constant and linear temperature profile, respectively.

The influences of the particle radius and volume fraction are also analyzed in detail for a two-layer slab subjected to uniform and linear temperature profiles. This study demonstrates that the use of a two-layer particle receiver instead of a single-layer receiver negligibly improves the receiver efficiency when the optical properties of the particles are optimized spectrally.

References

- [1] R. Bertocchi, J. Karni, and A. Kribus. Experimental evaluation of a non-isothermal high temperature solar particle receiver. *Energy*, 29:687–700, 2004.
- [2] A. Crocker and F. Miller. Fluid flow and radiation modeling of a cylindrical small particle solar receiver. In *SolarPaces: Concentrating Solar Power and Chemical Energy Systems, Granada - Spain*, September 2011.
- [3] R. Eberhart and Y. Shi. Particle swarm optimization: developments, applications and resources. In *Evolutionary Computation, Seoul-South Korea*, May 2001.
- [4] P.K. Falcone, J.E. Noring, and J.M. Hruby. Assessment of a solid particle receiver for a high temperature solar central receiver system. Technical report, Sandia National Laboratories, 1985.
- [5] B. Gobereit, L. Amsbeck, R. Buck, R. Pitz-Paal, and H. Muller-Steinhagen. Assessment of a falling solid particle receiver with numerical simulation. In *SolarPaces: Concentrating Solar Power and Chemical Energy Systems, Marrakech-Morocco*, September 2012.
- [6] A. Hunt. Small particle heat exchanger. Technical report, Lawrence Berkeley Laboratory, 1978.
- [7] A. Hunt and F. Miller. Small particle heat exchanger receivers for solar thermal power. In *SolarPaces: Concentrating Solar Power and Chemical Energy Systems, Perpignan-France*, September 2010.
- [8] H. Klein, J. Karni, R. Ben-Zvi, and R. Bertocchi. Heat transfer in a directly solar receiver/reactor for solid-gas reactions. *Solar Energy*, 81:1227–1239, 2007.
- [9] J. Martin and J. Vitko. ASCUAS: a solar central receiver utilizing a solid thermal carrier. Technical report, Sandia National Laboratories, 1982.
- [10] R. Poli, J. Kennedy, and T. Blackwell. Particle swarm optimization: An overview. *Swarm Intell*, 1:33–57, 2007.
- [11] M Romero, R Buck, and J Pacheco. An update on solar central receiver systems, projects and technologies. *Journal of Solar Energy Engineering*, 124:98–108, 2002.
- [12] S. Ruther and F. Miller. Monte Carlo radiation simulation of a cylindrical small particle solar receiver. In *SolarPaces: Concentrating Solar Power and Chemical Energy Systems, Perpignan-France*, September 2010.
- [13] J. Schutte and A. Groenworld. A study of global optimization using particle swarms. *Journal of Global Optimization*, 31:93–108, 2005.
- [14] A. Steinfeld and R. Palumbo. *Solar Thermochemical Process Technology*, chapter Encyclopedia of Physical Science and Technology, pages 237–256. R.A. Meyers Ed., 2001.

References

- [15] C.L. Tien and B.L. Drolen. Thermal radiation in particulate media with dependent and independent scattering. *Annual Review of Numerical Fluid Mechanics and Heat Transfer*, 1:1–32, 1987.

Chapter 5

Improvement of radiative performances using coated particles and mixtures in a high temperature solar particle receiver

Abstract

The use of silicon carbide (*SiC*), tungsten (*W*), zirconium carbide (*ZrC*), zirconium diboride (*ZrB₂*), hafnium carbide (*HfC*) and hafnium diboride (*HfB₂*) particles in a high temperature SPR is investigated. The refractive indexes of *SiC* and of *W* have been found in the literature. However, no complete information exists about the refractive indexes for other materials. The Kramers-Kronig dispersion relations are then employed in the determination of the refractive indexes from published reflectance data. The refractive index found in Chapter 4 using the PSO algorithm is recomputed in order to find a new refractive index that better agrees with the Kramers-Kronig dispersion relations. Three strategies are considered for reducing the radiative losses using real materials: first, using a single material, next, using a mixture of two materials, and finally, using coated particles. Results show that the particles size that minimizes the radiative losses is around $r = 1 \mu m$ for all materials as it was suggested in Chapter 4. For the use of mixtures, no noticeable reductions in the radiative losses are found. These results suggest that only marginal increases in SPR-performances may be expected with this solution. In contrast, the use of coated particles seem to achieve significant reductions in the radiative losses, when a reflective material (as *W* or UHTCs) is used in the core and *SiC* in the mantle. Thicknesses of around $50 nm$ may reduce of about 3% the radiative losses in comparison with those obtained with pure *SiC* particles.

5.1 Introduction

In order to reduce the radiative losses in a high temperature SPR, the material to be used should approach the radiative behavior of an ideal material. Several particle

5.2. Solar particle receiver conditions

materials have been already suggested as candidates for falling particle in SPRs. Silicon carbide (SiC), alumina (Al_2O_3), zirconia (ZrO_2) and two commercial alumina- and zircon-based materials were proposed for free-falling particle receivers [5, 6, 17]. Similarly, small carbon particles ($\sim 1 \mu m$) were suggested as valuable material to be used in high temperature entrained SPR [7, 9, 2]. Even though the high absorption behavior of these materials in the solar region, their emission in the IR region needs to be reduced. In consequence, other materials need to be investigated to find selective materials at high temperatures. Customarily, some ceramic and metal materials (i.e. SiC , Inconel 600 or Nichrome 80/20) were suggested for volumetric receivers [1]. More recently, ultra-high temperature ceramics (UHTCs) were suggested as relevant materials for high temperature receivers [15, 16]. Those materials having a high reflectivity in the IR spectrum have a selective behavior, but with the major drawback of a lower absorptivity in the visible region.

The purpose of the present chapter is to approach the optimized ideal radiative behavior of a high temperature SPR using real materials. Three configurations are considered: a homogeneous layer of a single material, a homogeneous layer of a mixture of two materials and a homogeneous layer of a single combination of core-mantle coated particles. Four ultra-high temperature ceramics (UHTCs), HfC , HfB_2 , ZrC and ZrB_2 , and two high temperature materials, SiC and W , are studied, owing to their spectral radiative properties. The losses for three configurations are compared with the theoretical radiative losses obtained using an optimized ideal material.

5.2 Solar particle receiver conditions

The model developed in Chapter 2 is considered in this chapter for studying different configurations. Such a model conceives the SPR as a 1D, homogeneous slab composed of particles suspended in a gas medium. A layer thickness $D = 1 m$ is considered while the monochromatic optical thickness changes according to the wavelength and volume fraction of particles. With the end to study the receiver behavior at higher temperature than the last optimization, the gas-particle mixture is submitted to a concentrated and collimated solar heat flux, normalized to the value $q_0 = 1500 kW/m^2$. The SPR is treated as well-stirred, and in consequence, the temperature is supposed to be uniform ($T = 1300 K$). Both optimum temperature and solar concentrated heat flux correspond to the maximum theoretical efficiency achievable for an ideal solar cavity-receiver [18]. The considered spectrum is between $0.3-12.4 \mu m$ and it is discretized into 251 narrow spectral bands, at least ($\Delta\lambda = 0.02 \mu m$). The monochromatic Radiative Transfer Equation (RTE) is solved by using the two-stream method. The Joseph *et al.* approximation [8] is adopted for the whole spectrum, owing to its better accuracy. The particle optical properties are modeled using the Lorenz-Mie theory. Adaptations of the BHMIE code [4] and of the DMILAY code [20] are used for the homogeneous particles and coated particles, respectively. The volumetric optical properties are then computed as a sum of the properties of each particle (independent scattering assumption) since the volume fraction is bounded to $f_v < 0.006$ [19]. The total radiative heat losses ($q^-(0)$) are considered as the right parameter to compare different configurations into a SPR. Figure 5.1 shows a schematic of the SPR model, and Table 5.1 presents the

conditions used for conducting the simulations.

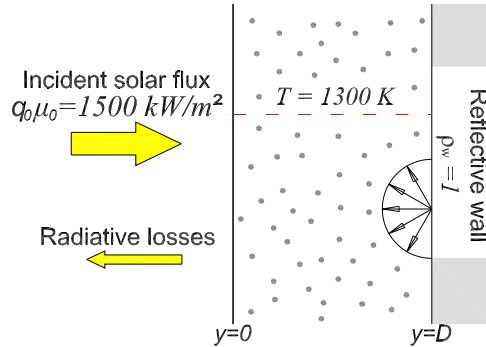


Figure 5.1: Schematic of a 1D, isothermal, homogeneous SPR

Uniform temperature profile	$T = 1300 K$
Collimated solar radiation	$q_0 \mu_0 = 1500 kW/m^2$
Wall reflectivity	$\rho_w = 1$

Table 5.1: Conditions used for the high temperature SPR simulations

5.3 Materials optical properties

The complex refractive index of the materials is the main parameter needed in order to compute the radiative losses in a SPR when the Lorenz-Mie theory is used. At this point, the most important drawback found is the lack of information about the spectral refractive index for several good candidates. In addition, a large spectrum interval must be considered in this study ($0.3 - 12.4 \mu m$).

For the materials studied here, the refractive index for the *SiC* and for the *W* are reported in Pégouiré [14] and Palik [13], respectively. To our best knowledge, no available refractive index data exist for the UHTCs. Nevertheless, the refractive index may be found with the help of the Kramers-Kronig dispersion relations, starting from the material reflectivity at normal incidence [21]. At this point, a distinction between reflectivity and reflectance should be done. Following the definitions give by Modest [11], the reflectivity is taken as an intrinsic property of the material (then, depends only of the refractive index), while reflectance is surface dependent property (roughness, purity, etc.). It follows that it is only possible to measure the reflectance, and the reflectivity remains for theoretical computation. Therefore, the reflectance for the hafnium carbide (*HfC*), hafnium boride (*HfB₂*), zirconium carbide (*ZrC*) and zirconium boride (*ZrB₂*) reported by Sani *et al.* (2011) are utilized to compute the refractive indexes of these materials. However, these values are only illustrative, because they were obtained from rough surfaces [16]. Nevertheless, it is assume that these data allow a good indication of the general optical behavior of such materials. In the following subsections, the Kramers-Kronig dispersion relations and the refractive index found for the mentioned UHTCs are discussed.

5.3. Materials optical properties

5.3.1 The reflectivity and the phase-shift Kramers-Kronig dispersion relations

The Kramers-Kronig dispersion relations connect the real and the imaginary parts of any function that follows rigorously the requirement of causality. When a normal wave gets onto a medium with a refractive index $m = n + ik$, the complex reflectivity amplitude should satisfy the Kramers-Kronig relationships, owing to its causality. The complex reflectivity amplitude may be expressed in terms of its amplitude r and its phase-shift angle θ as [4]

$$\ln(\tilde{r}(\omega)) = \ln(r(\omega)) + i\theta(\omega) \quad (5.1)$$

where ω is the wave frequency and the normal reflectivity is $R(\omega) = r(\omega)^2$. The Kramers-Kronig relations for the conjugate variables $\ln r(\omega)$ and $\theta(\omega)$, from which $\theta(\omega)$ is determined may be written as

$$\ln r(\omega') = \frac{2}{\pi} \int_0^\infty \frac{\omega\theta(\omega) - \omega'\theta(\omega')}{\omega^2 - \omega'^2} d\omega \quad (5.2)$$

$$\theta(\omega') = -\frac{2\omega'}{\pi} \int_0^\infty \frac{\ln r(\omega) - \ln r(\omega')}{\omega^2 - \omega'^2} d\omega \quad (5.3)$$

These relations implies that the optical properties at a single frequency (ω') are dependent on the spectral behavior at all frequencies. Equation 5.3 may be arranged in terms of the normal reflectivity (R) and by introducing the wavelength (λ).

$$\theta(\lambda') = \frac{\lambda'}{\pi} \int_0^\infty \frac{\ln [R(\lambda)/R(\lambda')]}{\lambda^2 - \lambda'^2} d\lambda \quad (5.4)$$

It follows that the refractive index may be connected with the complex reflectivity amplitude as [4]

$$\tilde{r} = \frac{1 - n^2 - k^2}{(1 + n)^2 + k^2} - i \frac{2k}{(1 + n)^2 + k^2} \quad (5.5)$$

Equation 5.6 then may be re-arranged to give

$$n(\lambda') = \frac{1 - R(\lambda')}{1 + R(\lambda') - 2\sqrt{R(\lambda')} \cos\theta(\lambda')} \quad (5.6)$$

$$k(\lambda') = \frac{-2\sqrt{R(\lambda')} \sin\theta(\lambda')}{1 + R(\lambda') - 2\sqrt{R(\lambda')} \cos\theta(\lambda')} \quad (5.7)$$

A serious difficulty in performing the integration of Eq. 5.4 is the contribution from the reflectivity at frequencies close to zero and towards infinity, where measured reflectivity data are missing. Thus, the extrapolation of the measured data must be done with great care [21]. Here, the integration of Eq. 5.4 is made by numerical integration, using the Simpson's rule. The singularity at $\lambda = \lambda'$ may be avoided by using the l'Hôpital's rule. The extrapolations follow the typical tendency for the materials studied as recommended by Wooten [21]. This integration method appears to be less sensitive to the extrapolations of data than other methods (e.g. the Maclaurin integration, as proposed in Ohta and Ishida [12]). The integration method and the validation of the Kramers-Kronig code are discussed in Appendix C.

5.3.2 The refractive index of the materials

The reflectance data for the ZrC , ZrB_2 , HfC and HfB_2 reported in Sani *et al.* [16] are employed for the calculations of the refractive indexes using the Kramers-Kronig dispersion relations. The reported reflectance data for these four materials are fitted and then plotted in Fig. 5.2, as well as the reflectances of SiC and W computed from their refractive index variations. In the solar region, the SiC is more absorptive than the other materials. The W , ZrC , ZrB_2 , HfC and HfB_2 having a medium reflectance in this region (see the insets in Fig. 5.2), their absorption in the solar region still needs to be improved. However, in the IR region, from $\lambda \approx 2 \mu m$ to $\lambda \approx 12 \mu m$ (see Figs. 4.1c and 4.1d), these materials become highly reflective avoiding the emission in such region. In contrast, the SiC remains highly absorptive (and thus highly emissive) from $\lambda \approx 0,8 \mu m$ to $\lambda \approx 9 \mu m$. In conclusion, a material having the SiC -optical properties in the solar spectrum and those of W in the far IR region could be assumed as almost ideal.

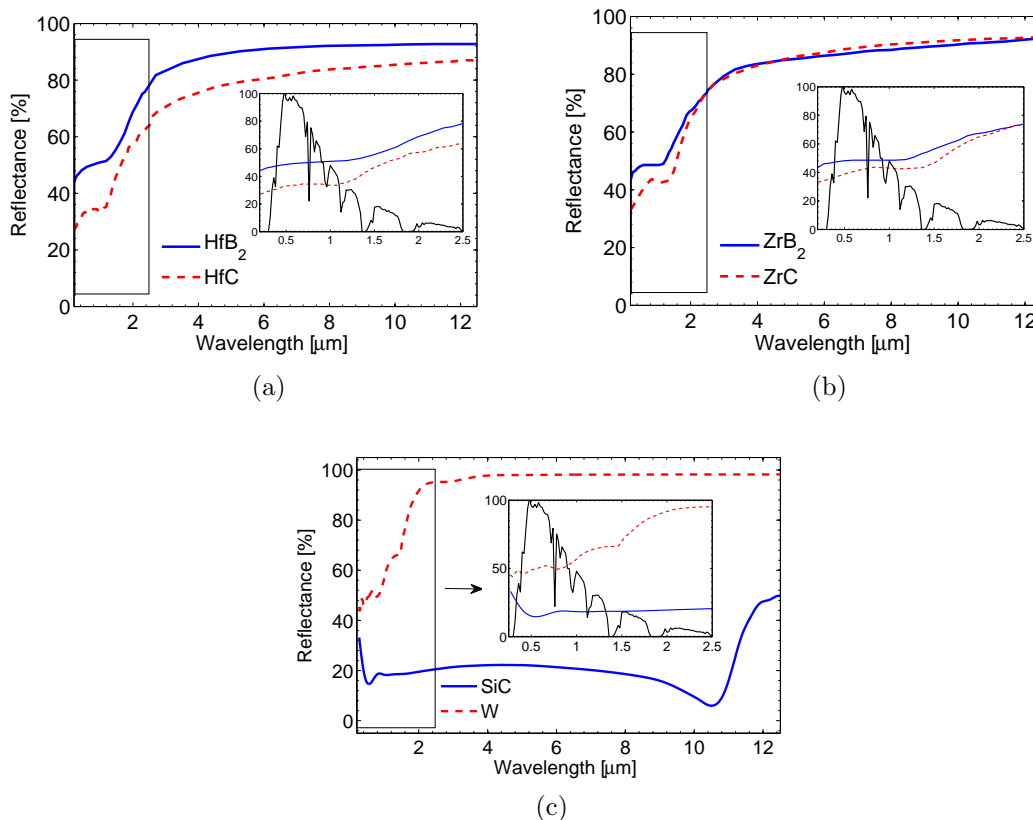


Figure 5.2: Reflectance for six materials suggested to be used in high temperature SPRs. The solar spectrum is shown in the insets (black continuous line). The SiC and W reflectivity were computed from the refractive indexes reported in the literature [13, 14]. For the others materials, measured data are shown

Figure 5.3 shows the refractive indexes computed for ZrC , ZrB_2 , HfC and HfB_2 and those reported in [13, 14] for SiC and W . In the spectral region considered ($0.2 - 12.4 \mu m$), the silicon carbide have an almost constant behavior, except at $11.3 \mu m$

5.4. Improvements of the radiative performances in a SPR

where a strong peak of reflection exists. The real part of the refractive index takes values close to 2 (see Fig. 5.3a) and the imaginary part takes small values, close to 0.1 (see Fig. 5.3b). Consequently, high absorption properties are predicted for the *SiC*. However, this behavior is not desirable in the near IR region because the *SiC* becomes highly emissive. For the *W*, the real part takes small values in the solar region while high values are seen in the IR region (see Fig. 5.3a). The imaginary part has middle values at small wavelengths (3.24 at $0.2 \mu m$), and it rises until very high values in the near IR region (see Fig. 5.3b). It is a typical metal behavior: the absorption is moderate in the solar region and the material becomes highly reflective when the wavelength increases. Owing to the metal-like behavior of the UHTCs materials, their refractive indexes are expected to be similar to the *W*-ones. In Figs 5.3c to 5.3d, it is seen that the real and imaginary parts monotonically increase from small to high values. These variations confirm the expected tendency for this kind of materials.

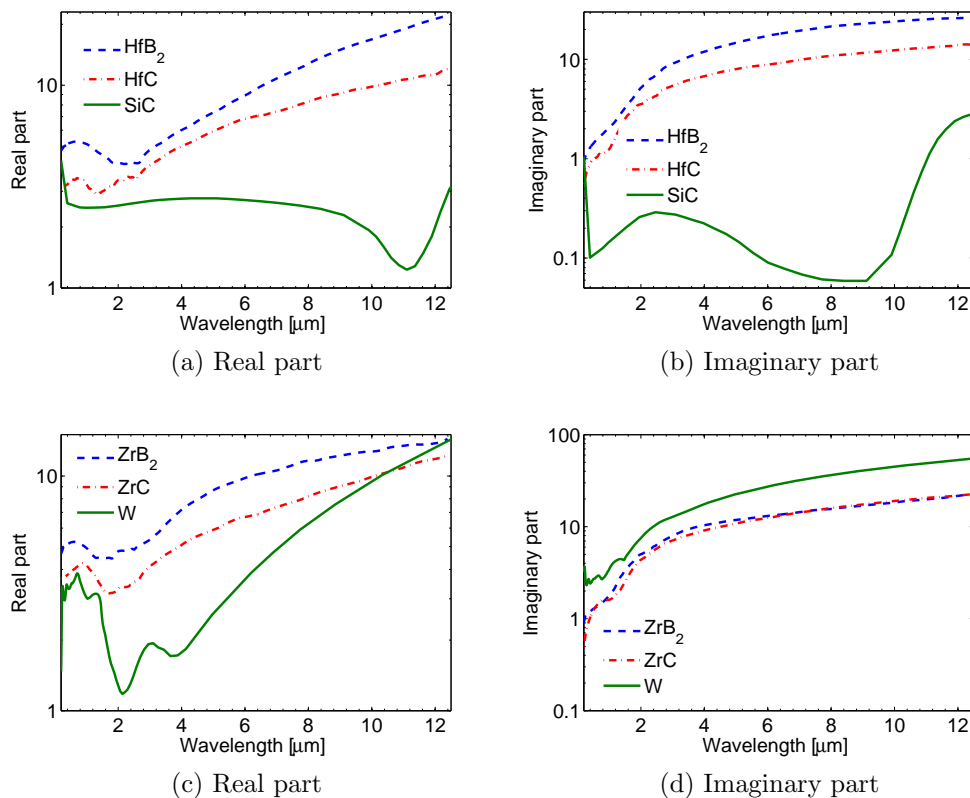


Figure 5.3: Real and imaginary parts of the refractive index (a) and (b) for the hafnium diboride, hafnium carbide and silicon carbide, (c) and (d) for the zirconium diboride, zirconium carbide and tungsten

5.4 Improvements of the radiative performances in a SPR

Different strategies which aim at minimizing the radiative losses calculated from the present SPR model are discussed in this section. The SPR model is used with three

different homogeneous particle mono-dispersions. First, using single material particles, next, using a mixture of two materials and finally using coated particles with only one mantle. All the cases are compared with the minimal radiative losses obtained by using an ideal optimized material.

5.4.1 The optimized ideal material

The optimization procedure carried out to find the spectral optimized refractive index for an ideal material that minimizes the radiative losses in a high temperature SPR is repeated under the conditions presented in Table 5.1. The research range considered in the optimization procedure is the same as in Table 4.5, with the exception for the real part of the refractive index, which is bounded between $1.5 \leq n \leq 4.5$. To avoid complicated spectral shape of the refractive index, the incident solar flux is computed as the emission of a blackbody using the Planck law at 5777 K . The incident flux is then normalized such as it is given in Table 5.1. The ideal refractive index found is presented in Fig. 5.4. It is used to compare the performance of the different SPR configurations analyzed with real particles. However, the refractive index reported does not follow the Kramers-Kronig dispersion relations (KK relations). The reason is that for a complex function, the dependence of the imaginary part on the complete spectral behavior of the real part (see Eq. 5.3) makes very difficult the implementation of the Kramers-Kronig relations in a PSO algorithm.

To obtain a refractive index that satisfies the Kramers-Kronig dispersion relations from the PSO refractive index, the following procedure is implemented. The normal reflectivity is computed from the refractive index found with the SPR model and the PSO algorithm (see Eq. 5.8 where the normal reflectivity is defined as the ratio between the reflected and the incident irradiance). This reflectivity is then used to compute the phase shift angle (see Eq. 5.4). Once the normal reflectivity and the phase shift angle are known, a new complex refractive index that agrees with the Kramers-Kronig relations may be calculated (see Eqs. 5.7 and 5.8).

$$R(\lambda) = \frac{(n(\lambda) - 1)^2 + k^2(\lambda)}{(n(\lambda) + 1)^2 + k^2(\lambda)} \quad (5.8)$$

Figure 5.4 shows the variations of the real and imaginary parts of the refractive index versus the wavelength. Those variations are found with both methods (named PSO and KK refractive indexes). Note that equation 5.8 may lead to determine more than one n and k couple which gives the same normal reflectivity. The PSO refractive index is the best value which allows the minimization of the radiative losses in the fixed research range, corresponding to representative values of dielectrics and metals ($1.5-4.5$ for n and $10^{-5} - 25$ for k). Any other combination of n and k in this research range increases the radiative losses. However, if this refractive index is used to obtain the reflectivity, this reflectivity may be used to obtain the refractive index that follows the Kramers-Kronig dispersion relations. Such KK refractive index is the only physically possible for that given reflectivity. The main consequence of this statement lies in the theoretical possibility of building a material with those optical properties. It can be achieved by combining different real materials.

5.4. Improvements of the radiative performances in a SPR

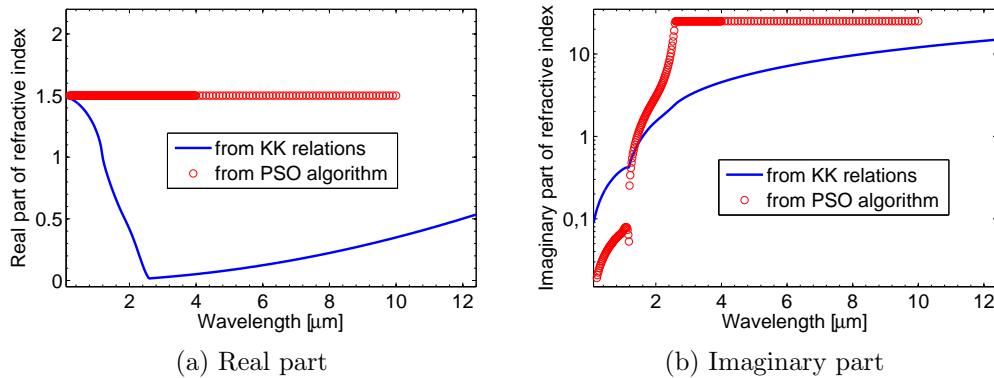


Figure 5.4: Real and imaginary parts of the refractive index for an ideal material. In circles those obtained with the Lorenz-Mie theory and the PSO algorithm and in continuous lines computed from reflectivity by using the Kramers-Kronig dispersion relations (see Table 5.1 for the receiver conditions)

Figure 5.4 shows that the variations of the KK imaginary part agrees quite well with those of the PSO imaginary part. Their values increase from small values (0.1 at $\lambda = 0.1\mu m$) to high values (12 at $\lambda = 10\mu m$). On the other hand, the KK real part variations vs λ greatly differ from those predicted with the PSO algorithm. In fact, the principal shortcoming is that the KK real part takes values lower than 1 in a very large spectral band (1.2 – 17 μm). n -values lesser than one are possible and always following the maximum speed of light principle. To explain these results, a distinction between wave group velocity and wave phase velocity (c_0/n) must be made. The phase velocity can achieve values higher than the speed of light, even if the wave information travels at the group velocity. Details about that point may be found in Bohren and Huffman [4] or in Bigelow *et al.* [3]. However, it is usually constrained to a narrow spectral band, in opposition to the results shown in Fig. 5.4a. In Fig. 5.5 the reflectivity computed from both refractive indexes are compared and no significant discrepancy is found. It is a numerical illustration of the above remark (below Eq. 5.8) on the possibility to find close values of the reflectivity while the real and complex parts of the refractive index are rather different.

5.4.2 Homogeneous layer with a single-material

The radiative losses in a SPR using a single material are studied in this section. The material selectivity due to its intrinsic optical properties is highlighted. Because the selectivity can be reached thanks to an optimization of the particle size, four different radii are considered. In all cases the volume fraction is large enough to achieve the asymptotic value of the radiative losses as it was discussed in section 4.6. The optimized ideal material is used to compare the performance for each case. The radiative losses for these simulations are shown in Table 5.2. The normalized radiative losses (outgoing flux to incident flux ratio) are also presented in parenthesis.

Several previous works suggested that the particle size that minimizes the radiative losses is close to $r = 1\mu m$ [10, 7]. The present results are in agreement with that

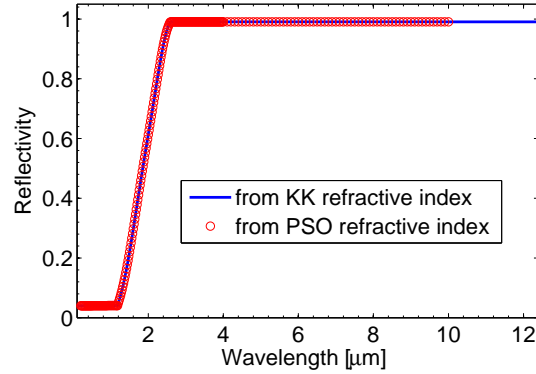


Figure 5.5: Normal reflectivity computed from the two computed refractive indexes shown in Fig. 5.4

	$r = 0.5 \mu m$ $f_v = 8 \times 10^{-6}$	$r = 1 \mu m$ $f_v = 1 \times 10^{-5}$	$r = 7.5 \mu m$ $f_v = 8 \times 10^{-5}$	$r = 50 \mu m$ $f_v = 8 \times 10^{-4}$
<i>Ideal</i>	108.2 (7.2)	103.7 (6.9)	109.0 (7.3)	110.0 (7.4)
<i>SiC</i>	195.0 (13.0)	178.0 (11.9)	188.2 (12.5)	189.8 (12.7)
<i>W</i>	244.7 (16.3)	226.9 (15.1)	240.6 (16.0)	253.3 (16.7)
<i>HfC</i>	208.3 (13.9)	193.5 (12.9)	202.0 (13.5)	205.8 (13.7)
<i>HfB₂</i>	246.9 (16.5)	229.1 (15.3)	241.2 (16.1)	248.8 (16.6)
<i>ZrC</i>	221.6 (14.8)	204.9 (13.7)	215.4 (14.4)	221.1 (14.7)
<i>ZrB₂</i>	247.2 (16.5)	230.3 (15.4)	242.1 (16.1)	249.1 (16.6)

Table 5.2: Radiative losses for the SPR model using four different particle sizes. The volume fraction is large enough to achieve asymptotic values of the radiative losses. The radiative losses are in kW/m^2 and the normalized radiative losses (in %) are shown in parenthesis

prediction. Materials with high absorptivity over a large spectral region (i.e. the *SiC*) have the best advantage for this particle size. The emission decreases due to the diminution of the Mie-absorption efficiency in the near IR region. In this case, the *SiC* behaves the best followed by the *HfC*. When the particle size changes from $r = 1 \mu m$ to $r = 50 \mu m$, the normalized radiative losses increase. The main increase comes from changes in sizes from $r = 1 \mu m$ to $r = 7.5 \mu m$, suggesting a high sensitivity to agglomeration phenomena when small particles are used. At high particle sizes, intrinsic selective materials as *HfC*, exhibit increases in their radiative losses, but lower than the *SiC*. Nevertheless, at $r = 50 \mu m$ the radiative losses remains higher than those obtained by the *SiC*, because of the high solar absorptivity of the *SiC*. In comparison with the ideal case (first row of Table 5.2), the use of *SiC*, which is the best of the analyzed materials, leads to at least a 5% increase in the radiative losses.

5.4. Improvements of the radiative performances in a SPR

5.4.3 Homogeneous layer composed of mixtures of *SiC* with another material

The use of a mixture of two materials with different spectral behaviors is expected to yields decreases in the radiative losses from a high temperature SPR. Materials having a high absorptivity in the solar region could be mixed with materials having a high reflectivity in the near IR region. Since all of the analyzed materials, with the exception of the *SiC*, have similar optical behaviors within the spectral range of interest, mixtures of these materials do not appear relevant. However, due to the high absorptivity of the *SiC*, its mixture with other materials is analyzed in order to try to obtain reductions of the radiative losses. Fig. 5.6 shows the radiative losses for *SiC* mixtures with the other materials considered. Two particle sizes $r = 1 \mu m$ and $r = 50 \mu m$ are used as examples of small and large particles. The volume fraction chosen for each particle size is large enough to achieve the threshold value of the radiative losses, as explained in section 5.4.2.

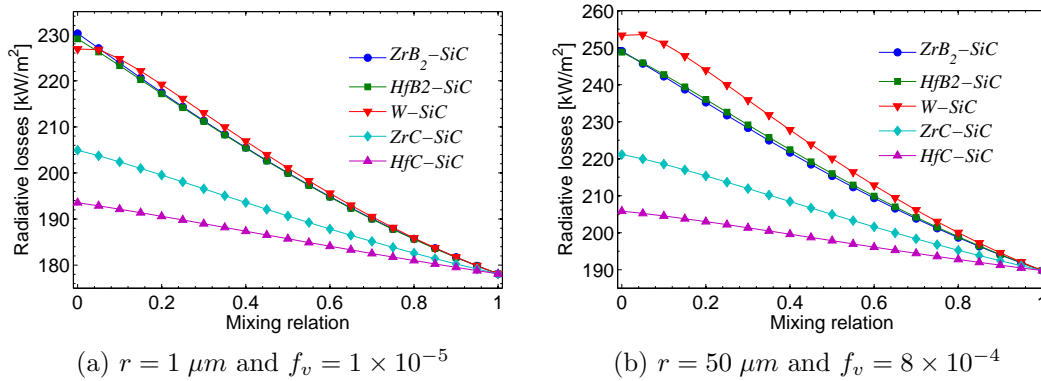


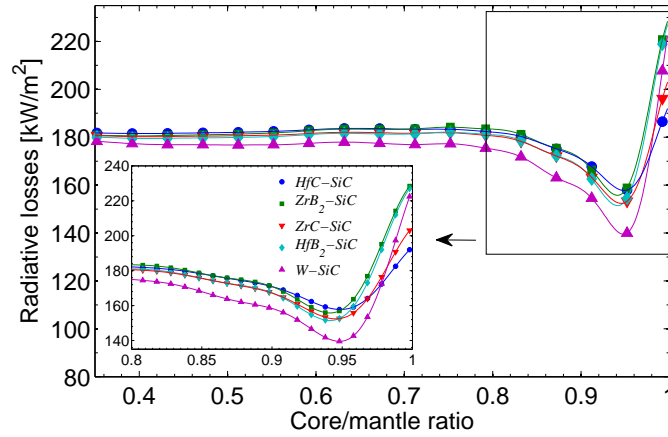
Figure 5.6: Radiative losses of a SPR using different material mixtures with two sizes: (a) $r = 1 \mu m$, (b) $r = 50 \mu m$. In both subfigures a mixing ratio of 1 means a 100 % *SiC* medium

In all cases, the radiative loss variations versus the mixing relation are close to a linear dependency, both for small and large particles. In conclusion, for the materials studied here, no improvement in the SPR-performances is predicted using mixtures of such materials.

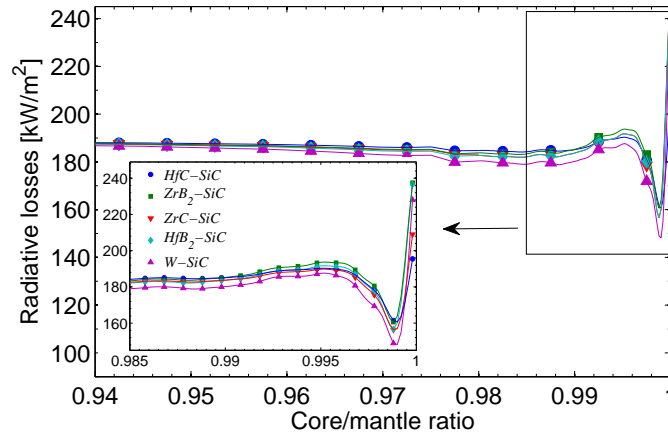
5.4.4 Homogeneous layer with coated particles

It is well known that the absorptance of a surface material may be changed through coating deposition. In this section a single core-mantle configuration for the particles is studied. Small and large particles are again considered with either $r = 1 \mu m$ or $r = 50 \mu m$ particle sizes. As discussed in section 5.4.3, materials with high absorptance in the solar region may complement materials with high reflectivity in the near IR region. Concerning the best core-mantle coating with the materials studied in this work, the use of *W* and UHTCs for the mantle does not appear to be advantageous. The very high values of their complex refractive index ($k \gg 1$) lead indeed to reflective

coated particles. It mainly prevents the solar incident radiation from crossing the mantle easily [4]. Only very small coating thicknesses lead to a different optical behavior of the coated particle compared to a particle made only with the mantle material. In what follows, the simulations are conducted out only for particles coated by *SiC*. This arrangement (*W* or UHTCs in the core and *SiC* at the mantle) seems to be the most appropriate. In Fig. 5.7 the results of simulations are presented for different core/mantle ratios defined as $r/(r + e)$, where r is the particle radius and e is the thickness of the coating.



(a) $r_{total} = 1 \mu m$ and $f_v = 1 \times 10^{-5}$



(b) $r_{total} = 50 \mu m$ and $f_v = 8 \times 10^{-4}$

Figure 5.7: Radiative losses of a SPR using coated particles. *W* and UHTCs are used for the core and *SiC* for the mantle. In both subfigures a core/mantle ratio of 1 means that no coating exists

Results show that the use of coated particles may reduce the radiative losses for both particle sizes. A minimum is predicted in the radiative losses: at a core/mantle ratio of 0.95 for particles of $r = 1 \mu m$ (i.e. $e = 52 nm$) and at a core/mantle ratio of 0.999 for particles of $r = 50 \mu m$ (i.e. $e = 50 nm$). Therefore, the optimum core/mantle ratios correspond to a *SiC*-thickness $e \approx 50 nm$. For mantle thicknesses greater than $1 \mu m$, no important effects appear due to the coating, and the optical behavior of

5.5. Conclusions

the coated sphere becomes similar to that of a pure *SiC* particle. It is due to that at very thin mantle thicknesses, the absorption of an incident wave is the result of interferences between the reflected wave by the two interfaces of the mantle [11]. For thinner coatings, the nature of the core material changes the overall radiative behavior of the particle. A minimum at $e \approx 50 \text{ nm}$ is still predicted for every other material studied. At this thickness the absorption is high in the solar region and the emission in the IR region decays to very small values.

In the following, the interest is focused on *W*-particles coated by *SiC*. For instance, in comparison with the pure *SiC*, reductions of 2.6% (38.5 kW/m^2) in the radiative heat losses are obtained for $r = 1 \mu\text{m}$ -particles and of 2.8% (41.6 kW/m^2) for $r = 50 \mu\text{m}$ -particles. In this case, the optical behavior of particles of *W* coated with *SiC* is close to the ideal one (e.g. for *SiC* – *W* particles with $r = 50 \mu\text{m}$ the radiative losses are $RL = 148.2 \text{ kW/m}^2$ vs. the $RL = 110 \text{ kW/m}^2$ for the ideal).

To illustrate this finding, the spectral variations of the absorption Mie-efficiencies for particles of *SiC* and *W* and, for *W* coated by a thin layer (50 nm) of *SiC* are plotted in Fig. 5.8 and, compared with that of the optimized ideal material. It can be seen that the coated *W-SiC* particle reaches similar values of the *SiC* absorption efficiency in the solar region, as well as similar *W*-values in the IR region. In conclusion, a high selectivity is predicted for the coated *W-SiC* particles and the radiative losses are close to those of the ideal material.

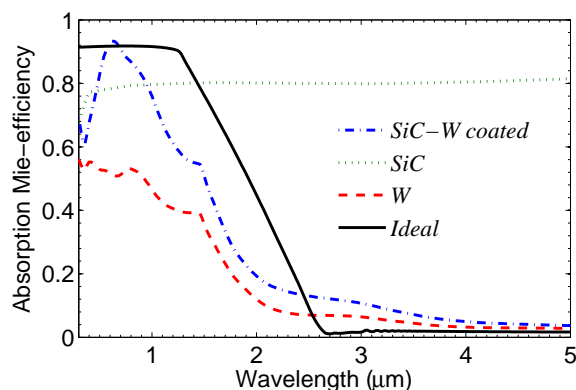


Figure 5.8: Comparison of the absorption Mie-efficiencies (Q_{abs}) for *W* and *SiC*, *W* coated with *SiC* and the optimized ideal material. The particle radius is $r = 50 \mu\text{m}$ in which the coating has a thickness of 50 nm

5.5 Conclusions

Four UHTCs, tungsten and silicon carbide have been studied as possible materials to be used in a high temperature SPR. The SPR is modeled as a $1D$ slab of spherical particles mono-dispersion, submitted to a concentrated and collimated solar flux ($q_0 = 1500 \text{ kW/m}^2$). The temperature inside the SPR is assumed uniform and constant at $T = 1300 \text{ K}$, like for a well-stirred receiver. The monochromatic radiative transfer equation is solved with a two-stream method. Spherical particles characterized by a

highly anisotropic scattering are considered. The BHMIE and DMILAY codes, that solve the Mie efficiencies for an homogeneous or for a coated particle, are employed. The refractive indexes reported in the literature are retained for the *W* and *SiC*. However, for the UHTCs, they are obtained from reflectance data, thanks to the Kramers-Kronig dispersion relations. Three different SPR configurations are studied: a homogeneous medium with only one kind of particles, a homogeneous medium with a mixture of two materials and a homogeneous medium with coated particles. These three cases are compared with the results obtained when particles are made with an ideal material.

In the three cases, the influence of the particle size is studied in the cases of, at least, two particle sizes ($r = 1 \mu m$ and $r = 50 \mu m$). The results show that when only one kind of particles is used, the best material must have a selective behavior. This selectivity may be obtained through changes in the particle size or through the use of an intrinsic selective material. For the *SiC*, which has a high absorptivity in all spectral regions, particle sizes around $r = 1 \mu m$ permit to obtain small emissivities in the near IR region while conserving high absorption properties in the solar region. At these particle sizes, the *SiC* behaves the best followed by the *HfC*, achieving radiative losses of 11.9 and 12.9% of the total incoming flux, respectively. At particle sizes around $r = 50 \mu m$, *SiC* also behaves the best followed by the *HfC*, with radiative losses of 12.7 and 13.7% of the total incoming flux, respectively. A single mixture is studied using a high absorptive material (*SiC*) blend with reflective materials (UHTCs and *W*). No significant radiative losses reduction is found using single mixtures with the materials considered here. Finally, particles of a reflective material coated by an absorptive material are studied. The *SiC* is used as the mantle and the core is in UHTC or *W*. Radiative losses that approach to the ideal minimal are found for thin *SiC* coatings. The best combination corresponds to a particle with a core of *W* coated by *SiC*. Improvements of 2.6% and 2.8% may be achieved using coating thickness of 50 nm with particles of $r = 1 \mu m$ and $r = 50 \mu m$, respectively. The present results suggest that the use of coated particles may lead to significant improvements in the radiative performances of a SPR working at high temperature.

References

- [1] A. Ávila-Marín. Volumetric receivers in solar thermal power plants with central receiver system technology: a review. *Solar Energy*, 85:891–910, 2011.
- [2] R. Bertocchi, J. Karni, and A. Kribus. Experimental evaluation of a non-isothermal high temperature solar particle receiver. *Energy*, 29:687–700, 2004.
- [3] M. Bigelow, N. Lepeshkin, H. Shin, and R. Boyd. Propagation of smooth and discontinuous pulses through materials with very large or very small group velocities. *Journal of Physics: Condensed Matter*, 18:3117–3126, 2006.
- [4] C. Bohren and D. Huffman. *Absorption and Scattering of Light by Small Particles*. John Wiley, 1983.
- [5] P.K. Falcone, J.E. Noring, and J.M. Hruby. Assessment of a solid particle receiver for a high temperature solar central receiver system. Technical report, Sandia National Laboratories, 1985.
- [6] J.M. Hruby. A technical feasibility study of a solid particle solar central receiver for high temperature applications. Technical report, Sandia National Laboratories, 1986.
- [7] A. Hunt. Small particle heat exchanger. Technical report, Lawrence Berkeley Laboratory, 1978.
- [8] J.H. Joseph, W.J. Wiscombe, and J.A. Weinman. The delta-Eddington approximation for radiative flux transfer. *Journal of the Atmospheric Sciences*, 33:2452–2459, 1976.
- [9] K. Kitzmiller and F. Miller. Thermodynamic cycles for small particle heat exchange receiver used in concentrating solar power plants. In *ASME 4th Conference on Energy Sustainability, Vol 2*, 2010.
- [10] H. Klein, J. Karni, R. Ben-Zvi, and R. Bertocchi. Heat transfer in a directly solar receiver/reactor for solid-gas reactions. *Solar Energy*, 81:1227–1239, 2007.
- [11] M. Modest. *Radiative Heat Transfer*. Academic Press, second edition, 2003.
- [12] K. Ohta and H. Ishida. Comparison among several numerical integration methods for Kramers-Kronig transformation. *Applied Spectroscopy*, 42:952–957, 1988.
- [13] E. Palik. *Handbook of Optical Constants of Solids*. Elsevier Science & Tech, 1985.
- [14] B. Pégourié. Optical properties of alpha silicon carbide. *Astronomy and Astrophysics*, 194:335–339, 1988.
- [15] E. Sani, L. Mercatelli, D. Fontani, J.L Sans, and D. Sciti. Hafnium and tantalum carbides for high temperature solar receivers. *Journal of Renewable and Sustainable Energy*, 3:063107, 2011.

- [16] E. Sani, L. Mercatelli, D. Jafrancesco, J.L. Sans, and D. Sciti. Ultra-high temperature ceramics for solar receivers: spectral and high temperature emittance characterization. *Journal of the European Optical Society Rapid Publications*, 7:12052, 2012.
- [17] K.A. Stahl, J.W. Griffin, B.S. Matson, and R.B. Pettit. Optical characterization of solid particle solar central receiver materials. Technical report, Sandia National Laboratories, 1986.
- [18] A. Steinfeld and R. Palumbo. *Solar Thermochemical Process Technology*, chapter Encyclopedia of Physical Science and Technology, pages 237–256. R.A. Meyers Ed., 2001.
- [19] C.L. Tien and B.L. Drolen. Thermal radiation in particulate media with dependent and independent scattering. *Annual Review of Numerical Fluid Mechanics and Heat Transfer*, 1:1–32, 1987.
- [20] O.B. Toon and T.P. Ackerman. Algorithms for the calculation of scattering by stratified spheres. *Applied Optics*, 20:3657–3660, 1981.
- [21] F. Wooten. *Optical Properties of Solids*. Academic Press, 1972.

Chapter 6

Numerical study of the radiative and convective heat transfer coupling in a high temperature SPR

Abstract

The modeling of the coupling between the radiative and convective heat transfer into a high temperature SPR is developed in this chapter. For that, a novel configuration is proposed in order to reduce the complexity of the modeling. The radiative model developed in chapter 2 is included in this new model. This model aims to develop an useful tool to conduct a parametric study of the radiative and conductive heat transfer coupling. The numerical approach, as well as the validation of the code are presented. The parametric study is conducted over the back wall reflectivity, the volume fraction and the particles material. The *SiC*, *HfC*, *W* and *W* coated by *SiC* are used. Results show that volume fractions that correspond to optical thicknesses around $\tau = 4$ are found as the values that maximizes the receiver efficiency for all materials. Concerning to the back wall reflectivity, high wall reflectivity values increase the receiver efficiency when the materials used are selective. Finally, the *W* coated by *SiC* is the material that behave the best, but followed closely by the *SiC*. It suggests that more strategies need to be investigated in order to increase the efficiency in SPRs.

6.1 Introduction

The coupling of the radiative and convective heat transfer in a high temperature SPR is here studied. A number of studies treated the interaction between forced convection and radiation in a SPR, see for example [9, 17, 4]. Sophisticated geometries corresponding to closely related designs of SPR were generally considered. It implies that complex numerical solutions by using commercially-like CFD programs were searched. A drawback linked to this approach is the limited possibility of a complete parametric analysis owing to the large number of geometrical and flow parameters, leading to prohibitively computational costs. In the radiative study developed in the previous

6.2. Model description

chapters, the optimal conditions, using ideal as well as real materials, that minimize the radiative losses in a SPR were suggested. However, the temperature distribution was assumed constant, as for the extreme case of a well-stirred receiver, or prescribed. Since the radiative losses depends on the temperature distribution into the receiver, the influence of the fluid flow on the temperature field must be investigated. To this end, a simplified model allowing the coupling of the radiative and convective heat transfers needs to be developed. In section 6.3 the assumptions allowing the derivation of a simple model are presented. The numerical approach and a step-by step validation are presented in section 6.4. And finally a preliminary parametric study to investigate the influence of the volume fraction and the material used on the receiver efficiency is lead in section 6.5.

6.2 Model description

Amongst the designs of high temperature SPRs reported in the literature, two main categories may be identified: the free-falling receivers [13] and the entrained particle receivers [7]. The convection phenomena for both designs is quite different, owing to the different concepts and particle sizes used ($\sim 600 \mu m$ for free-falling receivers and $\sim 1 \mu m$ for entrained particles receivers). In this work, the use of medium size particles entrained by the fluid flow is considered. This choice permits to reduce some disadvantages linked to small size particles (as particle agglomeration). The simplified geometry studied here drastically reduces the complexity of the modeling while, at the same time, is as realistic as possible. A schematic of the receiver is presented in Fig. 6.1.

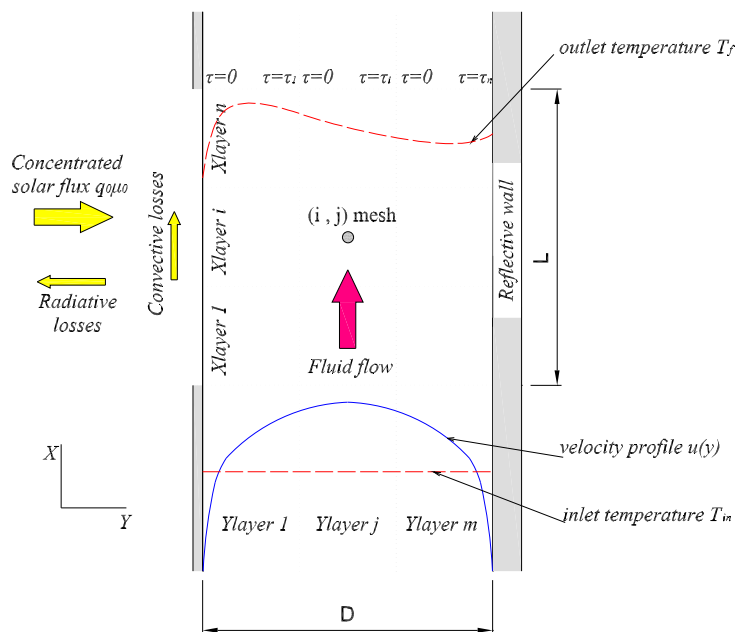


Figure 6.1: Schematic of the radiative-convective coupling model for a high temperature SPR

In this receiver, a gas-particle mixture flows through the space between two parallel plates in the x -direction. The incident concentrated solar radiation is collimated and perpendicular to the flow (y -direction). The width of the receiver (z -axis) is considered large enough to simplify the model as 2D. The depth (D in the y -axis) is constant, however the optical depth is varied through the variation of the volume fraction. Due to the size of the particles, the local temperature of the gas is the same as the particles contained in the macroscopic volume used to derive the conservation equations. Consequently, the fluid is considered as a participating media in the local thermal equilibrium. Moreover, because of the small concentration of particles, the thermal properties of the gas-particle mixture may be considered as the same as those corresponding to the carrier gas. The inlet flow is considered fully developed, turbulent and at a constant temperature. Serra [17] showed that the flow may be considered incompressible (from a velocity point of view) in this kind of receiver because the involved Mach numbers are very small. However, due to the high temperature gradients, the density can not be considered constant. The low-Mach equations will be used as in previous works, as in [6]. Therefore, the acoustic wave effects are ignored while the density variation is taken into account. In a complete model, the velocity into the receiver should be computed from the mass and momentum conservation equations. Nevertheless, to further simplify the model, constant thermal properties within small steps of length ΔX_i in the x -direction will be considered. Even though the thermal properties are considered constant in small steps, they vary over the length L , along the x -direction. This numerical approach permits to not solve the momentum equation, thanks to recalculations of the velocity profile through the mass conservation equation. More details on the approach are given in section 6.3.

The coupling of the radiative and convective heat transfer is done through the radiative flux divergence in the energy equation. The radiative heat fluxes in this case are computed using the radiative model developed before. The radiative transfer equation is solved with a two-stream method, based on the delta-Eddington approximation (called in this work Joseph *et al.*) [8].

6.3 Model development

6.3.1 General formulation of the energy equation

The derivation of the energy equation is based on the first law of thermodynamics in which the principle of local equilibrium is incorporated (internal energy per unit mass assumed to be a function of time and space and specified in terms of the local thermodynamic state). It is a mechanical energy balance that postulates that the time rate of change of internal and kinetic energy is balanced by the rate of heat transfer, the rate of surface works, the rate of work due to volume forces, the rate of energy absorbed or emitted owing to thermal radiation and, the rate of volume production of heat due to chemical reactions, Joules effect, etc. The fundamental derivation of the energy equation may be found in many standard textbooks (e.g. [1]).

The energy equation written in term of temperature for a compressible flow of a

6.3. Model development

semi-transparent Newtonian media reads [1, 15]

$$\rho_f C_p \frac{DT}{Dt} = \nabla \cdot (k_f \nabla T) + \beta_f T \frac{DP}{Dt} + \mu_f \Phi + \dot{Q}''' - \nabla \cdot \vec{q}_r(T) \quad (6.1)$$

where $\beta_f T DP/Dt$ is the work of the pressure forces, $\mu_f \Phi$ the work of the viscous forces (viscous heat dissipation) and, \dot{Q}''' the energy source term. For gas flows, the works of pressure and viscous forces are negligible provided that the Mach numbers are small, as demonstrated in what follows. It is supposed that no internal energy generation exists in a SPR (which is different from solar reactors), then the energy source term may be also neglected. For an ideal gas, $\beta_f T = 1$. The density (ρ_f) and velocity fields are solutions of the coupled system of conservation equations (Navier-Stokes and energy equations) and of the state equation.

For a steady flow and by invoking the continuity equation, the transport term may be written in the conservative form as

$$\rho_f C_p \vec{V} \nabla \cdot T = C_p \nabla \cdot (\rho_f \vec{V} T) \quad (6.2)$$

Therefore, the energy equation for an ideal gas flow in its steady-state form and without source terms is given by

$$C_p \nabla \cdot (\rho_f \vec{V} T) = \nabla \cdot (k_f \nabla T) + P \nabla \cdot \vec{V} + \mu_f \Phi - \nabla \cdot \vec{q}_r(T) \quad (6.3)$$

A simplified form of Eq. 6.3 may be derived from a scale analysis about the importance of the various terms. To this end, the most simplest procedure is to consider the dimensionless form of Eq. 6.3 based on three scales: \mathcal{L} for lengths, u_r for the velocity components and T_r for temperature. It follows that relevant scales for radiative flux, pressure and heat dissipation are: $\sigma_{SB} T_r^4$, $\rho_r u_r^2$ and $\mu_r (u_r/\mathcal{L})^2$, where $\sigma_{SB} = 5.67 \times 10^{-8} \text{ W}/(\text{m}^2 \text{K}^4)$ is the Stefan-Boltzmann constant and the subindex r means evaluated at the reference temperature. The dimensionless form of Eq. 6.3 reads

$$\begin{aligned} \left(\frac{\rho_r C_{p,r} u_r T_r}{\mathcal{L}} \right) C_p^* \tilde{\nabla} \cdot (\rho_f^* \vec{V}^* \theta) &= \left(\frac{k_r T_r}{\mathcal{L}^2} \right) \tilde{\nabla} \cdot (k_f^* \tilde{\nabla} \theta) - \left(\frac{\sigma_{SB} T_r^4}{\mathcal{L}} \right) \tilde{\nabla} \cdot \vec{q}_r^*(\theta) \\ &+ \left(\frac{\rho_r u_r^3}{\mathcal{L}} \right) P^* \tilde{\nabla} \cdot \vec{V}^* + \mu_r \left(\frac{u_r}{\mathcal{L}} \right)^2 \mu_f^* \Phi^* \end{aligned} \quad (6.4)$$

where $\tilde{\nabla} = \frac{1}{\mathcal{L}} \nabla$, $\theta = T/T_r$, $u^* = u/u_r$, $\vec{q}_r^* = \vec{q}_r/\sigma_{SB} T_r^4, \dots$, etc. By dividing the left-hand-side and right-hand-side of Eq. 6.4 by the dimensionless coefficient of the transport term, we obtain

$$\begin{aligned} C_p^* \tilde{\nabla} \cdot (\rho_f^* \vec{V}^* \theta) &= \left(\frac{k_r}{\rho_r C_{p,r} u_r \mathcal{L}} \right) \tilde{\nabla} \cdot (k_f^* \tilde{\nabla} \theta) - \left(\frac{\sigma_{SB} T_r^3}{\rho_r C_{p,r} u_r} \right) \tilde{\nabla} \cdot \vec{q}_r^*(\theta) \\ &+ \left(\frac{u_r^2}{C_{p,r} T_r} \right) P^* \tilde{\nabla} \cdot \vec{V}^* + \left(\frac{\mu_r u_r}{\rho_r C_{p,r} T_r \mathcal{L}} \right) \mu_f^* \Phi^* \end{aligned} \quad (6.5)$$

The dimensionless numbers in parenthesis in the right hand side of Eq. 6.5 may be expressed as

$$\begin{aligned}\frac{k_r}{\rho_r C_{p,r} u_r \mathcal{L}} &= \frac{a_{f,r}}{u_r \mathcal{L}} = \frac{1}{Pe} \\ \frac{\sigma_{SB} T_r^3}{\rho_r C_{p,r} u_r} &= \frac{\sigma_{SB} T_r^4}{k_r T_r / \mathcal{L}} \times \frac{k_r}{\rho_r C_{p,r} u_r \mathcal{L}} = \frac{N_R}{Pe} \\ \frac{u_r^2}{C_{p,r} T_r} &= Ec \\ \frac{\mu_r u_r}{\rho_r C_{p,r} T_r \mathcal{L}} &= \frac{u_r^2}{C_{p,r} T_r} \times \frac{\mu_r}{\rho_r u_r \mathcal{L}} = \frac{Ec}{Re}\end{aligned}$$

where $a_{f,r}$ is the thermal diffusivity evaluated at the reference temperature, Pe is the Peclet number ($Pe = RePr$ and Pr is the Prandtl number), N_R is the radiation-to-conduction parameter and Ec is the Eckert number, which characterizes the importance of the pressure work in comparison with convection. Therefore, the dimensionless form of the energy equation is

$$C_p^* \tilde{\nabla} \cdot (\rho_f^* \vec{V}^* \theta) = \frac{1}{Pe} \left[\tilde{\nabla} \cdot (k_f^* \tilde{\nabla} \theta) - N_R \tilde{\nabla} \cdot \vec{q}_r^*(\theta) \right] + Ec \left[P^* \tilde{\nabla} \cdot \vec{V}^* + \frac{\mu_f^* \Phi^*}{Re} \right] \quad (6.6)$$

For an ideal gas, it can readily be shown that

$$Ec = (\gamma - 1) Ma^2 \quad (6.7)$$

where $\gamma = C_p/C_v$ and Ma is the Mach number ($Ma = u_r/c_s$, reference fluid velocity-sound velocity ratio). A number of authors have shown that for SPRs, $Ma^2 \ll 1$ [17]. This coarse scale analysis permits to assume that the pressure and viscous dissipation terms can be neglected. Therefore, the energy equation for a flow with variable density may be expressed as

$$C_p^* \tilde{\nabla} \cdot (\rho_f^* \vec{V}^* \theta) = \frac{1}{Pe} \left[\tilde{\nabla} \cdot (k_f^* \tilde{\nabla} \theta) - N_R \tilde{\nabla} \cdot \vec{q}_r^*(\theta) \right] \quad (6.8)$$

6.3.2 Convection heat transfer in a parallel plate channel

The general form of the energy equation 6.8 for a parallel plate channel with a plate-spacing D (see Fig. 6.1) may be written in a dimensional form as

$$C_p(T) \left(\frac{\partial(\rho_f u T)}{\partial x} + \frac{\partial(\rho_f v T)}{\partial y} \right) = \frac{\partial}{\partial x} \left(k_f(T) \frac{\partial T}{\partial x} \right) + \frac{\partial}{\partial y} \left(k_f(T) \frac{\partial T}{\partial y} \right) - \left(\frac{\partial q_r}{\partial x} + \frac{\partial q_r}{\partial y} \right) \quad (6.9)$$

Inlet, outlet and wall thermal boundary conditions must be specified. Since a one dimensional, dynamically developed flow at uniform temperature is assumed at the inlet section (i.e. $T(0, y) = T_{in}$, $u(0, y)$ specified and $v = 0$), Eq. 6.9 reduces to

$$C_p(T) \frac{\partial(\rho_f u T)}{\partial x} = \frac{\partial}{\partial x} \left(k_f(T) \frac{\partial T}{\partial x} \right) + \frac{\partial}{\partial y} \left(k_f(T) \frac{\partial T}{\partial y} \right) - \left(\frac{\partial q_r}{\partial x} + \frac{\partial q_r}{\partial y} \right) \quad (6.10)$$

6.3. Model development

Eq. 6.10 may be further simplified if the Peclet number is large enough because the relative importance of the axial heat diffusion term ($\partial [k(T)\partial T/\partial x]/\partial x$) and the axial radiative heat transfer ($\partial q_r/\partial y \gg \partial q_r/\partial x$) decrease as Pe increases. It may be easily shown by considering constant thermo-physical properties (C_p , ρ_f and k_f are temperature independent). Therefore, the velocity profile may be written as $u(y) = u_m f(y)$ in any cross section, with $f(y)$ depending on the flow regime and satisfying the mass conservation constraint ($\int_0^D f(y)dy = D$). Equation 6.10 reads

$$u(y)\frac{\partial T}{\partial x} = a_f \left(\frac{\partial T}{\partial x^2} + \frac{\partial T}{\partial y^2} \right) - \frac{1}{\rho C_p} \left(\frac{\partial q_r}{\partial x} + \frac{\partial q_r}{\partial y} \right) \quad (6.11)$$

where $a_f = k_f/\rho_f C_p$ is the thermal diffusivity. Equation 6.11 is cast in dimensionless form by using the following dimensionless quantities

$$x^* = \frac{a_f x}{u_m D^2}, \quad y^* = \frac{y}{D}, \quad \theta = \frac{T - T_r}{\Delta T}, \quad u^* = \frac{u}{u_m}, \quad q_r^* = \frac{q_r}{\sigma_{SB} T_r^4}$$

where T_r and ΔT are a reference temperature and a reference temperature difference (for example $T_r = T_{in}$, $\Delta T = T_w - T_{in}$). It is readily shown that the dimensionless form of Eq. 6.11 is

$$u^*(y^*)\frac{\partial \theta}{\partial x^*} = \frac{1}{Pe^2} \frac{\partial^2 \theta}{\partial x^{*2}} + \frac{\partial^2 \theta}{\partial y^{*2}} - \frac{N_R}{Pe} \frac{\partial q_r^*}{\partial x^*} - N_R \frac{\partial q_r^*}{\partial y^*} \quad (6.12)$$

where $Pe = u_m D/a_f$ and $N_R = \sigma_{SB} T_r^4/(k_f \Delta T/D)$. Equation 6.12 clearly shows that the axial diffusion term may be neglected at high Pe numbers. In the current literature, this term is considered negligible if $Pe > 100$. Since the typical Reynolds numbers encountered in a SPR with air as the working fluid ($Pr \approx 0.7$ for T_r in the range $[300 K - 1500 K]$) are of few orders of magnitude greater than $Pe \approx 100$, the assumption of negligible axial conduction appears to be realistic. Also, if the radiative fluxes gradients are of the same magnitude order in the x and y direction, the axial radiative heat flux is negligible face to the transversal radiative heat flux. Note that this conclusion ($\partial q_r/\partial x$ negligible) does not imply that the radiative fluxes (q_r) are x -independent. Therefore, Equation 6.12 may be approximated as

$$u(y)\frac{\partial T}{\partial x} = a_f \left(\frac{\partial T}{\partial y^2} \right) - \frac{1}{\rho_f C_p} \frac{\partial q_r}{\partial y} \quad (6.13)$$

One of the main advantage linked with that approximation is that it is not required to specify a thermal condition at the outlet section. Therefore, the energy equation is of parabolic type and a marching procedure can be easily applied for numerically solving Eq. 6.13. A similar procedure but based on an appropriate choice of the reference temperature would lead to the following energy equation for flows with temperature-dependent thermophysical properties:

$$C_p \frac{\partial (\rho_f(T)uT)}{\partial x} = \frac{\partial}{\partial y} \left(k_f(T) \frac{\partial T}{\partial y} \right) - \frac{\partial q_r}{\partial y} \quad (6.14)$$

Nevertheless, the u -velocity profile cannot be assumed only y -dependent, while $\int_0^D \rho_f(T)u dy$ must be. We will consider later on an approximate procedure to numerically solve Eq. 6.14. Note that the heat thermal capacity (C_p) in Eq. 6.14 is presented as no temperature dependent. The C_p -temperature dependence in the range of temperatures used here, is low enough to take it as constant [17].

6.3.3 Approximate turbulent modeling

Since in a SPR the fluid flow is turbulent, a time-averaged model is considered. The classical Reynolds decompositions are applied

$$u = \bar{u} + u'; \quad v = \bar{v} + v'; \quad \text{and} \quad T = \bar{T} + T' \quad (6.15)$$

where the over line quantities represent the mean behavior averaged over a long enough period of time and the \cdot' quantities represent the unpredictable fluctuations (eddies). Then, equation 6.14 may be rewritten as

$$C_p \frac{\partial (\rho_f(\bar{T})\bar{u}\bar{T})}{\partial x} = \frac{\partial}{\partial y} \left(k_f(\bar{T}) \frac{\partial \bar{T}}{\partial y} - \rho_f C_p \overline{v'T'} \right) - \frac{\partial q_r}{\partial y} \quad (6.16)$$

The following algebraic model is introduced for the eddy heat flux [1]

$$-\rho_f C_p \overline{v'T'} = \rho_f C_p \epsilon_H \frac{\partial \bar{T}}{\partial y} \quad (6.17)$$

where ϵ_H is an empirical function called the thermal eddy diffusivity. The treatment of this term is the aim of turbulence modeling. The approximation used in the present model will be presented later. Therefore, the energy equation becomes

$$C_p \frac{\partial (\rho_f(\bar{T})\bar{u}\bar{T})}{\partial x} = \frac{\partial}{\partial y} \left((k_f(\bar{T}) + \rho_f(\bar{T})C_p\epsilon_H) \frac{\partial \bar{T}}{\partial y} \right) - \frac{\partial q_r}{\partial y} \quad (6.18)$$

The mass conservation and state equations are written as

$$\frac{\partial}{\partial x} (\rho_f(\bar{T})\bar{u}(y)) = 0 \quad (6.19)$$

$$P = \rho_f(\bar{T})\bar{R}\bar{T} \quad (6.20)$$

where \bar{R} is the gas constant ($\bar{R} = 286.7 \text{ J/kgK}$ for air).

In resume, the model is based on the following simplifications

- Steady state.
- Unidirectional flow.
- No influence of the gravity on the fluid flow ($Gr/Re^2 \ll 1$, where Gr is the Grashof number).
- Negligible viscous dissipation.
- Negligible effect of pressure work.

6.3.4 Thermal boundary conditions

Three boundary conditions are needed to solve Eq. 6.18. Note that these boundary conditions correspond to the fluid flow problem and do not consider the radiative part of the problem. The radiative boundary conditions were mentioned before (see section 2.3.4). They are as follows:

6.3. Model development

Inlet temperature

The temperature at the inlet of the receiver is considered constant along the depth. It is written as

$$\bar{T}(0, y) = T_{in} \quad 0 \leq y \leq D \quad (6.21)$$

Convective surface wall

It is assumed that a window is placed at the front of the receiver. It permits the incident solar flux to enter into the receiver while reducing the convective losses, but some re-emission flux go out through this boundary. Moreover, an amount of heat flux go out by conduction and convection because of the lower outside temperature. It leads to

$$k_f \frac{\partial T}{\partial y} \Big|_{y=0} = \frac{T(x, 0) - T_{amb}}{R_{thermal}} = \bar{U}(T(x, 0) - T_{amb}) \quad (6.22)$$

where $R_{thermal}$ is the thermal resistance of the window (conductive resistance $R_{cond} = e/k_v +$ external convection) and \bar{U} the conductance:

$$R_{thermal} = R_{cond} + \frac{1}{h_e} \quad \bar{U} = \frac{1}{R_{cond} + \frac{1}{h_e}} \quad (6.23)$$

Therefore

$$k_f \frac{\partial T}{\partial y} \Big|_{y=0} = \bar{U}(T(x, 0) - T_{amb}) \quad 0 \leq x \leq L \quad (6.24)$$

Bottom wall

The bottom surface of the receiver is supposed thermally insulated and purely reflective. Therefore

$$\frac{\partial \bar{T}}{\partial y} \Big|_{y=D} = 0 \quad 0 \leq x \leq L \quad (6.25)$$

6.3.5 Enthalpy flux balance

An overall energy balance over the whole channel volume $\Omega = L \times D$ [m^3/m] may be derived from Eq. 6.14 by using the flux-divergence (or Gauss) theorem

$$\int_{\Omega} C_p(T) \frac{\partial(\rho_f(T)uT)}{\partial x} d\Omega = \int_{\Omega} \frac{\partial}{\partial y} \left(k_f(T) \frac{\partial T}{\partial y} \right) d\Omega - \int_{\Omega} \frac{\partial q_r}{\partial y} d\Omega \quad (6.26)$$

leading to

$$\int_S C_p(T) \rho_f(T) \vec{u} \cdot \vec{n} T dS = - \int_S k_f(T) \nabla T \cdot \vec{n} dS - \int_S \vec{q}_r \cdot \vec{n} dS \quad (6.27)$$

By assuming impermeable and non-slip bounding walls ($\vec{u} = 0$ at $y = 0, D$), negligible axial heat diffusion and axial radiative flux, Equation 6.27 reads

$$\begin{aligned} & \int_0^D C_p(T)\rho_f(T)\vec{u} \cdot \vec{n}T|_{x=L} dy - \int_0^D C_p(T)\rho_f(T)\vec{u} \cdot \vec{n}T|_{x=0} dy \\ &= \int_0^L k_f(T)\frac{\partial T}{\partial y}\Big|_{y=0} dx - \int_0^L k_f(T)\frac{\partial T}{\partial y}\Big|_{y=D} dx + \int_0^L q_r(x, 0)dx - \int_0^L q_r(x, D)dx \end{aligned} \quad (6.28)$$

For a thermally insulated and purely reflecting wall at $y = D$, the second and fourth terms in right-hand side of Eq. 6.28 are equal to zero. Therefore, the following heat balance must be satisfied

$$\begin{aligned} & \int_0^D C_p(T)\rho_f(T)u(y)|_{x=L} dy - \int_0^D C_p(T)\rho_f(T)u(y)T|_{x=0} dy \\ &= \int_0^L k_f(T)\frac{\partial T}{\partial y}\Big|_{y=0} dx + \int_0^L q_r(x, 0)dx \end{aligned} \quad (6.29)$$

where the left-hand side of Eq. 6.29 represents the variation of the enthalpy heat flux between the inlet and outlet section of the channel. The inlet and outlet enthalpy flux are

$$\int_0^D C_p(T)\rho_f(T)u(y)T|_{x=0} dy = \dot{m}C_{p,in}T_{in} \quad (6.30)$$

$$\int_0^D C_p(T)\rho_f(T)u(y)T|_{x=L} dy = \dot{m} \frac{\int_0^D C_p(T)\rho_f(T)u(y)T|_{x=L} dy}{\int_0^D \rho_f u dy} \approx \dot{m}\bar{C}_{p,out}T_{m,out} \quad (6.31)$$

where \dot{m} is the mass flow rate and $\bar{C}_{p,out}$ and $T_{m,out}$ are the mean heat capacity and the mixing-cup temperature at the outlet channel section. If C_p is assumed constant in the outlet section ($|T(L, D) - T(L, 0)| < 500 K$ for air at atmospheric pressure), the enthalpy flux balance may be written according to the thermal B.C. at $y = 0$ as

$$\dot{m}[C_{p,out}T_{m,out} - C_{p,in}T_{in}] = -\bar{U} \int_0^L (T(x, 0) - T_{amb})dx + \int_0^L q_r(x, 0)dx \quad (6.32)$$

6.3.6 Velocity profiles

The fluid flow into the SPR model is considered turbulent and fully developed. The power law is used to model the velocity profile in such a SPR. However, this profile is not appropriate to compute the thermal eddy diffusivity. Therefore, the universal turbulent velocity profile is used for that. This approximation is valid for constant density. A consideration for its use in variable density flows will be treated later.

6.3. Model development

Power-law velocity profile

A number of experimental results have shown that the fully developed turbulent velocity profile in ducts may be well approximated by the power-law profile.

$$u^+ = A(y^+)^{1/n} \quad \text{for} \quad 0 \leq y^+ \leq D^+/2 \quad (6.33)$$

where the u^+ , y^+ are the dimensionless velocity and depth, and u_f is the friction velocity, as usual in turbulent notations, and the A constant is defined as

$$A = \frac{\bar{u}_{max}}{u_f} \frac{1}{(D^+/2)^{1/n}} \quad (6.34)$$

The dimensionless variables are

$$u^+ = \frac{\bar{u}(y)}{u_f} \quad ; \quad y^+ = \frac{yu_f}{\nu} \quad ; \quad u_f = \sqrt{\frac{\tau_w}{\rho_f}} \quad (6.35)$$

In the power-law velocity, the n -exponent depends on the Reynolds number. Some n and \bar{u}_m/\bar{u}_{max} values are reported in Table 6.1 according to the Re_D -value for a pipe flow.

Re	4000	1×10^5	4×10^5	1×10^6	2×10^6
n	6	7	8	9	10
\bar{u}_m/\bar{u}_{max}	0.791	0.817	0.837	0.852	0.865

Table 6.1: Exponent of the power-law relationship and ratio of the mean velocity to the maximum velocity in a smooth pipe

Since the data reported in Table 6.1 are for pipe flows, an empirical correlation (Blasius, Prandtl-Schlichting, Karman-Nikuradse, etc.) must be used to calculate the friction factor and the n -values in a parallel plate channel, where the main velocity (\bar{u}_m) is given by the following expression

$$\bar{u}_m = \frac{1}{D} \int_0^D \bar{u}_{max} \left(\frac{y}{D}\right)^{1/n} dy = \bar{u}_{max} \left(\frac{n}{n+1}\right) \quad (6.36)$$

Universal turbulent velocity profile

The power-law velocity profile is not appropriate for evaluating the turbulent thermal diffusivity, which varies from the wall to the duct centerline. Therefore, the use of the universal turbulent velocity profile (or various modifications based on other approximation of the mixing length) is suggested to derive the momentum eddy diffusivity ϵ_m . By assuming a constant turbulent Prandtl number, $Pr_t = \epsilon_m/\epsilon_H$, the thermal eddy diffusivity ϵ_H may be straightforwardly calculated. The universal turbulent velocity is composed of three layers as

$$\begin{aligned} u^+ &= y^+ & y^+ < 5 \\ u^+ &= 5 \ln y^+ + 5 & 5 < y^+ < 30 \\ u^+ &= 2,5 \ln y^+ + 5,5 & 30 < y^+ < D^+/2 \end{aligned} \quad (6.37)$$

The transverse turbulent heat flux may approximated as

$$\bar{q}(y) = \rho_f C_p (a_f + \epsilon_H) \frac{\partial T}{\partial y} = \rho_f C_p \left(\frac{\nu}{Pr} + \frac{\epsilon_m}{Pr_t} \right) \frac{\partial T}{\partial y} \quad (6.38)$$

where the problem reduces to compute the momentum eddy diffusivity ϵ_m . By introducing the dimensionless quantity

$$\epsilon^+ = 1 + \epsilon_m/\nu = \frac{1}{du^+/dy^+} \quad (6.39)$$

ϵ^+ may be directly calculated from Eq. 6.37. The main drawback linked to this choice of the Prandtl mixing length lies in the slow decay of ϵ_m and in its discontinuity at $y^+ = 30$. In consequence, the following van Driest expression of the mixing length appears to be more suitable

$$l_m^+ = K y^+ \left[1 - e^{-y^+/y_t^+} \right] \quad (6.40)$$

where l_m^+ is the dimensionless mixing length, K is the von Karman constant ($K = 0.41$) for a turbulent boundary layer over a flat plate and $y_t^+ = 26$, corresponding coarsely to the upper limit of the buffer layer where $\epsilon_m \approx \nu$. Since ϵ^+ may be written in the turbulent layers in term of the mixing length as

$$\epsilon^+ = 1 + l_m^{+2}/\epsilon^+ \quad \text{or} \quad \epsilon^{+2} - \epsilon^+ - l_m^{+2} = 0 \quad (6.41)$$

the positive root of Eq. 6.41 writes

$$\epsilon^+ = \frac{1 + \sqrt{1 + 4l_m^{+2}}}{2} \quad (6.42)$$

By using the van Driest formula (Eq. 6.40), it is obtained

$$\epsilon^+ = \frac{1}{2} + \frac{1}{2} \sqrt{1 + 4K^2 y^{+2} [1 - \exp(-y^+/y_t^+)]^2} \quad (6.43)$$

When $y^+ \gg y_t^+ \approx 26$ (say $y^+ > 5y_t^+$), $[1 - \exp(-y^+/y_t^+)]^2 \approx 1$ and $1 + 4K^2 y^{+2} \approx 4K^2 y^{+2}$. As a results, $\epsilon^+ = 0,5 + Ky^+ \approx Ky^+ = 0,4y^+$. The Prandtl formula is then recovered. Finally, from the definition of ϵ^+ and by assuming a constant turbulent Prandtl number, the following expression of ϵ_H is obtained.

$$\epsilon_H = \frac{\nu}{Pr_t} (\epsilon^+ - 1) = \frac{\nu}{2Pr_t} \left[\sqrt{1 + 4 \left(\frac{K u_f y}{\nu} \right)^2 [1 - \exp(-y/y_t)]^2} - 1 \right] \quad (6.44)$$

A list of ten available expressions of the momentum eddy diffusivity are reported in Sarma *et al.*[16], and another one depending on the velocity profile is also proposed [16].

$$\epsilon_H = \frac{\nu}{Pr_t} \left[0.0198(y^+ u^+) \left(1 - \exp\left(-\frac{y^+ u^+}{100}\right) \right)^2 \right] = \frac{1}{Pr_t} \left[0.0198(yu) \left(1 - \exp\left(-\frac{yu}{100\nu}\right) \right)^2 \right] \quad (6.45)$$

6.3. Model development

For both thermal eddy diffusivity expressions, the turbulent Prandtl number, which depends on the fluid properties, may be determined from [12]

$$\frac{1}{Pr_t} = 0.91 + 0.13Pr^{0.545} \quad 0.7 < Pr < 100 \quad (6.46)$$

An advantage found in the use of Eq. 6.45 is that the eddy diffusivities do not depend explicitly on the friction velocity and that a coarse approximation of their maximum values may be easily obtained. For instance, for air at $T = 500 \text{ K}$, $\nu \approx 8 \times 10^{-5} \text{ m}^2/\text{s}$ and thus for the application considered here, $\epsilon_{H,max} = 0,0198 yu/Pr_t$. By assuming that $Pr_t \approx 0,983$ ($Pr = 0.708$ in Eq. 6.46), the maximum thermal eddy diffusivity at the channel centerline ($y = D/2 = 0.5 \text{ m}$) where $\bar{u} = \bar{u}_{max} \approx 1.1\bar{u}_m$ for $n = 7$ is $\epsilon_{H,max} \approx 0.011\bar{u}_m$, i.e. two order of magnitude greater than $a_f = 1,1 \times 10^{-4}$ in the case $\bar{u}_m = 1 \text{ m/s}$.

Sutherland law

Since the thermal eddy diffusivity is expressed in function of ν , which depends on \bar{T} , a temperature dependence law of the kinematic viscosity must be used. The Sutherland law, based on kinetic theory of ideal gas and Lennard-Jones intermolecular-force potential, gives fairly accurate results for the dynamic viscosity variation with temperature over a wide range of temperatures (about 170 K to 1900 K for air). Sutherland's law can be expressed as:

$$\mu_f(T) = \mu_0 \left(\frac{T}{T_0} \right)^{3/2} \frac{T_0 + T_S}{T + T_S} \quad (6.47)$$

where μ_0 is the viscosity at the reference temperature T_0 and T_S is the Sutherland temperature. For air, $\mu_0 = 1.716 \times 10^{-5} \text{ kg/m.s}$ at $T_0 = 273.15 \text{ K}$ and $T_S = 110.4 \text{ K}$. Therefore

$$\mu_f(T) = 1.458 \cdot 10^{-6} \frac{T^{3/2}}{T + 110.4} \quad (6.48)$$

By assuming negligible variations of heat thermal capacity and Prandtl number with temperature for the application considered [17] ($C_p = 1005 \text{ J/kg.K}$, $Pr \approx 0.71$), it follows that the thermal conductivity may be written as

$$k_f(T) = \frac{\mu_f(T)C_p}{Pr} = \frac{1.465 \times 10^{-3}}{Pr} \frac{T^{3/2}}{T + 110.4} \quad (6.49)$$

6.3.7 Variable density flow consideration

Since the coupled system of conservation equations and state equation is not fully solved, the energy equation for variable density cannot be easily computed without introducing a more simplified approach than the one previously used. The simplest procedure is probably to consider that the density variation may be accounted for thanks to the use of a series of differential steps in order to incrementally represent the changes in density and velocity profile. In each step of length ΔX , chosen such as the increase in $\bar{T}_m(x)$ within the elementary volume $\Delta\Omega = D\Delta X$ is small enough, the thermophysical properties may be assumed constant. If $[X_i, X_{i+1}]$ is divided in n

meshes of length Δx , where X_i and X_{i+1} denote the borders of $\Delta\Omega$, then $X_i = x_i$ and $X_{i+1} = x_i + n\Delta x$. The thermophysical properties and velocity profile in $\Delta\Omega$ are those calculated from the mixing-cup temperature $\bar{T}_m(x_i)$ as follows

$$\bar{\rho}_f(x_i) = \left(\frac{P}{R}\right) \frac{1}{\bar{T}_m(x_i)} \quad (6.50)$$

where $P = 1 \text{ atm}$. Similarly, the other properties in $[X_i, X_{i+1}]$ are $C_{p,i} = C_p(\bar{T}_m(x_i))$, $k_i = k(\bar{T}_m(x_i))$, $\nu_i = \nu(\bar{T}_m(x_i))$. The mean velocity $\bar{u}_m(x) = \bar{u}_m(x_i)$ is deduced from the mass conservation at section $X_i = x_i$

$$\bar{u}_m(x_i) = \frac{\dot{m}}{\bar{\rho}_f(x_i)D} \quad (6.51)$$

The centerline temperature being taken as $\bar{u}_{max}(x_i)$, the velocity profile in $[X_i, X_{i+1}]$ may be estimated from the power-law approximation:

$$\begin{aligned} \bar{u}(y) &= \bar{u}_m(x_i) \frac{n+1}{n} \left(\frac{2y}{D}\right)^{1/n} & \text{for } 0 \leq y \leq \frac{D}{2} \\ \bar{u}(y) &= \bar{u}_m(x_i) \frac{n+1}{n} \left(\frac{2(D-y)}{D}\right)^{1/n} & \text{for } \frac{D}{2} \leq y \leq D \end{aligned} \quad (6.52)$$

The thermal eddy diffusivity profile is also assumed independent of x in $[X_i, X_{i+1}]$. The numerical solution of the energy equation in $\Delta\Omega$ leads to the temperature profile in section X_{i+1} , used in the step-marching procedure for calculating the thermophysical properties and $\bar{u}_m(X_i)$, before solving the temperature field in $[X_{i+1}, X_{i+2}]$. By considering that the thermo-physical properties are constant within $\Delta\Omega$, provided that the maximum temperature difference between sections X_i and X_{i+1} does not overcome 10 K , the channel length must be subdivided into N $\Delta\Omega$ -volumes. The number N must be *a priori* estimated for the assumed maximum temperature difference between the channel inlet and outlet sections. For example, $N = 50$ for $\bar{T}_{m,out} - T_{in} = 500 \text{ K}$. If there are $I_{max} = 1000$ meshes of length $\Delta x = L/1000$ over the x -direction, there are 20 meshes in each $[X_i, X_{i+1}]$.

6.3.8 Radiative heat dissipation

The coupling between the convection and the radiative heat transfer is done through the divergence of the radiative heat flux term. As explained in Chapter 2, to solve the monochromatic, mono-dimensional RTE, the spectral specific intensity $I_\lambda(\tau, \mu)$ is split into two components: the diffuse intensity, $I_{d,\lambda}(\tau, \mu)$, and the collimated intensity, $I_{c,\lambda}(\tau, \mu)$. Therefore, $I_\lambda = I_{d,\lambda} + I_{c,\lambda}$. The collimated intensity is the reduction of the collimated flux $q_{0,\lambda}$ in the main path direction (μ_0) and is written as

$$I_{c,\lambda}(\tau, \mu) = q_{0,\lambda} \exp\left(-\frac{\tau}{\mu_0}\right) \delta(\mu - \mu_0) \quad (6.53)$$

6.4. Numerical solution

And integrating in respect of the azimuthal angle over the 2π domain, the diffuse RTE may be written as [3, 15]

$$\mu \frac{dI_{d,\lambda}(\tau, \mu)}{d\tau} = -I_{d,\lambda}(\tau, \mu) + \frac{1}{2} \int_{-1}^{+1} p_{\lambda}(\mu, \mu') I_{d,\lambda}(\tau, \mu') d\mu' + G_{\lambda}(\tau, \mu) \quad (6.54)$$

$$G_{\lambda}(\tau, \mu) = \frac{1}{2} p_{\lambda}(\mu, \mu_0) q_{0,\lambda} \exp\left(-\frac{\tau}{\mu_0}\right) + (1 - \omega_0) I_{b,\lambda}(\tau) \quad (6.55)$$

being μ the angle direction, p the phase function, τ the optical depth, ω_0 the scattering albedo and I_b the blackbody emission.

Equation 6.53 is solved by analytical integration and Eq. 6.54 is solved by using a two-stream method with a Joseph *et al.* (delta-Eddington) approximation. Such model splits the radiative heat flux in two parts: a forward (q_{λ}^+) and a backward (q_{λ}^-) radiative fluxes (in practice, the directional radiative heat flux are integrated between the $0 \leq \theta < \pi/2$ and $\pi/2 \leq \theta < \pi$ angle directions).

$$q_{c,\lambda}(\tau) = q_{0,\lambda} \exp\left(-\frac{\tau}{\mu_0}\right) \quad (6.56)$$

and,

$$\begin{aligned} q_{d,\lambda}^+(\tau) &= \int_0^1 I_{d,\lambda}(\tau, \mu) \mu d\mu & \mu \geq 0 \\ q_{d,\lambda}^-(\tau) &= \int_{-1}^0 I_{d,\lambda}(\tau, \mu) \mu d\mu & \mu \leq 0 \end{aligned} \quad (6.57)$$

The radiative heat flux inside the receiver is found as

$$q_r(\tau) = \int_0^{\infty} [q_{c,\lambda}(\tau) + q_{d,\lambda}^+(\tau) - q_{d,\lambda}^-(\tau)] d\lambda \quad (6.58)$$

Finally, the divergence of the radiative heat transfer may be computed numerically from the radiative heat fluxes values.

6.4 Numerical solution

The numerical method implemented for solving the energy equation and some selected problems used to check the grid resolution, as well as the accuracy of preliminary computations starting from laminar flow and ending with the most closest configuration to those considered in the following are presented in Appendix D. In short, the cases discussed in Appendix D are on forced convection between two parallel plates with constant thermo-physical properties and without source term. Three sub-problems are considered:

- The first one when $u(y) = u_m = cte$ (slug flow),
- The second one is for a laminar flow (Poiseuille velocity profile),
- The third case is a turbulent flow with a power-law velocity profile and approximate expression of the thermal eddy diffusivity, as described in subsection 6.3.6.

Additional validations, much closer to what is our concern, are shown below.

6.4.1 Turbulent flow between two parallel plates with an uniform heat generation rate

A problem closer to the SPR model includes an uniform source term added in the energy equation and a boundary condition at the wall $y = 0$ with an overall heat transfer coefficient \bar{U} between the inner wall surface and the surroundings at T_{amb} . For this case, the energy equation writes

$$\bar{u}(y) \frac{\partial \bar{T}}{\partial x} = \frac{\partial}{\partial y} \left((a_f + \epsilon_H(y)) \frac{\partial \bar{T}}{\partial y} \right) + \dot{Q}''' \quad (6.59)$$

with the boundary conditions

$$\begin{aligned} \bar{T}(0, y) &= T_{in} \\ - \left(k_f \frac{\partial \bar{T}}{\partial y} \right) \Big|_{y=0} &= \bar{U} (\bar{T}(x, 0) - T_{amb}) \\ \frac{\partial \bar{T}}{\partial y} \Big|_{y=D} &= 0 \end{aligned} \quad (6.60)$$

The overall heat transfer coefficient may be estimated as

$$\frac{1}{\bar{U}} = \frac{e}{k_w} + \frac{1}{\bar{h}_e} \implies \bar{U} = \frac{k_w \bar{h}_e}{e \bar{h}_e + k_w} \quad (6.61)$$

where e is the thickness of the window, k_w is the thermal conductivity of the window and \bar{h}_e is the mean external convection coefficient. Since the inlet temperature is $T_{in} = 300 \text{ K}$ and no longer temperature gradients are expected, the thermo-physical properties are evaluated as constant and at $T = 310 \text{ K}$. They are reported in Table 6.2.

Density (ρ_f)	1.127	$[\text{kg}/\text{m}^3]$
Kinematic viscosity (ν)	16.97×10^{-6}	$[\text{m}^2/\text{s}]$
Conductivity (k_f)	0.0271	$[\text{W}/\text{mK}]$
Thermal capacity (C_p)	1005	$[\text{J}/\text{kgK}]$
Prandtl number (Pr)	0.708	

Table 6.2: Thermo-physical properties of the air at 310 K used in simulations of the convection between two parallel plates with constant properties

In what follows, a $n_x = 300 \times n_y = 2000$ grid is used. Two cases are considered: the first one when $\bar{U} = 0$ and the second one when $\bar{U} \neq 0$.

First case: $\bar{U} = 0$

The mixing cup temperature still varies linearly according to

$$\bar{T}_m(x) = T_{in} + \frac{\dot{Q}''' D}{\dot{m} C_p} x = T_{in} + \frac{\dot{Q}'''}{\rho \bar{u}_m C_p} x \quad (6.62)$$

6.4. Numerical solution

The conditions used are reported in Table 6.3.

Geometry depth (D)	1	[m]
Geometry length (L)	1	[m]
Mass flow rate (\dot{m})	0.5	[kg/s]
Inlet temperature (T_{in})	300	[K]
Overall transfer coefficient (\bar{U})	0	[W/m ² K]
Constant source term (\dot{Q}''')	1500	[W/m ³]

Table 6.3: Conditions used in simulations of a turbulent flow between two parallel plates with a constant source term

For the data reported in Tables 6.2 and 6.3, the expected increase in temperature is $\Delta T_m = \dot{Q}''' D_h / C_p = 3/1.005 = 2.99 K$. The mixing cup temperature and the temperature profiles at the mid-length and at the outlet of the channel are shown in Fig. 6.2. The variation of the mixing cup temperature satisfies Eq. 6.62 exactly. In any x -section, the temperature profile is symmetric about the channel axis ($\partial T / \partial y|_{y=D/2} = 0$). It is also normal to the adiabatic walls at $y = 0$ and $y = D$, as it can be seen from a zoom of the temperature profile close to the walls.

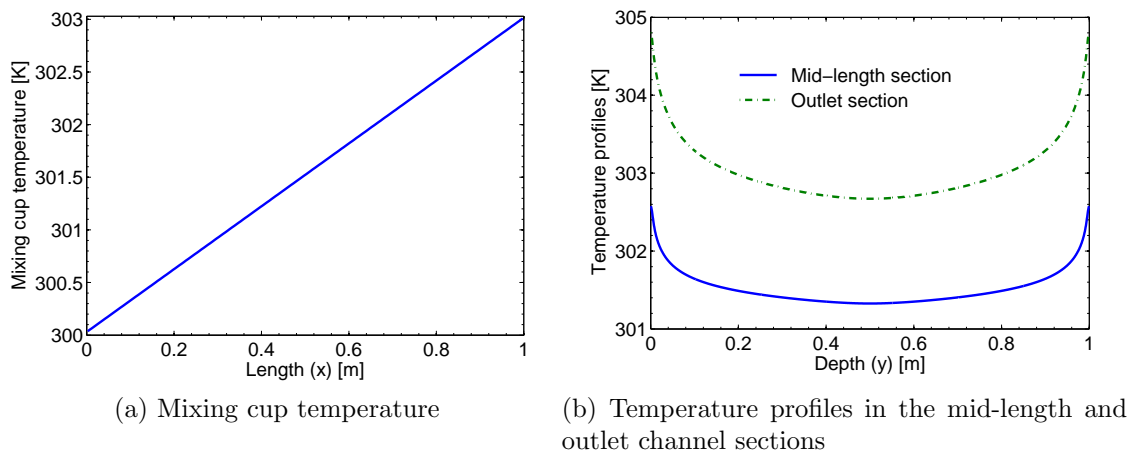


Figure 6.2: Temperatures for a turbulent flow between two adiabatic parallel plates with an uniform heat generation rate (see the conditions in Tables 6.2 and 6.3)

The temperature profiles at the outlet section computed for slug and Poiseuille flows are compared with the turbulent profile in Fig. 6.3. The slug velocity profile leads to a flat temperature profile, as it can be straightforwardly shown from the energy equation by setting $u(y) = u_m$ and $\epsilon_H = 0$. The Poiseuille profile leads to steep variations in temperature close to the walls. As expected, the turbulent profile is rather close to the slug profile, and between the slug and Poiseuille profiles.

Second case: $\bar{U} \neq 0$

To solve a problem still closer to the case of a solar receiver, the previous problem is considered by introducing a much higher heat generation term in the energy equation

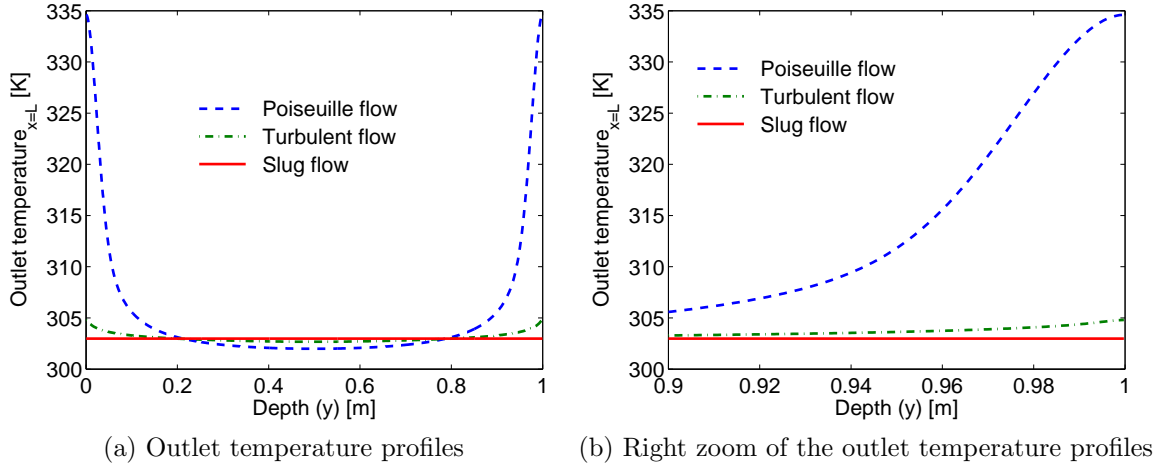


Figure 6.3: Outlet temperature profiles for a flow between two adiabatic parallel plates with a uniform heat generation term. Slug, Poiseuille and power-law turbulent velocity profiles are considered (see the conditions in Tables 6.2 and 6.3)

and by modifying the boundary condition at the wall $y = 0$ through the introduction of an overall heat transfer coefficient \bar{U} between the inner wall surface and the surroundings at T_{amb} (see Table 6.4). Therefore, the volumetric heating of the fluid is of the order of what is expected in a SPR and the wall (SPR window) is now cooled. The mean external convection heat transfer coefficient may be estimated as a typical value for turbulent free convection over a vertical plate: $\bar{h}_e = 20 \text{ W}/(\text{m}^2\text{K})$. In addition, if we consider a window with a thickness $e = 0.01 \text{ m}$ and thermal conductivity $k_w = 1 \text{ W}/\text{m}\cdot\text{K}$, the overall heat transfer coefficient may be coarsely evaluated as $\bar{U} = 16.7 \text{ W}/\text{m}\cdot\text{K}$.

Geometry depth (D)	1	[m]
Geometry length (L)	1	[m]
Mass flow rate (\dot{m})	0.5	[kg/s]
Inlet temperature (T_{in})	300	[K]
Wall heat flux (q_w)	0	[W/m ²]
Constant source term (\dot{Q}''')	3×10^5	[W/m ³]
Overall transfer coefficient (\bar{U})	16.7	[W/m ² K]
Ambient temperature (T_{amb})	300	[K]

Table 6.4: Conditions used in the simulations of a turbulent flow between two parallel plates with a large heat generation term and with a convective boundary condition

The variation of the mixing cup temperature may be approximated by solving the following overall energy balance

$$\dot{m}C_p \frac{dT_m}{dx} = \dot{Q}''' D - U_t(x)(T_m(x) - T_{amb}) \quad \text{with } T_m(0) = T_{in} \quad (6.63)$$

where the overall heat transfer coefficient $U_t(x)$, in which the local inner heat transfer

6.4. Numerical solution

coefficient $h_i(x)$ is accounted for, is defined as

$$U_t(x) = \frac{1}{\frac{1}{h_e} + R_{cond} + \frac{1}{h_i(x)}} = \frac{\bar{U} h_i(x)}{\bar{U} + h_i(x)} \quad (6.64)$$

According to the $h_i(x)$ value, the overall heat transfer coefficient varies between two limits

$$U_t(x) = \bar{U} \quad \text{if } h_i(x) \gg \bar{U}, \quad U_t(x) = h_i(x) \quad \text{if } h_i(x) \ll \bar{U} \quad (6.65)$$

The local inner heat transfer coefficient $h_i(x)$ must be determined by using an appropriate Nusselt number correlation for turbulent flows within a flat plate channel. Equation 6.63 may be rewritten as

$$\frac{dT_m}{dx} + B_1(x)T_m(x) = B_2(x) \quad \text{with } T_m(0) = T_{in} \quad (6.66)$$

where $B_1(x) = U_t(x)/\dot{m}C_p$ and $B_2(x) = (\dot{Q}''' D + U_t(x)T_{amb})/\dot{m}C_p$. The solution of Eq.6.66 reads [10]

$$T_m(x) = T_{in} \exp[-\bar{B}_1(x)x] + \int_0^x B_2(\xi) \exp[-(\bar{B}_1(x)x - \bar{B}_1(\xi)\xi)] d\xi \quad (6.67)$$

where

$$\bar{B}_1(x) = \frac{1}{x} \int_0^x B_1(\xi) d\xi \quad (6.68)$$

A coarse approximation for solving Eq.6.66 consists of replacing the local heat transfer coefficient $h_i(x)$ by the mean value \bar{h}_i (such an approximation will be discussed below). Therefore $\bar{B}_1(x) = \bar{B}_1$ and $B_2(x) = B_2$. The solution of Eq.6.67 becomes then

$$T_m(x) = (T_{in} - \frac{B_2}{\bar{B}_1}) e^{-\bar{B}_1 x} + \frac{B_2}{\bar{B}_1} \quad (6.69)$$

From the data reported in Tables 6.2 and 6.4, and by using the Colburn correlation, $Nu_{D_h} = 0.023 Re_{D_h}^{4/5} Pr^{1/3}$, we obtain (with $Re_{D_h} = 5.23 \times 10^4$ and $Pr = 0.708$) $Nu_{D_h} = 122$. Therefore, $\bar{h}_i = 1.65 \text{ W/m}^2 \text{ K}$ and $\bar{U}_t = 1.50 \approx \bar{h}_i$.

Since the local heat transfer coefficient $h_i(x)$ is of the order or larger than \bar{h}_i , the simplification leading to Eq. 6.69 appears to be reasonable. Furthermore, since $\bar{B}_1 = \bar{U}_t/\dot{m}C_p = 0.003 \text{ m}^{-1}$, we can assume that $\exp(-B_1 x) = 1 - B_1 x$ for $x \leq L = 1 \text{ m}$. It results that the mixing cup temperature varies linearly as

$$T_m(x) = (T_{in} - \frac{B_2}{\bar{B}_1})(1 - \bar{B}_1 x) + \frac{B_2}{\bar{B}_1} \quad (6.70)$$

We obtain also $B_2 = 598 \text{ K/m}$. It follows that $T_m(L/2) = 598 \text{ K}$ and $T_m(L) = 896 \text{ K}$.

Comparison between the numerically predicted variation of $T_m(x)$ plotted in Fig. 6.4a and Eq. 6.70 with the above \bar{B}_1 and B_2 values shows a fairly good agreement.

Fig. 6.4b shows that the wall temperature varies also almost linearly, and is close to the mixing-cup temperature. This numerical results cannot be straightforwardly derived analytically. It shows that the modeling of the thermal boundary condition at the outer window side must be improved by adding a non-linear radiative heat flux. The increase in windows temperature is moderate: $T(x, 0) \approx 400\text{ K}$ at $x \approx 0.4\text{ m}$ and, $T(x, -e) \approx T(x, 0)$ since R_{cond} is small. It should be added that the IR radiative losses for the case considered are much higher than the convective losses.

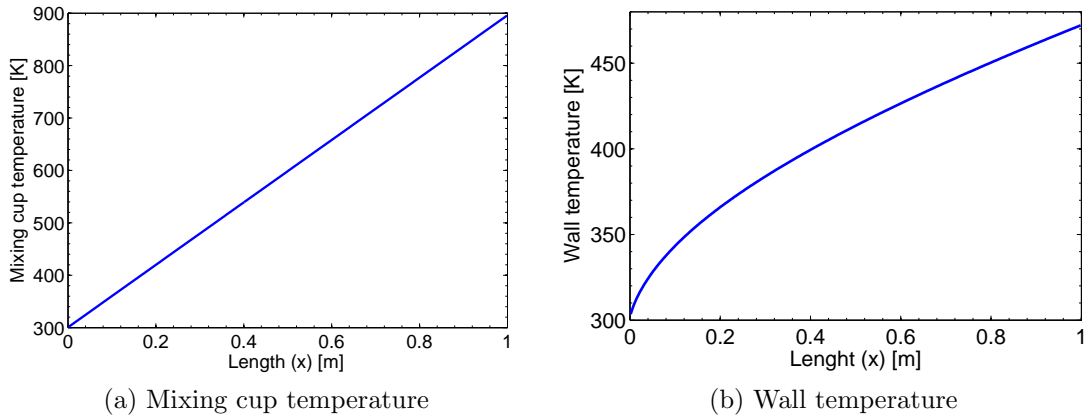


Figure 6.4: Mixing cup temperature and wall temperature variations for a turbulent flow between two parallel plates with an uniform heat generation rate and a convective boundary condition at the wall $y = 0$ (see Tables 6.2 and 6.4 for the set of parameters)

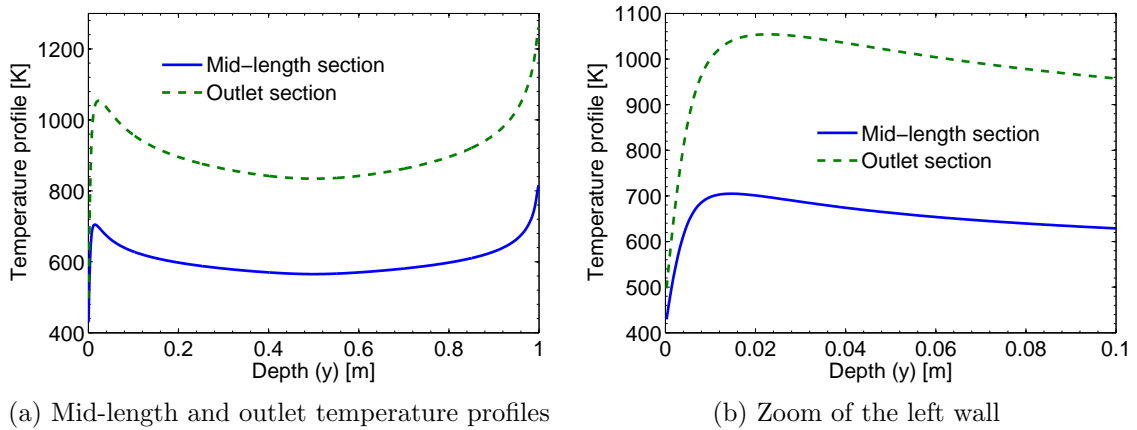


Figure 6.5: Mid-length and outlet temperature profiles for a turbulent flow between two parallel plates with a volume source term and a convective boundary condition (see Tables 6.2 and 6.4 for the set of parameters)

Figure 6.5 shows the temperature profiles at $x = L/2$ and $x = L$. The minimum temperature is at the window wall and the maximum one at the adiabatic wall (an enlargement shows that $\partial T/\partial y|_{y=D} = 0$). The temperature of the fluid-window interface being smaller than the inside temperature owing to the cooling convection, a

6.4. Numerical solution

temperature peak is observed very close to $y = 0$. The slope of $T(x, y)$ in the vicinity of $y = 0$ is obviously linked to the \bar{U} value.

The change in temperature in a cross section may reach about few hundreds of degree and increases in the downstream direction. Therefore, variations in thermophysical properties should be taken into account for the set of data considered.

6.4.2 Effects of temperature dependent thermo-physical properties

In this subsection, the effects of the variations of the thermo physical properties, except thermal capacity, are investigated.

Effects of temperature dependent thermal conductivity and dynamic viscosity

By assuming a constant density, the energy equation may be written as

$$\bar{u}(y) \frac{\partial \bar{T}}{\partial x} = \frac{\partial}{\partial y} \left[\left(\frac{k_f(\bar{T})}{\rho_f C_p} + \epsilon_H(\bar{T}) \right) \frac{\partial \bar{T}}{\partial y} \right] + \frac{1}{\rho_f C_p} \dot{Q}''' \quad (6.71)$$

The boundary conditions are still: a uniform inlet temperature ($T(0, y) = T_{in}$), a convective condition on the left wall ($-k_f \partial T / \partial y|_{y=0} = \bar{U}(T(x, 0) - T_{amb})$), and an adiabatic wall at the right side ($\partial T / \partial y|_{y=D} = 0$). The overall heat transfer coefficient \bar{U} is taken as 16.7 W/(mK) , as in the previous section. The dynamic viscosity $\mu_f(T)$ and thermal conductivity $k_f(T)$ are varied according to the Sutherland law (Eqs. 6.48 and 6.49). If the maximum temperature difference in the flow field is about 1000 K , both k_f and μ_f are increased by a factor of about 2.25.

In the present paragraph, ρ_f is assumed constant. Therefore, the thermal eddy diffusivity is calculated with $\nu_f(T) = \mu_f(T) / \rho_f$. The maximum error caused by this approximation may be coarsely estimated as follows: $\epsilon_H(T)$ (see Eq. 6-45) is a positive, increasing function for $0 \leq y \leq D/2$ with a maximum value very close to $\epsilon_H(D/2) = 0.0198(D/2\bar{u}_{max})/Pr_t$ since $(\rho_f D/2\bar{u}_{max})/(100\mu) > 10^2 \rho_f$ for the case considered (see Tables 6.2 and 6.4). The change in $\epsilon_H(T)$ due to variations in kinematic density is thus expected to be weak.

For constant density, the variations of the mixing cup temperature depends only on the thermal boundary conditions. Any change in $T_m(x)$ occurs when conductivity and viscosity variations with temperature are taken into account. The numerical results shown in Fig. 6.6 are in perfect agreement with this prediction.

Nevertheless, the temperature profiles are different, owing to the large temperature variations in a channel cross-section which influence k_f and μ_f . To study separately the influences of thermal conductivity and thermal eddy diffusivity variations, two cases are considered: first, the dynamic viscosity is constant while the thermal conductivity is variable; second, the conductivity and the dynamic viscosity vary with temperature.

In Fig. 6.7, both cases are compared with the case for constant thermal conductivity and viscosity. As it can be seen, the temperature profile depends weakly on the variations in k_f and in μ_f , except close to the cooled wall where the largest temperature gradient are predicted. In addition, the comparison between Fig. 6.7a and 6.7b shows that the change in thermal conductivity is the most important effect. Since the

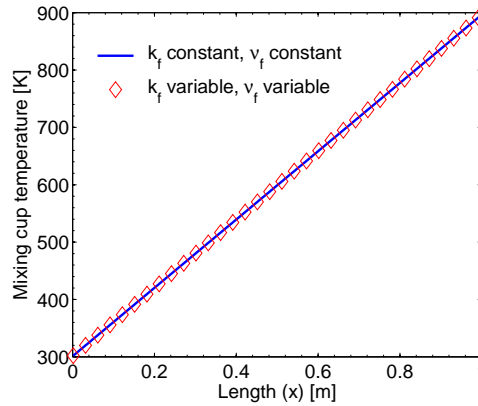


Figure 6.6: Comparison of the mixing cup temperature for a turbulent flow between parallel plates and constant source term using either constant or variable thermal conductivities (see Table 6.4 for the set of parameters)

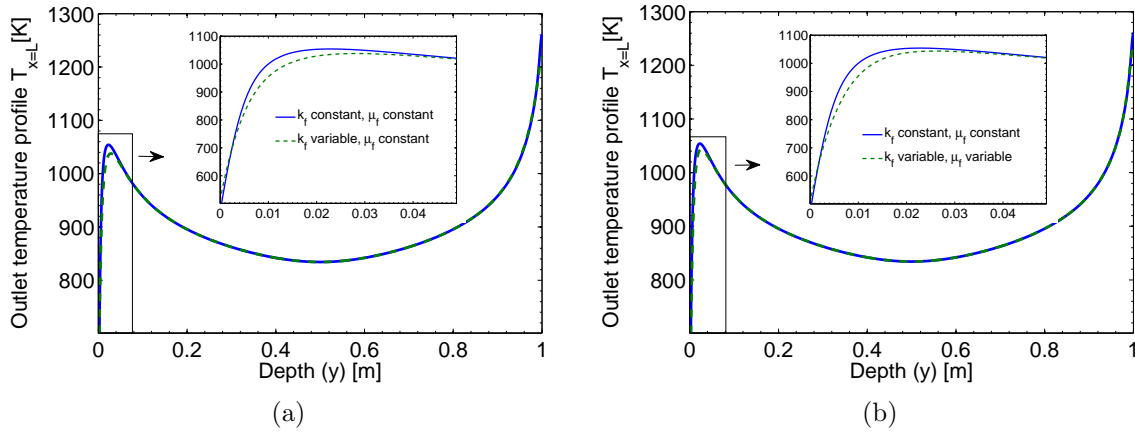


Figure 6.7: Comparisons of the outlet temperature profiles for a turbulent flow with constant and variable thermal conductivity and kinematic viscosity (see Tables 6.2 and 6.4 for the set of parameters). The insets shown a zoom for the close wall region

largest temperature difference is between the temperatures at the window wall and at the adiabatic wall (about $\Delta T = 800$ K), conductivity and viscosity increase by a factor 1.9 over the outlet section.

The variations of the thermal conductivity at the outlet section is shown in Fig. 6.8. These variations follow obviously a shape similar to that of the temperature variation. It is also seen that the averaged conductivity at the outlet section is about two times higher than the thermal conductivity at the inlet section. However, these differences have a marginal impact on the temperature distribution for turbulent flows because the eddy thermal diffusivity is much higher than the molecular diffusivity.

The differences in ϵ_H being rather small, as discussed above, the effects of temperature variations on ϵ_H are presented in Table 6.5 rather than graphically. As can be seen, ϵ_H is very weakly temperature dependent, except close to the cold wall where the molecular and eddy diffusivity are of same order of magnitude. Together with the large variations in k_f , these variations in ϵ_H contribute to the temperature changes shown

6.4. Numerical solution

in Fig. 6.7 in the vicinity of the cooled wall.

Based on this approximate model, we found also that the density close to the adiabatic wall is ≈ 1.5 times the density at the channel axis. Therefore, the density variations should be included in the flow modeling.

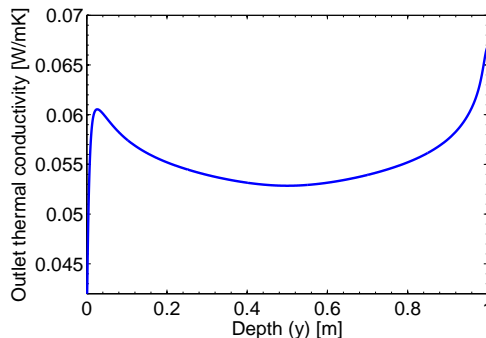


Figure 6.8: Variation of the thermal conductivity in the outlet section (calculated from the temperature profile shown in Fig. 6.7b)

	$0.015D$	$0.05D$	$0.1D$	$0.2D$	$0.35D$
Constant properties	8.312×10^{-5}	3.697×10^{-4}	8.142×10^{-4}	1.795×10^{-3}	3.396×10^{-3}
Variable properties	4.866×10^{-5}	3.644×10^{-4}	8.141×10^{-4}	1.795×10^{-3}	3.396×10^{-3}

Table 6.5: Comparison of the outlet thermal eddy diffusivity at different positions using constant and variable thermal properties (k_f and ν_f) for a turbulent flow into a channel ($L = D = 1\text{ m}$, $Re_{D_h} = 5.23 \times 10^4$)

Effects of temperature dependent density, thermal conductivity and dynamic viscosity

The energy equation, when the temperature dependence of the density is considered, may be approximately written as

$$\overline{\rho_f(\bar{T})u(y)C_p} \frac{\partial \bar{T}}{\partial x} = \frac{\partial}{\partial y} \left([k_f(\bar{T}) + \bar{\rho}_f(\bar{T})C_p\epsilon_H(\bar{T})] \frac{\partial \bar{T}}{\partial y} \right) + \dot{Q}''' \quad (6.72)$$

However, since the flow equations were not solved by using a Favre-averaging type technique, the quantity $\overline{\rho_f(y)u(y)}$ cannot be calculated. The mass conservation implies

$$\int_0^D \overline{\rho_f(x,y)u(x,y)} dy = (\overline{\rho_f u})_m(x)D = \dot{m} \quad (6.73)$$

The three main approximations employed in what follows are:

- $\overline{(\rho_f u)}_m \approx \bar{\rho}_{f,m} \bar{u}_m$,
- $\bar{\rho}_f(x,y) \approx \bar{\rho}_{f,m}(x)$,
- the power-law velocity profile derived for incompressible channel flows still applies in each x -section. However, the average velocity used in the u -profile is changed in the downstream direction according to $\bar{u}_m(x) = \dot{m}/\bar{\rho}_{f,m}(x)D$.

The consequence is that the energy equation is solved in the following form

$$\bar{\rho}_{f,m}(x)C_p\bar{u}(y)\frac{\partial\bar{T}}{\partial x} = \frac{\partial}{\partial y} \left([k_f(\bar{T}) + \bar{\rho}_{f,m}(x)C_p\epsilon_H(\bar{T})] \frac{\partial\bar{T}}{\partial y} \right) + \dot{Q}''' \quad (6.74)$$

Since $\bar{\rho}_{f,m}(x)$ decreases downstream as $1/T_m(x)$ (see Fig. 6.9a), the average density calculated from the ideal gas law with a constant pressure decreases by a factor of about 3. It can be expected *a priori* that changes in the temperature profiles occur also. Nevertheless, the overall mass conservation being satisfied according to the second approximation mentioned above ($\bar{\rho}_f(x, y) \approx \bar{\rho}_{f,m}(x)$), the average velocity increases, as well as the local $u(y)$ values while the $u(y)$ -profile is assumed keeping a power law. Let us consider now the transport term and the turbulent thermal conductivity in Eq. 6.74

- Transport term

$$\bar{\rho}_{f,m}(x)C_p\bar{u}(y) = \left(\frac{\dot{m}}{D}\right)\left(\frac{n+1}{n}\right)C_p\left(\frac{Y}{D/2}\right)^{1/n} \quad (6.75)$$

where $Y = y$ for $0 < y \leq D/2$ and $Y = D - y$ for $D/2 \leq y < D$. Since \dot{m} and C_p are constant, there is any change in $\bar{\rho}_{f,m}(x)C_p\bar{u}(y)$.

- Turbulent conductivity

$$\bar{\rho}_{f,m}C_p\epsilon_H = \frac{C_p}{Pr_t} \left[0.0198(\bar{\rho}_{f,m}y\bar{u}) \left(1 - \exp\left(-\frac{\bar{\rho}_{f,m}y\bar{u}}{100\mu}\right) \right)^2 \right] \quad (6.76)$$

Here again, it can be concluded that $\bar{\rho}_{f,m}y\bar{u}$ does not depends on x .

The final conclusion is that ϵ_H increases in the downstream direction, as can be seen in Fig. 6.9b while the turbulent thermal conductivity is constant. Figure 6.10 shows that these predictions are numerically satisfied. It can be added that the present computations strengthen that the turbulent conductivity is much higher than the molecular conductivity (see Figs. 6.10a and 6.10b).

The temperatures at different y -locations in the outlet section are reported in Table 6.6 for constant thermophysical properties (line 1) and for variable properties. As can be seen, significant differences occurs only close to the cooled wall and close to the adiabatic wall where changes in thermal conductivity have the largest effects, as previously discussed (see Fig. 6.8).

y		$0.015D$	$0.25D$	$0.5D$	$0.75D$	D
$T(L, y)$	$(\rho_f = cte, k_f = cte, \mu_f = cte)$	1042	876.8	834.2	877	1261
$T(L, y)$	$(\rho_f = cte, k_f = var, \mu_f = var)$	1017	876.8	834.2	877	1234
$T(L, y)$	$(\rho_f = var, k_f = var, \mu_f = var)$	1017	876.8	834.2	877	1234

Table 6.6: Outlet temperature comparisons at few y -positions for a turbulent flow into a channel ($L = D = 1 m$, $Re_{D_h} = 5.23 \times 10^4$), using constant or variable thermal properties

6.4. Numerical solution

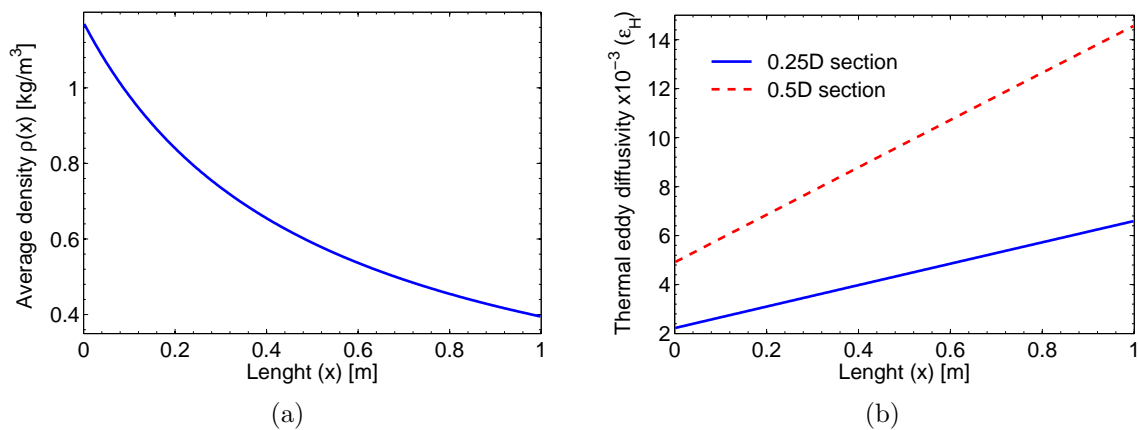


Figure 6.9: Downstream variation of the average density and the thermal eddy diffusivity at two y positions for a turbulent flow with variable thermal properties (see Tables 6.2 for the inlet thermal properties and 6.4 for the set of parameters)

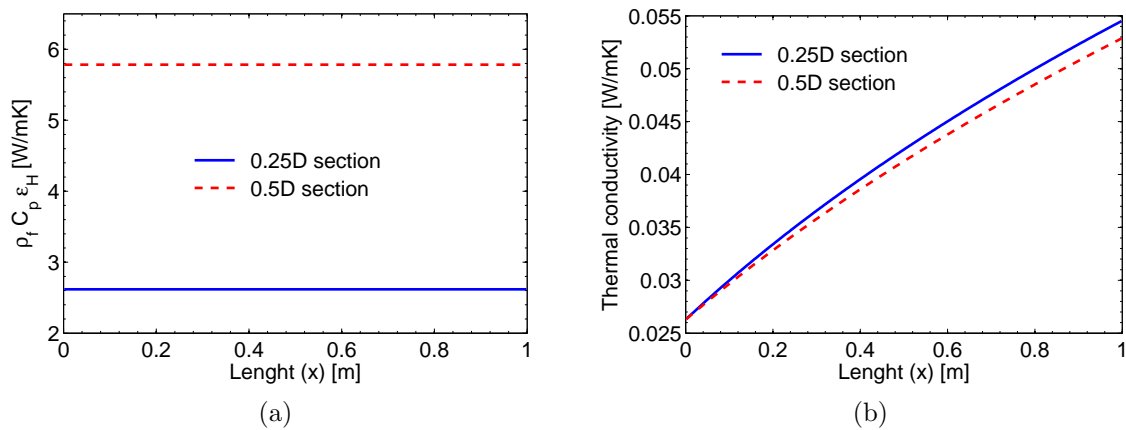


Figure 6.10: Downstream variation of $\rho_f C_p \epsilon_H$ product and the thermal conductivity at two y positions for a turbulent flow with variable thermal properties (see Tables 6.2 for the inlet thermal properties and 6.4 for the set of parameters)

The wall temperature at various x -variations are shown in Table 6.7. In comparison with the constant property assumption (line 1), the effects of property variations increase slightly from the inlet to the outlet sections, as expected. It can be also noted that the density variations have no effect on the wall temperature (see lines 2 and 3), in agreement with the above discussion.

x		0.25L	0.5L	0.75L	L
$T(x, 0)$	$(\rho_f = cte, k_f = cte, \mu_f = cte)$	375.6	413.7	444.8	472.1
$T(x, 0)$	$(\rho_f = cte, k_f = var, \mu_f = var)$	381.7	429.1	470	506.8
$T(x, 0)$	$(\rho_f = var, k_f = var, \mu_f = var)$	381.7	429.1	470	506.8

Table 6.7: Comparisons between the wall temperatures at few downstream locations ($L = D = 1\text{ m}$, $Re_{D_h} = 5.23 \times 10^4$), using constant or variable thermal properties

6.4.3 Absorbing, scattering and emitting slug flow between two parallel plates

The most essential part in the developed code is the coupling between the convective and radiative heat transfer. This coupling is done through the divergence of radiative flux term in the energy equation. No analytical exact solution exists for a problem involving this coupling, to be used as exact reference. However, a number of studies using approximations have been reported for the case of the heat transfer in a participating media between parallel plates. Most of them are constrained to treat a slug flow [11, 19]. In this section, the solution for the heat transfer in an absorbing, emitting and scattering slug flow between two parallel plates presented by Lii and Özişik [11] and replicated by [5] are used as reference. These reference solutions are approximative and no correspond to an exact solution. In consequence, they serve to indicate the well performance of the code and not to validate its accuracy. For instance, Silva et al [5] use the generalized integral transformed technique to solve the energy equation and a Garlekin method to solve the radiative transfer equation.

The problem considers an absorbing, emitting and isotropically scattering gray, incompressible, constant-property fluid in a thermally developing slug flow ($u(y) = u_m$) between two parallel-plates. The plates are spaced a distance D and they emit and reflect diffusely the radiation. The fluid enters at a constant temperature, and a constant temperature is imposed at the plate walls. Under these conditions the energy equation and the boundary conditions for the temperature are the following.

$$u_m \frac{\partial T}{\partial x} = a_f \frac{\partial^2 T}{\partial y^2} - \frac{1}{\rho_f C_p} \frac{\partial q_r}{\partial y} \quad (6.77)$$

$$T(x = 0) = 0 \quad (6.78)$$

$$T(y = 0) = T(y = D) = T_w$$

The radiative heat flux takes into account the emission, scattering and absorption of energy by the medium. It is written as

$$q_r = 2\pi \int_{-1}^{+1} I(\tau, \mu) \mu d\mu \quad (6.79)$$

where $\tau = \beta y$ is the optical depth (see Eq. 2.3), μ is the direction angle of the radiation and the specific intensity $I(\tau, \mu)$ should satisfies the radiative transfer equation (see Eq. 2.5). The radiative boundary conditions are given by the Stefan-Boltzmann law for the imposed temperature at the wall. Note that the optical depth τ (and consequently the volume extinction coefficient β) varies only in the y -direction, which permits to solve the radiative problem as $1D$.

To solve Eq. 6.77, Silva and al. [5] as well as Lii and Özişik [11], rewrite this equation in dimensionless form as

$$\frac{\partial}{\partial \xi} (\theta(\tau, \xi)) = \frac{\partial^2}{\partial \tau^2} (\theta(\tau, \xi)) - \frac{1}{4\pi N} \frac{\partial}{\partial \tau} Q_r(\tau, \xi) \quad (6.80)$$

6.4. Numerical solution

where the dimensionless quantities are

$$\begin{aligned} N &= k_f \beta / (4\sigma T_w^3), & Q_r(\tau, \xi) &= \pi q_r(\tau, \xi) / (\sigma T_w^4) \\ \theta(\tau, \xi) &= T(\tau, \xi) / T_w, & \tau_0 &= \beta(D/2), & \xi &= k_f \beta^2 x / (\rho_f u_m C_p) \end{aligned} \quad (6.81)$$

and the boundary conditions become

$$\begin{aligned} \theta(\tau, 0) &= \theta_0 = 0 \\ \theta(0, \xi) &= \theta(D, \xi) = \theta_1 = \theta_2 = 1 \end{aligned} \quad (6.82)$$

To conserve the original procedure the conduction-radiation parameter N is different of that defined before (section 6.3.1), k_f , ρ_f and C_p are the thermal conductivity, the density and the thermal capacity of the media respectively, β is the extinction coefficient and $\sigma_{SB} = 5.67 \times 10^{-8} [W/(m^2 K^4)]$ is the Stefan-Boltzmann constant.

The problem proposed by Lii and and Özişik [11] is solved by the code developed in this work. Since the velocity and the thermal properties do not change along the channel, they may be computed only once. At each step in the x -direction the temperature is computed in an iterative way, making use of the precedent known temperature. The radiative transfer equation is solved only in the y -direction using the two-stream method developed. The radiative boundary conditions are the diffuse emission by the walls following the Stefan-Boltzmann law. The thermo-physical properties are they given in Table 6.2. Two flow conditions for a radiative condition are compared. These conditions correspond to $\xi = 0.1$, $\xi = 0.05$ and $N = 0.1$. The dimensional conditions for the thermo-physical properties imposed are shown in Table 6.8.

Geometry depth (D)	1	[m]
Geometry length (L)	1	[m]
Inlet temperature (T_{in})	0	[K]
Mass flow rate 1 (\dot{m} at $\xi = 0.1$)	5.39×10^{-4}	[kg/s]
Mass flow rate 2 (\dot{m} at $\xi = 0.05$)	1.08×10^{-3}	[kg/s]
Mean velocity 1 (u_m at $\xi = 0.1$)	4.79×10^{-4}	[m/s]
Mean velocity 2 (u_m at $\xi = 0.05$)	9.57×10^{-4}	[m/s]
Wall temperature (T_w at $N = 0.1$)	133.7	[K]

Table 6.8: Parameters used in simulations of an absorbing, scattering and emitting slug flow between two parallel plates

The comparison of the dimensionless temperature profile at two distance is shown in Fig. 6.11. Since the N -value is small, these comparisons are representatives of a reasonably strong effect of the radiation. The conditions used for the simulation are shown in the figure, where ω_0 is the scattering albedo of the media.

The comparison shows a well behavior of the temperature profile computations made by the code. A small difference between the reference profile and the computed profile is found close to the centerline. It may be attributed to the coarse treatment of the radiative transfer.

On the objective of known the performance of the code to treat the coupling of the radiative and convective heat transfer, a good agreement with the references is found.

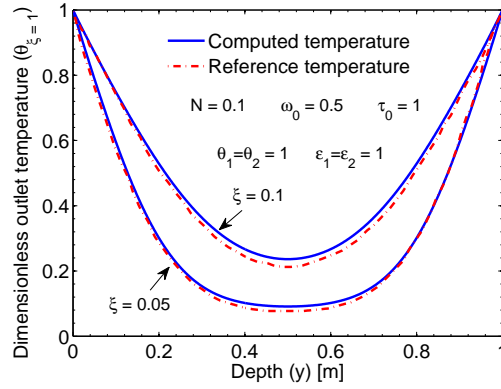


Figure 6.11: Dimensionless temperature profile at two dimensionless positions for an absorbing, emitting and isotropically scattering slug flow between two parallel-plates. The subindex 1 and 2 correspond to the walls

6.5 Radiative and convective heat transfer coupling

A number of simulations are carried out to investigate the performance of the model in the expected conditions of a SPR. To this end, thin and thick media are considered at a first stage as extreme situations to be studied. The simulations were conducted by assuming that the gas-particles mixture, composed by air and *SiC* particles, enters at a pre-heated temperature $T_{in} = 500 \text{ K}$. The fluid flow is submitted to an incident concentrated solar flux of $q_0 = 800 \text{ kW/m}^2$, as in high temperature solar CSP plants [18]. For the mass flow rate considered, the flow regime is turbulent since the Reynolds number at the inlet is $Re = 7.4 \times 10^4$. The increase in dynamic viscosity with temperature along the channel is assumed small enough to maintain the turbulent regime up to the outlet section. The radiative model developed in Chapter 2 is utilized to solve the radiative transfer equation into the channel. To ensure the local thermal equilibrium, small size *SiC* particles are chosen ($r = 10 \text{ }\mu\text{m}$) at a volume fraction corresponding to a thin and a thick optical media. Under those conditions, the energy equation given in Eq. 6.18, as well as the mass conservation and state equations (Eqs. 6.19 and 6.20) must be solved. The boundary conditions are those shown in section 6.3.4. The schematic of the receiver may be seen at Fig. 6.1.

The effective thermo-physical properties of the gas-particle mixture can be evaluated using various formulas available in the literature. For dilute dispersions of solid particles in a continuous fluid, the solid-gas mixtures are expected to have thermo-physical properties that obey the effective medium theories developed by Maxwell and by Brinkman as a function of the base fluid properties and particle volume fraction. The formulas selected in the present study are as follows:

- Effective dynamic viscosity (Brinkman's model [2]):

$$\mu_e = \frac{\mu_f}{(1 - f_v)^{2.5}} \quad (6.83)$$

where f_v is the particle volumetric fraction

6.5. Radiative and convective heat transfer coupling

- Effective thermal conductivity (Maxwell's model [14]):

$$k_e = k_f \left(\frac{(2k_f + k_p) - 2f_v(k_f - k_p)}{(2k_f + k_p) + f_v(k_f - k_p)} \right) \quad (6.84)$$

- Heat thermal capacity (Xuan and Roetzel formula [20]):

$$(\rho C_p)_e = (1 - f_v)(\rho C_p)_f + f_v(\rho C_p)_p \quad (6.85)$$

- Thermal diffusivity:

$$a_e = \frac{k_e}{(\rho C_p)_e} \quad (6.86)$$

The thermo-physical properties of air are temperature-dependent while those of the particles are assumed constant. The air and *SiC* thermo-physical properties are presented in Table 6.9 for the inlet temperature.

Air properties		
Density (ρ_f)	0.6964	[kg/m ³]
Kinematic viscosity (ν)	38.79×10^{-6}	[m ² /s]
Thermal conductivity (k_f)	0.0407	[W/mK]
Thermal capacity ($C_{p,f}$)	1030	[J/kgK]
Prandtl number (Pr)	0.684	
<i>SiC</i> properties		
Density (ρ_s)	3210	[kg/m ³]
Thermal conductivity (k_s)	100	[W/mK]
Thermal capacity ($C_{p,s}$)	850	[J/kgK]

Table 6.9: Thermo-physical properties used in the simulations for the air and for the *SiC* at $T = 500$ K

The receiver conditions are presented in Table 6.10.

Geometry depth (D)	1	[m]
Geometry length (L)	1	[m]
Concentrated solar flux (q_0)	800	[kW/m ²]
Inlet temperature (T_{in})	500	[K]
Mass flow rate (\dot{m})	1	[kg/s]
External temperature (T_{amb})	300	[K]
Overall heat transfer coefficient (\bar{U})	16.7	[W/m ² K]
Particles size (r)	10	[μ m]
Wall reflectivity (ρ_w)	1	

Table 6.10: Conditions used in simulations of a SPR

Optically thin media

As a first case, a very low volume fraction is imposed ($f_v = 7.5 \times 10^{-7}$) to represent an optically thin medium. This volume fraction leads to spectral optical thicknesses around $\tau \approx 0.15$ in all the spectrum. Due to the material characteristics (*SiC*) the scattering is highly anisotropic in the forward direction since the asymmetry factor is close to $g \approx 0.8$. Since the particle volume fraction used here is very small, the thermo-physical properties of the mixture are almost those of the gas.

Even though the high incident solar radiation, the mixing-cup temperature increment is low $\Delta T \approx 100 \text{ K}$, because of the low optical thickness. Therefore, high radiative losses are expected. Moreover, due to the small increase in the mixing-cup temperature, the close-wall fluid ($T_{y=0}$) remains also at low temperatures, decreasing at the proximity of the inlet section, having a minimum at $x \approx 0.3$ and increasing after that. This behavior is due to the higher inlet temperature than the ambient temperature. The close-wall fluid temperature and the mixing-cup temperature variation are presented in Fig. 6.12.

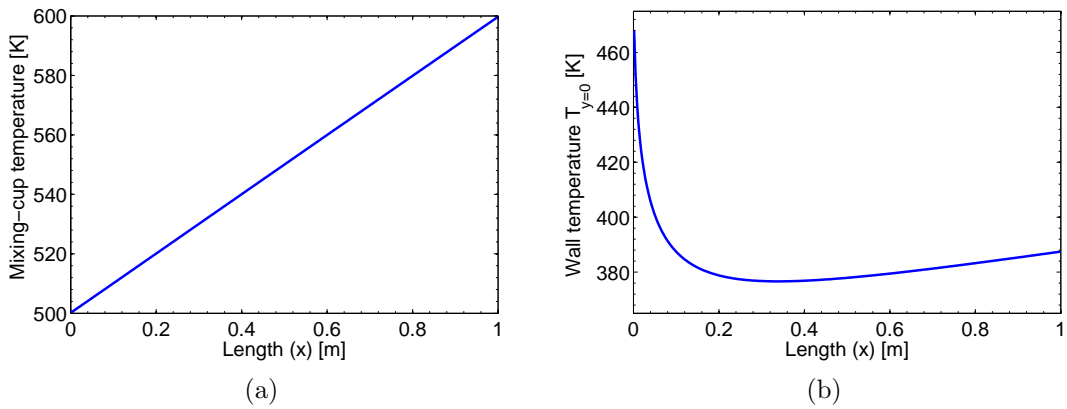


Figure 6.12: Mixing-cup (a) and wall (b) temperatures into the SPR model developed. A low volume fraction is imposed ($f_v = 7.5 \times 10^{-7}$) in order to represent an optically thin medium (see Tables 6.9 and 6.10 for the conditions)

The energy balance performed between the inlet and the outlet sections evidences that the radiative losses are the highest losses while the convective losses are small. In consequence, the receiver efficiency, defined as the ratio of the variation in flow enthalpy to the incident solar flux, is very low. These results are shown in Table 6.11.

Incident solar flux	800 kW/m
Convection losses	1.4 kW/m
Radiative losses	695.4 kW/m
Flow enthalpy increment	102.5 kW/m
Receiver efficiency	12.8 %

Table 6.11: Energy balance results for a SPR using a low volume fraction of particles (see Tables 6.9 and 6.10 for the conditions)

The divergence of the radiative heat does not experience large variations under the conditions used here. Therefore, the problem is similar to that of a fluid flow with an

6.5. Radiative and convective heat transfer coupling

uniform heat generation rate. The temperature profiles within the receiver are almost flat, but with a moderate temperature gradient close to the cooled wall. Maximal temperature differences of around $\Delta T \approx 210 \text{ K}$ are found between the window and the center-axis of the channel, and around $\Delta T \approx 50 \text{ K}$ between the center-axis of the channel and the adiabatic wall. It suggests that for these conditions (optically thin media) the strategy used to treat the density variation is valid. Figure 6.13 displays those results.

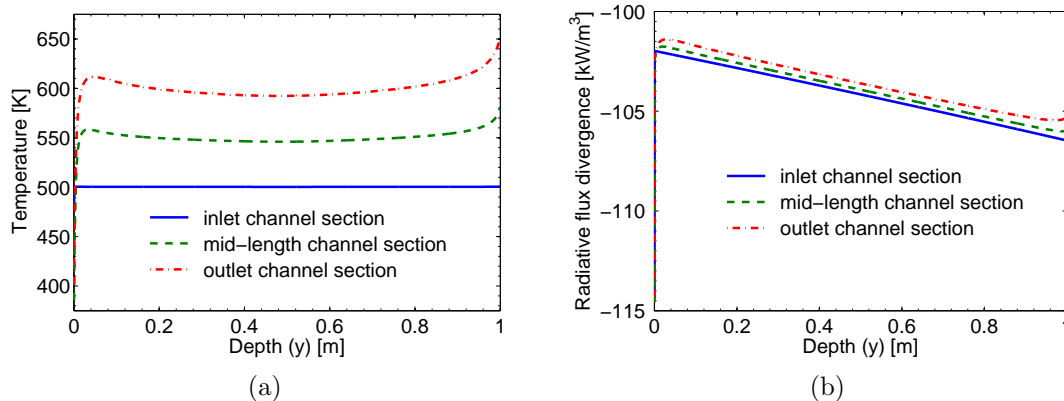


Figure 6.13: Temperature profiles and radiative heat divergence at three sections along the channel filled by an optically thin medium (see Tables 6.9 and 6.10 for the conditions)

Optically thick media

For the second case, a higher volume fraction is imposed ($f_v = 2.5 \times 10^{-5}$) in order to represent an optically thick medium. This case will permit to investigate if the model behaves correctly at high optical thicknesses. For such a volume fraction, the optical thickness is $\tau \approx 4.2$, while the asymmetry factor remains as in the last case ($g \approx 0.8$). The increment of the mixing-cup temperature is higher ($\Delta T \approx 700 \text{ K}$), approaching the temperatures expected in a high temperature SPR. However, the close-wall temperatures are also higher, close to the maximum temperature allowed for a window glass ($T_w = 840 \text{ K}$ at the outlet). It suggests that for this SPR configuration the front of the receiver needs to be cooled. The mixing-cup and the close-wall temperatures are shown in Fig. 6.14.

In contrast with the optically thin case, the radiative losses are smaller, and the flow enthalpy increase is higher, resulting in a high receiver efficiency. The convective losses are small in comparison with the other quantities. These results are reported in Table 6.12.

In this case the divergence of the radiative heat flux is highly variable, both along the x - and y -coordinates. The high temperature variations (emission) are the main responsible for the behavior of $\nabla \cdot \vec{q}_r$. The temperature gradient in the y -direction is small, even though the large temperature gradient in the x -direction, except close to the wall, where the temperature change may be around $\Delta T \approx 500 \text{ K}$. For instance, for the outlet temperature profile, $T = 850 \text{ K}$ at $y = 0$ (minimum temperature),

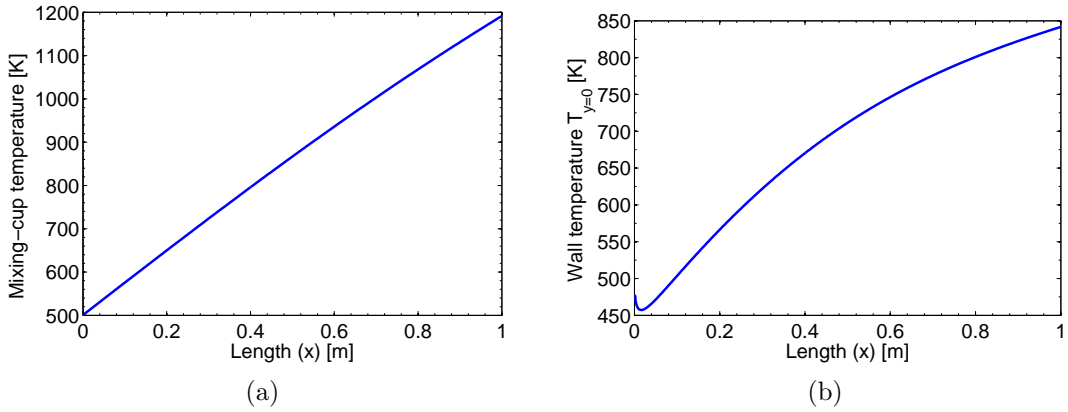


Figure 6.14: Mixing-cup (a) and wall (b) temperatures into the SPR. The volume fraction imposed is high ($f_v = 2.5 \times 10^{-5}$) to represent a thick medium (see Tables 6.9 and 6.10 for the conditions)

Incident solar flux	800 kW/m
Convection losses	6.5 kW/m
Radiative losses	81.2 kW/m
Flow enthalpy increment	711.8 kW/m
Receiver efficiency	89 %

Table 6.12: Energy balance results for a SPR using a high volume fraction of particles (see Tables 6.9 and 6.10 for the conditions)

$T = 1430 K$ at $y = 0.025D$ (maximum temperature) and $T = 1071 K$ at $y = 0.75D$ (second minimum temperature). The large temperature gradients close to the walls, especially close to the cooled wall, may lead to significant inaccuracies owing to the averaged treatment of the density in the proposed model. It suggests that the results of the model should be carefully interpreted at large optical thickness. Figure 6.15 shows the temperature profile and the divergence of the radiative heat flux divergence at three positions along the SPR channel.

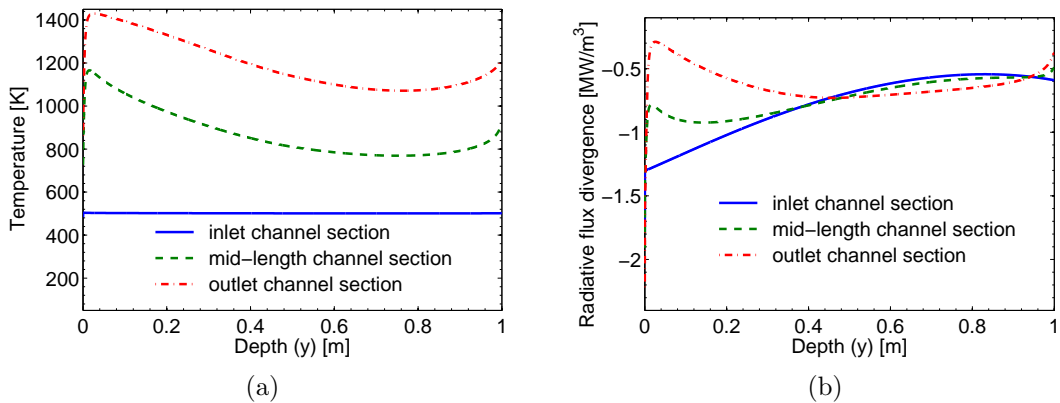


Figure 6.15: Profiles of the temperature and of the radiative heat flux divergence at three sections along the channel filled by an optically thick medium (see Tables 6.9 and 6.10 for the conditions)

6.6 Parametric study of a SPR with a radiative and convective coupling model

The coupled radiative and convective SPR model is used here to study the influence of a number of parameters on the SPR efficiency. Thus, the particle material, the number of particles and the reflectivity of the back wall are allowed to vary. In the simulations that follow, a gas-particles mixture, composed of air and a variety of particles, enters at a pre-heated temperature $T_{in} = 500 \text{ K}$. The fluid flow is submitted to an incident concentrated solar flux of $q_0 = 800 \text{ kW/m}^2$, as in high temperature CSP plants [18]. The losses due to the light reflection and transmission through the window, external wind and other losses have been excluded of the simulations. This approach is relevant since the main interest in this work is the radiative optimization inside the receiver. In further works, these losses should be considered.

The receiver efficiency is then used as the indicator to compare the receiver behavior under different conditions. It relates the enthalpy increment of the fluid with the incident solar flux as

$$\eta = \frac{\dot{m}C_p(T_{m,out} - T_{m,in})}{q_0L} \quad (6.87)$$

where the depth of the receiver is considered as 1 m .

The mass flow rate and the size of the particle are imposed constant for all simulations. This mass flow rate is high enough to ensure a turbulent flow (Reynolds number at the inlet $Re = 7.4 \times 10^4$). The small size of the particles ($r = 10 \mu m$) ensures that they are entrained into the fluid flow and that the temperature gradient between the center and the surface of the particles is low enough to consider thermal local equilibrium between the gas and the particles. Under those conditions, the energy equation given in Eq. 6.18, as well as the mass conservation and state equations (Eqs. 6.19 and 6.20) must be solved. The boundary conditions are those given in section 6.3.4. The receiver conditions are presented in Table 6.13.

Geometry ($D \times L$)	1 × 1	m
Concentrated solar flux (q_0)	800	kW/m^2
Inlet temperature (T_{in})	500	K
Mass flow rate (\dot{m})	1	kg/s
External temperature (T_{amb})	300	K
Overall heat transfer coefficient (\bar{U})	16.7	$\text{W/m}^2\text{K}$
Particles size (r)	10	μm

Table 6.13: Conditions used in simulations of a SPR

Since the presence of the particles in the mixture varies the thermal conductivity and the dynamic viscosity only slightly, these thermo-physical properties are taken as those of the air. Nevertheless, the density of the mixture is computed following the Xuan and Roetzel model (Eq. 6.84). The code assumes that the thermo-physical properties of the air change with the temperature and remain constant for the solid. The thermo-physical properties of the air at the inlet temperature, as well as the densities at room temperature of the solid materials used in the simulations are presented in Table 6.14.

For the ideal material and for the W coated with SiC , their densities are taken as those of SiC and W , respectively.

Inlet air properties ($T_{in} = 500 K$)		
Density (ρ_f)	0.6964	kg/m^3
Kinematic viscosity (ν_f)	38.79×10^{-6}	m^2/s
Conductivity (k_f)	0.0407	W/mK
Thermal capacity ($C_{p,f}$)	1030	J/kgK
Prandtl number (Pr)	0.684	

Solid densities		
SiC density (ρ_s)	3160	$[kg/m^3]$
W density (ρ_s)	19300	$[kg/m^3]$
HfC density (ρ_s)	12200	$[kg/m^3]$

Table 6.14: Thermo-physical properties used in the simulations for the air at $T = 500 K$ and densities for the solids

6.6.1 Influence of the back wall reflectivity and the volume fraction

The influence of the reflectivity of the back wall as well as the volume fraction on the receiver efficiency is studied in this section. Hence, the receiver efficiency is computed for two back wall reflectivity ($\rho_w = 1$ and $\rho_w = 0.2$) at several volume fractions. The first case ($\rho_w = 1$) leads to a theoretical case where the particles are the only responsible of the absorption, while the second one ($\rho_w = 0.2$) leads to a more realistic case where the wall absorbs and emits energy. In addition, the volume fraction is varied from small to high values in order to represent thin, medium and thick optical thicknesses. It will permit to identify the volume fraction regions where the radiative losses are minimized, hence, the receiver efficiency maximized.

Since the back wall is insulated, the model works when the reflectivity of the wall is $\rho_w = 1$ (i.e. the wall does not absorb energy, hence $T_{f,N} = T_w$). Obviously, real materials used for the walls in high temperature SPRs have reflectivity lower than this value. In practice, the effect of a low reflectivity at the wall is the increment of the wall temperature, having as consequence energy emission by the wall and convective transfer from the wall to the fluid. This temperature must be computed from an energy balance at the wall. Supposing the wall as a gray surface and maintaining the isolation from the wall to the solid, it reads

$$\alpha_w(q_c + q^+) \Big|_{y=D} - \varepsilon_w \sigma_{SB} T_w^4 - k_f \frac{dT}{dy} \Big|_{y=D} = 0 \quad (6.88)$$

where α_w and ε_w are the absorptivity and the emissivity of the wall, respectively. Then, T_w is set as a new boundary condition $T_{y=D} = T_w$.

Evaluating Eq. 6.88 numerically at the last y -cell (N cell) and applying the Kirchoff's law, it reads

$$\frac{\Delta y_N (1 - \rho_w)}{2k_{f,N}} \sigma_{SB} T_w^4 - T_w - \frac{\Delta y_N (1 - \rho_w)}{2k_{f,N}} (q_{c,N} + q_N^+) + T_{f,N} = 0 \quad (6.89)$$

6.6. Parametric study of a SPR with a radiative and convective coupling model

If $T_{f,N}$ is known, equation 6.89 may be solved using a numerical method adapted to find the roots of a real-valued function, as the Newton-Raphson method. However, since $T_{f,N}$ depends on the boundary condition (T_w) the coupled temperatures must be solved iteratively.

In order to be general in this analysis, the optimized ideal material presented in chapter 4 is used. Moreover, due to the extinction coefficient varies with the wavelength, the main optical thickness is computed as $\tau = D \int_0^\infty \beta_\lambda I_{0,\lambda} d\lambda / \int_0^\infty I_{0,\lambda} d\lambda$. The main optical thickness is then used to present the results. No big error is made by using this approximation since for all materials used in this work, the variation of the volume extinction coefficient with the wavelength is small. To illustrate that, the volume absorption and scattering coefficients for a volume fraction of $f_v = 2.5 \times 10^{-5}$ and using the optimized ideal material are plotted in Fig 6.16.

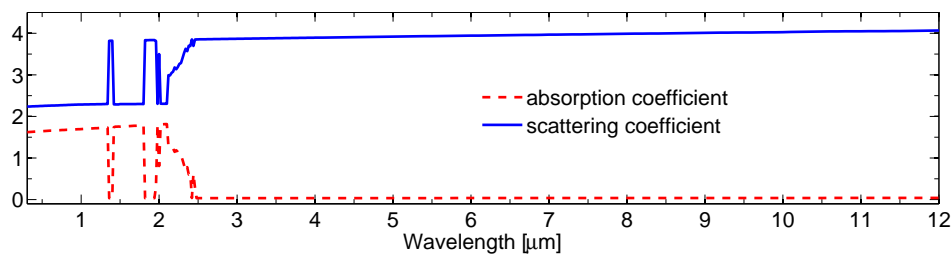


Figure 6.16: Absorption and scattering coefficients for a homogeneous medium composed by a gas-particles mixture. The particles material is the optimized ideal one (see chapter 4) and the volume fraction is $f_v = 2.5 \times 10^{-5}$

Results of the simulations show that at low volume fractions (thin optical thickness), the radiative flux that reach the back wall ($q_c + q^+$) is very high. In consequence, the maximum temperature is placed close to the back wall. In such a case, for a high wall reflectivity, the radiative flux is reflected and it goes out with few interactions with the particles, while for a low wall reflectivity, the back wall absorbs high amounts of energy, increasing its temperature, and consequently emitting high amounts of energy. In both cases, it leads to high radiative losses and therefore low receiver efficiencies.

Otherwise, at high volume fractions (thick optical thickness) the energy absorption occurs mainly close to the window and low amounts of energy pass through the particles slab. The radiative flux that reaches the back wall is low and the maximum temperature is placed close to the window. As a result, the wall reflectivity has low influence on the radiative losses. Figure 6.17 shows a comparison between the outlet temperatures when a number of volume fraction values are used for both wall reflectivity ($\rho_w = 1$ and $\rho_w = 0.2$).

As expected, the back wall temperature is higher when the reflectivity is lower (see Fig. 6.17b). This fact implies a slight change in the temperature profile, due to the convection at the back wall and the inclusion of the emission from the wall. Since the ideal material is selective, lower efficiencies are expected for lower wall reflectivity. Moreover, considering that the temperature profile strongly changes its shape, increasing the temperature close to the window when the optical thickness is greater than

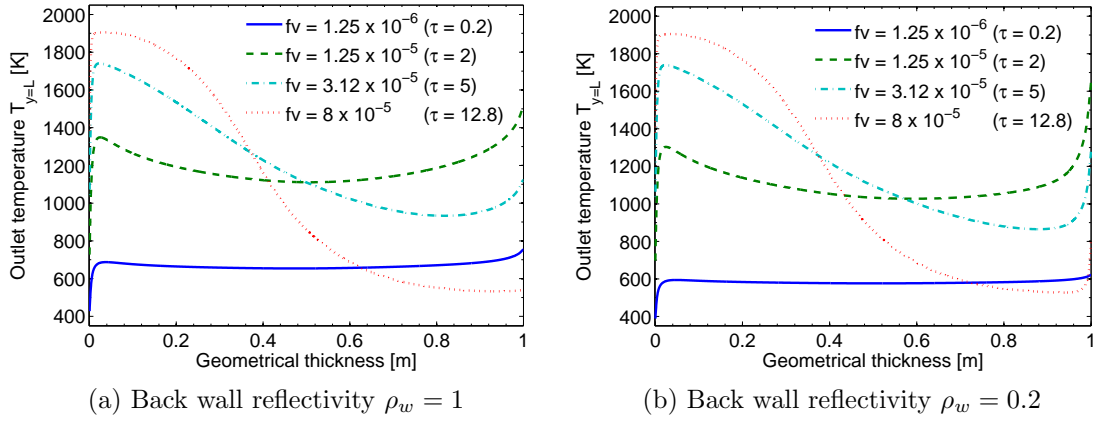


Figure 6.17: Outlet temperature profiles for a SPR at multiple volume fractions and at two back wall reflectivities. The material used is the optimized ideal one (see Tables 6.13 and 6.14 for the conditions and the set of parameters)

$\tau > 2$, it is also expected that an optimum volume fraction that maximizes the receiver efficiency exists.

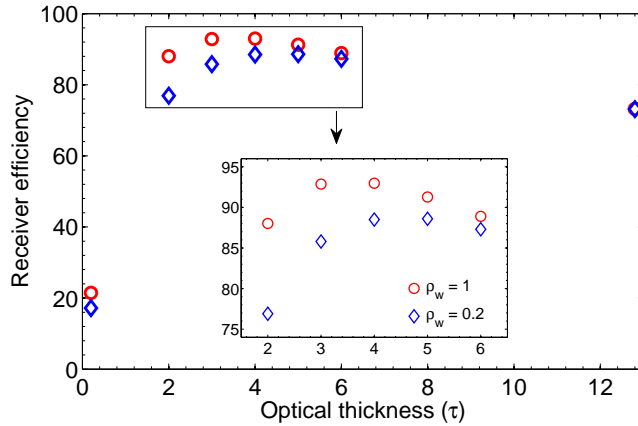


Figure 6.18: Receiver efficiencies at multiple volume fractions for two back wall reflectivity. The material used is the optimized ideal one (see Tables 6.13 and 6.14 for the conditions and the set of parameters)

Fig. 6.18 shows the receiver efficiency computed for several volume fractions and for the two wall reflectivity considered. This figure shows that a maximum receiver efficiency is achieved at optical thicknesses in the $\tau = 3-5$ region. Furthermore, in this region the variation of the wall reflectivity may be responsible of the receiver efficiency variations up to 11% (at $\tau = 3$ $\eta = 88.0\%$ when $\rho_w = 1$ and $\eta = 76.9\%$ when $\rho_w = 0.2$). Note that the optimum optical thickness obtained in this section ($\tau \approx 4$) is lower than that obtained in the optimization chapter when using a constant temperature ($\tau \approx 7$). It is due to the increment of the volume fraction in the actual model (more realistic) that increases the maximum temperature close to the wall, and the radiative losses.

To show the influence of the back wall reflectivity and the volume fraction on the convective and radiative losses, an energy balance is carried out. It is given for three

6.6. Parametric study of a SPR with a radiative and convective coupling model

volume fractions close to the optimal ($\tau = 3 - 5$). This balance is presented in Table 6.15.

		$\tau = 3$	$\tau = 4$	$\tau = 5$
$\rho_w = 1$	q_{conv}	5.9	7.2	8.5
	RL	51.4	49.1	61.4
	$\dot{m}C_p(T_{m,out} - T_{m,in})$	742.7	743.7	730.1
	η	92.8	93.0	91.3
$\rho_w = 0.2$	q_{conv}	5.8	7.2	8.5
	RL	107.6	84.7	82.7
	$\dot{m}C_p(T_{m,out} - T_{m,in})$	686.6	708.1	708.8
	η	85.8	88.5	88.6

Table 6.15: Energy balance for the SPR using an optimized ideal material and three volume fractions (see Tables 6.13 and 6.14 for the conditions and the set of parameters)

The convective losses are the lowest losses in all cases, being about 0.5 – 1% of the incident solar flux. These losses are slightly influenced by the back wall reflectivity, because similar temperatures are reached for both cases close to the window. Nevertheless, the radiative losses are different for the two wall reflectivities. For a high wall reflectivity ($\rho_w = 1$), due to the selectivity behavior of the ideal material, the solar flux is absorbed in the forward and in the backward direction. It increases the temperature of the particles (high absorption in the solar region) and reduces the radiative losses (low emission in the IR region). Again, because of the selective behavior of the ideal material, for a low wall reflectivity ($\rho_w = 0.2$), the energy emitted by the wall is not well absorbed by the particles. A big amount of the energy emitted by the wall then go out without being absorbed. In conclusion, to increase the SPR efficiency when a selective material is used, the back wall reflectivity should be as high as possible.

6.6.2 Influence of the particles material

To investigate the influence of the particles material on the SPR efficiency, some of the available material studied before are chosen. Particles of silicon carbide (SiC), tungsten (W), hafnium carbide (HfC) and tungsten coated with silicon carbide (W coated by SiC) are used. The results are compared with the result obtained using the optimized ideal material. The others UHTCs used in chapter 5 were dismissed in this study, owing to the similar behavior with the HfC . For the coated particles a mantle of 50 nm is used, as suggested in chapter 5. Due to that for a selective material, the best back wall reflectivity is the highest possible and taking into account that real materials have reflectivity lower than one, a back wall reflectivity of $\rho_w = 0.8$ is employed. Moreover, the volume fraction used is the one corresponding to an optical thickness of $\tau = 4$. This optical thickness is close to the optimal one found for all the materials used. These parameters are presented in Table 6.15. The other conditions are the same to those given in Table 6.13 as well as the thermo-physical properties of the air and the solids which are given in Table 6.14.

The temperature profiles at the outlet section are computed to show the differences of using materials with different optical properties. They are presented in Fig. 6.19.

Wall reflectivity (ρ_w)	0.8
Optical thickness (τ)	4.0

Table 6.16: Wall reflectivity and optical thickness employed in the parametric study using several real materials

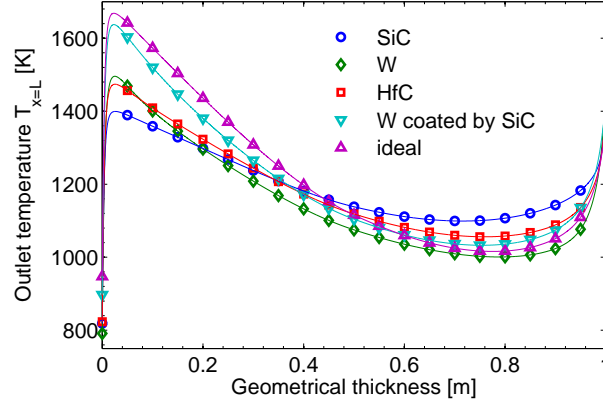


Figure 6.19: Outlet temperature profiles for the SPR using several materials. The SPR conditions, and the parameters used in simulation are given in Tables 6.13, 6.14 and 6.16

From Fig. 6.19, selective materials present the highest temperature differences in the outlet y -section, while non selective materials, have lower temperature differences at this section. For instance, for the ideal material a temperature gradient $\Delta T = 650 K$ (the maximum and minimum temperature are located at $y = 0.02 m$ and $y = 0.8 m$, respectively) and for the *SiC* the temperature gradient is $\Delta T = 300 K$ (the maximum and minimum temperature are located at $y = 0.02 m$ and $y = 0.7 m$, respectively). For all materials, the maximum temperature is located close to the window, being higher for selective materials. Note that even if the *W* and the *HfC* have close selective behaviors, the window temperature is the lowest between the analyzed materials, due to their poor absorptivity in the solar region. To compare the performances of the different materials, the energy balance is presented in Table 6.17. The performances for the optimized ideal material is included.

	ideal	<i>SiC</i>	<i>W</i>	<i>HfC</i>	<i>W</i> coated by <i>SiC</i>
$T_{m,x=L}$	1211.0	1193.0	1143.4	1182.2	1197.4
q_{conv}	7.1	6.0	5.3	5.9	6.5
RL	59.5	79.0	130.8	90.3	74
$\dot{m}C_p(T_{m,out} - T_{m,in})$	733.4	715.0	663.9	703.8	719.5
η	91.7	89.4	83	88.0	89.9

Table 6.17: Mixing-cup temperature at the outlet section and energy balance for the SPR using several materials and the optimized ideal one (see Tables 6.13, 6.14 and 6.16 for the conditions and the set of parameters)

In volumetric receivers, it is suitable that the temperature profile will be as flat as possible and with low temperatures located close to the window in order to reduce the

6.7. Conclusions

radiative losses. Here, even if selective materials achieve higher temperatures close to the window, they have better receiver efficiencies. It is due to this kind of materials have low emissivity in the $\lambda > 2.5 \mu\text{m}$ region. It implies also higher convective losses, but they are less than 1% of the incident solar flux ($q_0 = 800 \text{ kW/m}^2$). The enthalpy flow balance is also higher for selective materials, achieving higher mixing cup temperatures (for example $T_{m,x=L} = 1211 \text{ K}$ for the ideal material and $T_{m,x=L} = 1197 \text{ K}$ for the W coated by SiC).

Nevertheless, non-selective materials with high absorptivity as the SiC , have also low radiative losses. In this case, the particles absorb high amounts of energy in the solar region and emit also high amounts of energy in the IR region, cooling the particles in comparison with selective materials. It implies that the transport of radiative energy to deeper SPR regions is better. It may be shown in Fig. 6.20. The divergence of the radiative flux for the SiC case is flatter than for selective materials (as the ideal or the W coated by SiC), with lower values close to the window.

Slight selective materials, as the W and the HfC , have the highest radiative losses, hence the lowest receiver efficiencies indeed. The low absorptivity of these materials in the $0.2 - 2.5 \mu\text{m}$ spectral region is the responsible of this bad behavior, increasing the reflected losses component. Besides the convective losses are the lowest.

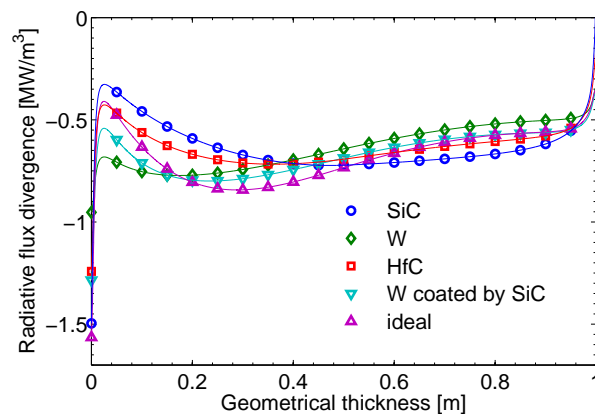


Figure 6.20: Radiative flux divergences for the SPR using several materials. The SPR conditions, and the parameters used in simulation are given in Tables 6.13, 6.14 and 6.16

6.7 Conclusions

The study of the coupling between the convection and radiation into a high temperature SPR is started in this chapter. For that, a novel configuration of receiver is proposed on the aim to simplifies the solution. Due to the nature of the problem a low-Mach model is used. To avoid solving the momentum equation the consideration that the density varies only in the x -direction is adopted. A code that solve the mass conservation, energy and state equations is developed for the proposed configuration. This code uses a control volume method to solve numerically the model using a non-uniform meshing. A validation is carried out for the developed code by comparing their results

with some known analytical and numerical results. Good agreement is found in those comparisons, given high confidence on the code behavior. A preliminary simulation is carried out to investigate the behavior of the model. For that a thin and a thick optical medium in the SPR are considered.

Next, a parametric study was conducted to investigate the influence of the back wall reflectivity, the volume fraction and the particle material. The other parameters (i.e. mass flow rate, particle radius, SPR geometry, etc.) were imposed to be constant. The receiver efficiency defined as the ratio of the enthalpy flow increment over the incident solar radiation is used as a comparative parameter.

Since the independent scattering hypothesis is used and the geometry is taken constant, the optical thickness varies only with the volume fraction, for a given material. Then, in this section the medium was varied from thin to thick optical thickness by varying the volume fraction. This parameter drives the energy absorption as well as the shape of the temperature profile inside the receiver. Indeed, an optimal optical thickness that maximizes the receiver efficiency exists. For the materials studied here, this optimal optical thickness is placed around $\tau \approx 4$. When small optical thicknesses are used, the particles does not absorb all the incident energy and the receiver efficiency is low. Thus, the temperatures inside remains low, but with an almost flat shape with a maximum close to the back wall. In contrast, with high optical thicknesses, all incident energy is absorbed increasing the medium temperature, but, increasing also the energy emission. At higher volume fractions, higher temperatures are achieved close to the window, increasing the radiative losses by emission.

Concerning the reflectivity of the back wall, for thick optical thicknesses slight influence on the receiver efficiency is found. In contrast, at thin and moderate optical thicknesses, differences until 11% in the receiver losses are found when the wall reflectivity change from $\rho_w = 1$ to $\rho_w = 0.2$. This influence is more important when the particles material used is selective. If ρ_w is small, the emission by the wall is important in the IR spectral region, where the particles have low absorptivity. Therefore, it is recommendable to use high back wall reflectivity when the particles are made of selective materials.

A number of materials (*SiC*, *W*, *HfC*, *W* coated by *SiC* and the optimized ideal) are then used in the SPR model with $\rho_w = 0.8$ and $\tau = 4$. Even though higher temperatures are reached close to the window with selective materials (i.e. ideal and *W* coated by *SiC*), they have higher receiver efficiencies. For this kind of materials the shape of the temperature profile is far to be flat reaching temperature gradients up to $\Delta T = 650 K$. In contrast, materials with high absorptivity in all the spectrum of interest (i. e. *SiC*) transport better the energy to deeper SPR regions, resulting in temperature profiles flatter than selective materials.

Finally, a perspective of this work is the improvement of the SPR model. Two main sources of errors are identified: the first concerns to the use of a 1D model, which neglects the radiative transfer in the x direction. The second one concerns to the imposition of a symmetric velocity profile along the receiver. Both phenomena directly influence on the temperature profiles and consequently in the receiver efficiency. Other perspective are the study of the use of a non-gray material in the back wall, as well as the use of a non-homogeneous volume fraction that increase with the depth. It will permit to have lower temperatures close to the window, reducing the emission losses.

References

- [1] A. Bejan. *Convection Heat Transfer*. Jhon Wiley & Sons, third edition, 2004.
- [2] H.C. Brinkman. The viscosity of concentrated suspensions and solutions. *Journal of Chemical Physics*, 20:571–581, 1952.
- [3] S. Chandrasekhar. *Radiative Transfer*. Dover Publication, 1960.
- [4] A. Crocker and F. Miller. Fluid flow and radiation modeling of a cylindrical small particle solar receiver. In *SolarPaces: Concentrating Solar Power and Chemical Energy Systems, Granada - Spain*, September 2011.
- [5] L. da Silva, P. Dias, M. Carvalho, and C. Cabral. Theoretical analysis of the channel flow with radiation in participating media through the use of the generalized integral transform technique. In *18th International Congress of Mechanical Engineering. Ouro Preto - Brasil*, 2005.
- [6] X. Daguene-Frick, A. Toutant, F. Bataille, and G. Olalde. Numerical investigation of a ceramic high-temperature pressurized-air solar receiver. *Solar Energy*, 90:164–178, 2013.
- [7] A. Hunt and F. Miller. Small particle heat exchanger receivers for solar thermal power. In *SolarPaces: Concentrating Solar Power and Chemical Energy Systems, Perpignan-France*, September 2010.
- [8] J.H. Joseph, W.J. Wiscombe, and J.A. Weinman. The delta-Eddington approximation for radiative flux transfer. *Journal of the Atmospheric Sciences*, 33:2452–2459, 1976.
- [9] H. Klein, J. Karni, R. Ben-Zvi, and R. Bertocchi. Heat transfer in a directly solar receiver/reactor for solid-gas reactions. *Solar Energy*, 81:1227–1239, 2007.
- [10] G. Lauriat. *Transferts de chaleur et de matière, convection interne, Master SM-M1*, chapter 7, pages 188–192. UPEM, 2014.
- [11] C. Lii and M. Özişik. Heat transfer in an absorbing, emitting and scattering slug flow between parallel plates. *Journal of Heat Transfer*, 95:538–540, 1973.
- [12] A. Malhotra and S.S. Kang. Turbulent Prandtl number in circular pipes. *International Journal of Heat and Mass Transfer*, 27:2158–2161, 1984.
- [13] J. Martin and J. Vitko. ASCUAS: a solar central receiver utilizing a solid thermal carrier. Technical report, Sandia National Laboratories, 1982.
- [14] J. Maxwell. *A treatise on Electricity and Magnetism*. Oxford University Press, 1904.
- [15] M. Modest. *Radiative Heat Transfer*. Academic Press, second edition, 2003.

- [16] P.K. Sarma, K. Chada, V. Dharma, P.S. Kishore, T. Subrahmanyam, and A.E. Bergles. Evaluation of momentum and thermal eddy diffusivities for turbulent flow in tubes. *International Journal of Heat and Mass Transfer*, 53:1237–1242, 2010.
- [17] S. Serra. *Couplage écoulements pariétaux et transferts thermiques dans les récepteurs solaires à haute température*. PhD thesis, Université de Perpignan Via Domitia, 2009.
- [18] A. Steinfeld and R. Palumbo. *Solar Thermochemical Process Technology*, chapter Encyclopedia of Physical Science and Technology, pages 237–256. R.A. Meyers Ed., 2001.
- [19] R. Viskanta. Heat transfer in a radiating fluid with slug flow in a parallel-plate channel. *Applied Scientific Research*, 13:291–311, 1964.
- [20] Y. Xuan and W. Roetzel. Conceptions for heat transfer correlation of nanofluids. *International Journal of Heat and Mass Transfer*, 43:3701–3707, 2000.

Chapter 7

General conclusions

In order to increase the global efficiency of the Concentrated Solar Power (CSP) plants, the performances of the receiver need to be optimized. A number of advances were recently reported on this subject, such as the use of volumetric receivers or the increases in the heat transfer performances of the surface receivers. Among these advances, Solar Particle Receivers (SPRs) are promising candidates to work at high temperatures ($T > 1100\text{ K}$). They will permit to use high efficient thermodynamic cycles, such as a combined cycle (Brayton cycle + Rankine cycle). Nevertheless, the influence of the different parameters involved in the various heat transfer modes remains to be better known. The optimization of these parameters is one of the procedures required for increasing a receiver efficiency.

To this end, a radiative model for a high temperature SPR is developed in this work. The SPR model consists in a $1D$ gas-particles mixture slab submitted to a concentrated and collimated solar flux. The slab is composed of multiple homogeneous layers with different radiative properties. It permits to treat non-homogeneities into the receiver, such as non-uniform temperature fields. The Radiative Transfer Equation (RTE) is solved with a two-stream method using a delta-Eddington approximation. This approximation is chosen owing to its relevant treatment of high anisotropies in the scattering as well as the media emission. The single-particle radiative properties are computed with the Lorenz-Mie theory, assuming a spherical shape of the particles. Due to the low amount of particles needed in this kind of receivers, the volume radiative properties are calculated following an independent scattering consideration. Owing to the simplifications considered in this model, it is well suited to the use in large numerical investigations, as the optimization proposed in this work. The accuracy of the two-stream method is investigated by comparing several results with a high accurate Monte Carlo method. At this stage, two approximations based in the delta-Eddington approximation for the two-stream method are tested: the Meador and Weaver approximation and the Joseph et al. approximation. In the case of the Meador and Weaver approximation, an important drawback is the non-physical solutions found for the slab emission when the scattering is highly anisotropic. For that reason, the Joseph et al. approximation is kept for the radiative modeling. Absolute errors less than 2% are found when this method is compared with the Monte Carlo method for the optimal conditions in a SPR.

The developed model is used to investigate the effect of adopting the concept of equivalent particle radius in a mono-dispersion instead a particle poly-dispersion. No noticeable influence on the radiative losses is found by using this concept. This result permits to work with particle mono-dispersion in the next SPRs simulations. A first optimization is carried out by using a Particle Swarm Optimization (PSO) algorithm to find the best particle radius, volume fraction and spectral complex refractive index combinations that minimize the radiative losses in a SPR. Results suggest that there exists a small particle radius ($\sim 1 \mu m$) that minimizes the radiative losses. It is because a cut-off wavelength appears in the single-particle absorption efficiency, close to the ideal cut-off wavelength given for a selective material. Smaller particle sizes locates this cut-off wavelength in the ultraviolet region, leading to low efficiency for light absorption in the visible region.

Large particles do not present a selective absorption property due to their size. However, for a material with a selective behavior due to its optical properties, it is possible to predict similar receiver radiative losses provided that the volume fraction is appropriate. Concerning the optimal ideal refractive index, the real part should take the lowest possible value, and the imaginary part should vary from ~ 0.1 in the $0.2 - 1.4 \mu m$ region to the highest possible value in the $> 2.5 \mu m$ region. This combination of the real and imaginary parts permits to distinguish a selective behavior composed of three spectral regions: a high absorptive region [$0.2 - 1.4 \mu m$], a transition region [$1.4 - 2.5 \mu m$] and a high reflective region [$> 2.5 \mu m$]. This composition leads to absorb most of the solar incident energy in the first region, to have the best emission-absorption balance in the transition region and avoid losses by emission in the third region.

Another theoretical solution yielding a non-emitting media in the third region is to lower the k -values to $k = 0$. It implies a transparent material in this region that does not emit at all. Crystals are representative solid materials with $k = 0$, while metals achieve high k -values. Besides, the k -values for ceramic materials tend to be greater than 0.1 for large wavelengths ($\lambda > 4 \mu m$). The choice of working with a highly reflective material is made to include ceramic materials and metals, which have been reported as good candidates to work in high temperature SPRs. A second optimization in a slab composed of two layers is conducted to investigate if the use of two different ideal materials reduces more the radiative losses than the use of a single selective material. No appreciable reductions are found by using two layers, the optimized materials are indeed found to behave similarly as the selective one.

Since an almost ideal optimal behavior is desirable by using real materials, six materials are studied as possible candidates to be used in SPRs: *SiC*, *W*, *ZrC*, *ZrB₂*, *HfC* and *HfB₂*. They are suggested as selective materials for high temperature solar receivers. At this point, a serious inconvenient is the lack of information on the refractive index of these materials (except for the *SiC* and *W* that are well known). The Kramers-Kronig dispersion relations are thus used to find their refractive indexes from published reflectance data. Since the reflectance data are not available for very well

polished samples, the results are only indicative.

Three receiver configurations are considered: a) a homogeneous slab with only one material, b) a slab with a two materials mixture and c) a homogeneous slab with coated particles. For the first configuration, results confirm that the best particle size is around $r \sim 1 \mu m$ for all materials. A noticeable finding is that the W , ZrC , ZrB_2 , HfC and HfB_2 lead to radiative losses close to their corresponding best one (when $r \sim 1 \mu m$), even if the particle size increases. That is due to the selective behavior of these materials. This fact will permit to work with larger particles with a small increase in the radiative losses provided that the materials are selective. Nevertheless, the selectivity of the above materials is not highly significant because their absorptivities in the solar region are in the medium range. The consequence is that the SiC is the material having the lowest radiative losses. It follows that other strategies or other materials need to be investigated. For the second configuration, any noticeable reduction in the radiative losses are found for each two-material mixture. The radiative losses follow a quasi-linear behavior between the extreme cases of only one material. For the third configuration, the SiC is used as a mantle and the other materials as the core of coated particles. A remarkable reduction of the radiative losses is found when the mantle have a thickness of around $\sim 50 nm$, without regard to the core size.

The radiative losses found under these conditions are close to those found by using an ideal material. The best combination corresponds to particles of W -core and SiC -mantle. These results suggest important reductions in the radiative losses by using coated particles.

Since the radiative losses depend on the temperature distribution into the receiver, a temperature profile with the lowest temperatures at the front of the receiver is convenient to reduce the slab emission. This effect is called volumetric effect and it is mainly driven by the fluid flow coupled with the radiative heat transfer. Therefore, it is highly influenced by the geometry utilized. To study the coupling between convection and radiation heat transfer, a simplified configuration of the receiver is suggested with the aim at finding preliminary results. The model considers a gas-particle turbulent flow between two parallel plates, one of the plate being the receiver window submitted to a collimated and concentrated solar flux. Due to the size of the particles, the gas-particle mixture is considered to be in local thermal equilibrium. Moreover, the small volume fractions used for this application permit to approximate the thermal properties of the gas-particle mixture as the thermal properties of the gas. Exception made for the density that is strongly influenced by the solid density. The relation proposed by Xuan and Roetzel is used to this end. The energy equation is solved using a low-Mach approximation together with analytical expressions for the velocity profile and thermal eddy diffusivity. The radiative heat dissipated into the fluid is calculated by using the two-stream model developed previously. A parametric study is conducted with this model with the aim at showing the influence of the optical parameters (wall reflectivity, volume fraction and the particle material) on the receiver losses. Results show that an optimal volume fraction exist that maximizes the receiver efficiency. Optical thickness close to $\tau \approx 4$ is the best for all materials studied. Concerning to the wall reflectivity, for thick optical thicknesses the influence is slight, contrarily at thin and

moderate optical thicknesses difference until 11% are found, when the wall reflectivity varies from $\rho_w = 0.2$ to $\rho_w = 1$. Selective materials achieve higher temperatures close to the window, however the radiative losses remain lower than gray materials. But, gray materials transport better the energy to deeper receiver regions, which has a consequence temperature profiles flatter.

Regarding the perspectives of this work, even if the radiative model developed here is a helpful tool to investigate the optimal radiative properties, its main drawback is that it is constrained to 1D problems, reducing its applicability for complex geometries. In future simulations, more accurate models should be implemented. For instance, the Monte Carlo method may be a valuable model to compute the radiative losses for appropriate SPR designs. Other simplifications, like the approximation of the phase function, need to be improved by the use of the Lorenz-Mie phase function. Since small particles were used in most of the simulations, a model that takes into account the influence of the particles agglomeration should be developed. Another important challenge for future works is to find materials, with selective behaviors and withstand thermal cycling and oxidation, that may be used in high temperature SPRs. This task is non trivial at all since the measurement of the refractive index is a very complicated matter. In this work, a computational code was developed to compute the refractive indexes using the Kramers-Kronig relations. Measured normal reflectivity reported in the literature were employed. Therefore, the measurements of the reflectivity of several new materials, candidates to be used in SPRs, should be undertaken.

Concerning the simplified flow model used in this work, it has allowed preliminary investigations of the interaction between radiative transfer and convection thanks to strong approximate formulations of the momentum and energy equations. Improved models should be employed in future works. First, the full system of conservation equations must be solved for large density variations due to temperature variations by introducing an improved turbulence model, leading to overcome the assumption of dynamically developed flows. Second, the homogeneous model should be revisited since the effects of non-uniform particle concentration on the convective heat transfer enhancement has been ignored. Instead of assuming that the particle move homogeneously with the fluid in presence of turbulent eddies, a transport model for a two-component mixture (gas + particles) including, for example, Brownian diffusion, thermophoresis, gravity, etc., should be considered in order to quantify the particle-fluid slip mechanisms according to the particle concentration and particle size. Finally, the geometry suggested should be improved in order to conceive an experimental SPR prototype.

Appendix A

The two-stream method approximation

A.1 The γ -terms in the Meador and Weaver two-stream approximation

The procedure to find the γ -terms involved in the simplified equations for the two-stream methods stated by Meador and Weaver is developed in this annexe. This procedure may be replicated for any approximation. Following the original paper, this procedure is conducted for a cold parallel problem. The emission terms included in the equations of the section 2.3 are omitted here. Meador and Weaver established that all two-stream methods satisfy simplified equations as

$$\frac{dq^+}{d\tau} = \gamma_1 q^+ - \gamma_2 q^- + q_0 \omega_0 \gamma_3 \exp\left(-\frac{\tau}{\mu_0}\right) \quad (\text{A.1})$$

$$\frac{dq^-}{d\tau} = \gamma_2 q^+ - \gamma_1 q^- - q_0 \omega_0 \gamma_4 \exp\left(-\frac{\tau}{\mu_0}\right) \quad (\text{A.2})$$

Equations A.1 and A.2 differ from those given in the original document, because a different geometry is used. In the present case, the main positive direction is the same as the incident flux, contrary to the original. Fig. A.1 repeats the representation of the geometry used here (similar to Fig. 2.3).

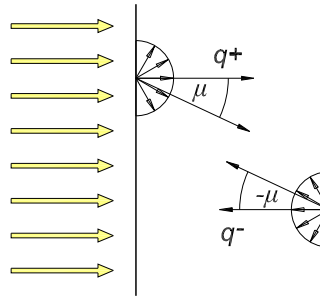


Figure A.1: Schematic of the plane parallel problem showing the positive and negative fluxes for the two-stream method

A.1. The γ -terms in the Meador and Weaver two-stream approximation

The two-stream method split the radiative flux into two parts: the positive flux that travels in the main path direction ($0 < \mu < 1$) and the negative flux that travels in the opposite direction ($-1 < \mu < 0$). The hemispheric integrals then are defined as

$$\frac{dq^+}{d\tau} = - \int_0^1 I(\tau, \mu) d\mu + \frac{1}{2} \int_0^1 \int_{-1}^{+1} p(\mu, \mu') I(\tau, \mu') d\mu' d\mu + \frac{1}{2} \int_0^1 p(-\mu, \mu_0) q_0 \exp\left(-\frac{\tau}{\mu_0}\right) d\mu \quad (\text{A.3})$$

$$\frac{dq^-}{d\tau} = \int_0^1 I(\tau, -\mu) d\mu - \frac{1}{2} \int_0^1 \int_{-1}^{+1} p(-\mu, \mu') I(\tau, \mu') d\mu' d\mu - \frac{1}{2} \int_0^1 p(\mu, \mu_0) q_0 \exp\left(-\frac{\tau}{\mu_0}\right) d\mu \quad (\text{A.4})$$

The principal conjecture in the two-stream method is the approximation of the specific intensity I_d . For the hybrid modified Eddington-delta function approximation (here called Meador and Weaver approximation), the specific intensity is defined as

$$I(\tau, \pm\mu) = \frac{1}{1 - g^2(1 - \mu_0)} \left\{ (1 - g^2) \left[\left(1 \pm \frac{3\mu}{2}\right) q^+ + \left(1 \mp \frac{3\mu}{2}\right) q^- \right] + g^2 \delta(\mu - \mu_0) q^\pm \right\} \quad (\text{A.5})$$

The modification of the standard Eddington approximation is done by the use of the χ_0 -term.

$$\chi_0 = \frac{1}{2\omega_0} \int_0^1 p(\mu_0, -\mu') d\mu' = 1 - \frac{1}{2\omega_0} \int_0^1 p(\mu_0, \mu') d\mu' \quad (\text{A.6})$$

The γ -terms may be found applying Eqs. A.5 and A.6 in Eq. A.3 or in Eq. A.4, leading to identical results. In what follows, the development for q^+ will be shown. For the first term in right-hand side on Eq. A.3, it produces

$$- \int_0^1 I(\tau, \mu) d\mu = - \frac{7 - 3g^2}{4[1 - g^2(1 - \mu_0)]} q^+ - \frac{1 - g^2}{4[1 - g^2(1 - \mu_0)]} q^- \quad (\text{A.7})$$

and for the second term

$$\begin{aligned} \frac{1}{2} \int_0^1 \int_{-1}^{+1} p(\mu, \mu') I(\tau, \mu') d\mu' d\mu &= \frac{1 - g^2}{2[1 - g^2(1 - \mu_0)]} \int_0^1 \int_{-1}^{+1} \left(1 + \frac{3\mu'}{2}\right) p(\mu, \mu') q^+ d\mu' d\mu \\ &+ \frac{1 - g^2}{2[1 - g^2(1 - \mu_0)]} \int_0^1 \int_{-1}^{+1} \left(1 - \frac{3\mu'}{2}\right) p(\mu, \mu') q^- d\mu' d\mu \\ &+ \frac{g^2}{2[1 - g^2(1 - \mu_0)]} \int_0^1 \int_{-1}^{+1} \delta(\mu' - \mu_0) p(\mu, \mu') q^\pm d\mu' d\mu \end{aligned} \quad (\text{A.8})$$

The scattering phase function in the Eddington approximation reads

$$p(\mu, \mu') = \omega_0(1 + 3g\mu\mu') \quad (\text{A.9})$$

that gives as a result

$$\begin{aligned} \frac{1}{2} \int_0^1 \int_{-1}^{+1} p(\mu, \mu') I(\tau, \mu') d\mu' d\mu &= \frac{(4 + 3g) - g^2(4 + 3g)}{4[1 - g^2(1 - \mu_0)]} \omega_0 q^+ + \frac{(4 - 3g) - g^2(4 - 3g)}{4[1 - g^2(1 - \mu_0)]} \omega_0 q^- \\ &+ \frac{4\omega_0 g^2(1 - \beta_0)}{4[1 - g^2(1 - \mu_0)]} q^+ + \frac{4\omega_0 g^2 \beta_0}{4[1 - g^2(1 - \mu_0)]} q^- \end{aligned} \quad (\text{A.10})$$

For the third term in right-hand side of Eq. A.3, the χ_0 -term is used

$$\frac{1}{2} \int_0^1 p(-\mu, \mu_0) q_0 \exp\left(-\frac{\tau}{\mu_0}\right) = q_0 \omega_0 (1 - \chi_0) \exp\left(-\frac{\tau}{\mu_0}\right) \quad (\text{A.11})$$

Using these results, Eq. A.3 may be written as

$$\begin{aligned} \frac{dq^+}{d\tau} &= -\frac{7 - 3g^2 - \omega_0(4 + 3g) + \omega_0 g^2(4\beta_0 + 3g)}{4[1 - g^2(1 - \mu_0)]} q^+ \\ &- \frac{1 - g^2 - \omega_0(4 - 3g) - \omega_0 g^2(4\beta_0 + 3g - 4)}{4[1 - g^2(1 - \mu_0)]} q^- \\ &+ q_0 \omega_0 (1 - \chi_0) \exp\left(-\frac{\tau}{\mu_0}\right) \end{aligned} \quad (\text{A.12})$$

Comparing it with the simplified expression given in Eq. A.1 and knowing that $\gamma_3 + \gamma_4 = 1$ (energy conservation), the γ -terms are obtained

$$\gamma_1 = -\frac{7 - 3g^2 - \omega_0(4 + 3g) + \omega_0 g^2(4\beta_0 + 3g)}{4[1 - g^2(1 - \mu_0)]} \quad (\text{A.13})$$

$$\gamma_2 = \frac{1 - g^2 - \omega_0(4 - 3g) - \omega_0 g^2(4\beta_0 + 3g - 4)}{4[1 - g^2(1 - \mu_0)]} \quad (\text{A.14})$$

$$\gamma_3 = 1 - \chi_0 \quad \text{and} \quad \gamma_4 = \chi_0 \quad (\text{A.15})$$

As explained before, the γ -terms given here differ of those given in the original document. However, the following relations exist between the γ -terms of Meador and Weaver (with subscripts M) and the γ -terms of this work.

$$\begin{aligned} \gamma_{1M} &= -\gamma_1 \\ \gamma_{2M} &= -\gamma_2 \\ \gamma_{3M} &= \gamma_4 \\ \gamma_{4M} &= \gamma_3 \end{aligned} \quad (\text{A.16})$$

A.2 The multi-layer, two-stream solution using a tridiagonal matrix

The multi-layer two-stream solution to model a SPR is explained in this section, following the original development made by Toon et al. However, as in the case of the Meador and Weaver model, the geometry is different. In this case the SPR is conceived as a horizontal slab of particles dispersion, where the incident flux arrives following the positive direction. Such a SPR permits working with inhomogeneous properties inside through the decomposition into multiple homogeneous layers. It is specially useful to model a SPR with an inhomogeneous temperature profile or composed by two-layer with different particles. The model is given for a monochromatic spectrum, but for simplicity the λ index has been omitted. Fig. A.2 repeats the schematic given in Fig. 2.1 for a multi-layered SPR.

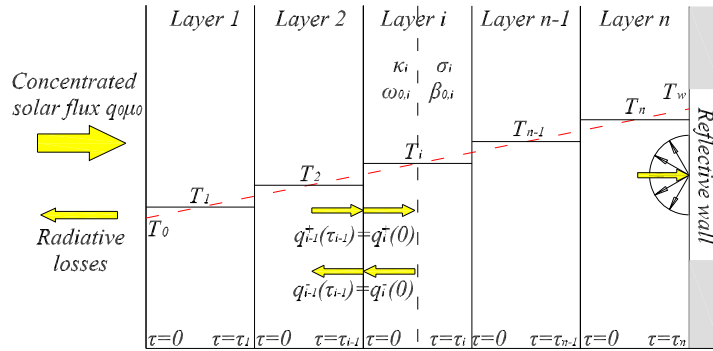


Figure A.2: Schematic of a multi-layered solar particle receiver

The radiative diffuse fluxes inside the layer i may be expressed by Eqs. A.17 and A.18

$$q_i^+(\tau) = \gamma_{2,i} K_{1,i} \exp(\nu_i \tau) + \gamma_{2,i} K_{2,i} \exp(-\nu_i \tau) + G_i^+(\tau) \quad (\text{A.17})$$

$$q_i^-(\tau) = (\gamma_{1,i} - \nu_i) K_{1,i} \exp(\nu_i \tau) + (\gamma_{1,i} + \nu_i) K_{2,i} \exp(-\nu_i \tau) + G_i^-(\tau) \quad (\text{A.18})$$

where the source terms (G_i^\pm) are

$$G_i^+(\tau) = \frac{q_0 \omega_{0,i} \mu_0}{1 - \nu_i^2 \mu_0^2} [\alpha_{2,i} \mu_0 - \gamma_{3,i}] \exp\left(-\frac{\tau_c + \tau}{\mu_0}\right) + 2\pi \left[\frac{1 - \omega_{0,i}}{\gamma_{1,i} - \gamma_{2,i}} \right] I_{b,i}(T_i) \quad (\text{A.19})$$

$$G_i^-(\tau) = \frac{q_0 \omega_{0,i} \mu_0}{1 - \nu_i^2 \mu_0^2} [\alpha_{1,i} \mu_0 + \gamma_{4,i}] \exp\left(-\frac{\tau_c + \tau}{\mu_0}\right) + 2\pi \left[\frac{1 - \omega_{0,i}}{\gamma_{1,i} - \gamma_{2,i}} \right] I_{b,i}(T_i) \quad (\text{A.20})$$

The optical depth (τ) is bounded between $0 \leq \tau \leq \tau_i$, which begins at the end of the layer $i-1$ (see Fig. A.2). The cumulative optical depth (τ_c) of the $i-1$ first layers is defined as

$$\tau_c = \sum_{j=1}^{i-1} \tau_j \quad (\text{A.21})$$

As noted by Toon et al., a difficulty with the solution of Eqs. A.17 and A.18 lies in the limiting case when $\omega_0 = 0$ (pure absorption) and $g = 0$ (isotropic scattering).

In such cases, those equations become decoupled generating numerical complications in the matrix inversion. To avoid this problem, the K -terms are scaled as

$$Y_{1,i} = \frac{K_{1,i} + K_{2,i}}{2} \quad (\text{A.22})$$

$$Y_{2,i} = \frac{K_{1,i} - K_{2,i}}{2} \quad (\text{A.23})$$

hence,

$$K_{1,i} = Y_{1,i} + Y_{2,i} \quad \text{and} \quad K_{2,i} = Y_{1,i} - Y_{2,i} \quad (\text{A.24})$$

Then, Equations A.17 and A.18 become

$$\begin{aligned} q_i^+(\tau) = & Y_{1,i} [\gamma_{2,i} \exp(k_i\tau) + \gamma_{2,i} \exp(-k_i\tau)] \\ & + Y_{2,i} [\gamma_{2,i} \exp(k_i\tau) - \gamma_{2,i} \exp(-k_i\tau)] + G_i^+(\tau) \end{aligned} \quad (\text{A.25})$$

$$\begin{aligned} q_i^-(\tau) = & Y_{1,i} [(\gamma_{1,i} - k_i) \exp(k_i\tau) + (\gamma_{1,i} + k_i) \exp(-k_i\tau)] \\ & + Y_{2,i} [(\gamma_{1,i} - k_i) \exp(k_i\tau) - (\gamma_{1,i} + k_i) \exp(-k_i\tau)] + G_i^-(\tau) \end{aligned} \quad (\text{A.26})$$

To simplify the notation the E -terms are defined as follows

$$E_{1,i}(\tau) = \gamma_{2,i} \exp(k_i\tau) + \gamma_{2,i} \exp(-k_i\tau) \quad (\text{A.27})$$

$$E_{2,i}(\tau) = \gamma_{2,i} \exp(k_i\tau) - \gamma_{2,i} \exp(-k_i\tau) \quad (\text{A.28})$$

$$E_{3,i}(\tau) = (\gamma_{1,i} - k_i) \exp(k_i\tau) + (\gamma_{1,i} + k_i) \exp(-k_i\tau) \quad (\text{A.29})$$

$$E_{4,i}(\tau) = (\gamma_{1,i} - k_i) \exp(k_i\tau) - (\gamma_{1,i} + k_i) \exp(-k_i\tau) \quad (\text{A.30})$$

The results are

$$q_i^+(\tau) = Y_{1,i} E_{1,i}(\tau) + Y_{2,i} E_{2,i}(\tau) + G_i^+(\tau) \quad (\text{A.31})$$

$$q_i^-(\tau) = Y_{1,i} E_{3,i}(\tau) + Y_{2,i} E_{4,i}(\tau) + G_i^-(\tau) \quad (\text{A.32})$$

The boundary conditions permit to establish the matrix equation. They were exposed in section 2.3 and are repeated here.

$$q_1^+(0) = 0 \quad (\text{A.33})$$

$$q_i^+(\tau_i) = q_{i+1}^+(0) \quad (\text{A.34})$$

$$q_i^-(\tau_i) = q_{i+1}^-(0) \quad (\text{A.35})$$

$$q_n^-(\tau_n) = \rho_w \left[q_n^+(\tau_n) + q_0 \mu_0 \exp\left(-\frac{\tau_c + \tau_n}{\mu_0}\right) \right] + (1 - \rho_w) \pi I_b(T_w) \quad (\text{A.36})$$

where the first boundary condition implies that no diffuse flux exists at the front of the SPR. The last one states that the backward flux coming from the SPR back is the sum of the reflected forward flux (diffuse and direct) and the emission from the wall. The others specify the radiative heat flux continuity at a layer interface, both in backward

A.2. The multi-layer, two-stream solution using a tridiagonal matrix

and forward directions (see Fig. A.2). Their application on Eqs. A.31 and A.32 leads to

$$Y_{1,1}E_{1,1}(0) + Y_{2,1}E_{2,1}(0) = -G_1^+(0) \quad (\text{A.37})$$

$$Y_{1,i}E_{1,i}(\tau_i) + Y_{2,i}E_{2,i}(\tau_i) - Y_{1,i+1}E_{1,i+1}(0) - Y_{2,i+1}E_{2,i+1}(0) = G_{i+1}^+(0) - G_i^+(\tau_i) \quad (\text{A.38})$$

$$Y_{1,i}E_{3,i}(\tau_i) + Y_{2,i}E_{4,i}(\tau_i) - Y_{1,i+1}E_{3,i+1}(0) - Y_{2,i+1}E_{4,i+1}(0) = G_{i+1}^-(0) - G_i^-(\tau_i) \quad (\text{A.39})$$

$$\begin{aligned} & Y_{1,n}E_{3,n}(\tau_n) + Y_{2,n}E_{4,n}(\tau_n) + G_n^-(\tau_n) \\ &= \rho_w [Y_{1,n}E_{1,n}(\tau_n) + Y_{2,n}E_{2,n}(\tau_n) + G_n^+(\tau_n)] + q_0\mu_0 \exp\left(-\frac{\tau_{c,n}}{\mu_0}\right) + (1 - \rho_w)\pi I_b(T_w) \end{aligned} \quad (\text{A.40})$$

Equations A.37 to A.40 form a pentadiagonal matrix system that may be solved by standard techniques. However, Toon et al. noticed that they may be arranged to produce a tridiagonal matrix, which improves the computational time needed to be solved. The following operations must be performed

$$E_{4,i+1}(0) \times \text{Eq. A.38} - E_{2,i+1}(0) \times \text{Eq. A.39} \quad (\text{A.41})$$

and

$$E_{3,i}(\tau_i) \times \text{Eq. A.38} - E_{1,i}(\tau_i) \times \text{Eq. A.39} \quad (\text{A.42})$$

The resulting equations are

$$\begin{aligned} & Y_{1,i} [E_{1,i}(\tau_i)E_{4,i+1}(0) - E_{3,i}(\tau_i)E_{2,i+1}(0)] \\ & + Y_{2,i} [E_{2,i}(\tau_i)E_{4,i+1}(0) - E_{4,i}(\tau_i)E_{2,i+1}(0)] \\ & + Y_{1,i+1} [E_{3,i+1}(0)E_{2,i+1}(0) - E_{1,i+1}(0)E_{4,i+1}(0)] \\ &= E_{4,i+1}(0) [G_{i+1}^+(0) - G_i^+(\tau_i)] - E_{2,i+1}(0) [G_{i+1}^-(0) - G_i^-(\tau_i)] \end{aligned} \quad (\text{A.43})$$

and

$$\begin{aligned} & Y_{2,i} [E_{2,i}(\tau_i)E_{3,i}(\tau_i) - E_{4,i}(\tau_i)E_{1,i}(\tau_i)] \\ & + Y_{1,i+1} [E_{3,i+1}(0)E_{1,i}(\tau_i) - E_{1,i+1}(0)E_{3,i}(\tau_i)] \\ & + Y_{2,i+1} [E_{4,i+1}(0)E_{1,i}(\tau_i) - E_{2,i+1}(0)E_{3,i}(\tau_i)] \\ &= E_{3,i}(\tau_i) [G_{i+1}^+(0) - G_i^+(\tau_i)] - E_{1,i}(\tau_i) [G_{i+1}^-(0) - G_i^-(\tau_i)] \end{aligned} \quad (\text{A.44})$$

A new notation is implemented for the Y constants

$$Y_{1,i} = Y_{l-1} \quad \text{and} \quad Y_{2,i} = Y_l \quad (\text{A.45})$$

where $l = 2i$. Equations A.43 and A.44 may be written in a tridiagonal matrix form as

$$A_l Y_{l-1} + B_l Y_l + C_l Y_{l+1} = D_l \quad (\text{A.46})$$

the A_l, B_l, C_l and D_l constants for **l even** between $2 \leq l \leq n - 1$ are

$$\begin{aligned} A_l &= -2k_{i+1} E_{1,i}(\tau_i) \\ B_l &= -2k_{i+1} E_{2,i}(\tau_i) \\ C_l &= 4\gamma_{2,i+1} k_{i+1} \\ D_l &= -2k_{i+1} [G_{i+1}^+(0) - G_i^+(\tau_i)] \end{aligned} \quad (\text{A.47})$$

and for **l odd** between $3 \leq l \leq n - 1$ are

$$\begin{aligned} A_l &= 4\gamma_{2,i} k_i \\ B_l &= 2\gamma_{1,i+1} E_{1,i}(\tau_i) - 2\gamma_{2,i+1} E_{3,i}(\tau_i) \\ C_l &= -2k_{i+1} E_{1,i}(\tau_i) \\ D_l &= E_{3,i}(\tau_i) [G_{i+1}^+(0) - G_i^+(\tau_i)] - E_{1,i}(\tau_i) [G_{i+1}^-(0) - G_i^-(\tau_i)] \end{aligned} \quad (\text{A.48})$$

For $l = 1$ (first layer) the A_1, B_1, C_1 and D_1 constants may be found with direct comparison with Eq. A.37, hence

$$\begin{aligned} A_1 &= 0 \\ B_1 &= 2\gamma_{2,1} \\ C_1 &= 0 \\ D_1 &= -G_1^+(0) \end{aligned} \quad (\text{A.49})$$

and for $l = n$ (last layer) the A_n, B_n, C_n and D_n constants, with Eq. A.40

$$\begin{aligned} A_n &= E_{3,n}(\tau_n) - \rho_w E_{1,n}(\tau_n) \\ B_n &= E_{4,n}(\tau_n) - \rho_w E_{2,n}(\tau_n) \\ C_n &= 0 \end{aligned} \quad (\text{A.50})$$

$$D_n = \rho_w G_n^+(\tau_n) - G_n^-(\tau_n) + \rho_w q_0 \mu_0 \exp\left(-\frac{\tau_{c,n}}{\mu_0}\right) + (1 - \rho_w) \pi I_b(T_w)$$

And the source functions are evaluated as

$$G_i^+(0) = \frac{q_0 \omega_{0,i} \mu_0}{1 - k_i^2 \mu_0^2} [\alpha_{2,i} \mu_0 - \gamma_{3,i}] \exp\left(-\frac{\tau_{c,i-1}}{\mu_0}\right) + 2\pi \frac{1 - \omega_{0,i}}{\gamma_{1,i} - \gamma_{2,i}} I_{b,i}(T_i) \quad (\text{A.51})$$

$$G_i^-(0) = \frac{q_0 \omega_{0,i} \mu_0}{1 - k_i^2 \mu_0^2} [\alpha_{1,i} \mu_0 + \gamma_{4,i}] \exp\left(-\frac{\tau_{c,i-1}}{\mu_0}\right) + 2\pi \frac{1 - \omega_{0,i}}{\gamma_{1,i} - \gamma_{2,i}} I_{b,i}(T_i) \quad (\text{A.52})$$

A.3. The radiative losses for the cold solar particle receiver

$$G_i^+(\tau_i) = \frac{q_0\omega_{0,i}\mu_0}{1 - k_i^2\mu_0^2}[\alpha_{2,i}\mu_0 - \gamma_{3,i}] \exp\left(-\frac{\tau_{c,i}}{\mu_0}\right) + 2\pi \frac{1 - \omega_{0,i}}{\gamma_{1,i} - \gamma_{2,i}} I_{b,i}(T_i) \quad (\text{A.53})$$

$$G_i^-(\tau_i) = \frac{q_0\omega_{0,i}\mu_0}{1 - k_i^2\mu_0^2}[\alpha_{1,i}\mu_0 + \gamma_{4,i}] \exp\left(-\frac{\tau_{c,i}}{\mu_0}\right) + 2\pi \frac{1 - \omega_{0,i}}{\gamma_{1,i} - \gamma_{2,i}} I_{b,i}(T_i) \quad (\text{A.54})$$

A.3 The radiative losses for the cold solar particle receiver

The cold parallel problem is the simplest simplification of this model. For that problem, an analytic solution is available. In this section the radiative losses for such a problem is found. It will be used to compare the good behavior of the TSLAYER subroutine, which is the main subroutine in the SPR model. As shown in section 2.3, the solution for the radiative fluxes using the two-stream method involves the K_1 and K_2 constants, which depend on the boundary conditions.

$$q^+(\tau) = \gamma_2 K_1 \exp(\nu\tau) + \gamma_2 K_2 \exp(-\nu\tau) + \frac{q_0\omega_0\mu_0}{1 - \nu^2\mu_0^2}[\alpha_2\mu_0 - \gamma_3] \exp\left(-\frac{\tau}{\mu_0}\right) \quad (\text{A.55})$$

$$q^-(\tau) = (\gamma_1 - \nu)K_1 \exp(\nu\tau) + (\gamma_1 + \nu)K_2 \exp(-\nu\tau) + \frac{q_0\omega_0\mu_0}{1 - \nu^2\mu_0^2}[\alpha_1\mu_0 + \gamma_4] \exp\left(-\frac{\tau}{\mu_0}\right) \quad (\text{A.56})$$

The boundary conditions are for the forward radiative flux at the inlet ($\tau = 0$) and for the backward radiative flux at the diffusively emitting wall ($\tau = \tau_n$), assumed to have a reflectivity ρ_w

$$q_d^+(0) = 0 \quad (\text{A.57})$$

$$q_d^-(\tau_n) = \rho_w \left[q_d^+(\tau_n) + q_0\mu_0 \exp\left(-\frac{\tau_n}{\mu_0}\right) \right] + (1 - \rho_w)\pi I_b(T_w) \quad (\text{A.58})$$

Using the boundary conditions, Equations A.57 and A.58 become

$$K_2 = -\frac{q_0\mu_0\omega_0}{\gamma_2(1 - \nu^2\mu_0^2)}(\alpha_2\mu_0 - \gamma_3) - K_1 \quad (\text{A.59})$$

$$\begin{aligned} & K_1 \exp(\nu\tau_n)(\rho_w\gamma_2 + \nu - \gamma_1) + K_2 \exp(-\nu\tau_n)(\rho_w\gamma_2 - \nu - \gamma_1) \\ &= \frac{q_0\mu_0\omega_0}{1 - \nu^2\mu_0^2} [(\alpha_1\mu_0 + \gamma_4) - \rho_w(\alpha_2\mu_0 - \gamma_3) - \rho_w\omega_0^{-1}(1 - \nu^2\mu_0^2)] \exp\left(-\frac{\tau_n}{\mu_0}\right) \end{aligned} \quad (\text{A.60})$$

The solution of the system of Eq. A.59 and Eq. A.60 gives the K_1 and K_2 constants as

$$\begin{aligned} K_1 &= \frac{q_0\mu_0\omega_0}{(1 - \nu^2\mu_0^2)[(\rho_w\gamma_2 + \nu - \gamma_1) \exp(\nu\tau_n) - (\rho_w\gamma_2 - \nu - \gamma_1) \exp(-\nu\tau_n)]} \\ &\times \left\{ [(\alpha_1\mu_0 - \rho_w\alpha_2\mu_0 + \rho_w\gamma_3 + \gamma_4) - \rho_w\omega_0^{-1}(1 - \nu^2\mu_0^2)] \exp\left(-\frac{\tau_n}{\mu_0}\right) \right. \\ &\left. + \frac{1}{\gamma_2}(\alpha_2\mu_0 - \gamma_3)(\rho_w\gamma_2 - \nu - \gamma_1) \exp(-\nu\tau_n) \right\} \end{aligned} \quad (\text{A.61})$$

Appendix A. The two-stream method approximation

$$\begin{aligned}
 K_2 = & - \frac{q_0 \mu_0 \omega_0}{(1 - \nu^2 \mu_0^2) [(\rho_w \gamma_2 + \nu - \gamma_1) \exp(\nu \tau_n) - (\rho_w \gamma_2 - \nu - \gamma_1) \exp(-\nu \tau_n)]} \\
 & \times \left\{ [(\alpha_1 \mu_0 - \rho_w \alpha_2 \mu_0 + \rho_w \gamma_3 + \gamma_4) - \rho_w \omega_0^{-1} (1 - \nu^2 \mu_0^2)] \exp\left(-\frac{\tau_n}{\mu_0}\right) \right. \\
 & \left. + \frac{1}{\gamma_2} (\alpha_2 \mu_0 - \gamma_3) (\rho_w \gamma_2 + \nu - \gamma_1) \exp(\nu \tau_n) \right\} \quad (\text{A.62})
 \end{aligned}$$

The normalized radiative losses (RL) are defined as the backward flux (q^-) minus the incident flux (q_0) at $\tau = 0$.

$$RL = \frac{q^-(0)}{q_0 \mu_0} = \frac{-K_1(\nu - \gamma_1)}{q_0 \mu_0} + \frac{K_2(\nu + \gamma_1)}{q_0 \mu_0} + \frac{\omega_0}{1 - \nu^2 \mu_0^2} (\alpha_1 \mu_0 + \gamma_4) \quad (\text{A.63})$$

After some manipulations Equation A.63 becomes

$$\begin{aligned}
 RL = & \frac{\omega_0}{(1 - \nu^2 \mu_0^2) [(\rho_w \gamma_2 + \nu - \gamma_1) \exp(\nu \tau_n) - (\rho_w \gamma_2 - \nu - \gamma_1) \exp(-\nu \tau_n)]} \\
 & \times \left\{ (1 - \nu \mu_0) [(\rho_w \alpha_2 - \alpha_1) + \nu(\rho_w \gamma_3 + \gamma_4)] \exp(\nu \tau_n) \right. \\
 & - (1 + \nu \mu_0) [(\rho_w \alpha_2 - \alpha_1) - \nu(\rho_w \gamma_3 + \gamma_4)] \exp(-\nu \tau_n) \\
 & \left. - 2\nu [(\alpha_1 \mu_0 - \rho_w \alpha_2 \mu_0 + \rho_w \gamma_3 + \gamma_4) - \rho_w \omega_0^{-1} (1 - \nu^2 \mu_0^2)] \exp\left(-\frac{\tau_n}{\mu_0}\right) \right\} \quad (\text{A.64})
 \end{aligned}$$

Appendix B

The Monte Carlo method

The Monte Carlo Method (MCM) refers to a statistical numerical method for solving physical problems. It was developed to predict the average behavior of nuclear weapons, through the simulation of the history of many individual neutrons. Since the method involves random numbers, its name was taken from the principality of Monte Carlo, well known for its casinos. This method has been used to solve many different problems in radiative heat transfer. Several books and articles are devoted to review its application in this domain. One great advantage of the MCM is the intuitive physical comprehension of the method. It follows that even complicated problems may be easily solved using such a method. In this section, an intuitive explanation of the basics of the method is shown. More details of the method may be found in specialized handbooks as in Dunn and Shultis. Special interest is brought to the applications in participating media and in solar applications.

B.1 The Monte Carlo method for the radiative transfer in a participating media

The Monte Carlo method applied to the radiative transfer in a participating media consists of describing the behavior of a statistically significant number of photon bundles into the media. The control of their behavior (called history) is based on probabilistic models of the underlying physics. The energy packet then interacts with the medium through the absorption, scattering and emission and with the boundaries through the reflection, transmission, absorption or emission. Therefore, the main condition of the MCM is the independence of each event. Even though the ease implementation of this method, some disadvantages are linked to its stochastic nature. Since the results are statistical, they are linked to an inherent inaccuracy. Moreover, Dufresne *et al.* reported that the agreement of the reciprocity principle for certain implementations is given in a statistical way, which means that it is agreed only when the number of events tends to infinity. To avoid the inconvenient mentioned above a large number of bundles should be utilized. As a consequence, large increases in the computational time are needed to reach the accuracy required for engineering applications. Since the recent advances in computational technology, the method is becoming rapidly very popular. Even if it still remains high time consuming in comparison with other methods. Nowa-

B.1. The Monte Carlo method for the radiative transfer in a participating media

days, the MCM is used as a reference to evaluate faster methods, such as in this work, or for solving specific problems.

The most general MCM simulate the photon bundle history from the emission to its end by absorption. Along the path, the information about the amount of the power transferred from a zone to another is collected. This concept is the basis of the forward methods. From the original forward method, some alternative Monte Carlo methods has been proposed for particular purposes. For instance, the inverse MC method is used to solve radiative transfer inverse problems. The backward MC method is proposed profiting the principle of reciprocity in radiative transfer. Other variations include the null-collision formulation and the net-exchange formulation.

Probability distributions and random numbers

A main characteristic in the MCM is the non dependence of the events. A sequence of independent events between them is known as a Markov chain. To ensure this characteristic in a MCM implementation, the physical phenomena should be represented by a probability density function (PDF), acting on an independent and identically distributed random variables. The Monte Carlo method states that

$$R_1 = \int_{\xi_{min}}^{\xi} dP(\xi) \quad (B.1)$$

The uniformly choose of the random numbers between $0 \leq R_1 \leq 1$ ensures the independence of the events. At this point, all the authors agree about the drawback of the computationally generation of true random numbers. Nowadays however, non inadequate behavior has been reported by using the standard random number generators for Monte Carlo computations. A number of textbooks develops the random number relationships for participating media, for example in Modest. For instance, a brief list of such random numbers is presented in Table B.1.

Integral formulation of the radiative transfer equation

The integral formulation of the RTE is suitable to be solved by a Monte Carlo method. This formulation may be easily found in radiative textbooks.

$$I_\lambda(r, \hat{s}) = I_{0,\lambda}(r_0, \hat{s}) \exp \left[- \int_0^s \beta_\lambda ds'' \right] + \int_0^s S_\lambda(r', \hat{s}) \exp \left[- \int_0^{s''} \beta_\lambda ds'' \right] \beta_\lambda ds'' \quad (B.2)$$

In Eq. B.2, subscript 0 means the specific intensity of the source radiation, $S(r)$ is the internal radiation source and \hat{s} is the main path direction. The specific intensity at the r position and in the \hat{s} direction is the sum of the direct intensity contribution coming from the r_0 position, and the emission and scattering coming from other directions and entering in the main path at the r' position along the \hat{s} direction. Since the attenuation exponentials are equivalent to the path lengths given for the absorption and scattering random numbers, Equation B.2 may be easily implemented in a MCM.

	Cumulative and random number	Inversed expression
Wavelength emission	$R_\lambda = \frac{\pi}{\kappa\sigma_{SB}T^4} \int_0^\lambda \kappa_\lambda I_{b,\lambda} d\lambda$	$\lambda = \lambda(R_\lambda, x, y, z)$
Azimuthal angular direction	$R_\psi = \frac{\psi}{2\pi}$	$\psi = 2\pi R_\psi$
Polar angular direction	$R_\theta = \frac{1}{2} \int_0^\theta \sin \theta d\theta$	$\theta = \cos^{-1}(1 - 2R_\theta)$
Absorption path length	$R_\kappa = \exp\left(-\int_0^{l_\kappa} \kappa_\lambda ds\right)$	$l_\kappa = \frac{1}{\kappa_\lambda} \ln \frac{1}{R_\kappa}$
Scattering path length	$R_\sigma = \exp\left(-\int_0^{l_\sigma} \sigma_\lambda ds\right)$	$l_\sigma = \frac{1}{\sigma_\lambda} \ln \frac{1}{R_\sigma}$

Table B.1: Random number relations for participating media. The inversed expressions are for an isotropic phase function (directions) and for an homogeneous medium (path lengths)

Accuracy considerations

Since the Monte Carlo method is a statistical method, the results vary around the true solution. If the random numbers are truly random, it is expected that the accuracy will increase with the number of photon bundles. The Monte Carlo solution will be exact when an infinite number of bundles are used. Nevertheless, the same statistical nature of the method permits a straightforward computation of its associated error. If considers that all the bundles have the same amount of energy, the sampling result $S_R(N)$ may be expressed as the sum of the N bundles results.

$$S_R(N) = \frac{1}{N} \sum_{i=1}^N S_R(N_i) \quad (\text{B.3})$$

Statistically, the N bundle results are equivalent to the N times measurement of the same physic phenomena. It permits to compute the error through the calculation of the statistical variance.

$$\sigma_{MC} = \frac{1}{N(N-1)} \sum_{i=1}^N (S_R(N_i) - S_R(N))^2 \quad (\text{B.4})$$

Modest in his textbook explains that the central limit theorem states that the mean $S_R(N)$ of N measurements $S_R(N_i)$ follows a Gaussian distribution. It implies that the solution method approaches the true solution $S_R(\infty)$ with 68.3% confidence within the limits of $S_R(N) \pm \sigma_{MC}$, with 95% confidence within $S_R(N) \pm 2\sigma_{MC}$, or with 99% confidence within $S_R(N) \pm 2.58\sigma_{MC}$.

B.1. The Monte Carlo method for the radiative transfer in a participating media

Example of implementation of the Monte Carlo method

To illustrate the method, in the followings a forward Monte Carlo algorithm to model the transmittance and the reflectance of a participating medium slab will be explained. Between the several forward methods proposed in the literature, the path length method reported by Avriillier *et al.* is reproduced. This example consists in the scattering and absorption of an incident light into a scattering and absorbing medium. The method used, follows the ray path between two scattering events. During the path, a part of photons is absorbed, decreasing the original weight of the bundle. After each scattering event, the weight of the bundle is the number of non-absorbed photons. The illustrative algorithm (which considers a homogeneous and uniform 1D geometry with an absorbing and isotropic scattering cold media) is as follows, and its graphical representation is given in Fig. B.1.

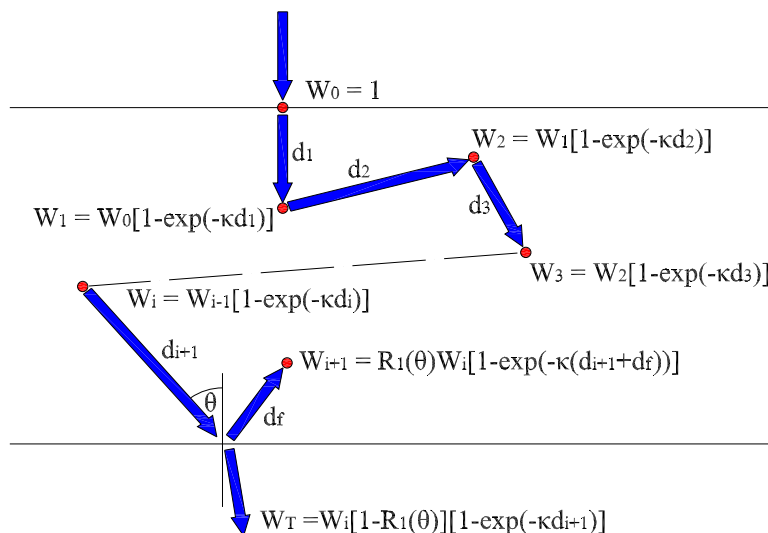


Figure B.1: Schematic of a energy packet history in a forward path length Monte Carlo method. W is the energy weight of the bundle, κ is the absorption coefficient, R_1 is a random number between $[0 - 1]$ and θ is the incident angle at the boundary

1. A photon bundle that follows the incident direction is created with a initial weight of one.

$$W_0 = 1 \quad (\text{B.5})$$

2. The path length is the probability of the bundle to achieve a new scattering event. It is calculated as

$$d_i = -\frac{\ln(R_1)}{\sigma} \quad (\text{B.6})$$

where R_1 is a random number uniformly distributed between $[0 - 1]$ and σ is the volume scattering coefficient.

3. Along the path length the weight of the bundle is reduced due to the absorption of some photons by the factor $\exp[-\kappa d]$

$$W_i = W_{i-1}[1 - \exp(-\kappa d_{i-1})] \quad (\text{B.7})$$

4. After each scattering event a new direction is sampled following the phase function of the media (remember that the phase function is the probability of a scattered photon to follow a given direction). For an isotropic, mono-dimensional media, the direction is found as

$$\theta_i = \cos^{-1}(1 - 2R_1) \quad (\text{B.8})$$

5. When the bundle cross a slab surface, it is reflected or transmitted. The direction and the weight then are easily computed as the formulation used before.

6. After many interactions, the weight left of the photon bundle has a very low energy. If the photon bundle reaches a value lower than a threshold value (determined by the precision of the method) then may be considered eliminated. This procedure has a consequence that the energy is not conserved. To conserve the energy, then, the Russian roulette technique may be used. This technique uses a constant value M to assign the elimination or not of the photon bundle that reaches the threshold value. If the bundle survive, a new weight is assigned as MW . Mathematically, it is expressed as

$$\begin{aligned} W = MW & \quad R_1 \leq 1/M \\ W = 0 & \quad R_1 > 1/M \end{aligned} \quad (\text{B.9})$$

7. This procedure is repeated by a sufficiently number of the rays. The precision of the method depends of the number of the rays used to simulate the phenomena.

Appendix C

The Kramers-Kronig dispersion relations

The model presented in section 5.3 to obtain the refractive index from the reflectance data using the Kramers-Konig relations is validated. Two numerical methods of integration are analyzed to avoid the singularity at $\lambda = \lambda_0$: trapezoidal integration with L'Hôpital's rule and Maclaurin's formulae integration. To this end, the Lorentzian function is firstly used to compare analytical results with those obtained using the subroutine. Secondly, the *SiC* refractive index is used to compute the reflectance, which is used to find again the refractive index. The best integration method will be considered for the computations of the refractive index.

C.1 Comparison using the Lorentzian function

The Lorentzian function is defined as

$$k(\nu) = \frac{k_{max}(\gamma_L/2)^2}{(\nu - \nu_0)^2 + (\gamma_L/2)^2} - \frac{k_{max}(\gamma_L/2)^2}{(\nu + \nu_0)^2 + (\gamma_L/2)^2} \quad (C.1)$$

where its Kramers-Kronig transformation is given exactly in the following analytic form

$$n(\lambda) = k_{max} \left[-\frac{(\nu - \nu_0)(\gamma_L/2)}{(\nu - \nu_0)^2 + (\gamma_L/2)^2} + \frac{(\nu + \nu_0)(\gamma_L/2)}{(\nu + \nu_0)^2 + (\gamma_L/2)^2} \right] \quad (C.2)$$

ν is the wavenumber, k_{max} is the maximum value of the first term, γ_L is the bandwidth at half height, and ν_0 the wavenumber at the maximum intensity. The parameters used in the computations are

$$k_{max} = 0.5; \quad \nu_0 = 2000 \text{ cm}^{-1}; \quad \gamma_L = 40 \text{ cm}^{-1} \quad (C.3)$$

The integration is done for the $1000 - 3000 \text{ cm}^{-1}$ range with a $\Delta\nu = 2 \text{ cm}^{-1}$. The analytical computations are made in wavenumber and transformed to wavelength to present the results. Nevertheless, the numerical integration are made directly in wavelength. The real part is calculated from Eq. C.2 and it is extrapolated as a constant value equal to the boundary computed values (see Fig. C.1a). Figure C.1 shows the comparison between the analytical and numerical results for the real and imaginary parts of the Lorentzian function.

C.2. Comparison using the *SiC* refractive index

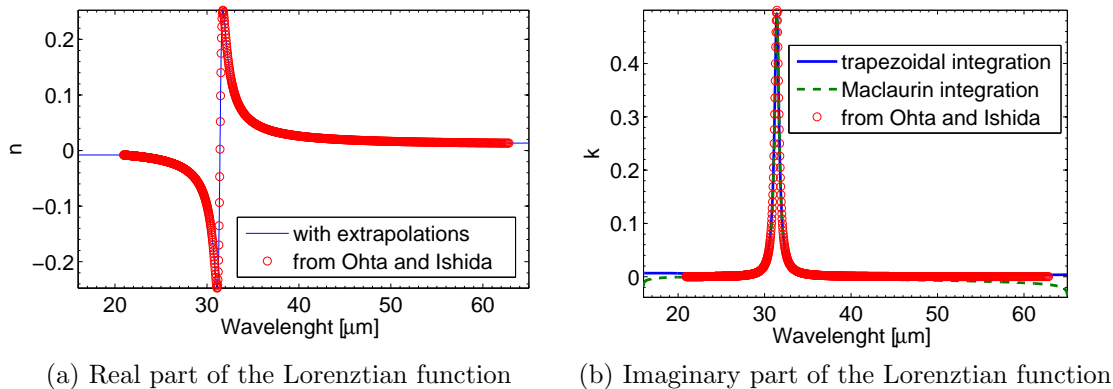


Figure C.1: Real and imaginary part of the Lorentzian function. (a) Circles analytical, solid line analytical extrapolated. (b) Circles analytical, solid line trapezoidal integration, dashed line Maclaurin integration

Figure C.1b presents the imaginary part of the Lorentzian function computed analytically (circles), computed with a numerical trapezoidal integration (solid line) and, computed with a numerical Maclaurin integration (dashed line). The agreement with the analytical results, for intermediate values, is sufficiently accurate. However, the trapezoidal integration seems to be lesser sensible to the extrapolations of the real part than the Maclaurin integration.

C.2 Comparison using the *SiC* refractive index

The refractive index of the silicon carbide, reported by Pégouiré and utilized in chapter 5, is used to validate the Kramers-Kronig subroutine. The procedure adopted is that the normal reflectance is computed from the refractive index with the Fresnel's law (Eq. 5.8). Next, Equation 5.4 permits to compute the phase-shift angle from the reflectance calculated before. Finally, the refractive index is re-calculated with Eqs. 5.6 and 5.7. Figure C.2 shows the real and the imaginary parts of the *SiC* refractive index computed by the Kramers-Kronig relations. Again, the two integration methods (the trapezoidal method (solid line) and the Maclaurin method (dashed line)) are compared with the original data.

As in the last subsection, intermediate values are in good agreement with the original data, independently of the integration method used. However, in the extreme extrapolated data the Maclaurin method works the worst in comparison with the trapezoidal method. As noted before by Wooten, the use of the Kramers-Kronig relations is very sensitive to the extrapolation of the reflectance data, but also to the integration method. Although the trapezoidal integration works the best in this comparison, it is no exempt of drawbacks. For example, the computed imaginary part of the refractive index becomes negative close to the $0.3 \mu m$.

As a conclusion, these comparisons confirm that caution must be taken when using data extrapolations. The Kramers-Kronig dispersion relations are indeed very sensitive

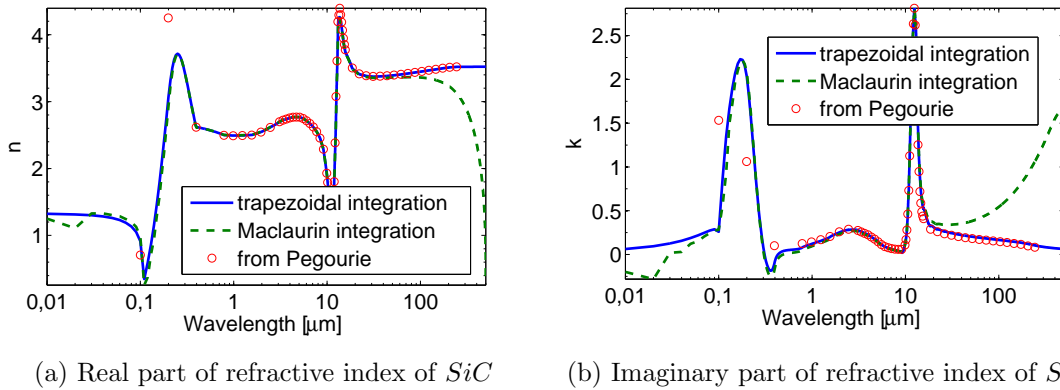


Figure C.2: Real and imaginary part of the refractive index of SiC . Circles from Pégourié, solid line trapezoidal integration, dashed line Maclaurin integration

to the extrapolations at the extremities of the measured data samples. Large errors may occur at very small wavelengths (high energy) owing to large scattering at those wavelengths. In addition, about the numerical integration method, the trapezoidal method seems to work better at the boundaries of the available data, being lesser sensible to the extrapolation procedures.

Appendix D

Numerical method for solving the energy equation and validation tests.

The numerical method is briefly presented in the following. The code was written by using the MATLAB environment. Some tests of accuracy are then presented and discussed. As it is possible, comparisons with available analytical solutions are systematically considered.

D.1 Control volume method discretization

To ensure energy conservation in the discretization and to work with a non-uniform mesh (refined close to the walls), Eq. 6.18 is numerically solved using a control volume method. According to this method, the energy equation is integrated over a control volume. An uniform mesh in the x -direction and a nonuniform mesh in the y -direction are utilized. It permits to have more accurate information of the phenomena close to the walls. A non uniform meshing with constant coefficient (C_m) increment in the y -direction is used. It is defined as

$$\Delta y_i = C_m \Delta y_{i-1} \quad i \geq 2 \text{ and } y < D/2 \quad (\text{D.1})$$

and,

$$\Delta y_1 = \frac{\frac{D}{2}(C_m - 1)}{C_m^{N/2} - 1} \quad (\text{D.2})$$

For y -values greater than $D/2$, the mesh is symmetrical to the $D/2$ axis, and $N/2$ is the number of cell taken into account between $0 < y < D/2$. The schematic of the control volume mesh and a wall control volume are shown in Fig. D.1.

Following these premises, and taken into account that the thermal eddy diffusivity

D.1. Control volume method discretization

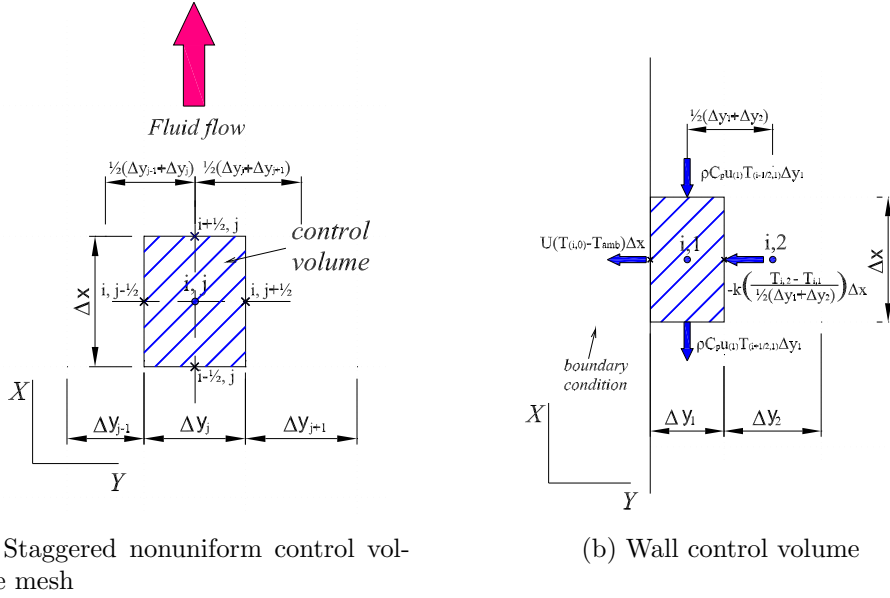


Figure D.1: Schematic of a control volume mesh used in the discretization and a wall control volume showing the convective boundary condition

depends on the y position, Eq. 6.18 for the mesh (i, j) results in

$$\begin{aligned}
 C_p \left((\rho_f \bar{u} \bar{T})_{i+\frac{1}{2},j} - (\rho_f \bar{u} \bar{T})_{i-\frac{1}{2},j} \right) \Delta y_j = \Delta x \left[(k_f + \rho_f C_p \epsilon_H)_{i,j+\frac{1}{2}} \left(\frac{T_{i,j+1} - T_{i,j}}{\frac{1}{2}(\Delta y_j + \Delta y_{j+1})} \right) \right. \\
 \left. - (k_f + \rho_f C_p \epsilon_H)_{i,j-\frac{1}{2}} \left(\frac{T_{i,j} - T_{i,j-1}}{\frac{1}{2}(\Delta y_{j-1} + \Delta y_j)} \right) - \left(q_{r,i,j+\frac{1}{2}} - q_{r,i,j-\frac{1}{2}} \right) \right]
 \end{aligned}
 \tag{D.3}$$

In order to obtain a discretization involving a diagonally dominant matrix, an upwind formulation on the transport term must be used.

$$\begin{aligned}
 C_p \left((\rho_f \bar{u} \bar{T})_{i,j} - (\rho_f \bar{u} \bar{T})_{i-1,j} \right) \Delta y_j = \Delta x \left[(k_f + \rho_f C_p \epsilon_H)_{i,j+\frac{1}{2}} \left(\frac{T_{i,j+1} - T_{i,j}}{\frac{1}{2}(\Delta y_j + \Delta y_{j+1})} \right) \right. \\
 \left. - (k_f + \rho_f C_p \epsilon_H)_{i,j-\frac{1}{2}} \left(\frac{T_{i,j} - T_{i,j-1}}{\frac{1}{2}(\Delta y_{j-1} + \Delta y_j)} \right) - \left(q_{r,i,j+\frac{1}{2}} - q_{r,i,j-\frac{1}{2}} \right) \right]
 \end{aligned}
 \tag{D.4}$$

Equation D.4 may be written as

$$\begin{aligned}
 & -\frac{2\Delta x(k_f + \rho_f C_p \epsilon_H)_{i,j-\frac{1}{2}}}{\Delta y_j(\Delta y_{j-1} + \Delta y_j)} T_{i,j-1} \\
 & + \left[\frac{2\Delta x(k_f + \rho_f C_p \epsilon_H)_{i,j-\frac{1}{2}}}{\Delta y_j(\Delta y_{j-1} + \Delta y_j)} + \frac{2\Delta x(k_f + \rho_f C_p \epsilon_H)_{i,j+\frac{1}{2}}}{\Delta y_j(\Delta y_j + \Delta y_{j+1})} + C_p(\rho_f \bar{u})_{i,j} \right] T_{i,j} \\
 & - \frac{2\Delta x(k_f + \rho_f C_p \epsilon_H)_{i,j+\frac{1}{2}}}{\Delta y_j(\Delta y_j + \Delta y_{j+1})} T_{i,j+1} = -\frac{\Delta x}{\Delta y_j} \left(q_{r,i,j+\frac{1}{2}} - q_{r,i,j-\frac{1}{2}} \right) + C_p(\rho_f \bar{u} \bar{T})_{i-1,j}
 \end{aligned} \tag{D.5}$$

The form of this equation corresponds to a diagonal matrix as

$$-A_j T_{i,j-1} + B_j T_{i,j} - C_j T_{i,j+1} = D_j \tag{D.6}$$

where the A , B , C and D constant are

$$\begin{aligned}
 A_j &= \frac{2\Delta x(k_f + \rho_f C_p \epsilon_H)_{i,j-\frac{1}{2}}}{\Delta y_j(\Delta y_{j-1} + \Delta y_j)} \\
 B_j &= \left[\frac{2\Delta x(k_f + \rho_f C_p \epsilon_H)_{i,j-\frac{1}{2}}}{\Delta y_j(\Delta y_{j-1} + \Delta y_j)} + \frac{2\Delta x(k_f + \rho_f C_p \epsilon_H)_{i,j+\frac{1}{2}}}{\Delta y_j(\Delta y_j + \Delta y_{j+1})} + C_p(\rho_f \bar{u})_{i,j} \right] \\
 C_j &= \frac{2\Delta x(k_f + \rho_f C_p \epsilon_H)_{i,j+\frac{1}{2}}}{\Delta y_j(\Delta y_j + \Delta y_{j+1})} \\
 D_j &= -\frac{\Delta x}{\Delta y_j} \left(q_{r,i,j+\frac{1}{2}} - q_{r,i,j-\frac{1}{2}} \right) + C_p(\rho_f \bar{u} \bar{T})_{i-1,j}
 \end{aligned} \tag{D.7}$$

Since $-A_j + B_j - C_j = u_j > 0$, the matrix is strictly diagonally dominant and always admits a non-oscillatory solution. Note that the discretization of the radiative flux divergence conserves the notation $(j + \frac{1}{2})$ and $(j - \frac{1}{2})$. It is because the radiative fluxes are computed at the limits of the mesh and not within it. As usually recommended, the $(k_f + \rho_f C_p \epsilon_H)$ coefficients are approximated by using harmonic means.

$$\begin{aligned}
 (k_f + \rho_f C_p \epsilon_H)_{i,j-\frac{1}{2}} &= \frac{2}{\frac{1}{(k_f + \rho_f C_p \epsilon_H)_{i,j-1}} + \frac{1}{(k_f + \rho_f C_p \epsilon_H)_{i,j}}} \\
 &= 2 \frac{(k_f + \rho_f C_p \epsilon_H)_{i,j-1} (k_f + \rho_f C_p \epsilon_H)_{i,j}}{(k_f + \rho_f C_p \epsilon_H)_{i,j-1} + (k_f + \rho_f C_p \epsilon_H)_{i,j}} \\
 (k_f + \rho_f C_p \epsilon_H)_{i,j+\frac{1}{2}} &= \frac{2}{\frac{1}{(k_f + \rho_f C_p \epsilon_H)_{i,j}} + \frac{1}{(k_f + \rho_f C_p \epsilon_H)_{i,j+1}}} \\
 &= 2 \frac{(k_f + \rho_f C_p \epsilon_H)_{i,j} (k_f + \rho_f C_p \epsilon_H)_{i,j+1}}{(k_f + \rho_f C_p \epsilon_H)_{i,j} + (k_f + \rho_f C_p \epsilon_H)_{i,j+1}}
 \end{aligned} \tag{D.8}$$

D.1. Control volume method discretization

Numerical treatment of the boundary conditions

The boundary conditions presented in subsection 6.3.4 are discretized to close the matrix given by the inner Eq. D.5.

Inlet temperature condition at $x = 0$

$$T(0, j) = T_{in} \quad (D.9)$$

This boundary condition permits to calculate the $T(1, j)$, which in the next step will be used to calculate $T(2, j)$ and so on.

Convective surface wall condition at $y = 0$

The Fourier boundary condition applied at $y = 0$ is expressed as

$$-k_f \frac{\partial T}{\partial y} \Big|_{y=0} = \bar{U}(T(i, 0) - T_{amb}) \quad (D.10)$$

where T_{amb} is the exterior temperature, and \bar{U} is the overall transfer coefficient. Note that the boundary condition is based on the temperature close to the wall as well as the numerical solution of Eq. D.5 solves the temperature in the center of the control volume, a linear extrapolation is used to find this temperature (see Fig. D.1b). It is expressed as $T_{i,0} = 3/2T_{i,1} - 1/2T_{i,2}$. Applying this boundary condition, the coefficients of the matrix given by Eq. D.5 are

$$\begin{aligned} A_1 &= 0 \\ B_1 &= \frac{2\Delta x(k_f + \rho_f C_p \epsilon_H)_{i,1+\frac{1}{2}}}{\Delta y_1(\Delta y_1 + \Delta y_2)} - \frac{3\bar{U}\Delta x(k_f + \rho_f C_p \epsilon_H)_{i,1-\frac{1}{2}}}{2k_{f,i,1-\frac{1}{2}}\Delta y_1} + C_p(\rho_f \bar{u})_{i,1} \\ C_1 &= \frac{2\Delta x(k_f + \rho_f C_p \epsilon_H)_{i,1+\frac{1}{2}}}{\Delta y_1(\Delta y_1 + \Delta y_2)} - \frac{\bar{U}\Delta x(k_f + \rho_f C_p \epsilon_H)_{i,1-\frac{1}{2}}}{2k_{f,i,1-\frac{1}{2}}\Delta y_1} \\ D_1 &= -\frac{\Delta x}{\Delta y_1} \left(q_{r,i,1+\frac{1}{2}} - q_{r,i,1-\frac{1}{2}} \right) - \frac{\bar{U}\Delta x(k_f + \rho_f C_p \epsilon_H)_{i,1-\frac{1}{2}}}{k_{f,i,1-\frac{1}{2}}\Delta y_1} T_{amb} + C_p(\rho_f \bar{u} \bar{T})_{i-1,1} \end{aligned} \quad (D.11)$$

Adiabatic surface wall condition at $y = D$

A null flux is imposed at the wall when $y = D$. This condition is written as

$$\frac{\partial T}{\partial y} \Big|_{y=D} = 0 \quad (D.12)$$

Applying this condition, the last matrix coefficients becomes

$$\begin{aligned}
 A_N &= \frac{2\Delta x(k_f + \rho_f C_p \epsilon_H)_{i, N-\frac{1}{2}}}{\Delta y_N(\Delta y_N + \Delta y_{N-1})} \\
 B_N &= \frac{2\Delta x(k_f + \rho_f C_p \epsilon_H)_{i, N-\frac{1}{2}}}{\Delta y_N(\Delta y_N + \Delta y_{N-1})} + C_p(\rho_f \bar{u})_{i, N} \\
 C_N &= 0 \\
 D_N &= -\frac{\Delta x}{\Delta y_N} \left(q_{r i, N+\frac{1}{2}} - q_{r i, N-\frac{1}{2}} \right) + C_p(\rho_f \bar{u} \bar{T})_{i-1, N}
 \end{aligned} \tag{D.13}$$

D.2 Code validations

The accuracies of preliminary numerical results are analyzed in this section. As far as possible, comparisons with analytical solutions are conducted. It is a preliminary step by step study which aims at checking different subroutines of increasingly complexity. In chapter 6 the final step lies in the modeling of turbulent convection in participating media, with large temperature differences between the channel inlet and outlet sections. Grid refinements are carried out at the following different steps.

Fluid flow with constant thermo-physical properties between two parallel plates

The most simplified case is that of the forced convection between two parallel plates with constant thermo-physical properties and without source term. It is used as a preliminary test of the numerical method described above and the code writing for solving the energy equation. Three problems are considered in what follows:

- The first one when $u(y) = u_m = cte$ (slug flow),
- The second one is for a laminar flow (Poiseuille velocity profile),
- The third case is a turbulent flow with a power-law velocity profile and approximate expression of the thermal eddy diffusivity, as described in subsection 6.3.6.

For the first problem, an analytical solution can be readily derived, while there is no analytical solution available in the literature for the second and third problems, owing to the non-symmetrical thermal boundary conditions. However, since the axial variation of the mixing cup-temperature, $T_m(x) = \int_0^D u(y)T(x, y)dy / \int_0^D u(y)dy$, is linear from the inlet to the outlet section (even for thermally developing flow) comparisons between analytical and numerical variations of $T_m(x)$ may be used to check the accuracy of the numerical solutions. For both laminar flows, the energy equation may be written as

$$u(y) \frac{\partial T}{\partial x} = a_f \frac{\partial^2 T}{\partial y^2} \tag{D.14}$$

D.2. Code validations

with the boundary conditions

$$\begin{aligned}
 T(0, y) &= T_{in} \\
 -k_f \frac{\partial T}{\partial y} \Big|_{y=0} &= q_w \\
 \frac{\partial T}{\partial y} \Big|_{y=D} &= 0
 \end{aligned} \tag{D.15}$$

In what follows, the thermo-physical properties are evaluated at $T = 310 \text{ K}$ and are reported in Table D.1.

Density (ρ_f)	1.127	$[\text{kg}/\text{m}^3]$
Kinematic viscosity (ν)	16.97×10^{-6}	$[\text{m}^2/\text{s}]$
Conductivity (k_f)	0.0271	$[\text{W}/\text{mK}]$
Thermal capacity (C_p)	1005	$[\text{J}/\text{kgK}]$
Prandtl number (Pr)	0.708	

Table D.1: Thermo-physical properties of the air at 310 K used in simulations of the convection between two parallel plates with constant properties

The flow parameters used, for the two laminar simulations that follows, are reported in Table D.2.

Geometry depth (D)	1	$[\text{m}]$
Geometry length (L)	1	$[\text{m}]$
Mass flow rate (\dot{m})	0.01	$[\text{kg}/\text{s}]$
Inlet temperature (T_{in})	300	$[\text{K}]$
Wall heat flux (q_w)	100	$[\text{W}/\text{m}^2]$

Table D.2: Parameters used in the simulations of a laminar flow between two parallel plates with constant thermo-physical properties

For the data reported in Table D.1 and D.2, the Reynolds number, $Re_{D_h} = 2\dot{m}/(\rho_f\nu)$, is $Re_{D_h} \approx 1046$ ($D_h = 2D$).

Analytical solution for slug flow $u(y) = u_m$

The slug flow between parallel plates has a straightforward solution reported in many Heat Transfer handbooks. The dimensionless temperature, depth and distance may be defined as

$$\theta(x, y) = \frac{T(x, y) - T_{in}}{q_w D_h / k_f} \quad ; \quad y^* = \frac{y}{D_h} \quad ; \quad x^* = \frac{a_f x}{u_m D^2} \tag{D.16}$$

The dimensionless temperature profile for the boundary conditions given in Eq. D.15 is

$$\theta(x^*, y^*) = x^* + \frac{3y^{*2} - 1}{6} - 2 \sum_{n=1}^{\infty} \frac{(-1)^n}{n^2 \pi^2} \cos(n\pi y^*) e^{-n^2 \pi^2 x^*} \tag{D.17}$$

Appendix D. Numerical method for solving the energy equation and validation tests.

The mixing-cup and wall temperature are thus given by:

$$\begin{aligned}\theta_m(x^*) &= \int_0^1 \theta dy^* = x^* \\ \theta_w(x^*) &= x^* + \frac{1}{3} - 2 \sum_{n=1}^{\infty} \frac{1}{n^2 \pi^2} e^{-n^2 \pi^2 x^*}\end{aligned}\tag{D.18}$$

Consequently, the local Nusselt number varies as

$$Nu(x) = \frac{12}{1 - 6 \sum_{n=1}^{\infty} \frac{1}{n^2 \pi^2} e^{-n^2 \pi^2 x^*}} \Leftrightarrow \lim_{x^* \rightarrow \infty} Nu(x) = 12\tag{D.19}$$

For a flat velocity profile, the above analytical solution still holds in a channel of width D (hydraulic diameter $D_h = 2D$) if the the wall at $y = D$ is adiabatic and the flux q_w is prescribed at $y = 0$. The dimensional form of the equations for the fluid temperature (Eq. D.17) is

$$T(x, y) = T_{in} + \frac{q_w D}{k_f} \left[\frac{a_f x}{u_m D^2} + \frac{3(y/D)^2 - 1}{6} - 2 \sum_{n=1}^{\infty} \frac{(-1)^n}{n^2 \pi^2} \cos\left(\frac{n\pi y}{D}\right) e^{-n^2 \pi^2 \left(\frac{a_f x}{u_m D^2}\right)} \right]\tag{D.20}$$

and at the heated wall

$$T_w(x) = T_{in} + \frac{q_w D}{k_f} \left[\frac{a_f x}{u_m D^2} + \frac{1}{3} - 2 \sum_{n=1}^{\infty} \frac{1}{n^2 \pi^2} e^{-n^2 \pi^2 \left(\frac{a_f x}{u_m D^2}\right)} \right]\tag{D.21}$$

Such an alternate series term converges very slowly for very small values of the exponential argument. The flow is thermally developed when

$$\frac{\partial T}{\partial x} = \frac{dT_w}{dx} = \frac{dT_m}{dx} = \frac{q_w}{\rho_f u_m D C_p}\tag{D.22}$$

or

$$\frac{d}{dx} \left[\sum_{n=1}^{\infty} \frac{1}{n^2 \pi^2} e^{-n^2 \pi^2 \left(\frac{a_f x}{u_m D^2}\right)} \right] = -\frac{a_f}{u_m D^2} \left[\sum_{n=1}^{\infty} e^{-n^2 \pi^2 \left(\frac{a_f x}{u_m D^2}\right)} \right] = 0\tag{D.23}$$

Since the term of the above series are positive and < 1 , the summation may be assumed convergent for a $n - x$ couple value such as $n^2 \pi^2 \left(\frac{a_f x}{u_m D^2}\right) > 10$ (since $\exp(-10) = 4.5 \times 10^{-5}$). For a distance x from the inlet section, the minimum number of term to be considered is therefore of the order of $n^2 \approx u_m D^2 / a_f x = Pe_{D_h} / (2x/D)$ or $n \approx \sqrt{Pe_{D_h} D / 2x}$, where the Peclet number is defined as $Pe = u_m D_h / a_f$. In the case studied (Tables D.1 and D.2), $D = 1\text{ m}$, $Re_{D_h} \approx 1046$ and $Pe_{D_h} = 740.4$. Thus, the number of terms must be $n > \sqrt{370.2} x^{-1/2} \approx 20 x^{-1/2}$ in order that comparisons with the numerical data make sense. In conclusion, the calculation of the analytical solution is relevant provided that $n \geq 200$ for $x > 0.01\text{ m}$.

The search for an accurate grid resolution is based on the changes in the axial, wall and mixing cup temperatures, and local heat transfer coefficient at the mid-length and

D.2. Code validations

n_y	40	80	160	320	640
$T(L/2, D/2)$	300	300	300	300	300
$T_w(L/2)$	439.926	449.349	451.817	452.441	452.597
$T_m(L/2)$	304.975	304.975	304.975	304.975	304.975
$h(L/2)$	0.741	0.693	0.681	0.678	0.677
$T(L, D/2)$	300	300	300	300	300
$T_w(L)$	506.841	513.705	515.459	515.90	516.01
$T_m(L)$	309.950	309.950	309.950	309.95	309.95
$h(L)$	0.508	0.491	0.487	0.486	0.485

Table D.3: Axial, wall and mixing cup temperatures (K), and local heat transfer coefficient ($h = q_w / (T_w - T_m) W/m^2 K$) at channel mid-length and at the outlet section according to the grid resolution n_y in the channel cross-section ($n_x = 160$, $L = D = 1 m$, $Re_{D_h} = 1046$, $T_{in} = 300 K$, $q_w = 100 W/m^2$)

n_x	40	80	160	320	640
$T(L/2, D/2)$	300	300	300	300	300
$T_w(L/2)$	451.091	451.575	451.817	451.938	451.999
$T_m(L/2)$	304.975	304.975	304.975	304.975	304.975
$h(L/2)$	0.684	0.682	0.681	0.680	0.680
$T(L, D/2)$	300	300	300	300	300
$T_w(L)$	514.949	515.289	515.459	515.544	515.587
$T_m(L)$	309.95	309.95	309.95	309.95	309.95
$h(L)$	0.488	0.487	0.487	0.486	0.486

Table D.4: Axial, wall and mixing cup temperatures (K), and local heat transfer coefficient ($h = q_w / (T_w - T_m) W/m^2 K$) at channel mid-length and at the outlet section according to the grid resolution n_x in the channel cross-section ($n_y = 160$, $L = D = 1 m$, $Re_{D_h} = 1046$, $T_{in} = 300 K$, $q_w = 100 W/m^2$)

<i>Analytical solution</i> ($n = 200$)						
$T(L/2, D/2)$	$T_w(L/2)$	$T_m(L/2)$	$h(L/2)$	$T_w(L)$	$T_m(L)$	$h(L)$
300	452.505	304.975	0.678	515.945	309.95	0.485
<i>Numerical solution</i> (200×500)						
$T(L/2, D/2)$	$T_w(L/2)$	$T_m(L/2)$	$h(L/2)$	$T_w(L)$	$T_m(L)$	$h(L)$
300	452.611	304.975	0.677	516.02	309.95	0.485
<i>Discrepancies</i>						
0 K	0.106 K	0 K	0.0%	0.08 K	0 K	0.0%

Table D.5: Comparisons between axial, wall and mixing cup temperatures (K), and local heat transfer coefficient ($W/m^2 K$) at the channel mid-length and at the outlet section ($L = D = 1 m$, $Re_{D_h} = 1046$, $T_{in} = 300 K$, $q_w = 100 W/m^2$)

at the outlet of the channel according to the n_x and n_y values. For both n_x and n_y variations, the mesh number in the orthogonal direction is 160. Results are presented in Tables D.3 and D.4 for the n_y and n_x variations, respectively.

The highest temperatures are located in the close wall region and in the thermally

developing region, where large temperature gradients are observed. However, the channel length being much smaller than the thermal developing length, the heat is mainly transferred in the thermal boundary layer along the heated wall whose thickness is much smaller than the channel width. Therefore, the channel length considered here is not large enough in order that significant change in the core flow temperature occurs. Consequently, $T(x, D/2)$ is very close to T_{in} at $x = L$. The wall temperature is thus the best indicator of the mesh resolution. From Tables D.3 and D.4, it can be seen that the problem is more sensitive to the y -grid resolution, reaching an acceptable accuracy provided that $n_y \geq 320$.

An uniform grid consisting in 200×500 control volumes is kept for the comparison with the analytical results. In Table D.5 and Fig. D.2, the outlet analytical temperature profile based on Eq. D.20 is compared with the numerical profile. The local heat transfer coefficients at $x = L/2$ and at $x = L$ are reported in Table D.5. In Fig. D.2, the inset presents an enlargement of the temperature profile close to the heated wall. As can be seen, the agreement is very good.

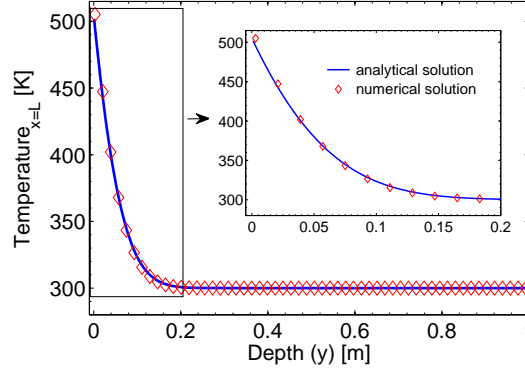


Figure D.2: Comparison between the analytical and numerical outlet temperature profiles for a slug flow between two parallel plates with a prescribed wall heat flux (see Tables D.1 and D.2 for the set of parameters)

Numerical solution for laminar (Poiseuille) flows

A slight modification brought to the previous problem lies in the use of a parabolic velocity profile. The origin of the coordinate system being located at the heated plate, the Poiseuille velocity profile reads

$$u(y) = \frac{By}{2}(y - D) \quad \text{with} \quad B = \frac{1}{\mu_f} \frac{dp}{dx} < 0 \quad (\text{D.24})$$

It results that

$$u_{max} = -\frac{BD^2}{8}, \quad u_m = -\frac{BD^2}{12} \quad \implies \quad u_m = \frac{2}{3}u_{max} \quad (\text{D.25})$$

Therefore

$$u(y) = 6u_m \frac{y}{D} \left(1 - \frac{y}{D}\right) \quad (\text{D.26})$$

D.2. Code validations

From the energy equation (Eq. D.14) and the boundary conditions (Eq. D.15), an energy balance between sections x and $x + dx$ leads to

$$\dot{m}C_p \frac{dT_m}{dx} = q_w \quad \text{with } T_m(0) = T_{in} \quad (\text{D.27})$$

Therefore

$$T_m(x) = T_{in} + \frac{q_w}{\dot{m}C_p} x \quad (\text{D.28})$$

and

$$T_m(L) = T_{in} + \frac{q_w}{\dot{m}C_p} L \quad (\text{D.29})$$

The above solution is valid whatever the velocity profile is, including turbulent profiles, provided that the thermal boundary conditions are kept.

As for the slug flow, a meshing study is conducted, utilizing similar mesh variations. The thermal properties and the parameters for such simulations are given in Tables D.1 and D.2, respectively. The results of the mesh study are presented in Tables D.6 and D.7

n_y	40	80	160	320	640
$T(L/2, D/2)$	300	300	300	300	300
$T_w(L/2)$	646.616	649.51	650.009	650.106	650.126
$T_m(L/2)$	305.069	304.999	304.981	304.977	304.976
$T(L, D/2)$	300	300	300	300	300
$T_w(L)$	741.070	743.099	743.465	743.538	743.554
$T_m(L)$	310.044	309.974	309.956	309.952	309.951

Table D.6: Axial, wall and mixing cup temperatures (K) at channel mid-length and at the outlet section according to the grid resolution n_y in the channel cross-section ($n_x = 160$, $L = D = 1 m$, $Re_{D_h} = 1046$, $T_{in} = 300 K$, $q_w = 100 W/m^2$)

n_x	40	80	160	320	640
$T(L/2, D/2)$	300	300	300	300	300
$T_w(L/2)$	648.549	649.522	650.009	650.253	650.374
$T_m(L/2)$	304.981	304.981	304.981	304.981	304.981
$T(L, D/2)$	300	300	300	300	300
$T_w(L)$	742.541	743.157	743.465	743.619	743.696
$T_m(L)$	309.956	309.956	309.956	309.956	309.956

Table D.7: Axial, wall and mixing cup temperatures (K) at channel mid-length and at the outlet section according to the grid resolution n_x in the channel cross-section ($n_y = 160$, $L = D = 1 m$, $Re_{D_h} = 1046$, $T_{in} = 300 K$, $q_w = 100 W/m^2$)

Due to the lower velocities close to the no-slip heated wall, the wall temperatures are higher than those predicted for a slug flow with the same flow rate, while the temperature gradients are smaller. Briefly, the grid study leads to similar conclusion:

Appendix D. Numerical method for solving the energy equation and validation tests.

an acceptable mesh independence is found for $n_x \geq 160$ and $n_y \geq 320$. As for the slug flow, a $n_x = 200$ and $n_y = 500$ grid resolution is kept in this subsection. The parabolic velocity profile is shown in Fig. D.3a. Figure D.3b shows a comparison between analytical (Eq. D.29) and numerical solutions for the mixing cup temperature variation.

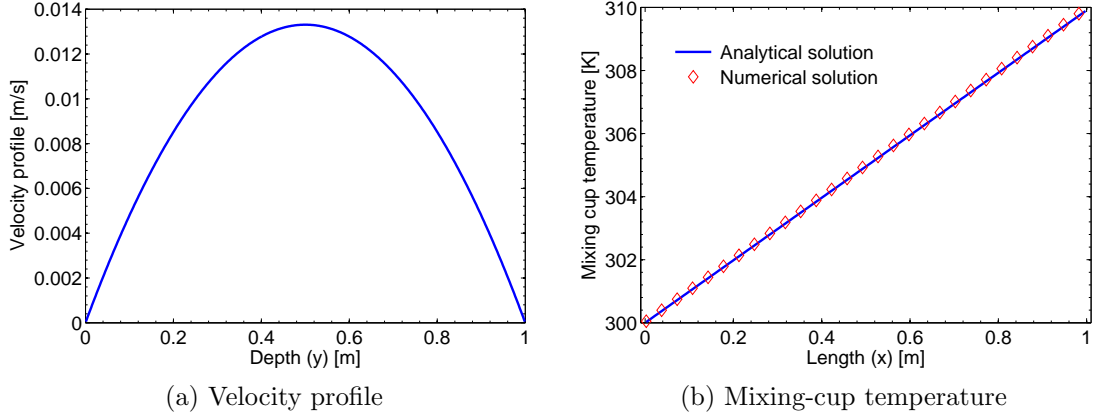


Figure D.3: Velocity profile (a) and analytical and numerical mixing-cup temperature (T_m) comparison (b) for a Poiseuille flow between two parallel plates with a prescribed wall heat flux (see Tables D.1 and D.2 for the set of parameters)

The mixing cup temperature comparison (Fig. D.3b) shows a good agreement between the analytical and numerical results. The discrepancies are negligibly small (differences in $T_m(L)$ less than 0.1 K). The heat transfer coefficients at $x = L/2$ and at $x = L$ can be calculated from the data reported in Table D.6. In comparison with the slug flow, it is found that both $h(L/2)$ and $h(L)$ decrease by a factor larger than 2. This results may be deduced from the comparisons between the shapes of the temperature profiles shown in the enlargements displayed in Fig. D.4. Therefore, the above results are, as expected, well physically based.

Numerical solution for turbulent $u(y)$ -flows

In the case of a turbulent flow, the thermal eddy diffusivity should be considered in the solution of the energy equation. If a basic turbulence modeling is used, as in the present work. The energy equation is

$$\bar{u}(y) \frac{\partial \bar{T}}{\partial x} = \frac{\partial}{\partial y} \left((a_f + \epsilon_H(y)) \frac{\partial \bar{T}}{\partial y} \right) \quad (\text{D.30})$$

with the boundary conditions $T(0, y) = T_{in}$, $-k_f \partial T / \partial y|_0 = q_w$ and $\partial T / \partial y|_D = 0$.

Obviously, no fully analytical solution may be derived for this problem. Following the step-by-step validation of the numerical procedure, the results are nevertheless checked from physical insights and comparisons with that has been discussed in the previous subsections. According to subsection 6.3.6, the power-law velocity profile used

D.2. Code validations

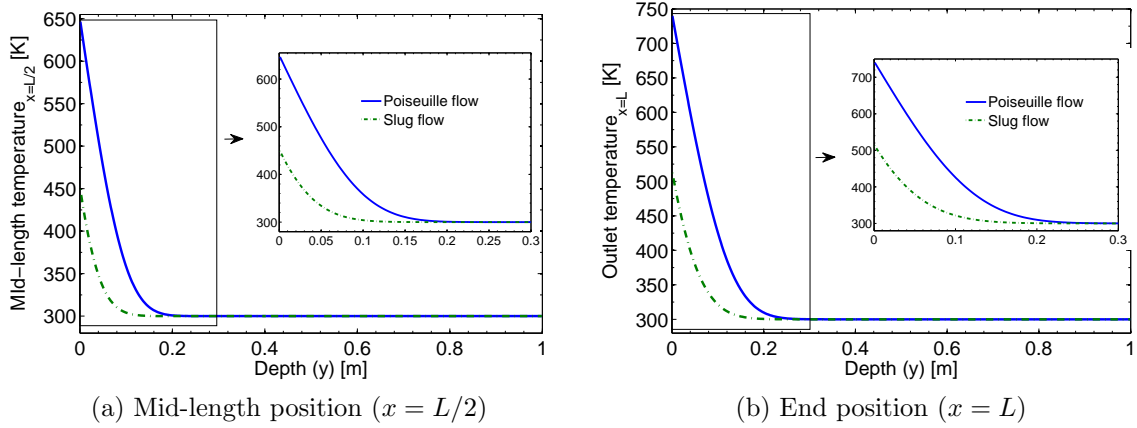


Figure D.4: Comparison between the slug and Poiseuille temperature profiles in cross-sections at channel mid-length and at the outlet ($L = D = 1\text{ m}$, $Re_{D_h} = 1046$, $T_{in} = 300\text{ K}$, $q_w = 100\text{ W/m}^2$)

is

$$\begin{aligned}\bar{u}(y) &= \bar{u}_{max} \left(\frac{y}{D/2} \right)^{1/n} & 0 \leq y \leq D/2 \\ \bar{u}(y) &= \bar{u}_{max} \left(\frac{D-y}{D/2} \right)^{1/n} & D/2 \leq y \leq D\end{aligned}\tag{D.31}$$

The mean velocity reads

$$\bar{u}_m = \frac{2}{D} \int_0^{D/2} \bar{u}_{max} \left(\frac{y}{D/2} \right)^{1/n} dy = \bar{u}_{max} \left(\frac{2}{D} \right)^{\frac{n+1}{n}} \int_0^{D/2} y^{1/n} dy = \bar{u}_{max} \frac{n}{n+1}\tag{D.32}$$

Therefore

$$\begin{aligned}\bar{u}(y) &= \bar{u}_m \frac{n+1}{n} \left(\frac{y}{D/2} \right)^{1/n} & 0 \leq y \leq D/2 \\ \bar{u}(y) &= \bar{u}_m \frac{n+1}{n} \left(\frac{D-y}{D/2} \right)^{1/n} & D/2 \leq y \leq D\end{aligned}\tag{D.33}$$

The thermal eddy diffusivity is computed following the formulation given by Eq. 6.45. This approximation has the advantage that may be solved without using the friction velocity. It is expressed as

$$\epsilon_H(y) = \frac{1}{Pr_t} \left[0.0198(yu) \left(1 - \exp\left(-\frac{yu}{100\nu}\right) \right)^2 \right]\tag{D.34}$$

with the turbulent Prandtl computed as

$$\frac{1}{Pr_t} = 0.91 + 0.13Pr^{0.545}\tag{D.35}$$

Appendix D. Numerical method for solving the energy equation and validation tests.

Geometry depth (D)	1	[m]
Geometry length (L)	1	[m]
Mass flow rate (\dot{m})	0.5	[kg/s]
Inlet temperature (T_{in})	300	[K]
Wall heat flux (q_w)	1500	[W/m ²]

Table D.8: Parameters used in simulation of a turbulent flow in a channel with constant thermo-physical properties and without source term

To conduct a grid study, the molecular thermal properties are kept as those reported in Table D.1. The flow parameters used here are given in Table D.8.

For the parameters given in Table D.8, the average velocity based on the inlet density ($\rho_f = 1.127 \text{ kg/m}^3$) is $\bar{u}_m = 0.4437 \text{ m/s}$. The Reynolds number is thus $Re_{D_h} = 5.23 \times 10^4$. The exponent in the power law profile for these conditions may be taken as $n = 7$. Consequently $\bar{u}_{max} = 0.507 \text{ m/s}$. The turbulent Prandtl number being $Pr_t = 0.983$, the maximum thermal eddy diffusivity is $\epsilon_H(D/2) = 5.106 \times 10^{-3} \text{ m}^2/\text{s}$, and $\epsilon_H(D/2)/a_f = \epsilon_H(D/2)Pr/\nu = 213$. For $y \geq 0.08$, the molecular thermal diffusivity is less than about $\epsilon_H/10$. Therefore, it can be considered that the flow is fully turbulent over about 80% of the channel width.

The profiles of the turbulent velocity and thermal eddy diffusivity-molecular diffusivity ratio are plotted in Fig. D.5. As may be seen, the increase in thermal eddy diffusivity is symmetric about the channel axis and almost linear over most of the channel width.

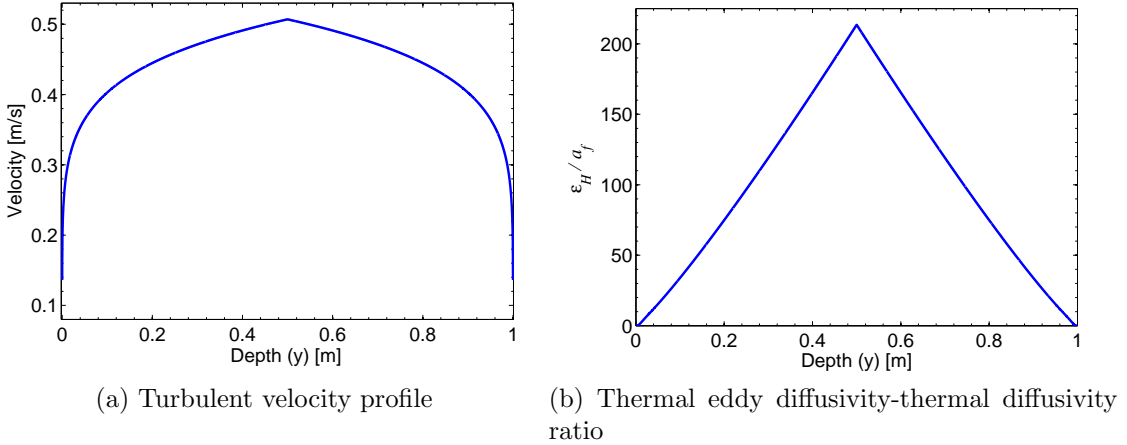


Figure D.5: Velocity profile (a) and thermal eddy diffusivity-thermal diffusivity ratio for a turbulent flow between two parallel plates (see Tables D.1 and D.2 for the set of parameters)

For $q_w = 1500 \text{ W/m}^2$, the outlet mixing-cup temperature should be $T_m(L) = 302,98 \text{ K}$. Fig. D.6 shows that this prediction is numerically recovered.

As in previous paragraphs, a mesh study is conducted to determine an optimal grid resolution. The results are reported in Tables D.9 and D.10. The n_x convergence may be assumed for $n_x \geq 160$, as for laminar flow since the axial temperature gradient is

D.2. Code validations

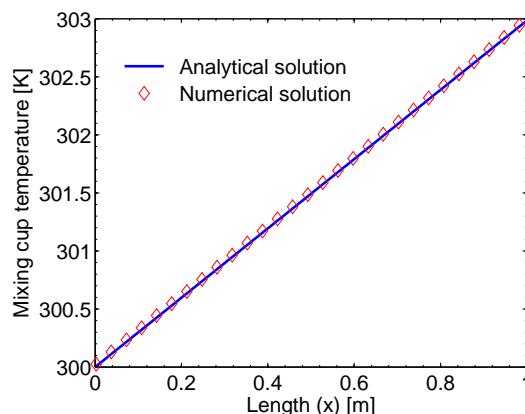


Figure D.6: Mixing-cup temperature (T_m) comparison for a turbulent flow between two parallel plates (see Tables D.1 and D.2 for the set of parameters)

about the same (i.e. same q_w). In contrast, the convergence of the wall temperature (Table D.10) requires more meshes owing to the step change in the thermal eddy diffusivity in the near wall region ($y^+ \leq 30$). In conclusion, a non-uniform y -grid should be more appropriate to properly capture the temperature distribution in the near-wall region. However, it is not taken into account because the wall temperature gradients are, for the practical application considered, much smaller than the volumetric heat dissipated in a SPR.

n_x	40	80	160	320	640
$T(L/2, D/2)$	300	300	300	300	300
$T_w(L/2)$	612.007	613.707	614.563	614.992	615.208
$T_m(L/2)$	301.576	301.576	301.576	301.5768	301.576
$h(L/2)$	4.832	4.806	4.793	4.786	4.783
$T(L, D/2)$	300	300	300	300	300
$T_w(L)$	734.949	736.054	736.606	736.883	737.021
$T_m(L)$	303.068	303.068	303.068	303.068	303.068
$h(L)$	3.473	3.464	3.46	3.458	3.457

Table D.9: Axial, wall and mixing cup temperatures (K), and local heat transfer coefficient ($h = q_w/(T_w - T_m)$ W/m^2K) at channel mid-length and at the outlet section according to the grid resolution n_x in the channel cross-section ($n_y = 160$, $q_w = 1500 W/m^2$, $\dot{m} = 0.5 kg/s$, $L = D = 1 m$, $Re_{D_h} = 5.2287 \times 10^4$, $T_{in} = 300 K$)

Finally, a comparison between the temperature distributions for the three velocity profiles considered before (i.e. slug, Poiseuille and power-law profiles) is carried out in chapter 6. If the comparison with the slug flow case is relevant (because some approximate analytical solutions leading to Nusselt number correlations are based on this approximation, for example the Karman-Boelter-Martinelli correlation), the comparison with the Poiseuille velocity profile is used just to check that the turbulent temperature profile cannot be over this theoretical bound.

The conditions presented in Tables D.1 and D.8 and a 200×1000 grid for the computations are used. The results are presented in Fig. D.7. As expected, the turbulent

Appendix D. Numerical method for solving the energy equation and validation tests.

n_y	40	80	160	320	640	1280
$T(L/2, D/2)$	300	300	300	300	300	300
$T_w(L/2)$	409.191	506.463	614.563	677.531	696.957	701.152
$T_m(L/2)$	301.895	301.676	301.576	301.53	301.51	301.5
$h(L/2)$	13.98	7.325	4.793	3.989	3.793	3.753
$T(L, D/2)$	300	300	300	300	300	300
$T_w(L)$	487.346	624.557	736.606	789.88	805.176	808.109
$T_m(L)$	303.387	303.168	303.068	303.023	303.002	302.993
$h(L)$	8.154	4.667	3.46	3.081	2.987	2.97

Table D.10: Axial, wall and mixing cup temperatures (K), and local heat transfer coefficient ($h = q_w/(T_w - T_m)$ W/m^2K) at channel mid-length and at the outlet section according to the grid resolution n_y in the channel cross-section ($n_x = 160$, $q_w = 1500 W/m^2$, $\dot{m} = 0.5 kg/s$, $L = D = 1 m$, $Re_{D_h} = 5.2287 \times 10^4$, $T_{in} = 300 K$)

flow results are between the laminar and the slug flow cases. Since the difference between \bar{u}_m and \bar{u}_{max} is rather small ($\bar{u}_{max} = 8/7\bar{u}_m$), the turbulent profiles are much closest to the slug temperature profile than to the Poiseuille ones.

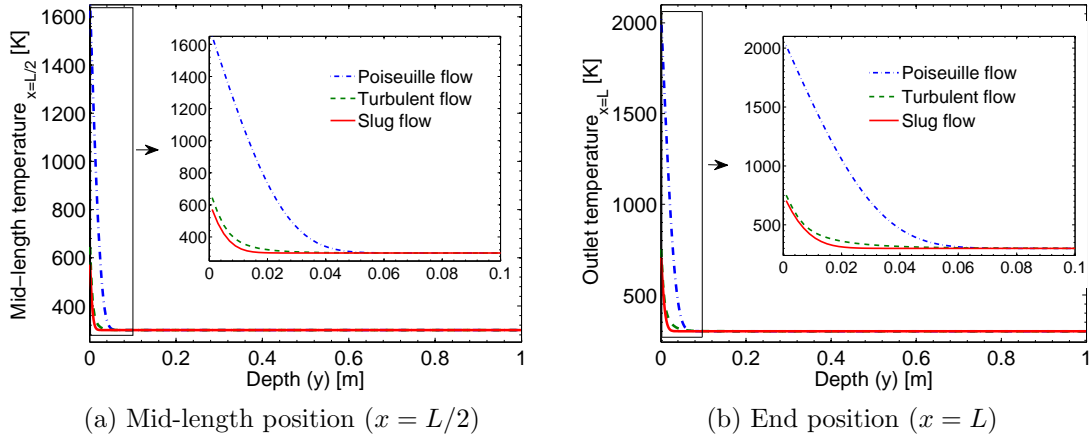


Figure D.7: Temperatures profiles at the mid-length and end positions for a laminar, turbulent and slug flow. Identical thermo-physical properties and flow conditions are used for the three simulations (see Tables D.1 and D.2 for the set of parameters)

List of Tables

2.1	Validation cases for the TSLAYER subroutine. In column 2 a schematic of each case, in column 3 a brief explanation and in column 4 the methods taken as reference.	35
2.2	Comparison of the radiative losses for an anisotropic and cold slab of particles dispersion ($x = 10$, $q_{0,\lambda} = 200 \text{ kW/m}^2\mu\text{m}$)	35
2.3	Comparison of the radiative losses for an anisotropic and emitting slab of particles dispersion ($x = 10$, $T = 1000\text{K}$, $q_{0,\lambda} = 200 \text{ kW/m}^2\mu\text{m}$)	36
2.4	Comparison of the radiative losses for an anisotropic and emitting slab of particles dispersion. A linear temperature profile starting at $T_0 = 800\text{K}$ and ending at $T_w = 1600\text{K}$ is used ($x = 10$, $q_{0,\lambda} = 200 \text{ kW/m}^2\mu\text{m}$)	36
2.5	Optical particle properties used in the comparison of an anisotropic and emitting two-layer medium	37
2.6	Volume radiative coefficients computed with the VPPOLY subroutine and taken from Modest [15]. The particles gamma distribution parameters are $a = 2$, $b = 1.7594$ and $N_0 = 10^{10} \text{ m}^{-3}$ and the wavelength is $\lambda = 3.1416 \mu\text{m}$	38
3.1	χ_0 -term computed for two parameter sizes with the Lorenz-Mie and the Henyey-Greenstein phase functions ($m = 2.58 + 0.107i$ and $\lambda = 0.5 \mu\text{m}$)	46
3.2	γ -terms and slab emissivity for a purely absorptive ($\omega_0 = 0$) and optically thick ($\tau \rightarrow \infty$) media without incident flux. The comparison is done for the two-stream approximations studied	49
3.3	Comparison of the maximal spectral error and the integrated normalized radiative losses for a high temperature SPR using the optimized ideal material. MC means Monte Carlo method, TS means two-stream method, HG means Henyey-Greenstein phase function, M&W means Meador and Weaver approximation and J&al. means Joseph <i>et al.</i> approximation	52
4.1	Constraint factors used in the PSO algorithm	59
4.2	Parameter ranges used for the cold particle receiver optimization. The particle radius and most probable radius are in μm	60
4.3	Optimized radiative losses for a cold SPR using a mono-dispersion and a poly-dispersion of particles ($\lambda = 0.5 \mu\text{m}$)	60
4.4	Conditions used for the particle receiver optimization	64
4.5	Parameter ranges used in the particle receiver optimization	64

List of Tables

4.6	Optimized parameters for a single-layer SPR with two different temperature profiles	65
4.7	Representative cases considered for the study of a SPR composed by two layers. A linear temperature profile (700 – 1100 K) is assumed . .	70
4.8	Optical thickness, radiative losses and receiver efficiency for the two cases reported in Table 4.7	70
5.1	Conditions used for the high temperature SPR simulations	77
5.2	Radiative losses for the SPR model using four different particle sizes. The volume fraction is large enough to achieve asymptotic values of the radiative losses . The radiative losses are in kW/m^2 and the normalized radiative losses (in %) are shown in parenthesis	83
6.1	Exponent of the power-law relationship and ratio of the mean velocity to the maximum velocity in a smooth pipe	100
6.2	Thermo-physical properties of the air at 310 K used in simulations of the convection between two parallel plates with constant properties . .	105
6.3	Conditions used in simulations of a turbulent flow between two parallel plates with a constant source term	106
6.4	Conditions used in the simulations of a turbulent flow between two parallel plates with a large heat generation term and with a convective boundary condition	107
6.5	Comparison of the outlet thermal eddy diffusivity at different positions using constant and variable thermal properties (k_f and ν_f) for a turbulent flow into a channel ($L = D = 1 m$, $Re_{D_h} = 5.23 \times 10^4$)	112
6.6	Outlet temperature comparisons at few y -positions for a turbulent flow into a channel ($L = D = 1 m$, $Re_{D_h} = 5.23 \times 10^4$), using constant or variable thermal properties	113
6.7	Comparisons between the wall temperatures at few downstream locations ($L = D = 1 m$, $Re_{D_h} = 5.23 \times 10^4$), using constant or variable thermal properties	114
6.8	Parameters used in simulations of an absorbing, scattering and emitting slug flow between two parallel plates	116
6.9	Thermo-physical properties used in the simulations for the air and for the <i>SiC</i> at $T = 500 K$	118
6.10	Conditions used in simulations of a SPR	118
6.11	Energy balance results for a SPR using a low volume fraction of particles (see Tables 6.9 and 6.10 for the conditions)	119
6.12	Energy balance results for a SPR using a high volume fraction of particles (see Tables 6.9 and 6.10 for the conditions)	121
6.13	Conditions used in simulations of a SPR	122
6.14	Thermo-physical properties used in the simulations for the air at $T = 500 K$ and densities for the solids	123
6.15	Energy balance for the SPR using an optimized ideal material and three volume fractions (see Tables 6.13 and 6.14 for the conditions and the set of parameters)	126

6.16	Wall reflectivity and optical thickness employed in the parametric study using several real materials	127
6.17	Mixing-cup temperature at the outlet section and energy balance for the SPR using several materials and the optimized ideal one (see Tables 6.13, 6.14 and 6.16 for the conditions and the set of parameters)	127
B.1	Random number relations for participating media. The inversed expressions are for an isotropic phase function (directions) and for an homogeneous medium (path lengths)	149
D.1	Thermo-physical properties of the air at 310 K used in simulations of the convection between two parallel plates with constant properties . .	162
D.2	Parameters used in the simulations of a laminar flow between two parallel plates with constant thermo-physical properties	162
D.3	Axial, wall and mixing cup temperatures (K), and local heat transfer coefficient ($h = q_w/(T_w - T_m) W/m^2K$) at channel mid-length and at the outlet section according to the grid resolution n_y in the channel cross-section ($n_x = 160, L = D = 1 m, Re_{D_h} = 1046, T_{in} = 300 K, q_w = 100 W/m^2$)	164
D.4	Axial, wall and mixing cup temperatures (K), and local heat transfer coefficient ($h = q_w/(T_w - T_m) W/m^2K$) at channel mid-length and at the outlet section according to the grid resolution n_x in the channel cross-section ($n_y = 160, L = D = 1 m, Re_{D_h} = 1046, T_{in} = 300 K, q_w = 100 W/m^2$)	164
D.5	Comparisons between axial, wall and mixing cup temperatures (K), and local heat transfer coefficient (W/m^2K) at the channel mid-length and at the outlet section ($L = D = 1 m, Re_{D_h} = 1046, T_{in} = 300 K, q_w = 100 W/m^2$)	164
D.6	Axial, wall and mixing cup temperatures (K) at channel mid-length and at the outlet section according to the grid resolution n_y in the channel cross-section ($n_x = 160, L = D = 1 m, Re_{D_h} = 1046, T_{in} = 300 K, q_w = 100 W/m^2$)	166
D.7	Axial, wall and mixing cup temperatures (K) at channel mid-length and at the outlet section according to the grid resolution n_x in the channel cross-section ($n_y = 160, L = D = 1 m, Re_{D_h} = 1046, T_{in} = 300 K, q_w = 100 W/m^2$)	166
D.8	Parameters used in simulation of a turbulent flow in a channel with constant thermo-physical properties and without source term	169
D.9	Axial, wall and mixing cup temperatures (K), and local heat transfer coefficient ($h = q_w/(T_w - T_m) W/m^2K$) at channel mid-length and at the outlet section according to the grid resolution n_x in the channel cross-section ($n_y = 160, q_w = 1500 W/m^2, \dot{m} = 0.5 kg/s, L = D = 1 m, Re_{D_h} = 5.2287 \times 10^4, T_{in} = 300 K$)	170

D.10 Axial, wall and mixing cup temperatures (K), and local heat transfer coefficient ($h = q_w / (T_w - T_m)$ W/m²K) at channel mid-length and at the outlet section according to the grid resolution n_y in the channel cross-section ($n_x = 160$, $q_w = 1500$ W/m², $\dot{m} = 0.5$ kg/s, $L = D = 1$ m, $Re_{D_h} = 5.2287 \times 10^4$, $T_{in} = 300$ K) 171

List of Figures

1	Schematic of a Concentrated Solar Power plant using a combined cycle	2
2	Schematic representation of absorption and heat transfer of a surface and a volumetric receiver (Fig. taken from [9])	2
1.1	Devices proposed by Hunt [17, 18] (a) Schematic view of the system which includes a radiation receiver (b) Schematic view of the embodiment of the radiation receiver	8
1.2	Schematic of a Small Particle Heat Exchanger Receiver (SPHER) by Hunt [19]	9
1.3	Axial cross-sectional view of a central solar receiver proposed by Kribus <i>et al.</i> [29]	9
1.4	Solar particle receiver by Karni and Bertocchi [21] (a) Schematic illustration of a solar energy receiver (b) Cross-section in the solar energy receiver	10
1.5	Cross-sectional view of a solar particle "rotating-cavity" receiver by Haueter et al [13]	10
1.6	Cross-sectional view of vortex solar reactor [33] (a) Without helical carving (b) With helical carving	11
1.7	Free-falling particles receiver by Kolb [28] (a) Solar particle receiver (b) Suction-recirculation device for stabilizing particle flows within a SPR .	12
1.8	Face-down free-falling down solid particle receive. A below view in the left side and a segment of cavity in the right side [11]	12
1.9	Schematics of early researches on direct-absorption fluidized bed receivers [26]	13
1.10	Schematic of a section-change fluidized bed receiver by Bounaceur [4] .	13
2.1	Schematic for the model formulation of a 1D solar particle receiver . . .	19
2.2	Absorption, scattering and emission by a differential volume of a participating medium	19
2.3	Forward and backward fluxes for a plane parallel problem in a two-stream method	22
2.4	Scattering regime map for independent and dependent scattering [18] .	27
2.5	Gamma size distribution function. In this example, $a=2$, $b=1.7594$, $N_0 = 10^{10}/m^3$, $r_{mp} = 1.14$, $r_{32} = 2.84$ and $r_{mp}/r_{32} = 0.4$	29
2.6	Geometrical optics representation of radiation scattering phenomena by a single spherical particle	30

List of Figures

2.7	Schematic of the scattering cross section by a single particle	31
2.8	Flowchart of the algorithm used to compute the monochromatic radiative losses	34
2.9	Hemispherical fluxes (q^+ and q^-) into an anisotropic and emitting two-layer media. The continuous lines are computed with the TSLAYER subroutine and the crosses with the bvp4c solver ($x = 10$ in both layers, the linear temperature profile starts at $T_0 = 800K$ and ends at $T_w = 1600K$ and $q_{0,\lambda} = 200 kW/m^2\mu m$)	37
3.1	Lorenz-Mie and Henyey-Greenstein phase functions for a particle with two different parameter sizes ($\lambda = 0.5 \mu m$ and $m = 2.58 + i0.107$, which correspond to the <i>SiC</i> at this wavelength)	44
3.2	Asymmetry factor for a spherical particle computed from the Lorenz-Mie formulation (continuous line) and from the integration of the phase function (diamonds) ($m = 2.58 + 0.107i$ and $\lambda = 0.5 \mu m$)	45
3.3	Comparison of the radiative losses when using the Lorenz-Mie and the Henyey-Greenstein phase functions in a cold SPR model solved with a two-stream method ($m = 2.58 + 0.107i$ and $\lambda = 0.5 \mu m$)	46
3.4	Radiative losses for a SPR computed with a Monte Carlo (errorbars) and two two-stream (solid lines for the Joseph <i>et al.</i> and dashed lines for the Meador and Weaver approximations) methods. The SPR is assumed cold, submitted to a concentrated and collimated solar flux and with a reflective wall at the back ($\rho_w = 1$).	47
3.5	Radiative losses for a SPR computed with a Monte Carlo (bars) and a two-stream (solid lines for the Joseph <i>et al.</i> and dashed lines for the Meador and Weaver approximations) methods. The SPR is assumed only emissive without incident flux ($\rho_w = 1$)	49
3.6	Radiative losses computed with the two-stream method and a reference Monte Carlo method [4]. The MC method uses the Henyey-Greenstein phase function approximation. The refractive index, particle size and volume fraction used are the optimal found for a constant temperature profile ($T = 1100 K$) and a solar radiation concentration $C = 600$	51
3.7	Radiative losses computed with the two-stream method and a reference Monte Carlo method [4]. The MC method uses the Lorenz-Mie phase function. The refractive index, particle size and volume fraction used are the optimal found for a constant temperature profile ($T = 1100 K$) and a solar radiation concentration $C = 600$	51
4.1	Transport albedo (ω_t) and absorption efficiency (Q_{abs}) variation vs the refractive index for a single spherical particle	62
4.2	Normalized radiative losses by varying (a) the real part of the refractive index, (b) the imaginary part of the refractive index, and (c) the volume fraction	63
4.3	Schematic of the temperature profile in a volumetric receiver. The dashed lines represent the limiting temperature profiles and the solid line represents the expected temperature profile	64

4.4	Concentrated solar radiation, emissive power, receiver losses, refractive index, asymmetry factor and scattering albedo for an optimized SPR with a constant temperature profile ($T = 1100 K$)	66
4.5	Concentrated solar radiation, emissive power, receiver losses, refractive index, asymmetry factor and scattering albedo for an optimized SPR with a linear temperature profile (700 – 1100 K)	67
4.6	Radiative losses vs. volume fraction for an optimized SPR with constant and linear temperature profiles. The circle on the curves denotes the threshold value	68
4.7	Optimized radiative losses for different particle radius (r in μm). The volume fraction for each particle radius corresponds to the threshold value and the temperature profiles is constant ($T = 1100 K$)	69
4.8	Optimized refractive index, asymmetry factor and scattering albedo for a SPR composed by two layers following the conditions of case 1: $r_1 = 1.3 \mu m$, $f_{v,1} = 7.5 \times 10^{-6}$, $r_2 = 1.3 \mu m$ and $f_{v,2} = 7.5 \times 10^{-6}$ and linear temperature profile (700 – 1100 K)	71
4.9	Optimized refractive index, asymmetry factor and scattering albedo for a SPR composed by two layers following the conditions of case 2: $r_1 = 100 \mu m$, $f_{v,1} = 6 \times 10^{-4}$, $r_2 = 1.3 \mu m$ and $f_{v,2} = 7.5 \times 10^{-6}$ and linear temperature profile (700 – 1100 K)	71
5.1	Schematic of a 1D, isothermal, homogeneous SPR	77
5.2	Reflectance for six materials suggested to be used in high temperature SPRs. The solar spectrum is shown in the insets (black continuous line). The <i>SiC</i> and <i>W</i> reflectivity were computed from the refractive indexes reported in the literature [13, 14]. For the others materials, measured data are shown	79
5.3	Real and imaginary parts of the refractive index (a) and (b) for the hafnium diboride, hafnium carbide and silicon carbide, (c) and (d) for the zirconium diboride, zirconium carbide and tungsten	80
5.4	Real and imaginary parts of the refractive index for an ideal material. In circles those obtained with the Lorenz-Mie theory and the PSO algorithm and in continuous lines computed from reflectivity by using the Kramers-Kronig dispersion relations (see Table 5.1 for the receiver conditions)	82
5.5	Normal reflectivity computed from the two computed refractive indexes shown in Fig. 5.4	83
5.6	Radiative losses of a SPR using different material mixtures with two sizes: (a) $r = 1 \mu m$, (b) $r = 50 \mu m$. In both subfigures a mixing ratio of 1 means a 100 % <i>SiC</i> medium	84
5.7	Radiative losses of a SPR using coated particles. <i>W</i> and UHTCs are used for the core and <i>SiC</i> for the mantle. In both subfigures a core/mantle ratio of 1 means that no coating exists	85
5.8	Comparison of the absorption Mie-efficiencies (Q_{abs}) for <i>W</i> and <i>SiC</i> , <i>W</i> coated with <i>SiC</i> and the optimized ideal material. The particle radius is $r = 50 \mu m$ in which the coating has a thickness of 50 nm	86

List of Figures

6.1	Schematic of the radiative-convective coupling model for a high temperature SPR	92
6.2	Temperatures for a turbulent flow between two adiabatic parallel plates with an uniform heat generation rate (see the conditions in Tables 6.2 and 6.3)	106
6.3	Outlet temperature profiles for a flow between two adiabatic parallel plates with a uniform heat generation term. Slug, Poiseuille and power-law turbulent velocity profiles are considered (see the conditions in Tables 6.2 and 6.3)	107
6.4	Mixing cup temperature and wall temperature variations for a turbulent flow between two parallel plates with an uniform heat generation rate and a convective boundary condition at the wall $y = 0$ (see Tables 6.2 and 6.4 for the set of parameters)	109
6.5	Mid-length and outlet temperature profiles for a turbulent flow between two parallel plates with a volume source term and a convective boundary condition (see Tables 6.2 and 6.4 for the set of parameters)	109
6.6	Comparison of the mixing cup temperature for a turbulent flow between parallel plates and constant source term using either constant or variable thermal conductivities (see Table 6.4 for the set of parameters)	111
6.7	Comparisons of the outlet temperature profiles for a turbulent flow with constant and variable thermal conductivity and kinematic viscosity (see Tables 6.2 and 6.4 for the set of parameters). The insets shown a zoom for the close wall region	111
6.8	Variation of the thermal conductivity in the outlet section (calculated from the temperature profile shown in Fig. 6.7b)	112
6.9	Downstream variation of the average density and the thermal eddy diffusivity at two y positions for a turbulent flow with variable thermal properties (see Tables 6.2 for the inlet thermal properties and 6.4 for the set of parameters)	114
6.10	Downstream variation of $\rho_f C_p \epsilon_H$ product and the thermal conductivity at two y positions for a turbulent flow with variable thermal properties (see Tables 6.2 for the inlet thermal properties and 6.4 for the set of parameters)	114
6.11	Dimensionless temperature profile at two dimensionless positions for an absorbing, emitting and isotropically scattering slug flow between two parallel-plates. The subindex 1 and 2 correspond to the walls	117
6.12	Mixing-cup (a) and wall (b) temperatures into the SPR model developed. A low volume fraction is imposed ($f_v = 7.5 \times 10^{-7}$) in order to represent an optically thin medium (see Tables 6.9 and 6.10 for the conditions)	119
6.13	Temperature profiles and radiative heat divergence at three sections along the channel filled by an optically thin medium (see Tables 6.9 and 6.10 for the conditions)	120
6.14	Mixing-cup (a) and wall (b) temperatures into the SPR. The volume fraction imposed is high ($f_v = 2.5 \times 10^{-5}$) to represent a thick medium (see Tables 6.9 and 6.10 for the conditions)	121

6.15	Profiles of the temperature and of the radiative heat flux divergence at three sections along the channel filled by an optically thick medium (see Tables 6.9 and 6.10 for the conditions)	121
6.16	Absorption and scattering coefficients for a homogeneous medium composed by a gas-particles mixture. The particles material is the optimized ideal one (see chapter 4) and the volume fraction is $f_v = 2.5 \times 10^{-5}$	124
6.17	Outlet temperature profiles for a SPR at multiple volume fractions and at two back wall reflectivities. The material used is the optimized ideal one (see Tables 6.13 and 6.14 for the conditions and the set of parameters)	125
6.18	Receiver efficiencies at multiple volume fractions for two back wall reflectivity. The material used is the optimized ideal one (see Tables 6.13 and 6.14 for the conditions and the set of parameters)	125
6.19	Outlet temperature profiles for the SPR using several materials. The SPR conditions, and the parameters used in simulation are given in Tables 6.13, 6.14 and 6.16	127
6.20	Radiative flux divergences for the SPR using several materials. The SPR conditions, and the parameters used in simulation are given in Tables 6.13, 6.14 and 6.16	128
A.1	Schematic of the plane parallel problem showing the positive and negative fluxes for the two-stream method	137
A.2	Schematic of a multi-layered solar particle receiver	140
B.1	Schematic of a energy packet history in a forward path length Monte Carlo method. W is the energy weight of the bundle, κ is the absorption coefficient, R_1 is a random number between $[0 - 1]$ and θ is the incident angle at the boundary	150
C.1	Real and imaginary part of the Lorentzian function. (a) Circles analytical, solid line analytical extrapolated. (b) Circles analytical, solid line trapezoidal integration, dashed line Maclaurin integration	154
C.2	Real and imaginary part of the refractive index of <i>SiC</i> . Circles from Pégourié, solid line trapezoidal integration, dashed line Maclaurin integration	155
D.1	Schematic of a control volume mesh used in the discretization and a wall control volume showing the convective boundary condition	158
D.2	Comparison between the analytical and numerical outlet temperature profiles for a slug flow between two parallel plates with a prescribed wall heat flux (see Tables D.1 and D.2 for the set of parameters)	165
D.3	Velocity profile (a) and analytical and numerical mixing-cup temperature (T_m) comparison (b) for a Poiseuille flow between two parallel plates with a prescribed wall heat flux (see Tables D.1 and D.2 for the set of parameters)	167
D.4	Comparison between the slug and Poiseuille temperature profiles in cross-sections at channel mid-length and at the outlet ($L = D = 1 m$, $Re_{D_h} = 1046$, $T_{in} = 300 K$, $q_w = 100 W/m^2$)	168

D.5	Velocity profile (a) and thermal eddy diffusivity-thermal diffusivity ratio for a turbulent flow between two parallel plates (see Tables D.1 and D.2 for the set of parameters)	169
D.6	Mixing-cup temperature (T_m) comparison for a turbulent flow between two parallel plates (see Tables D.1 and D.2 for the set of parameters) .	170
D.7	Temperatures profiles at the mid-length and end positions for a laminar, turbulent and slug flow. Identical thermo-physical properties and flow conditions are used for the three simulations (see Tables D.1 and D.2 for the set of parameters)	171